SAPIENZA
UNIVERSITÀ DI ROMA

ASCENSION
Advancing Space Access Capabilities – Reusability and Multiple Satellite Injection

Ph.D. Thesis

Expansion-Deflection Nozzle Design and Performance Optimization for Upper-Stage Applications

Candidate
Felix Weber
Advisor
Prof. Daniele Bianchi
Co-Advisor
Prof. Francesco Nasuti

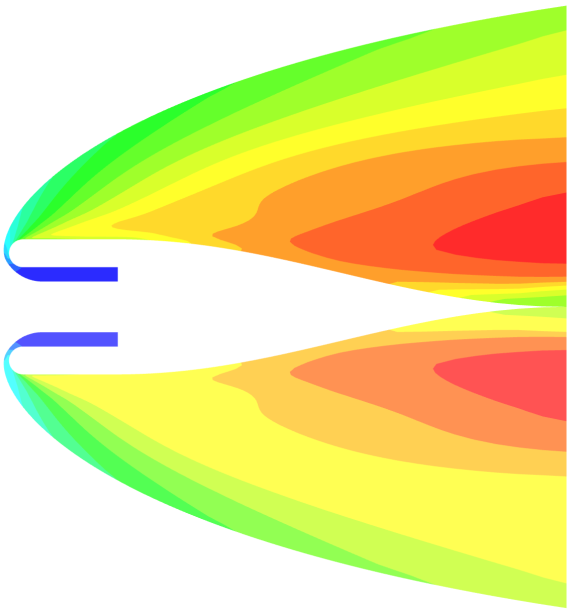

Author's e-mail: felix.weber@uniroma1.it
Author's address: Dipartimento di Ingegneria Meccanica e Aerospaziale
Università di Roma "La Sapienza"
Via Eudossiana, 18
00184 Roma – Italia
web: `http://www.dima.uniroma1.it`
Submitted: October 21, 2024

Abstract

ED nozzles have been studied for many years as a possible replacement for conventional rocket nozzles. For moderate nozzle pressure ratios, ED nozzles suffer from overexpansion losses and aspiration drag, making them inferior to plug nozzles and even dual bell nozzles. In high-altitude operation, ED nozzles show advantages over conventional nozzles due to lower divergence losses and, thus, possibly shorter design lengths promising higher performance-to-weight ratios as the plug nozzle. However, in contrast to plug nozzles, they feature less radial throat distances from the symmetry axis, reducing the wall surface exposed to the peak heat flux and thus the needed heat pick up from the cooling system. All these combined make the ED nozzle a promising concept for the upper stages. The ED nozzles in this work are designed with a dedicated design methodology that calculates the ideal contour, providing isentropic expansion. The supersonic walls are calculated using an approximate contouring method based on the MOC, which is integrated into different design procedures to find the desired nozzle iteratively. The design of the subsonic walls is kept as simple as possible, using only straight lines and arcs. Then, a *VINCI*-sized upper-stage Baseline ED and a conventional nozzle are designed, and preliminary CFD simulations are conducted to select suitable meshes for the parametric analyses. The parametric analyses investigate the influence of various geometrical parameters on the performance. The geometrical parameters are the outer nozzle dimensions, i. e. the truncation length and radius, the specific heat ratio design value, the radial throat shifting, the throat wall curvature radii, and the geometrical scaling factor. The CFD methods are verified and validated using the two conventional test case engines *RL10A-3-3A* and the *SSME*, providing less and more thrust than the *VINCI* reference engine.

Contents

Nomenclature

Latin Notations

a	Speed of sound, NASA polynomial coefficient for thermophysical properties
atm	Pressure of standard atmosphere $\approx 1013\ hPa$
A	Area, Passage area of the flow
b	NASA polynomial coefficient for transport properties
c^*	Characteristic velocity
c_p	Specific heat capacity at constant pressure
c_v	Specific heat capacity at constant volume
C_F^0	Thrust coefficient under adapted conditions
C_F	Thrust coefficient
e	Specific total energy, Mathematical constant
E	Energy, Total energy
f	Volumetric force per unit mass
F	Thrust, Fuel
g_0	Gravitational constant of the earth $\approx 9.80665\ \frac{m}{s^2}$
G	Gibbs energy
$\Delta\overline{h_f^0}$	Enthalpy of formation
h	Height, Specific enthalpy
H	Enthalpy
H_s	Scale height
I_{sp}	Specific impulse
k	Thermal conductivity
m	Mass, Slope of linear function
$\dot{m}$	Mass flow rate
m_{end}	Final rocket mass
m_f	Fuel mass
m_{init}	Initial rocket mass
m_r	Rocket mass
M	Mach number
$\mathcal{M}$	Molar Mass
M_R	Mass relation of a rocket
n	y-Axis crossing of linear function, Running and counting variable
$\vec{n}$	Surface normal vector
N	Number, Molar amount
O	Oxidizer
p, P	Pressure

Q	Heat Energy
r, R	Radius
r_{non}	Non-dimensional external wall radius of arc in internal expansion region
R_c	External wall radius of arc in internal expansion region
R_i	y-coordinate of origin of last internal characteristic along external wall
$\mathcal{R}_s$	Specific gas constant
$\mathcal{R}_u$	Universal gas constant $\approx 8.314\ \frac{J}{K \cdot mol}$
s	Specific entropy
S	Surface area of a characteristic line, Entropy, Control Surface
$\vec{S}$	Surface of the control volume
t	Time
T	Temperature
$\vec{u}, \vec{v}$	Velocity vector (In general)
u	Specific internal energy
U	Internal energy
Δv	Maximum change of velocity of the vehicle
$V, \mathcal{V}$	Volume
W	Weight, Work
x, y, z	Cartesian coordinates
Y	Mass fraction
X	Mole fraction

Greek Notations

α	Angle (In general), Geometrical angle between characteristic line and reference axis
γ	Specific heat ratio/ Specific heat capacity ratio
Γ	Diffusion constant, Vandenkerckhove function
∂	Partial derivation
Δ	Difference
ε	Nozzle expansion ratio
η	Non-dimensional y-coordinate
η_b	Non-dimensional radius of ED nozzle central body
η_c	Non-dimensional y-coordinate of arc center point in internal expansion region
η_i	Non-dimensional y-coordinate of origin of last internal characteristic along external wall
Θ	General: Angle, Also: Angle between velocity vector and reference axis
λ	Thermal conductivity
μ	Dynamic viscosity, Mach angle
ν	Prandtl-Meyer function
ρ	Density
ϕ	Viscosity interaction coefficient
Φ	Amount of a certain quantity
ξ	Non-dimensional x-coordinate

ξ_c	Non-dimensional x-coordinate of arc center point in internal expansion region
ξ_i	Non-dimensional x-coordinate of origin of last internal characteristic along external wall
ψ	Thermal conductivity interaction coefficient
$\vec{\nabla}$	Nabla operator

Indices

0	Seal level condition
1	Throat wall contour point along outer wall
2	Throat wall contour point along inner wall
a	Ambient condition
b	Base (also Central Body) of the ED nozzle
c, cc	Nozzle (combustion) chamber
e	Nozzle exit
i	Last internal Characteristic
inf, ext	Inferior (external) wall
$init$	Initial (Value)
mix	Mixture
$orth$	Orthogonal
Ref	Reference
s	Species
sup, int	Superior (internal) wall
t, th	Nozzle throat, total (t)
$trunc$	Truncation
vac	Vacuum
w	Nozzle Wall
x	Current/ Momentary (Value)

Abbreviations

ANC	Advanced Nozzle Concept
ASCenSIon	Advancing Space Access Capabilities - Reusability and Multiple Satellite Injection
CADB	Chemical Automatics Design Bureau
CC	Combustion Chamber
CEA	Chemical Equilibrium with Applications
CFD	Computational Fluid Dynamics
DLR	From German: German Aerospace Center
DNS	Direct Numerical Simulation
EADS-ST	European Aeronautic Defence and Space Company - Space Transportation GmbH

EC	European Commission
ECA	From French: Cryogenic Evolution of Type A
ED	Expansion-Deflection (Nozzle)
ESA	European Space Agency
ESC-A	From French: Cryogenic Upper Stage of Type A
ESC-B	From French: Cryogenic Upper Stage of Type B
ESR	Early-Stage Researcher
ESTEC	European Space Research and Technology Centre
FL	Full Length
FVM	Finite Volume Method
GCS	Grid Convergence Study
GNC	Guidance, Navigation and Control
GTO	Geostationary transfer orbit
H	Atomic Hydrogen
H2	Molecular Hydrogen
H2020	Horizon 2020
H2O	WATER
LH2	Liquid Hydrogen
LOX	Liquid Oxygen
ME	From French: Mid-Life Evolution
MOC	Method of Characteristics
NASA	National Aeronautics and Space Administration
NE	Nozzle Extension
NPR	Nozzle Pressure Ratio
NS	Navier-Stokes
O	Atomic Oxygen
O2	Molecular Oxygen
OH	Hydroxid
P/L	Payload
Ph.D	From Latin: Philosophy Doctor
RLV	Reusable Launch Vehicle
SLS	Sea-Level-Standard
SRB	Solid Rocket Booster
SSME	Space Shuttle Main Engine
SSTO	Single-Stage-to-Orbit
STS	Space Transportation System
TCA	Thrust Chamber Assembly
TEKAN	From German: Technology Development for Cryogenic Propulsion

TIC	Truncated Ideal Contour
TOC	Thrust Optimized Contour
USA	United States of America
VL	Vertical Landing

List of Figures

List of Tables

Chapter 1

Introduction

1.1 Background

Space research has always enabled mankind to push the boundaries of what is possible and allows new perspectives on their planet and the universe. Even though space pioneers like Robert Goddard were mocked as dreamers 100 years ago, they pursued visionary goals. Goddard, the father of modern rocket propulsion, was the first to prove that thrust and propulsion can occur in a vacuum, needing no air to push against. This assertion fueled the primal desire of humanity to one day overcome Earth's gravity and reach space, the moon, or other planets using rockets. Driven by this goal, Goddard was the first to successfully launch a liquid-fueled rocket carrying even scientific payloads such as camera equipment and a barometer. The Germans eventually took up Goddard's ideas, which led to the development of the *V2* rocket weapon during the Second World War. After the Second World War, many German scientists, including Wernher von Braun, immigrated to the USA or the Soviet Union. The so-called *Space Race* between these two superpowers began and spurred tremendous and rapid developments in rocketry in just a couple of decades. This culminated in the design of the *Saturn V* rocket, taking the first astronauts to the moon on the 21st of July 1969. After that, the time of great leaps in human space exploration was over, and engineers concentrated on optimization.
One example is the development of the *Space Shuttle* (as shown in Fig. 1.1) as an early reusable spaceship with its first STS-1 mission in 1981. More precisely, the *Space Shuttle* was partially reusable since the external fuel tank that held the fuel for the Space Shuttle Main Engine (*SSME*) was not reusable and burned up in an uncontrolled atmospheric reentry, typically over the Pacific Ocean. All the other components were completely reusable, such as the orbiter itself and the solid rocket boosters (SRBs) that operated in parallel with the main engines for the first two minutes of the flight [1]. Their responsibility was to provide additional thrust needed for the orbiter to escape the Earth's gravitational pull. At approximately 45 km of altitude, the boosters separated to descend on parachutes and land in the Atlantic Ocean. Then, ships recovered them, returned them to land, and they were refurbished for reuse.
A recent example of launcher reusability development is the *SpaceX* rocket program. The 21st of December 2015 has to be mentioned since this is one of the most significant dates in this field in the last decades. The reason is that *SpaceX* demonstrated a first-stage recovery by applying retro-propulsive vertical landing (VL) on the land of their two-staged *Falcon 9* launcher. By achieving this milestone, a new age of reusable launch vehicles (RLV) was established since, up to this date, the first stages (also called main stages) were never reusable. However, since the second rocket stage after the payload delivery is still safely disposed of after the deorbit burn, also this launch vehicle remains partially reusable. However, *SpaceX* is already developing a

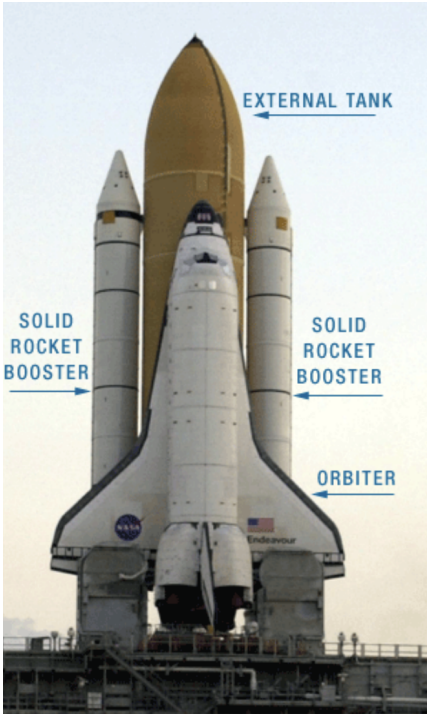

Figure 1.1: The components of the *Space Shuttle* system: the orbiter, external tank, and solid rocket boosters [1]

fully reusable two-stage launch vehicle named *Starship*.
But why is reusability such a big driver of modern space engineering? The reason is that reusability promises two advantages. The first advantage is the decrease in space debris, which has a positive environmental impact (sustainability). The second advantage is the reduction of launch costs. This did not work out in the case of the *Space Shuttle* since, after every mission, the spacecraft had to be prepared for the next launch and costly refurbished for reuse. Besides the US, the European aerospace industry is currently staking on sustainability [2]. This was declared within the scope of the European Green Deal that was introduced on the 11th of December 2019 by the European Commission (EC). To foster this goal and to enable cost-efficient, independent space access for Europe, the ASCenSIon (Advancing Space Access Capabilities - Reusability and Multiple Satellite Injection) project was launched in 2020. It is an innovative training and research network [3] that focuses on cutting-edge space research, particularly on launcher systems that are (partially) reusable and capable of injecting multiple payloads into multiple orbits. ASCenSIon is funded by the EU's Horizon 2020 (H2020) research and innovation program under the Marie Sklodowska-Curie grant agreement. It connects fifteen early-stage researchers (ESRs) and twenty-four partner organizations all across Europe.
Each of those fifteen Ph. D. students covers their research field within the ASCenSIon consortium. These include, for instance, guidance, navigation, and control (GNC), aerothermodynamics of reentry for the recovered stages, and, among others, the propulsion system. Covering many different research fields is inevitable since the development of RLV is a very complex and interdisciplinary field. In addition, interactions happen naturally. For instance, many aspects are crucial when developing the propulsion system, such as the turbopumps, suitable propellants, and the nozzle. The rocket nozzle, which this Ph. D. thesis is about, is an essential component as it determines the expansion efficiency of the exhaust gases and the overall mass balance of the propulsion system.

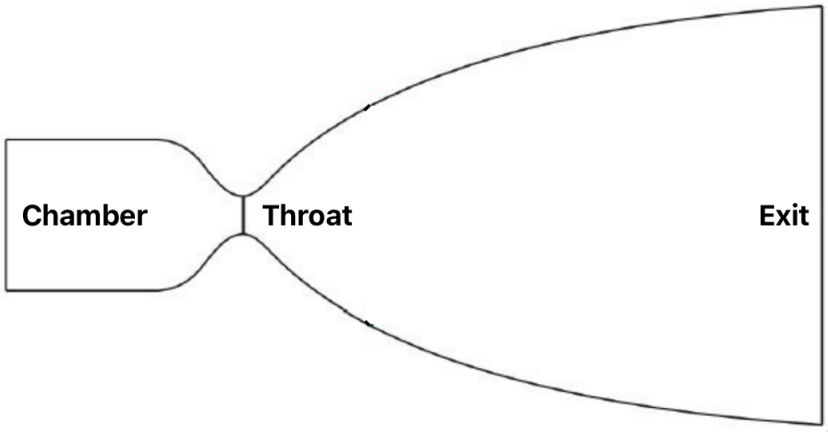

Figure 1.2: Generic conventional convergent-divergent rocket nozzle

1.2 Motivation

During the rocket's ascent, i. e. on its way into space to deliver payloads like satellites into orbit, the ambient pressure p_a decreases with altitude. In the following, a distinction is made between two areas. First, an area where the ambient pressure decreases with increasing altitude (low-altitude operation), and second, the high-altitude operation where the ambient pressure remains zero in full vacuum conditions. The barometric formula 1.1 describes the exponential decrease in atmospheric pressure with increasing height h. The pressure p_0 is the atmospheric pressure at sea level. The quantity H_s is the scale height and can be described by Eq. 1.2 with the sea level density ρ_0 and the Earth's gravitational constant g_0.

$$p_a(h) = p_0 \cdot e^{\frac{-h}{H_s}} \tag{1.1}$$

$$H_s = \frac{p_0}{\rho_0 \cdot g_0} \tag{1.2}$$

Until now, only conventional convergent-divergent nozzles have been used for real launcher applications. Different operation modes arise if these nozzles are operated in low-altitude conditions, negatively impacting the performance. In high-altitude operation, conventional nozzles show design disadvantages. More details are given in Subsections 1.2.1 and 1.2.2.

1.2.1 Conventional nozzle: low-altitude operation

In liquid rocket engines with high mass flow rates, turbopumps transport the fuel and oxidizer under high pressure in the combustion chamber. In addition to high-pressure energy, the propellants contain chemical energy converted into thermal energy during the isobaric combustion process. The total energy of this hot pressurized exhaust gas after the combustion process is referred to as enthalpy. Then, the exhaust gas expands rapidly in the rocket nozzle shown in Fig. 1.2. During the expansion, the temperature and pressure drop, and the enthalpy is converted into kinetic energy [4]. In the subsonic flow regime between the chamber and throat, the expansion is initiated by reducing the nozzle cross-sectional area. In the throat, the exhaust gas reaches sonic conditions $M = 1$. In the supersonic flow regime after the throat, the gas dynamic dependencies turn around, so further expansion to $M > 1$ can only occur by increasing the nozzle cross-sectional area.

Under the assumption of isentropic expansion between the chamber and exit, the stagnation or total flow properties of pressure, temperature, and density remain constant. Equation 1.3 shows the isentropic relation for pressure. The quantity p_c is the chamber pressure, M_e is the exit Mach number, and γ is the specific heat ratio. The latter is considered constant in this equation. Equation 1.3 clarifies that small exit pressures p_e are realizable by high exit Mach numbers, i. e. high expansion ratios ε. The expansion ratio is defined as the ratio of the exit and throat area of the nozzle $\frac{A_e}{A_t}$.

$$\frac{p_e}{p_c} = \left(1 + \frac{\gamma - 1}{2} \cdot {M_e}^2\right)^{\frac{-\gamma}{\gamma-1}} \tag{1.3}$$

However, the expansion ratio is fixed for conventional convergent-divergent nozzles. Hence, also $\frac{p_e}{p_c}$ in Eq. 1.3 is fixed. As a result, the exit pressure equals the ambient pressure ($p_e = p_a$) only for one altitude along the ascent trajectory. This is the design altitude of the nozzle. The nozzle works as efficiently as possible for the design point since the outflow is perfectly adapted to the ambient pressure. For the design point, the 1D thrust coefficient C_F is calculated for constant γ only from the velocity contribution C_F^0 by Eq. 1.4. The quantity Γ is the Vandenkerckhove function and is just a function of the specific heat ratio γ, as shown in Eq. 1.5.

$$C_{F,design} = C_F^0 = \Gamma \cdot \sqrt{\frac{2 \cdot \gamma}{\gamma - 1}\left(1 - \left(\frac{p_e}{p_c}\right)^{\frac{\gamma-1}{\gamma}}\right)} \tag{1.4}$$

$$\Gamma = \sqrt{\gamma \cdot \left(\frac{2}{\gamma + 1}\right)^{\frac{\gamma+1}{\gamma-1}}} \tag{1.5}$$

The biggest drawback of conventional nozzles is that there is just one design point during the rocket's ascent. When the nozzle operates at altitudes different from the design point, the exit pressure differs from the local ambient pressure, and non-adapted nozzle flows result. In this case, Eq. 1.4 must be extended by an additional pressure term:

$$C_{F,off-design} = C_F^0 + \varepsilon \cdot \left(\frac{p_e}{p_c} - \frac{p_a}{p_c}\right) \tag{1.6}$$

A distinction is made between two non-adapted flow conditions. On the one hand, the local ambient pressure can be higher than the nozzle exit pressure. This is called overexpansion and happens for altitudes lower than the design altitude. The result is a lower thrust coefficient than in the design point due to a negative pressure term, as shown in Fig. 1.3. In the case of nozzles with high expansion ratios operating close to the ground, the local ambient pressure is much higher than the nozzle exit pressure. As a result, flow separation from the nozzle walls can occur since the exhaust flow gets contracted by the ambient pressure. This results in high side loads [5] that cause high structural stresses or even the destruction of the nozzle. Many criteria can predict at which pressure ratio p_e/p_a flow separation is most likely to happen. Summerfield [6], for instance, proposed a ratio of around $0.35 - 0.40$.
On the other hand, the local ambient pressure can be lower than the nozzle exit pressure for altitudes higher than the design altitude. This operational mode, called underexpansion, results in positive pressure terms that even slightly increase the thrust coefficient w. r. t. the design value. However, as shown in Fig. 1.3, for the over- and underexpansion, the thrust coefficient is always lower than for perfectly adapted conditions. The adaptation losses are particularly high in case of overexpansion. Multi-staging is used to keep them as low as possible. Each stage nozzle has a different expansion ratio and is designed for a different altitude. According to [7], in this way, the adaptation losses can be reduced to maximal 15 % in the case of *Vulcain 1* and *SSME*.

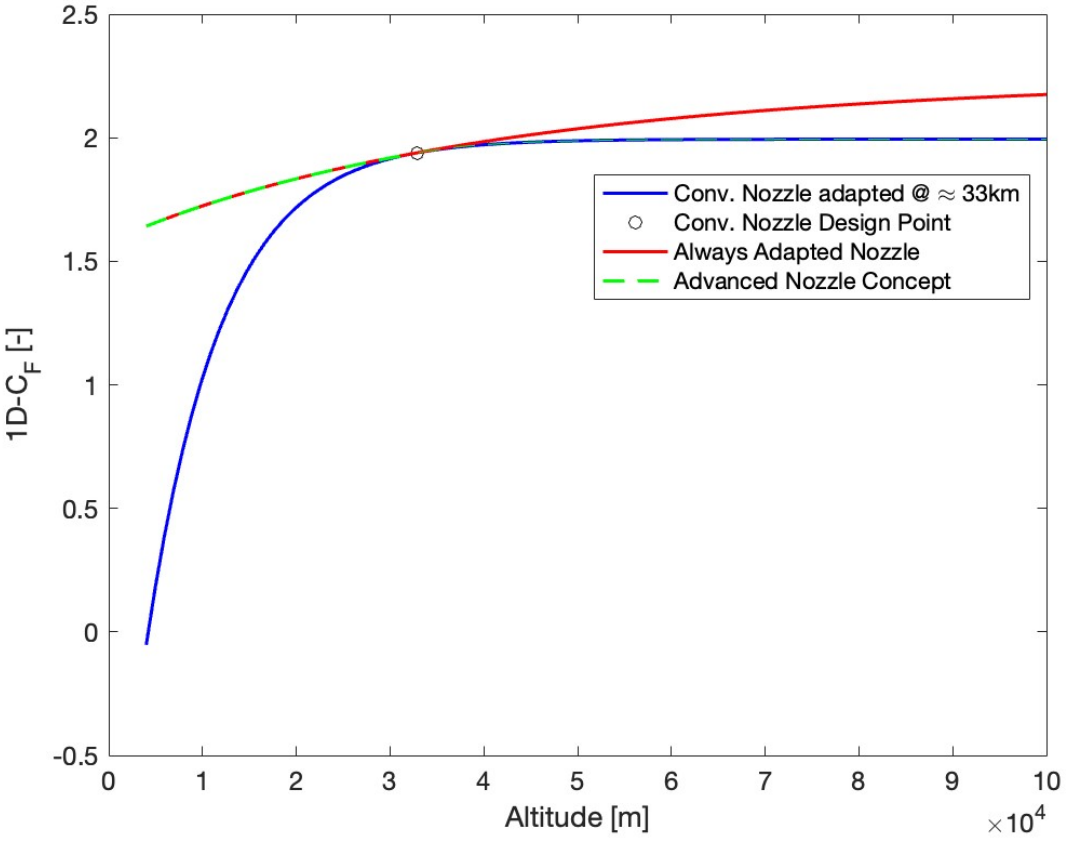

Figure 1.3: 1D Thrust coefficient C_F for a conventional nozzle with a chamber pressure of $p_c = 60$ bar, expansion ratio of $\varepsilon = 200$ and constant specific heat ratio of $\gamma = 1.2$ compared to an ideal nozzle adapted to all altitude and advanced nozzle concept (ED and plug nozzles)

1.2.2 Conventional nozzle: high-altitude operation

Under full vacuum conditions, the ambient pressure p_a is zero, and the term $\frac{p_a}{p_c}$ in Eq. 1.6 is omitted. Inserting the isentropic relation for $\frac{p_e}{p_c}$ (Eq. 1.3) in Eq. 1.6, the vacuum thrust coefficient in Eq. 1.7 can be derived. This equation shows that the vacuum thrust coefficient for constant γ is only a function of the exit Mach number and the expansion ratio. Consequently, the highest possible expansion ratio is desirable to achieve the highest possible vacuum performance.

$$C_{F,vac} = \Gamma \cdot \sqrt{\frac{\gamma \cdot {M_e}^2}{1 + \frac{1}{2} \cdot (\gamma - 1) \cdot {M_e}^2}} + \frac{\varepsilon}{(1 + \frac{1}{2} \cdot (\gamma - 1) \cdot {M_e}^2)^{\frac{\gamma}{\gamma - 1}}} \tag{1.7}$$

For conventional nozzles, high expansion ratios inevitably lead to relatively long designs to keep divergence losses low. This is another drawback of conventional convergent-divergent nozzles besides the lack of altitude adaptation. The reason is that long nozzles increase the nozzle weight and require more space in the longitudinal direction. For upper stages, longitudinal space is always very limited in contrast to radial space. There are two options for reducing the nozzle length. First, the nozzle can be truncated, resulting in a smaller expansion ratio and higher divergence performance losses. Second, a shorter nozzle can be designed for the same expansion ratio, i. e. exit radius, which also increases divergence losses. Hence, reducing the nozzle length always causes reduced performance, i. e. thrust coefficient. Therefore, with conventional nozzles, the choice is between a well-performing longer and heavier nozzle or a compacter and lighter design with less performance.
Extendable nozzle extensions (NE), like in the case of the *RL10* propulsion system [8] (see Fig. 1.4), can be used for upper stages. This guarantees that the nozzle is compact when stored, enabling a shorter and lighter interstage. Only when the nozzle is used, the nozzle extension is employed, increasing the expansion ratio and the thrust coefficient. However, the complexity increases when the extension mechanism is added to the design.

1.2.3 Conventional nozzle: interim conclusion

In Subsection 1.2.1, it is discussed in more detail that conventional nozzles suffer substantially from the lack of altitude adaptation in low-altitude operations. This has a negative impact on the thrust coefficient C_F. In Subsection 1.2.2, it is mentioned that high-performing conventional vacuum nozzles are inevitably long and heavy. To comply with the maximal acceptable dimensions, a reduction of the thrust coefficient has to be accepted. Therefore, conventional nozzles have either the problem of low performance or high mass, i. e. they feature relatively low performance-to-weight ratios.
The thrust coefficient is a nozzle quality factor and should be as high as possible. The reason is that increasing the thrust coefficient C_F also increases the engine thrust F provided that the chamber pressure p_c and the throat area A_t, i. e. the mass flow rate $\dot{m}$ remains constant, as shown in Eq. 1.8. Accordingly, an increase in C_F also implies an increase in the specific impulse I_{sp}, which is a quality factor of the whole propulsion system, as shown in Eq. 1.9.

$$F = p_c \cdot A_t \cdot C_F \tag{1.8}$$

$$I_{sp} = \frac{F}{\dot{m} \cdot g_0} \tag{1.9}$$

The Tsiolkovsky rocket Eq. 1.10 describes the change of velocity Δv of a rocket (accessible orbit) as a function of the specific impulse I_{sp} of the propulsion system and the mass ratio MR. The

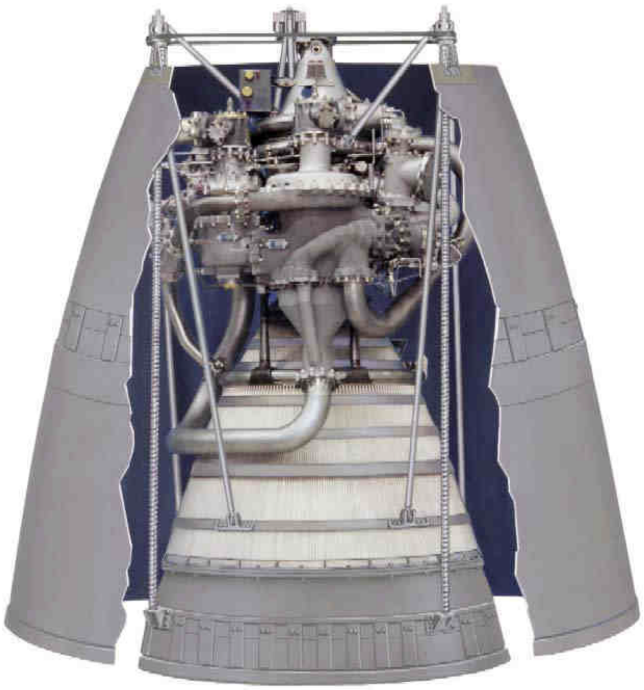

Figure 1.4: RL10B-2 engine with nozzle extension in stowed condition – interstage configuration [9]

mass ratio describes the ratio of the initial mass m_{init}, i. e. the rocket mass m_r and the fuel mass m_f, and the final mass m_{end}, as shown. in Eq. 1.11. Simplified, the final mass can be defined as the rocket mass m_r after all the propellants are burned. In the following, the effect of increasing the I_{sp}/W ratio, i. e. increasing the I_{sp} and decreasing the propulsion system mass W, is discussed by means of the Tsiolkovsky equation.

$$\Delta v = I_{sp} \cdot g_0 \cdot ln(M_R) \tag{1.10}$$

$$M_R = \frac{m_{init}}{m_{end}} = \frac{m_r + m_f}{m_r} \tag{1.11}$$

An increase in I_{sp} has two advantages. First, the rocket can reach a higher orbit Δv for a constant mass ratio. Second, the mass ratio can be decreased for a constant target orbit Δv, which characterizes an efficient rocket design. A low mass ratio means that the rocket mass (including the payload mass) can be increased for a constant fuel mass. Moreover, the fuel mass can be reduced for a constant rocket mass.
By decreasing the weight W of the propulsion system, for instance, by a lighter nozzle, the rocket mass m_r is reduced. This has two advantages. First, the mass ratio of the rocket increases for a constant fuel mass m_f. For a constant I_{sp}, a higher orbit Δv can be reached. Second, for a constant orbit Δv and I_{sp}, the mass savings of the propulsion system can be used to increase the payload mass provided that the fuel mass and the mass ratio remain constant.
In any case, increasing the I_{sp} and decreasing the weight W of the propulsion system positively impacts the whole space mission since space access can get cheaper and more efficient. However, the mass ratio has a logarithmic effect on the accessible orbit Δv in contrast to the I_{sp}. Consequently, the I_{sp} should not be optimized to the detriment of the mass ratio M_R.

1.3 The expansion-deflection (ED) nozzle

Advanced nozzle concepts (ANC) like plug/ aerospike, dual bell, and expansion-deflection (ED) nozzles have been explored to address the disadvantages of conventional convergent-divergent nozzles since the 1950s and 60s. Even though all of these nozzles show qualities to be used in launch systems, this Ph. D. thesis focuses on the ED nozzle.
Subsection 1.3.1 gives a brief overview of the main design characteristics of the ED nozzles. In Subsections 1.3.2 and 1.3.3, the operating modes of the ED nozzle are discussed. A distinction is made between low- and high-altitude operations. In addition, the current state of research is discussed. System-related aspects of the ED nozzle are discussed briefly in Subsection 1.3.4. The Section is concluded in the Subsection 1.3.5.

1.3.1 Design characteristics

In the context of ED nozzles, the work by Rao [10] has to be mentioned, as this forms the basis of the ED nozzle design. Figure 1.5 shows a generic ED nozzle. The flow is first accelerated to sonic flow conditions in the throat ($M = 1$) after the combustion chamber, equivalent to conventional nozzles. The throat differs from a conventional nozzle as it is displaced and possibly inclined w. r. t. the symmetry axis as shown in Fig. 1.5. Downstream of the throat, the gas **expands** through an internal and external expansion fan. The latter originates from the central body of the ED nozzle. As a result, the flow is **deflected**, and a full axial flow is obtained at the end of the external expansion. The name **expansion-deflection** nozzle is derived from this expansion process. According to [11], the nozzle length can be significantly reduced w. r. t. bell nozzles since the external expansion occurs around a simple corner in a centered expansion fan. Rao [12] claimed that a length reduction of up to 50% is possible, provided that the ED and the bell nozzles are designed with a minimum length scheme [11]. However, the compactness advantage also applies to plug nozzles, as shown by [13].
Basically, at the origin of the external expansion fan, the flow gets inevitably separated from the central body as it cannot follow the significant change in direction. However, how much the flow expands and is deflected around the central body at this point also depends on the base pressure. Depending on this pressure, the ED nozzle experiences different operating modes.

1.3.2 Low-altitude operation

In low altitudes, the local ambient pressure p_a outside the nozzle is the highest during the ascent phase, and the nozzle pressure ratio $NPR = \frac{p_c}{p_a}$ is the lowest. In this case, an *Open-Wake* operation mode is formed, as shown in Fig. 1.6. This means the nozzle is not fully flowing, and a void is formed from the exit plane to the central body. A recirculation of ambient air opposite to the flow direction of the expanding gas characterizes this zone. As a result, the base pressure p_b is relatively high and theoretically contributes to thrust. The nozzle flow has a constant pressure-free boundary with the recirculation zone and adapts its expansion ratio depending on the pressure in the recirculation zone [7]. Hence, for low NPR, the gas expansion is relatively weak, and the wall pressure of the ED nozzle is relatively high, as shown in Fig. 1.7. According to Rao [10], this is referred to as compressive turning. The adaptation happens through a system of recompression and expansion waves, which is noticeable in wavelike wall pressure behavior along the nozzle wall. Rao [10] was the first to describe the adaptation capability of the ED nozzle, which is the key property of ED nozzles in low-altitude operations. As the ambient pressure decreases and the NPR increases during the rocket's ascent, the base pressure p_b decreases. This allows the exhaust gas to expand even more and continuously increase the expansion ratio. As a result, the flow envelope moves toward the center line, and the wall

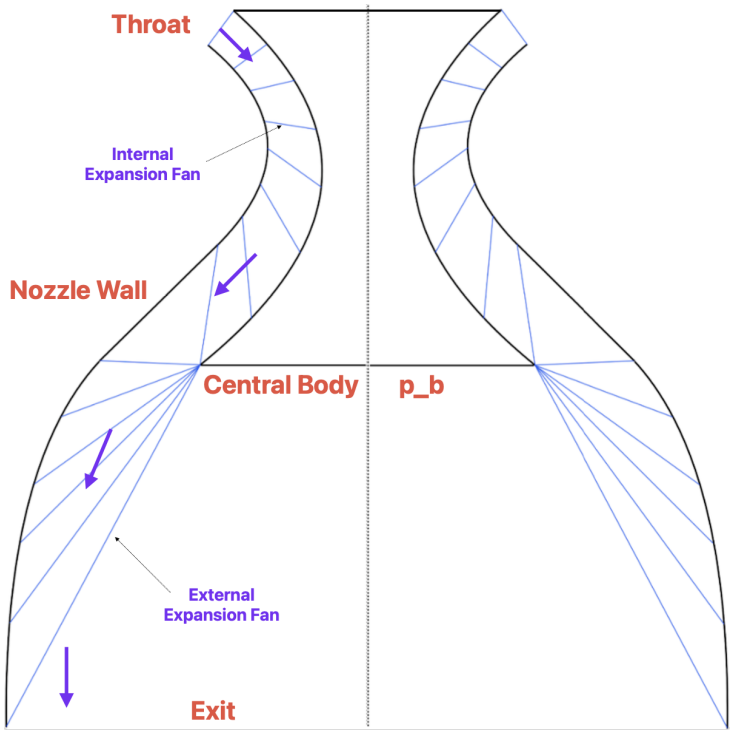

Figure 1.5: Generic ED nozzle with basic design characteristics

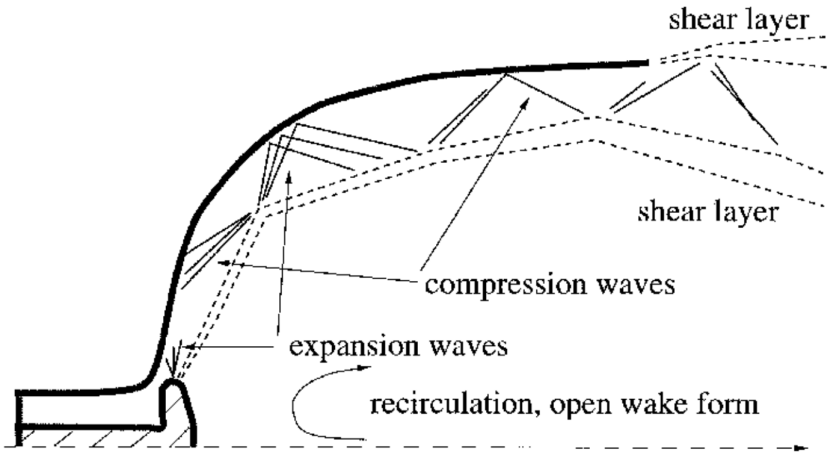

Figure 1.6: ED nozzle open-wake operation mode [7]

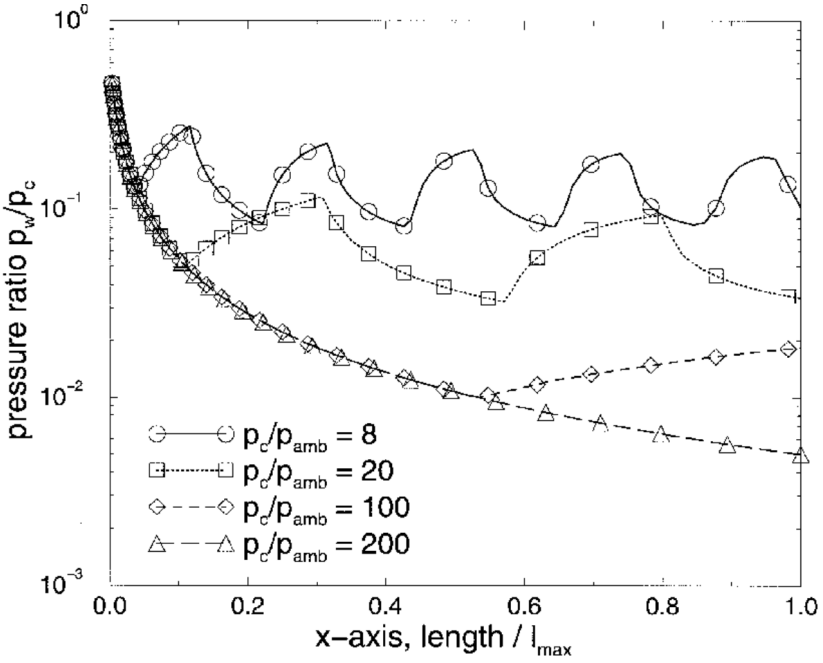

Figure 1.7: Wall pressure along linear subscale plug nozzle (equivalent to ED nozzle) [7]

pressure decreases and features a less frequent fluctuating behavior, as shown in Fig. 1.7. The altitude adaptation of the ED nozzle continues until the geometrical expansion ratio of the nozzle is reached. Theoretically, as long as the nozzle adapts, it demonstrates ideal maximum performance, i. e. thrust coefficient C_F. This is higher than that of conventional nozzles that cannot adapt due to the fixed geometrical expansion ratio, as discussed in Section 1.2.1. The ED nozzle has always been the subject of extensive research since Single-Stage-to-Orbit (SSTO) applications are theoretically possible. Wasko (NASA) [14] has to be mentioned in this context since he performed comprehensive cold-flow tests in the late 60s and 70s and compared the ED and plug nozzles regarding altitude adaptation. Wasko proved that the pressure inside the recirculation zone of the ED nozzle is slightly lower than the actual local ambient pressure outside the nozzle due to the sucking effect of the hot gas. This phenomenon is called the aspiration effect and is equivalent to the ED nozzle adapting to a slightly higher altitude. Hence, the ED nozzle suffers from overexpansion losses. Moreover, additional friction losses occur at the shear layer between the recirculating and expanding flow, also called aspiration drag. The overexpansion and aspiration drag lead to real limitations as the performance is adversely affected. According to [7], also the plug nozzles suffer from overexpansion and aspiration drag. However, these losses are less pronounced than those of the ED nozzle [14].
Taylor [15] compared the ED and dual bell nozzles on altitude compensation through cold flow tests at nozzle pressure ratios encompassing the entire compensating regime. Even though the dual bell nozzle features only a two-stage altitude compensation and suffers from aspiration drag in low-altitude operations, it performed better than the ED nozzle.
It can be concluded that the ED nozzle can benefit from compactness, but the flow patterns in low-altitude operation are complex and challenging to harness [16]. Hence, the ED nozzle cannot demonstrate higher low-altitude performance than the plug and dual bell nozzles. For low-altitude operations, this is the reason for the lack of interest in the ED nozzle for many years, and the research shifted more toward the plug and dual bell nozzles. A European example is Pangea Aerospace, which is more focused on plug nozzles with projects such as the 20 kN

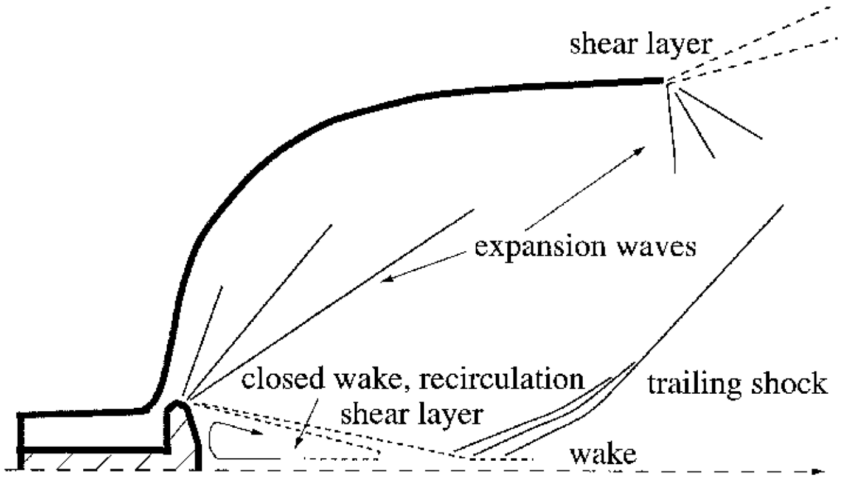

Figure 1.8: ED nozzle closed-wake operation mode [7]

Demo P1 and 300 kN *ARCOS* (in development) LOX/LCH_4 engines. These nozzles combine the advantages of a compact design and promising performance.

1.3.3 High-altitude operation

High-altitude operation is reached when the ambient pressure p_a and the base pressure p_b decrease to such an extent during the rocket's ascent that the expanding hot gas flow converges behind the central body, as shown in Fig. 1.8. A trailing shock forms, turning the flow in the axial direction. In high-altitude operations, the ED nozzle reaches its geometrical expansion ratio, which will not continue to increase even at higher altitudes. Altitude adaptation ceases, and the nozzle behaves like a conventional nozzle. The nozzle exit plane is fully flowed with a supersonic flow. Thus, disturbances related to ambient pressure cannot work their way upstream, and the recirculation zone in front of the central body is completely evacuated [17]. The pressure of the recirculation zone and the base pressure remain unaffected by the ambient pressure. Hence, the base pressure is low and does not contribute substantially to the nozzle thrust. Also, the wall pressure remains unaffected and decreases in the axial direction toward the nozzle exit without the wave pattern typical for low-altitude operations.
A special feature of high-altitude operation is that the aspiration drag is omitted. For further decreases in ambient pressure, the nozzle suffers only from underexpansion, similar to conventional nozzles. In Subsection 1.2.2, it is discussed that conventional nozzles must be designed relatively long for high expansion ratios to keep the divergence losses low. ED nozzles generally have lower divergence losses than conventional nozzles [7]. Provided that the conventional and ED nozzles are designed for the same expansion ratio, the ED nozzle can be designed shorter for the same performance. In addition, the ED nozzle can feature higher performance for the same length. However, these advantages also apply to plug nozzles, as demonstrated by Nasuti et. al. [13]. In cold flow tests, Taylor [15] experimentally proved higher performance than conventional nozzles in high-altitude operations, also for the dual bell nozzles.
The compact design and high vacuum performance make the ED nozzle interesting for upper-stage applications. Noteworthy is the work by Löbbecke [18] and Koelle [19] in 1964/65 at *Bölkow* (now *Airbus Defence and Space*) in Ottobrunn [16]. Even though a contour is used in these investigations, yielding only non-optimal performance, the mechanical nozzle concept proposed is interesting. The reason is that a combustion chamber was foreseen integrated into the central body of the ED nozzle, reducing the length even more. This is the earliest trace of an inverse

Figure 1.9: Russian ED nozzle RD0126E for potential upper-stage applications [22]

thrust chamber configuration [16].
In addition, the *Chemical Automatics Design Bureau* (CADB) in Russia worked intensively on ED nozzles [20]. The cryogenic *RD-0126E* LOX/LH_2 rocket engine in Fig. 1.9 was developed that was initially foreseen for the upper stage of the *Soyuz-2.1* launcher. The thrust chamber is also designed as a reverse flow configuration [16]. Since the wall heat transfer in ED nozzles is higher than for conventional nozzles, the nozzle was integrated into an expander engine cycle to increase performance. Despite two successful test campaigns on pressure-fed test strands in that the nozzle demonstrated a specific impulse of approximately 472 s, the development was finished in favor of a conventional nozzle [16].
The TEKAN (Technologie-Entwicklung für Kryogene Antriebe) project was a cooperation between the DLR and EADS-ST (nowadays *Airbus Defence and Space*), focused on future cryogenic rocket propulsion [21]. In 2000, it was stated that by replacing *Ariane 4* with *Ariane 5*, the payload could be increased by 6 to 11 t for the geostationary transfer orbit (GTO) by solely improving the propulsion system. The research focused on several engine aspects, such as heat transfer, cooling, mechanical loads, and materials. In addition, the propellant injection, mixing, and modeling were addressed. The ED nozzle was discussed for high-altitude operation due to the advantage of a short overall geometric envelope [16]. An annular and inverted (reverse flow) thrust chamber was designed, and numerical flow field studies and an experimental test campaign at the *Keldysh Research Center* were conducted with dry cold air [16]. The cold flow tests and the CFD simulations showed good agreement and confirmed the high vacuum efficiency of the ED nozzle. The wall heat flux of the ED and an equivalent conventional bell nozzle was compared numerically for the LOX/LH_2 *VINCI*-size. The simulations demonstrated a comparable peak heat flux density for both nozzles despite strong flow redirection of the sub- and supersonic flow in the case of the ED nozzle.

In 2005, the preliminary investigation for *VINCI* within the TEKAN project was extensively continued by EADS-ST [16]. The contour of the ED nozzles was designed as a truncated ideal contour (TIC) assuming Prandtl-Meyer expansion, i. e. isentropic expansion. Various ED nozzles with different lengths and truncation exit radii, i. e. expansion ratios were designed, and the I_{sp} was evaluated with the design tool. The combustion, friction, and chemical kinetic performance losses, as well as the thrust contribution of the central body, were evaluated empirically. For the same I_{sp} and expansion ratio of the ED and conventional nozzles, the ED nozzle could be

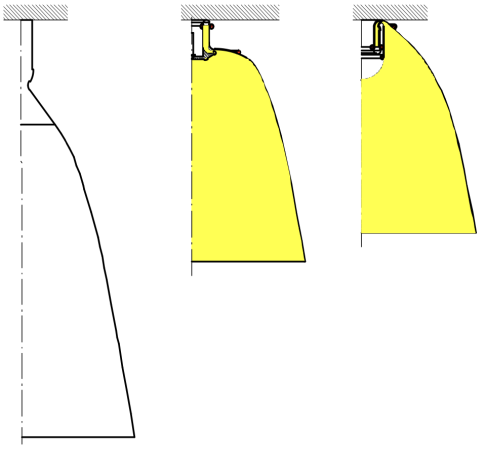

Figure 1.10: Conventional bell and ED nozzle (without and with reverse flow combustion chamber arrangement) [16]

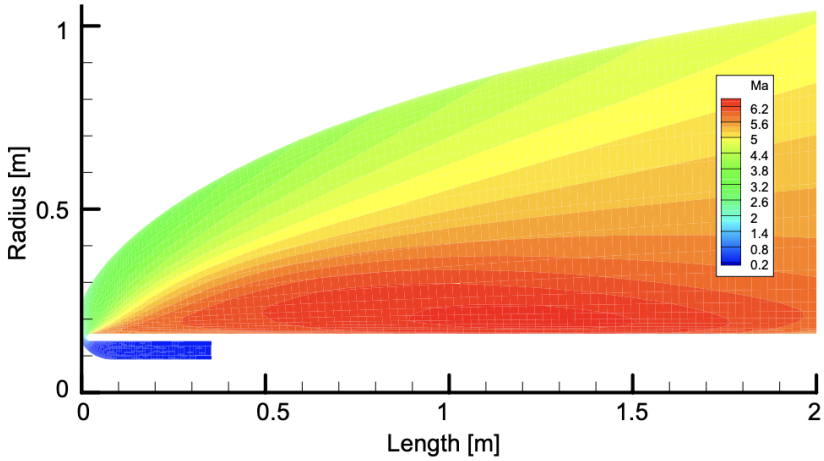

Figure 1.11: Eulerian solution for reference ED TCA [16]

designed for approximately half of the length of the conventional nozzle, as shown in Fig. 1.10. However, the TIC design tool had to be verified since it is, from a rigorous point of view, only applicable to two-dimensional planar flows due to the Prandtl-Meyer assumption [16]. Accordingly, the contours were compared to those obtained from the axisymmetric two-dimensional method of characteristic (MOC). It was shown that the maximum contour deviations are less than 1 %. In addition, Eulerian and viscous CFD simulations were performed for the contours designed with the simplified design approach using FASTRAN (at ESTEC) and Davis-Vol (at EADS-ST). The nozzle geometry was designed by neglecting the central body, and a straight base was realized instead. Circular arcs were used to contour the walls in the throat region. The Eulerian simulations could confirm the Mach contour lines, and no shock development was visible in accordance with the design assumption of isentropic expansion. The sonic line featured a minor S-shape in contrast to the design. The I_{sp} prediction differed from the design value by less than 0.2 %. Viscous performance losses were approximately 1 %. Chemical kinetics were neglected in the simulations.

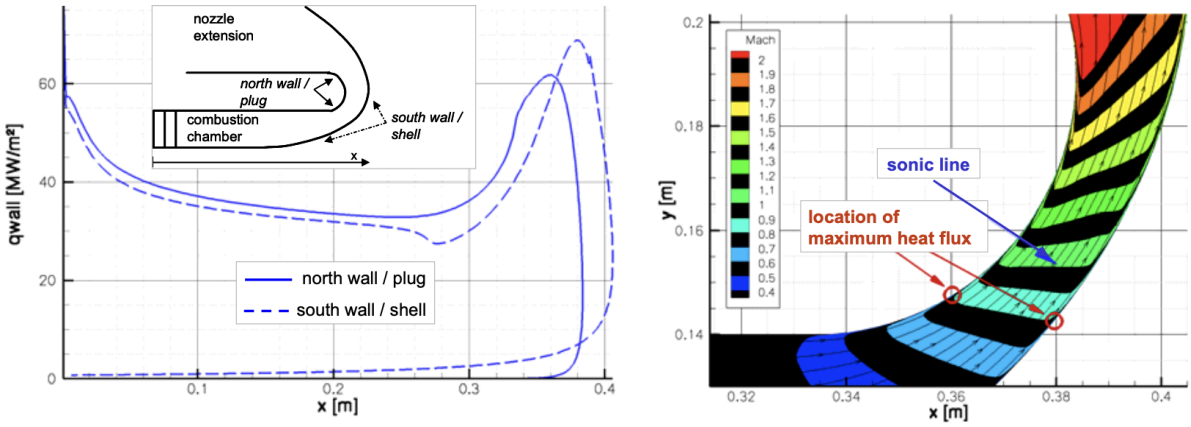

Figure 1.12: ED nozzle wall heat flux density distribution (left) and location of respective peaks in throat region (right) [16]

1.3.4 System aspects

Besides the performance, the wall heat flux was addressed by EADS-ST [16]. The heat flux assessment is very important since heat exchange affects the cooling, the engine cycle, the nozzle integration, and, thus, the mass of the whole propulsion system. Hence, the heat fluxes have an indirect influence on the entire mission. EADS-ST conducted a very complete and detailed investigation. The heat fluxes were analyzed using the in-house tool Rockflam-II. It was shown that the ED nozzle chamber features a heat flux density plateau in the combustion chamber, which is approximately 5 % higher along the internal wall, as shown in Fig. 1.12. In addition, the heat flux density along the external wall in the throat is approximately 10 % higher than along the internal wall, probably due to different boundary layer developments. The heat flux peaks are located marginally upstream of the sonic line. However, the peak heat flux of the ED is comparable to that of conventional bell nozzles and is just slightly higher due to the annular throat. Analyses have shown that assuming a maximum allowed wall temperature of 700 K (Cu-alloy liner and electroplated Ni-jacket), the ED nozzle suffers $10-30$ % more heat exchange than the conventional *VINCI* engine. This is due to a higher radial throat wall distance from the symmetry axis, as shown in Fig. 1.13. The higher radial throat distance increases the wall surface exposed to the peak heat flux and, thus, the needed heat pick up from the cooling system [16].

Different cooling concepts were discussed to reduce thermal loads and energetic losses in performance. A trade-off study was conducted, and the co-flow heat exchanger was selected as the most suitable due to its simplicity. Engine cycle analyses were performed by *Snecma Moteurs*, and it was found that the I_{sp} could be increased by 2 s [16]. In manufacturing, the annular reverse flow thrust chamber and the injector head were defined as the main design drivers. Moreover, concepts (gimbals) are discussed of how the nozzle and the thrust chamber can be connected to the expander cycle, and a payload assessment of the integrated 2 m ceramic nozzle was conducted. It was shown that the payload could be increased by around 180 kg for a GTO mission due to lower integrated mass. Hence, the I_{sp}/W ratio can be increased. This would not be true for a 2.5 m nozzle. Even though a longer nozzle realizes higher I_{sp}, an annular gimbal cardan would be needed instead of the conventional ball-type cardan to satisfy the geometrical length constraint of the integrated nozzle. The higher cardan weight would nullify the I_{sp} gain. To counteract that, lightweight materials such as composite materials for the annular gimbal could be used.

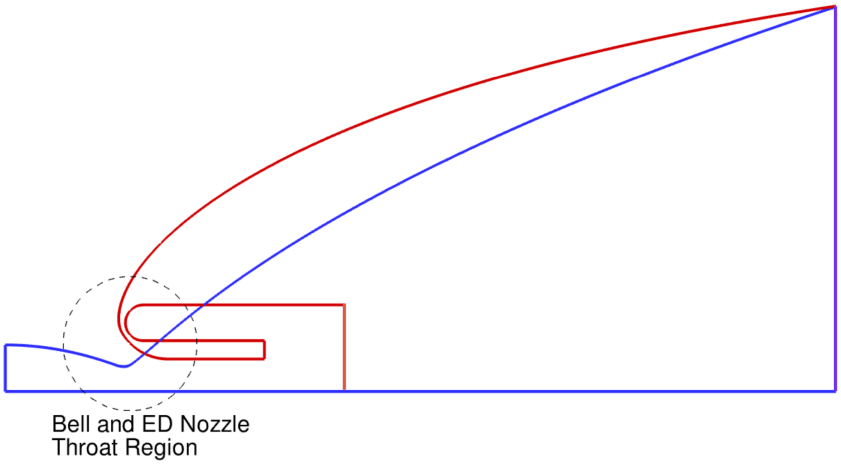

Figure 1.13: Generic bell and ED nozzle designed for the same throat area and position of symmetry axis

1.3.5 Interim conclusion

In Subsection 1.3.2, it is discussed that ED nozzles continuously adapt to the local ambient pressure, demonstrating, in theory, ideal performance. However, they suffer from overexpansion losses and aspiration drag [14], making them inferior to plug nozzles and even dual bell nozzles for moderate nozzle pressure ratios [15]. In high-altitude operation, ED nozzles show advantages over conventional nozzles due to lower divergence losses [7], as mentioned in Subsection 1.3.3. Hence, ED nozzles promise shorter design lengths and higher performance-to-weight ratios [16] as the plug nozzle [13]. However, in contrast to plug nozzles, ED nozzles feature less radial throat distances from the symmetry axis, reducing the wall surface exposed to the peak heat flux and, thus, the needed heat pick up from the cooling system [16]. All these combined make the ED nozzle a promising concept for the upper stages.

1.4 ED nozzle analysis

In section 1.3, it is mentioned that the flow field inside an ED nozzle is complex. This is due to flow separation at the central body and the formation of a recirculation zone, which interacts with the core flow within a mixing region [11]. Hence, the analysis of the ED nozzle flow field is difficult.
In the 1960s, the computational resources and methods were limited, and only simple analyses were possible. Rao developed a minimum length ED nozzle design method based on the MOC [12] [11]. The method is computationally stable and efficient and assumes the flow to be inviscid. The sonic line inside the throat, i. e. the starting point of the MOC is calculated via an analytical technique based on power series expansions similar to the method of Sauer [23]. The analytical method is only valid for throat angles close to 90°, as shown in Fig. 1.14. The reason is that this throat angle allows a wide range of expansion ratios and lengths. Schorr [24] applied similar methods for throat angles lower than 90° and noted a performance drop for throat angles lower than 60°. Rao assumed the base pressure p_b of the central body to be zero. Hence, the performance analysis can only be considered conservative since the base pressure is always higher than zero and contributes to performance. This deficiency in performance prediction is particularly evident for low-altitude and less for high-altitude operations, i. e. vacuum operation. In contrast to Rao, Mueller [25] concentrated on the recirculation region in front of the central body. He assumed a closed-wake operation along the entire range of pressure ratios, simplifying

the analysis. The work by Mueller focused on methods by which the flow and pressure distribution within the recirculation region can be predicted. He did not attempt to optimize the performance and considered ED nozzles featuring low throat angles of approximately $20 - 45°$ and an ideal contour.

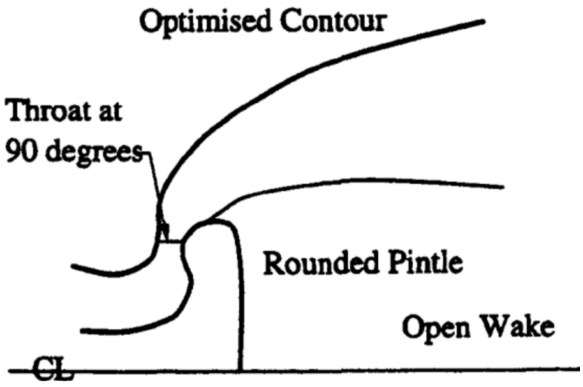

Figure 1.14: Rao type ED nozzle [11]

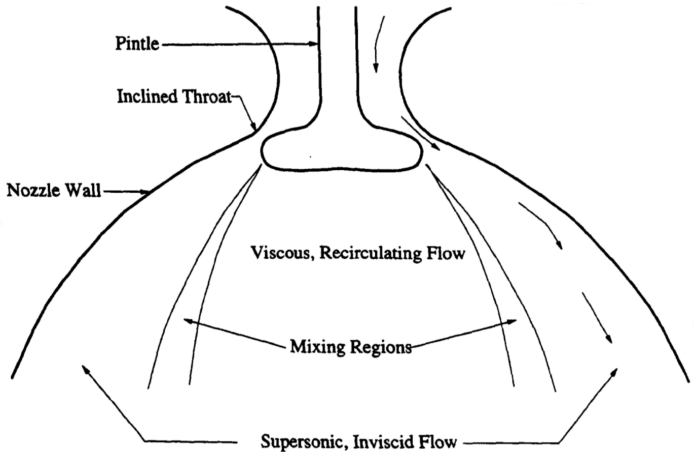

Figure 1.15: Nozzle flow field subdivided for analysis approach [11]

Due to inferior altitude adaptation w. r. t. plug nozzles, there was only a little interest in ED nozzles from the 1970s. Only as computational methods got more advanced and more computational resources became available, the research in ED nozzles was slowly revived. In the late 1990s, Taylor and Hempsell investigated a coupled approach to model the full-flowing vacuum flow field of the ED nozzle and to predict the performance [26]. The subsonic region of the nozzle, including the throat, was modeled using inviscid CFD simulations to obtain the first right-running characteristic line. Then, the MOC was used to calculate the inviscid flow field (see Fig. 1.15), as Rao [12]. For the recirculation area, semi-empirical equations were used to estimate the central body's base pressure and thrust contribution.

1.5 Objectives and structure of the work

This Ph. D. focuses on the ED nozzle design and performance optimization for upper-stage applications. Chapter 2 is dedicated to the ideal design of ED nozzles. This includes the approximate contouring method in Section 2.1. This method is integrated into different design procedures introduced in Section 2.2. Section 2.3 is dedicated to the design of the subsonic nozzle walls. Based on that, a Baseline ED nozzle is designed based on *VINCI* engine characteristics, as done by EADS-ST (see Section 2.4). Due to the availability of precise CFD methods and sufficient computing resources, the flow field is analyzed by full CFD simulations. The CFD methods are discussed in more detail in Chapter 3. In Chapter 4, for two test cases, the CFD models are verified, and the results are validated. In Chapter 5, the CFD models are applied to the Baseline ED, and a comparable conventional nozzle, verified, and suitable meshes are selected for the parametric analyses. In the parametric analyses, the influence of various geometrical parameters on the nozzle performance is investigated. However, a distinction is made between performance losses due to divergence, viscosity, and heat exchange. Therefore, Eulerian, viscous-adiabatic and viscous-isothermal simulations are performed. The results of the parametric analyses are discussed in Chapter 6, and the thesis is concluded in Chapter 7.

Chapter 2

ED nozzle design

2.1 Approximate contouring method

The ideal supersonic wall contours of the ED nozzle, providing isentropic, i. e. shock-free expansion, are calculated with the Angelino method [27]. This method was initially proposed by Gianfranco Angelino in 1964 to design plug nozzles. Friction effects are not taken into account, and the expansion process is considered adiabatic. The Angelino method is based on the Prandtl-Meyer expansion, which comes with certain assumptions. First, the characteristic lines over which the flow properties are constant are considered straight. Second, the specific heat ratio γ of the expanding gas is fixed to a constant value. Third, the Angelino method is applied in this work to design axisymmetric nozzles even though the Prandtl-Meyer expansion is only valid for strictly two-dimensional planar flows. These assumptions inevitably lead to deviations from the exact Method of Characteristics (MOC), so the Angelino method can be considered an approximate solution. However, Angelino stated that by comparing his method with the MOC (on a plug contour with constant specific heat ratio γ), there is a good agreement since the expansion waves computed from the MOC do not significantly depart from straight lines, as can be seen in Fig. 2.1. As a result, the contours for both solution methods do not differ significantly. Similarities between the MOC and the Angelino method were also confirmed by Nasuti et. al. [13].
Accordingly, the Angelino method is a simple trigonometric contouring solution with good accuracy and near-zero computational cost. Due to flowfield similarities between ED and plug nozzles, the Angelino method is used in this work to design also ED nozzles. For this, a dedicated *MATLAB* routine is developed (see appendix A.1), which is discussed in more detail in the following.

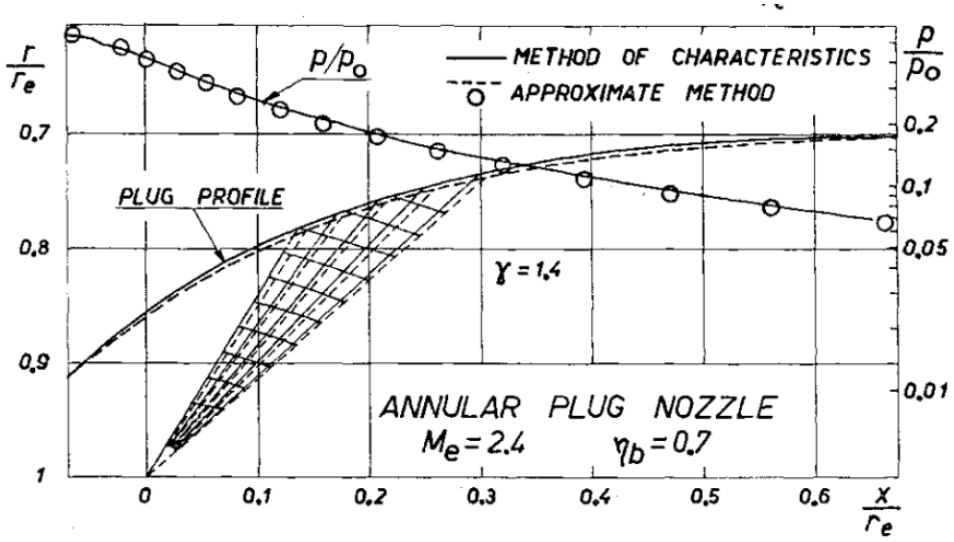

Figure 2.1: Comparison of the approximate and exact solutions in the plug nozzle design [27]

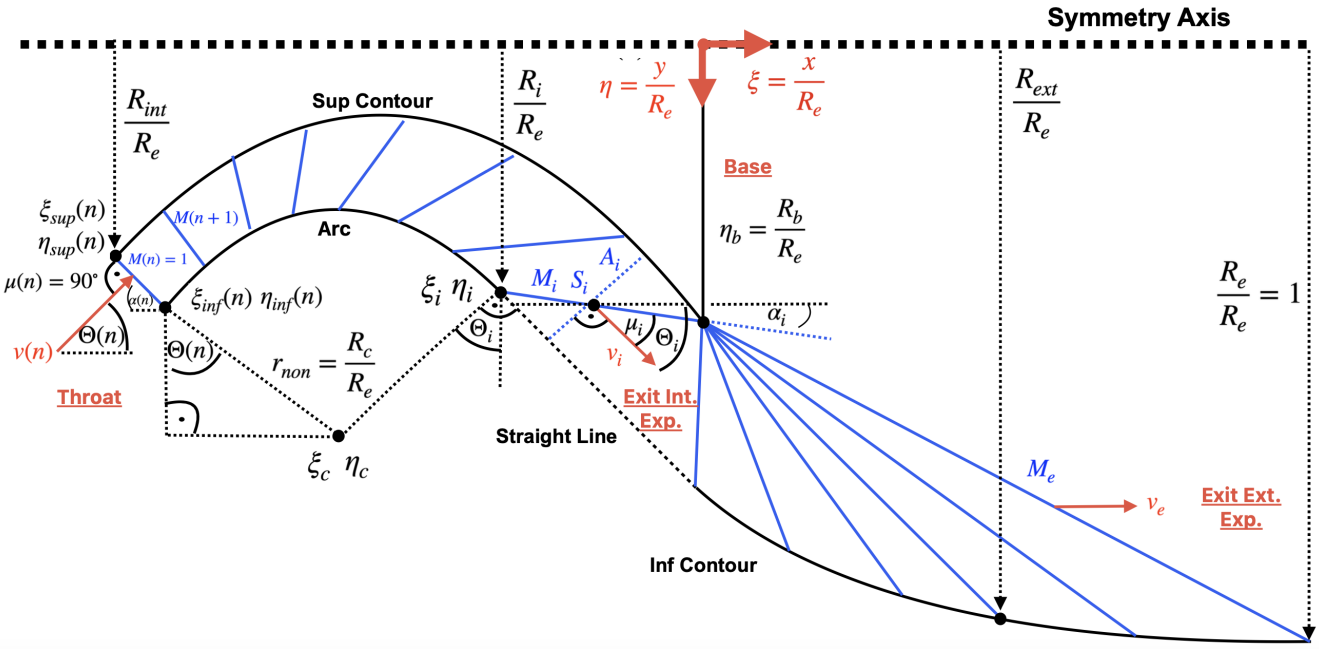

Figure 2.2: Generic ED nozzle with coordinates normalized to the exit radius R_e

A generic ED nozzle is shown in Fig. 2.2 with coordinates normalized to the exit radius R_e. The origin of the coordinate system is located along the central body on the symmetry axis of the nozzle. From the throat, where sonic flow conditions apply ($M = 1$), the expanding gas is first accelerated up to M_i in the internal expansion region and subsequently to the exit Mach number M_e through an external expansion fan. This originates from the central body of the ED nozzle. As a result of this whole expansion process, which is represented by an infinite number of consecutive expansion waves, the velocity vector is continuously turned, and the orientation Θ to the reference axis, i. e. the x-axis changes. After the last external characteristic, a full axial flow is obtained. Figure 2.3 shows exemplary in which components the angle Θ can be divided. In order to determine them, angular relationships are established.

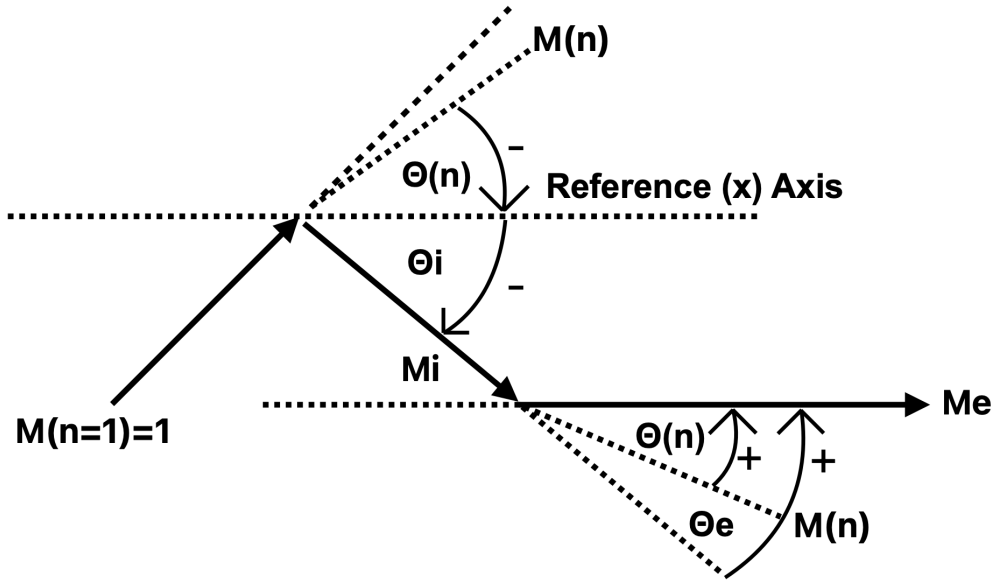

Figure 2.3: Angle balance of a generic ED nozzle and the respective sign direction

External expansion:

The external expansion is considered first. The equation 2.1 describes the orientation of the local external velocity vector $\Theta(n)$ to the reference (x) axis at a generic position n. The quantity $\Theta(n)$ is calculated from the difference between the Prandtl-Meyer functions ν of $M(n)$ and the exit Mach number M_e. The higher the difference between the Prandtl-Meyer functions, the higher the turning angle $\Theta(n)$ of the velocity vector. Equation 2.2 shows the values for $\Theta(n)$ at the beginning and end of the external expansion region. Full axial flow is obtained at the full length of the ED nozzle. Hence, $\Theta(n)$ is zero in the exit.

$$\Theta(n) = \nu(M(n), \gamma) - \nu(M_e, \gamma) \tag{2.1}$$

$$\Theta(n) = \begin{cases} \Theta_e = \nu(M_i, \gamma) - \nu(M_e, \gamma), & \text{Exit Int. Exp.: M(n)=}M_i \\ 0, & \text{Exit Ext. Exp.: M(n)=}M_e \end{cases} \tag{2.2}$$

Internal expansion:

The orientation of the internal velocity vector $\Theta(n)$ can be described by Eq. 2.3. Since $-\Theta_i = \Theta_e$, as shown in Fig. 2.3, Eq. 2.3 can be linked with Eq. 2.2 and simplified to Eq. 2.4.

$$\Theta(n) = -\Theta_i - \nu(M(n), \gamma) + \nu(M_i, \gamma) \tag{2.3}$$

$$\Theta(n) = 2 \cdot \nu(M_i, \gamma) - \nu(M_e, \gamma) - \nu(M(n), \gamma) \tag{2.4}$$

At the beginning and end of the internal expansion region, the internal velocity vector $\Theta(n)$ becomes:

$$\Theta(n) = \begin{cases} \Theta_{th} = 2 \cdot \nu(M_i, \gamma) - \nu(M_e, \gamma), & \text{Throat: M(n)=1} \\ \Theta_i = \nu(M_i, \gamma) - \nu(M_e, \gamma), & \text{Exit Int. Exp.: M(n)=}M_i \end{cases} \tag{2.5}$$

The **contouring process starts** with the calculation of the coordinates ξ_i and η_i. These coordinates describe the origin of the last internal characteristic line along the external nozzle wall. The trigonometric Eq. 2.6 can be established.

$$sin\alpha_i = \frac{\pi \cdot (\eta_b^2 - (\frac{R_i}{R_e})^2)}{S_i} \tag{2.6}$$

The quantity S_i is the surface area of the last internal characteristic. It is calculated by the actual passage area of the flow A_i and the Mach angle μ_i, as shown in Eq. 2.7. The former is orientated orthogonally to the velocity vector at the end of the internal expansion. The latter is the angle between the characteristic line and the velocity vector and is calculated by $asin\frac{1}{M_i}$.

$$S_i = \frac{A_i}{sin\mu_i} = A_i \cdot M_i \tag{2.7}$$

The actual passage area A_i is derived from the *Areas law* in Eq. 2.8a and the assumption that the nozzle exit area A_e is formed without the area of the central body. Finally, A_i can be expressed by Eq. 2.8d.

$$A(M,\gamma) = \varepsilon(M,\gamma) \cdot A_t \tag{2.8a}$$

$$A_i = \varepsilon_i \cdot A_t \tag{2.8b}$$

$$A_i = \varepsilon_i \cdot \frac{A_e}{\varepsilon_e} \tag{2.8c}$$

$$A_i = \frac{\varepsilon_i}{\varepsilon_e} \cdot \pi \cdot (1 - \eta_b^2) \tag{2.8d}$$

The Eq. 2.9 for the surface area S_i of the last internal characteristic is finally derived by inserting Eq. 2.8d into Eq. 2.7.

$$S_i = \frac{\varepsilon_i}{\varepsilon_e} \cdot M_i \cdot \pi \cdot (1 - \eta_b^2) \tag{2.9}$$

By substituting Eq. 2.9 into Eq. 2.6, the Eq. 2.10 for the radial coordinate component η_i is derived. The Eq. 2.11 for the axial coordinate ξ_i comes from another trigonometric relation.

$$\frac{R_i}{R_e} = \eta_i = -\sqrt{\eta_b^2 - sin\alpha_i \cdot \frac{\varepsilon_i}{\varepsilon_e} \cdot M_i \cdot (1 - \eta_b^2)} \tag{2.10}$$

$$\xi_i = \frac{-(-\eta_b - \eta_i)}{tan\alpha_i} \tag{2.11}$$

The angle α_i is a geometrical angle between the internal characteristic line and the reference (x) axis and is defined by Eq. 2.12.

$$\alpha_i = \Theta_i + \mu_i = \Theta_i + asin\frac{1}{M_i} \tag{2.12}$$

The quantities ε_i and ε_e in Eq. 2.10 are the expansion ratios after the internal and external expansion region. Generally, for isentropic expansion, the (local) expansion ratio ε is only a function of the local Mach number $M(n)$ across the respective characteristic line and the specific heat ratio γ, as shown in Eq. 2.13. Hence, ε_i and ε_e are calculated with the Mach number M_i and M_e and the constant specific heat ratio γ.

$$\varepsilon(M(n),\gamma) = \frac{A(n)}{A_t} = \frac{1}{M(n)} \cdot \left(\frac{1 + \frac{1}{2} \cdot (\gamma - 1) \cdot M(n)^2}{\frac{1}{2} \cdot (\gamma + 1)} \right)^{\frac{\gamma+1}{2 \cdot (\gamma-1)}} \tag{2.13}$$

For isentropic expansion, the same dependencies apply to the Prandtl-Meyer function ν, as shown in Eq. 2.14. Figure 2.4 shows ν graphically as a function of M and γ.

$$\nu(M(n),\gamma) = \sqrt{\frac{\gamma+1}{\gamma-1}} \cdot atan\sqrt{\frac{\gamma-1}{\gamma+1} \cdot (M^2 - 1)} - atan\sqrt{M^2 - 1} \tag{2.14}$$

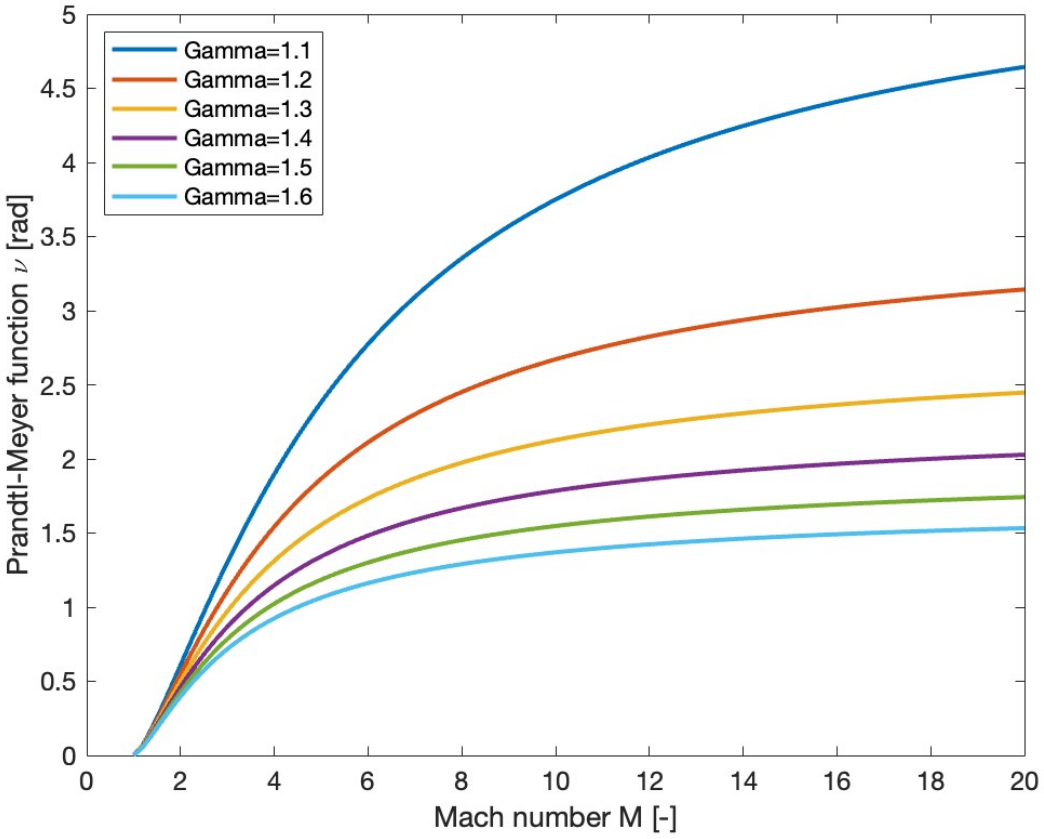

Figure 2.4: Prandtl-Meyer function ν as function of Mach number M and specific heat ratio γ

In the **second step**, the point (ξ_c/η_c) is calculated based on the coordinates ξ_i and η_i. The external wall in the internal expansion region is designed as a circular arc, as shown in Fig. 2.2. Accordingly, the point (ξ_c/η_c) can be calculated by the two trigonometric Eq. 2.15 and 2.16. The quantity r_{non} is the dimensionless arc radius $\frac{R_c}{R_e}$.

$$\xi_c = \xi_i + r_{non} \cdot sin\Theta_i \tag{2.15}$$

$$\eta_c = \eta_i + r_{non} \cdot cos\Theta_i \tag{2.16}$$

In the **third step**, the superior (sup) and inferior (inf) wall contours of the internal expansion region are calculated. It is started along the throat characteristic $(n = 1)$ with the calculation of the inferior contour point using the trigonometric Eq. 2.17 and 2.18.

$$\xi_{inf}(n) = \xi_c - r_{non} \cdot sin\Theta(n) \tag{2.17}$$

$$\eta_{inf}(n) = \eta_c + r_{non} \cdot cos\Theta(n) \tag{2.18}$$

Then, the superior wall contour point is computed along the same characteristic line, starting with the radial coordinate. The equation for the radial coordinate is derived from the trigonometric Eq. 2.19. The surface $S(n)$ of the characteristic lines is calculated from the *Areas law* in Eq. 2.8a. Finally, Eq. 2.20 follows for the radial coordinate. The axial coordinate is computed from Eq. 2.21. Subsequently, n is increased, and the procedure is repeated for the other internal characteristics up to the last internal characteristic line between the wall contour points (ξ_i/η_i)

and $(0/\eta_b)$. From $(0/\eta_b)$, a straight line up to the symmetry axis is drawn to realize the central body, as shown in Fig. 2.2.

$$sin\alpha(n) = \frac{\pi \cdot (\eta_{inf}(n)^2 - (\frac{R_{int(n)}}{R_e})^2)}{S(n)} \tag{2.19}$$

$$\frac{R_{int}(n)}{R_e} = \eta_{sup}(n) = -\sqrt{\eta_{inf}(n)^2 - sin\alpha(n) \cdot \frac{\varepsilon(n)}{\varepsilon_e} \cdot M(n) \cdot (1 - \eta_b^2)} \tag{2.20}$$

$$\xi_{sup}(n) = \xi_{inf}(n) - \frac{\eta_{sup}(n) - \eta_{inf}(n)}{tan\alpha(n)} \tag{2.21}$$

In the **last step**, the external wall contour is computed using Eq. 2.22 to 2.24. Equivalent to the third step, the external contour is calculated iteratively from the first to the last, i. e. design characteristic. The external wall contour between the last internal and first external point is a straight line.

$$sin\alpha(n) = \frac{\pi \cdot ((\frac{R_{ext(n)}}{R_e})^2 - \eta_b^2)}{S(n)} \tag{2.22}$$

$$\frac{R_{ext}(n)}{R_e} = \eta_{inf}(n) = -\sqrt{\eta_b^2 + sin\alpha(n) \cdot \frac{\varepsilon(n)}{\varepsilon_e} \cdot M(n) \cdot (1 - \eta_b^2)} \tag{2.23}$$

$$\xi_{inf}(n) = \frac{\eta_{inf}(n) + \eta_b}{tan\alpha(n)} \tag{2.24}$$

Besides the Mach number M, macroscopic flow properties like pressure p, temperature T, and density ρ can be assigned to each characteristic line. In the case of isentropic expansion, the total values (Index t) of the macroscopic flow properties like total pressure p_t, total temperature T_t, and total density ρ_t remain constant during the expansion process. Hence, the macroscopic flow properties for each position within the nozzle can be calculated based on the chamber conditions (Index c). Equation 2.25a shows the total temperature in the chamber and an arbitrary position within the nozzle. Since the flow in the chamber is considered in resting state ($M_c = 0$), the equation simplifies to Eq. 2.25b. The same is shown for pressure and density in Eq. 2.26 and 2.27.

$$T_c \left(1 + \frac{\gamma - 1}{2} M_c^2\right) = T(n) \left(1 + \frac{\gamma - 1}{2} M(n)^2\right) \tag{2.25a}$$

$$T(n) = \frac{T_c}{1 + \frac{\gamma-1}{2} \cdot M(n)^2} \tag{2.25b}$$

$$p(n) = \frac{p_c}{(1 + \frac{\gamma-1}{2} \cdot M(n)^2)^{\frac{\gamma}{\gamma-1}}} \tag{2.26}$$

$$\rho(n) = \frac{\rho_c}{(1 + \frac{\gamma-1}{2} \cdot M(n)^2)^{\frac{1}{\gamma-1}}} \tag{2.27}$$

For each characteristic line, the speed of sound $a(n)$ and the magnitude of the velocity vector $v(n)$ can be calculated by Eq. 2.28 and 2.29.

$$a(n) = \sqrt{\gamma \cdot \mathcal{R}_s \cdot T(n)} \tag{2.28}$$

$$v(n) = M(n) \cdot a(n) \tag{2.29}$$

2.2 Design procedures

Figure 2.5 shows a generic ED nozzle with its main geometrical parameters. It can be seen that the throat is always shifted in a radial direction from the symmetry axis by the two parameters y_1 and y_2. In addition, the throat inclination Θ_{th} can be either zero, i. e. provide full axial throat inflow, or different from zero, as shown in Fig. 2.5 (for roughly +45°). In the case of zero throat inclination, the design throat area equals that of an annulus. In contrast, it equals the lateral surface of a truncated cone for throat inclinations that differ from zero. The combination of throat shifting and possible inclination w. r. t. the symmetry axis is one reason why the ED nozzle design is more complex than that of conventional nozzles.

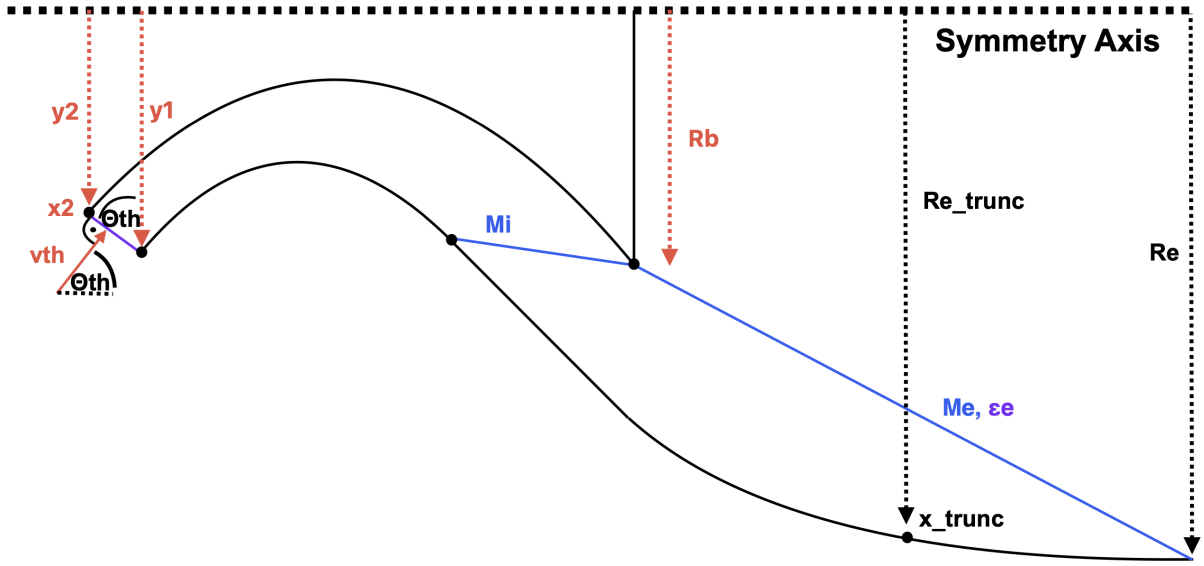

Figure 2.5: Radial shift and inclination of the throat of a generic ED nozzle

The throat displacement, i. e. y_1 as well as y_2, can be controlled over the base radius R_b. However, the ED design is done for a desired value of y_2. Since the throat characteristic in the design is assumed to be a straight line (as discussed in Section 2.1), the radial throat coordinate y_1 depends on the throat area A_t and the throat inclination Θ_{th}.
The throat area A_t is a design input variable. However, the setup of the throat inclination Θ_{th} is more complex. The reason is that Θ_{th} is a function of the three parameters M_i, M_e, and γ (see Eq. 2.5). The quantity ν in Eq. 2.5 is the Prandtl-Meyer function. The Mach number M_e is a function of the full-length (FL) expansion ratio ε_e and γ from Eq. 2.13.

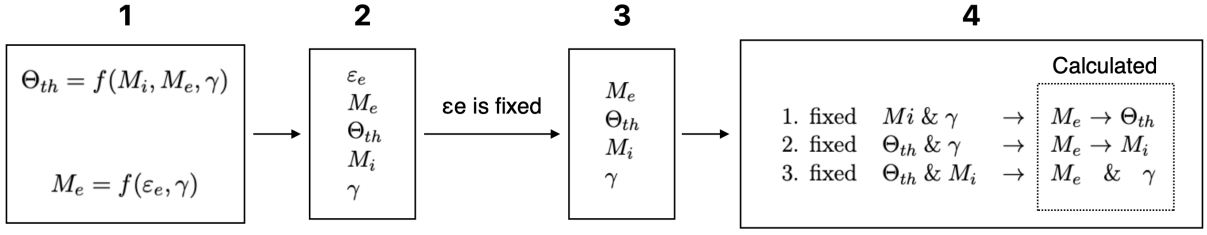

Figure 2.6: Derivation of the design procedures for the throat inclination Θ_{th}

From Eq. 2.5 and 2.13, the five parameters $\varepsilon_e, M_e, \Theta_{th}, M_i$, and γ can be defined, as shown in the second block of Fig. 2.6. To close the system of two equations, three parameters always need to be known, i. e. fixed. In this way, there are two equations and just two unknowns. The first parameter that is always fixed is ε_e. Hence, the quantity M_e is not fixed and always calculated. In the end, the three parameters Θ_{th}, M_i, and γ remain from which two parameters always need to be fixed. For this, three possible combinations, i. e. design procedures exist. These are shown in the fourth block of Fig. 2.6 together with the respective two parameters that need to be calculated. It can be seen that the throat inclination Θ_{th} is not an input, i. e. a fixed parameter in the first design approach in contrast to the second and third design procedures.
Besides the throat shifting y_2 and inclination Θ_{th} w. r. t. the symmetry axis (see Fig. 2.5), the ED nozzles in this work are also designed for a desired axial throat coordinate x_2. This means that the entire throat contour point (x_2/y_2) is an input. The throat contour point (x_1/y_1) results automatically. Moreover, also the truncation radius $R_{e,trunc}$ for a desired truncation length x_{trunc} is a user input. This flexibility in the contouring calculation is crucial if different ED nozzles are to be designed, for instance, for parameter studies, as in the following. Appendix A.1 shows the *MATLAB* code.

2.2.1 Variable throat inclination

Figure 2.7 illustrates the first design procedure. Calculating a desired ED nozzle according to certain input parameters is an iterative procedure in which the two control variables R_b and ε_e at the beginning of the outer and inner loop need to be found.

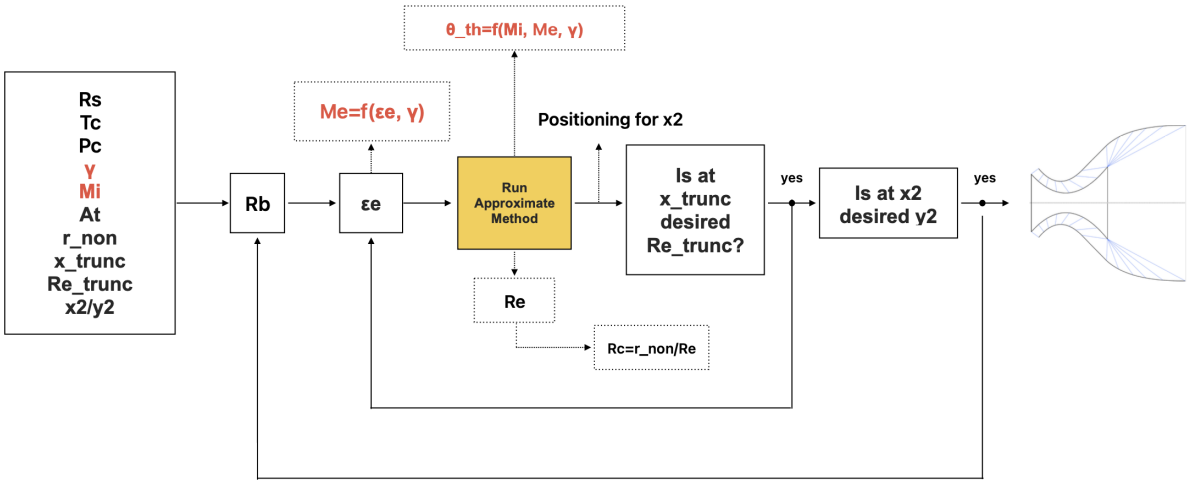

Figure 2.7: First design procedure

Starting from the inputs (located in the left block in Fig. 2.7), an initial guess for the base radius R_b is assumed at the beginning of the outer loop. Then, the inner loop is entered, and an initial guess for the full-length expansion ratio ε_e is also assumed. Then, the Mach number M_e is calculated from ε_e and γ (input) by solving Eq. 2.13 iteratively. For this, the function $\Delta\varepsilon(M_e)$ in Eq. 2.30 is introduced within the code. It is only a function of M_e since γ as an input variable and ε_e at the beginning of the inner loop in Fig. 2.7 remain constant during the calculation. By setting Eq. 2.30 equal to zero, the calculation of M_e is converted into a root problem. The code uses the *MATLAB* function *fzero* for this. First, an initial value interval $[M_{e,init,1}\ M_{e,init,2}]$ is

defined around the root M_e, and then, the bisection method combined with the secant and or inverse quadratic method, is applied iteratively [28].

$$\Delta\varepsilon(M_e) = \varepsilon(M_e) - \varepsilon_e = 0 \xrightarrow[M_{e,init,2}]{\underline{\textbf{fzero}}\ M_{e,init,1}} M_e \tag{2.30}$$

Afterwards, the approximate contouring method is executed. The throat inclination Θ_{th} is calculated from M_i (input), M_e and γ (input) by Eq. 2.5. Subsequently, the nozzle wall contours are positioned so that the axial throat position x_2 meets the desired input value. Then, for the initial guesses of R_b (start outer loop) and ε_e (start inner loop), the truncation radius $R_{e,trunc,x}$ is calculated at the truncation position x_{trunc} (input). In case $R_{e,trunc,x}$ is different from the desired input value of $R_{e,trunc}$, ε_e at the beginning of the inner loop is adapted iteratively until $R_{e,trunc,x}$ equals $R_{e,trunc}$. For this, the function $\Delta r(\varepsilon_e)$ in Eq. 2.31 is introduced for the whole inner loop within the code. By setting Eq. 2.31 equal to zero, the calculation of ε_e is converted into a root problem. The *MATLAB* method *fzero* is used by using the initial value interval $[\varepsilon_{e,init,1}\ \varepsilon_{e,init,2}]$.

$$\Delta r(\varepsilon_e) = Re_{trunc,x}(\varepsilon_e) - Re_{trunc} = 0 \xrightarrow[\varepsilon_{e,init,2}]{\underline{\textbf{fzero}}\ \varepsilon_{e,init,1}} \varepsilon_e \tag{2.31}$$

After leaving the inner loop, the radial throat position $y_{2,x}$ is calculated at the input throat coordinate x_2. In the case $y_{2,x}$ is different from y_2 (input), the base radius R_b at the beginning of the outer loop for that applies $y_{2,x} = y_2$ needs to be found iteratively. Hence, Δy_2 in Eq. 2.32 becomes zero.

$$\Delta y_2 = |y_{2,x}(R_b, \varepsilon_e)| - |y_2| \tag{2.32}$$

2.2.2 Fixed throat inclination

If the throat inclination Θ_{th} is an input parameter in the design, a distinction is made between the second and third design procedures in Fig. 2.8 and 2.9. These procedures work like the first design procedure in Fig. 2.7. However, w. r. t. the first design procedure, there are several different design input parameters that change certain calculation steps within the code. These changes are discussed in more detail in this Subsection, starting with the second design procedure.

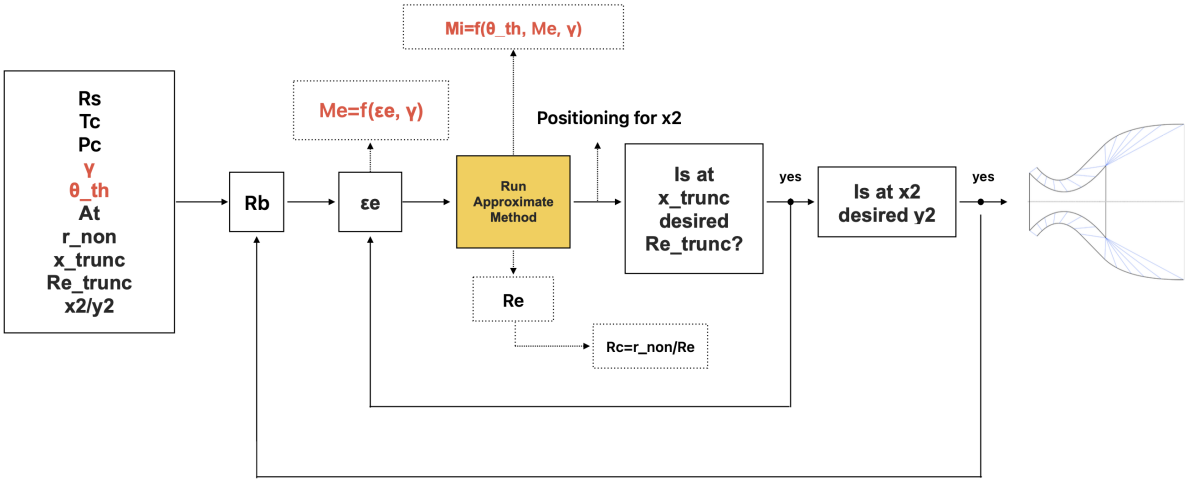

Figure 2.8: Second design procedure

In the second design procedure, the throat inclination Θ_{th} and the constant design value of the specific heat ratio γ are input variables. Within the inner loop, the Mach number at the end of the internal expansion M_i is calculated from Θ_{th} (input), M_e, and γ (input) by solving Eq. 2.5 iteratively. Therefore, the function $\Delta\Theta_{th}(M_i)$ in Eq. 2.33 is introduced. It only depends on M_i since Θ_{th} and γ are input parameters, and M_e is already calculated at the beginning of the inner loop. By setting function $\Delta\Theta_{th}(M_i)$ equal to zero, the calculation of M_i can be converted into a root-finding procedure. In the code, the *MATLAB* function *fzero* is used with the initial value interval $[M_{i,init,1}\ M_{i,init,2}]$.

$$\Delta\Theta_{th}(M_i) = \Theta_{th,x}(M_i) - \Theta_{th} = 0 \xrightarrow[M_{i,init,2}]{\overset{\textbf{fzero}}{M_{i,init,1}}} M_i \tag{2.33}$$

In the third design procedure, the throat inclination Θ_{th} and the Mach number at the end of the internal expansion M_i are input parameters. The difference to the first and second design procedures is that M_e and γ are calculated by solving Eq. 2.13 and 2.5 iteratively. For this, the two functions $\Delta\varepsilon_e(M_e,\gamma)$ and $\Delta\Theta_{th}(M_e,\gamma)$ in Eq. 2.34 are introduced and equated with zero. Since both equations contain the variables M_e and γ, they must be solved simultaneously using a root-finding procedure. For this, the *MATLAB* function *fsolve* based on the thrust-region-dogleg algorithm is used for the two initial values for M_e and γ [29].

$$\left.\begin{aligned}\Delta\varepsilon_e(M_e,\gamma) = \varepsilon(M_e,\gamma) - \varepsilon_e &= 0\\ \Delta\Theta_{th}(M_e,\gamma) = \Theta_{th}(M_e,\gamma) - \Theta_{th} &= 0\end{aligned}\right\} \xrightarrow[\gamma_{init}]{\overset{\textbf{fsolve}}{M_{e,init}}} M_e\ \&\ \gamma \tag{2.34}$$

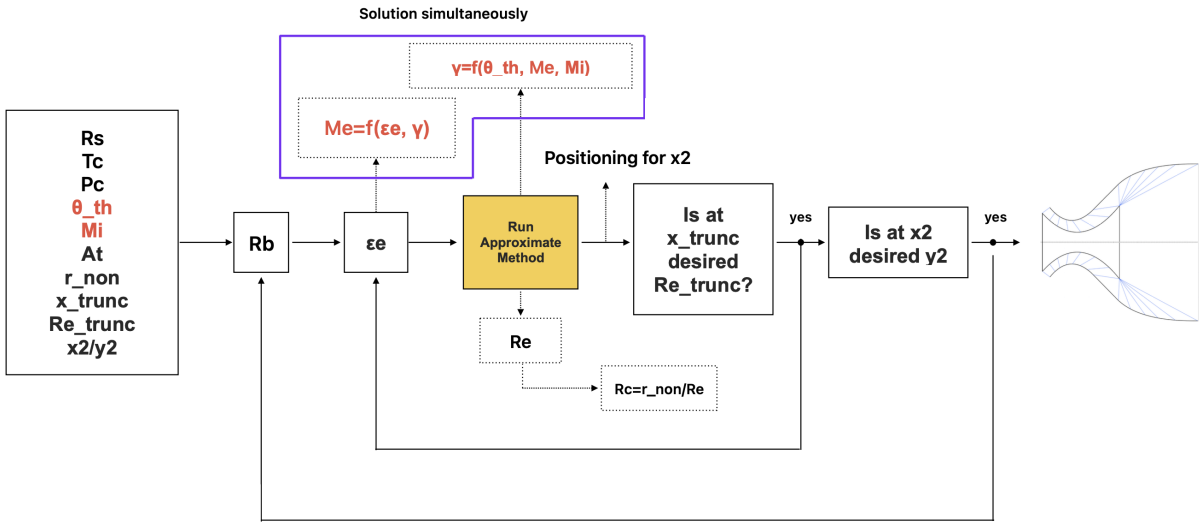

Figure 2.9: Third design procedure

2.3 Subsonic wall contouring

In Fig. 2.2, the throat angle Θ_{th} is introduced as the angle between the throat velocity vector and the reference (x) axis. However, sonic conditions apply in the throat, and the throat Mach number M_{th} equals one. As a result, the Mach angle angle μ_{th}, i. e. the angle between the straight sonic line in the throat and the velocity vector equals 90°. Hence, the throat angle Θ_{th} can also be defined as the angle between the straight throat characteristic and the y-axis.

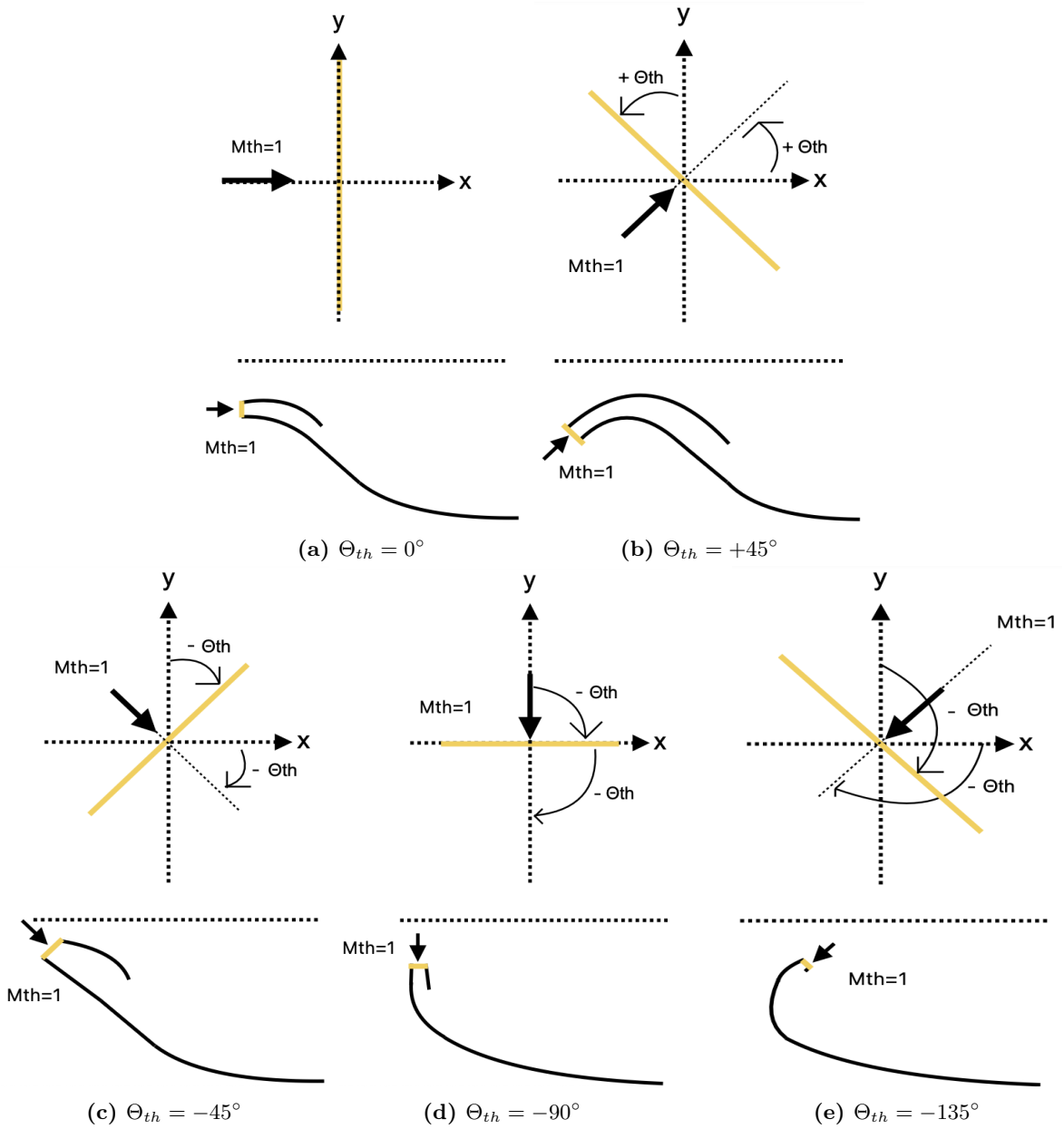

(a) $\Theta_{th} = 0°$ **(b)** $\Theta_{th} = +45°$

(c) $\Theta_{th} = -45°$ **(d)** $\Theta_{th} = -90°$ **(e)** $\Theta_{th} = -135°$

Figure 2.10: Various generic ED nozzles with different throat configurations

As already discussed in Eq. 2.5, the throat angle Θ_{th} of an ED nozzle depends on the exit Mach numbers after the internal and external expansion regions M_i and M_e and the constant design value of the specific heat ratio γ. Depending on these values, the throat angle can take different values so that, in general, any number of ED nozzles with various throat configurations can be designed. Some of these configurations are shown in Fig. 2.10. The Fig. 2.10e shows a generic reverse flow configuration. This is also referred to as counterflow configuration and should be particularly highlighted. This design features large negative throat angles Θ_{th}. According to Eq. 2.5, for a given specific heat ratio γ and full-length exit Mach number M_e, these are just realizable for very small internal Mach numbers M_i. Usually, for such a design, M_i is just slightly larger than 1. Firstly, this means that the deflection of the velocity vector due to the internal expansion is almost zero. Secondly, the internal expansion region gets very short.

The approximate contouring method, integrated into the three design procedures (shown in Fig. 2.6), only provides the supersonic wall profiles. These start with the throat characteristic for which $M = 1$ applies, and in Fig. 2.11, they are marked as *inf*- and *sup*-contours. However, the expanding exhaust gas must be guided and accelerated from initially approximately $M = 0$ in the combustion chamber (CC) up to the throat. This is done within the subsonic nozzle section. The subsonic wall profiles are calculated independently of the approximate contouring method. This is included in a separate dedicated *MATLAB* routine (see Appendix A.2).
The design of the subsonic wall profiles is kept as simple as possible. Therefore, the nozzle sections *I* to *VII* are realized by straight lines and two arcs with radii R_1 and R_2 (see Fig. 2.11). Along the internal (*sup*) wall, only the throat point is taken from the contouring calculation. The quantities x_{cc} and y_{Base} represent the axial combustion chamber location and the radius of the ED central body. Both quantities are input parameters. The inner wall radius R_2 results automatically from y_{Base}. Regarding the outer wall radius R_1, the ratio R_1/R_2 is an input.

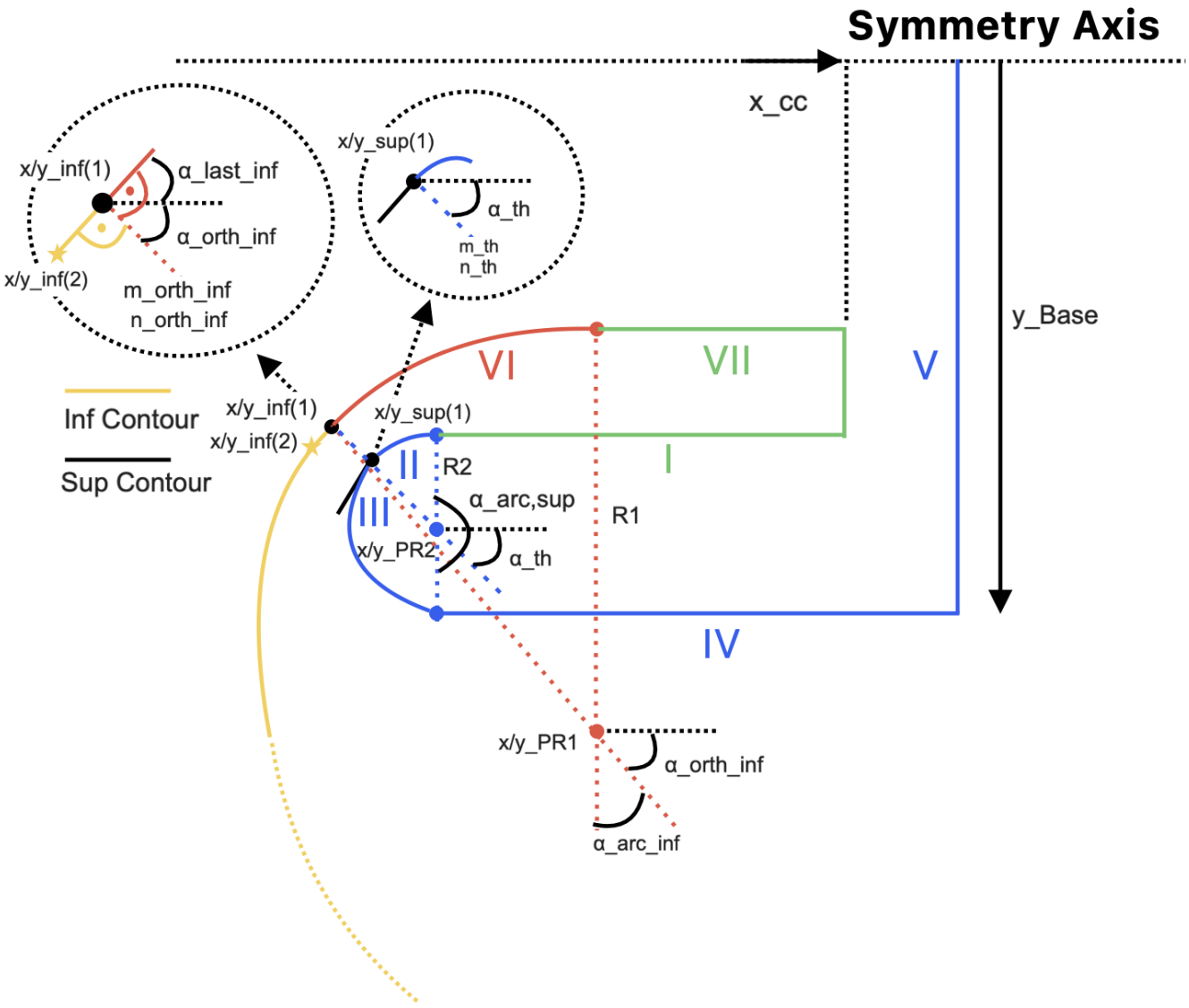

Figure 2.11: Generic ED nozzle in reverse flow configuration and principle of the subsonic wall contouring

The **subsonic contouring starts** with the calculation of the angle $\alpha_{last,inf}$ by Eq. 2.35. This is the angle between the first and the second wall contour points along the *inf*- contour downstream of the throat w. r. t. the symmetry axis, as shown in Fig. 2.11.

$$\alpha_{last,inf} = atan\left(\frac{y_{inf}(1) - y_{inf}(2)}{x_{inf}(1) - x_{inf}(2)}\right) \tag{2.35}$$

Then, another line is assumed that is orthogonal to the line segment inclined by $\alpha_{last,inf}$. This is the red dashed line in Fig. 2.11. It forms the angle $\alpha_{orth,inf}$ in Eq. 2.36 with the symmetry axis. Moreover, the line features the slope $m_{orth,inf}$ in Eq. 2.37 and the y-axis-intercept $n_{orth,inf}$ in Eq. 2.38. The line can be described by a line equation of the general form $y = mx + n$.

$$\alpha_{orth,inf} = -\left(\frac{\pi}{2} - \alpha_{last,inf}\right) \tag{2.36}$$

$$m_{orth,inf} = tan(\alpha_{orth,inf}) \tag{2.37}$$

$$n_{orth,inf} = y_{inf}(1) - m_{orth,inf} \cdot x_{inf}(1) \tag{2.38}$$

In the **second step**, a line between the first wall contour points along the *inf*- and *sup*-contours is assumed. This is the blue dashed line in Fig. 2.11. It has the angle α_{th} in Eq. 2.39 w. r. t. the symmetry axis, which is equal to the throat inclination angle Θ_{th}. Moreover, the line features a slope m_{th} in Eq. 2.40 and the y-axis-intercept n_{th} in Eq. 2.41. This is necessary to set up the line equation.

$$\alpha_{th} = atan\left(\frac{y_{sup}(1) - y_{inf}(1)}{x_{sup}(1) - x_{inf}(1)}\right) \tag{2.39}$$

$$m_{th} = tan(\alpha_{th}) \tag{2.40}$$

$$n_{th} = y_{sup}(1) - m_{th} \cdot x_{sup}(1) \tag{2.41}$$

In the **third step** the point x/y_{PR2} is calculated. This point is the center point of the arc segments *II* and *III*, and it is located on the blue dashed line. The radial coordinate y_{PR2} can be described by Eq. 2.42. The radius R_2 is a function of y_{PR2} and the radius of the central body y_{Base}, as shown in Eq. 2.43.

$$y_{PR2} = y_{sup}(1) + sin(\alpha_{th}) \cdot R_2 \tag{2.42}$$

$$R_2 = y_{PR2} - y_{Base} \tag{2.43}$$

By inserting Eq. 2.43 for R_2 into Eq. 2.42, Eq. 2.44 for y_{PR2} is derived. The axial coordinate x_{PR2} in Eq. 2.45 is calculated trigonometrically.

$$y_{PR2} = \frac{y_{sup}(1) - sin(\alpha_{th}) \cdot y_{Base}}{1 - sin(\alpha_{th})} \tag{2.44}$$

$$x_{PR2} = x_{sup}(1) + \frac{y_{PR2} - y_{sup}(1)}{tan(\alpha_{th})} \tag{2.45}$$

The wall coordinates of the *sup*- arc segment *II* in Fig. 2.11 are calculated by Eq. 2.46 and 2.47. The angle $\alpha_{arc,sup}$ is a list with the start value α_{th} and the end value $-90°$. The *sup*- arc segment *III* is also calculated by Eq. 2.46 and 2.47 with angles $\alpha_{arc,sup}$ from $90°$ to α_{th}. As shown in Fig. 2.11, only the throat point $x/y_{sup}(1)$ located between the wall segments *II* and *III* is used along the *sup*- contour from the approximate method.

$$y_{arc,sup} = y_{PR2} - sin(\alpha_{arc,sup}) \cdot R_2 \tag{2.46}$$

$$x_{arc,sup} = x_{PR2} - cos(\alpha_{arc,sup}) \cdot R_2 \tag{2.47}$$

In the **fourth step**, the subsonic wall profile *VI* is calculated. The wall section *VI* is an arc with center point x/y_{PR1}. The axial and radial coordinates of this center point are calculated by Eq. 2.48 and 2.49.

$$y_{PR1} = y_{inf}(1) + sin(\alpha_{orth,inf}) \cdot R_1 \tag{2.48}$$

$$x_{PR1} = x_{inf}(1) + cos(\alpha_{orth,inf}) \cdot R_1 \tag{2.49}$$

The wall contour points of the *arc*- segment *VI* are calculated by Eq. 2.50 and 2.51. The angle $\alpha_{arc,inf}$ is a list with start value $\alpha_{orth,inf}$ and end value $-90°$.

$$y_{arc,inf} = y_{PR1} - sin(\alpha_{arc,inf}) \cdot R_1 \tag{2.50}$$

$$x_{arc,inf} = x_{PR1} - cos(\alpha_{arc,inf}) \cdot R_1 \tag{2.51}$$

Two things are crucial for the design of wall section *VI*. First, the point x/y_{PR1} must be located on the red dashed line. In this way, the *inf*- contour and the wall segment *VI* are orthogonal to the red dashed line. Second, a suitable radius R_1 needs to be specified, i. e. not too large and not too small. In this way, it can be ensured that the *inf*- contour and the wall segment *VI* are connected as smoothly as possible, i. e. without major discontinuities in the wall profile at the contour point $x/y_{inf}(1)$.
The nozzle wall sections *IV*, *V*, *VII*, and *I* are straight walls. The wall sections *I* and *VII* are designed up to the axial combustion chamber location x_{cc}.

2.4 Baseline ED nozzle

On the 5th of July 2023, the last launch of the European *Ariane 5ECA* took place. The *Ariane 5ECA* was the last version of the *Ariane 5* rocket family to be launched and, like all development versions before, characterized by two liquid stages in addition to the solid rocket boosters. The first stage was powered by the *Vulcain-2* engine. For the second stage, i. e. the ESC-A upper stage, the *HM-7B* engine [30] was used. The upper stage was only intended as a temporary solution, so opportunities were explored to increase the thrust and augment the payload capabilities. First, it was considered to integrate several *HM-7B* engines, which would have required a complete and expensive redesign of the whole upper stage. Instead, the development of a new upper stage driven by just one but more powerful *VINCI* engine [31] was agreed upon. Besides a slightly modified version of the already known main stage, this resulted in the new *Ariane 5ME* launcher concept. However, due to internal decisions by the *European Space Agency* (ESA), further developments of the *Ariane 5ME* were ultimately canceled in 2014, and priority was given to the *Ariane 6* program as Europe's future launcher [32]. In this regard, the *VINCI* engine was again confirmed as an upper-stage engine exploiting existing developments [33].
The *VINCI* upper-stage engine is considered the reference case on the basis of which a comparable Baseline ED nozzle is designed. The second design procedure is used, which is already discussed in Subsection 2.2.2 and Fig. 2.8. Accordingly, the Baseline ED nozzle features a TIC, and thus, it can also be referred to as TIC-ED. The input parameters for the sub- and supersonic wall contouring are determined in various ways. First, they are taken from the conventional *VINCI* engine introduced in Subsection 2.4.1. Second, they are calculated with the CEA software (McBride and Gordon [34] and [35]). More details are given in Subsection 2.4.2. Third, they are taken from an additional reference ED nozzle from the literature. This is discussed in more detail in Subsection 2.4.3.

Figure 2.12: *VINCI* engine foreseen for *Ariane 6* upper-stage applications [36]

2.4.1 *VINCI* upper stage engine

		VINCI	*HM-7B*
Engine cycle		Closed Expander	Gas Generator
Propellants		LOX/LH_2	LOX/LH_2
Number of re-ignitions		5	0
Oxidizer/Fuel ratio	O/F	5.85	4.9
Chamber pressure	$\mathbf{p_c}$ **[bar]**	**61.2**	**37**
Mass flow rate	$\dot{m}$ $[\frac{kg}{s}]$	39.5	14.8
Truncation expansion ratio	ε_{trunc} $[-]$	240	83.1
Vacuum thrust	F_{vac} $[kN]$	180	64.8

Table 2.1: *VINCI* and *HM-7B* engine parameters

Table 2.1 shows the main engine parameters of the *VINCI* and *HM-7B* engines derived from EADS-ST [16] and other sources from academia, research and industry [37] [38] [31] [39] [40]. The *VINCI* engine delivers almost three times the thrust of its predecessor *HM-7B* to meet the requirement of a larger upper stage to realize a payload increase. In addition, the *VINCI* engine is integrated into a closed expander cycle, operated with LOX/LH_2 propellant combination and re-ignitable up to five times. The chamber pressure p_c is an input parameter for the supersonic wall contouring and highlighted.

2.4.2 CEA software nozzle analysis

Additional parameters for the supersonic wall contouring are calculated using the CEA software (Chemical Equilibrium with Applications), which has been developed at NASA Lewis Research Center for more than 60 years. The CEA software calculates the nozzle expansion one-dimensionally for variable specific heat ratio γ. The calculations in this Section are done under Bray's assumption for chemistry, i. e. equilibrium flow until the sonic section and frozen flow downstream. The propellants considered are cryogenic oxygen ($t(k) = 90\ K$) and hydrogen ($t(k) = 20\ K$) with the propellant mixture ratio O/F and chamber pressure p_c listed in Tab. 2.1.
For several axial positions within the nozzle, such as the chamber, throat, and exit, the CEA software calculates the thermodynamic, thermophysical, and transport properties of the mixture and the individual species and mass fractions [41]. Species with mass fractions lower than 10^{-4} are neglected in the CEA output.
Table 2.2 shows some of the outputs of the CEA software. The chamber temperature T_c and the specific heat ratio in the throat γ_{th} are input parameters for the supersonic wall contouring and highlighted. Moreover, the individual exhaust gas species, the species mass fractions $Y_{s,i}$, the mixture molar mass $\mathcal{M}_{mix}$, and the characteristic velocity c^* are shown. The latter is a quality factor for the combustion.

Characteristic velocity			c^*	$[\frac{m}{s}]$	2368.9
Chamber temperature			$\mathbf{T_c}$	**[K]**	**3555.66**
Throat specific heat ratio			$\gamma_{\mathbf{th}}$	$[-]$	**1.138**
1	H	Mass fraction	$Y_{s,1}$	$[-]$	0.00285
2	O	Mass fraction	$Y_{s,2}$	$[-]$	0.00397
3	H_2	Mass fraction	$Y_{s,3}$	$[-]$	0.04023
4	OH	Mass fraction	$Y_{s,4}$	$[-]$	0.05451
5	H_2O	Mass fraction	$Y_{s,5}$	$[-]$	0.89076
6	O_2	Mass fraction	$Y_{s,6}$	$[-]$	0.00762
Mixture		Mass fraction	Y_{mix}	$[-]$	1.000
Mixture		Molar Mass	$\mathcal{M}_{mix}$	$[\frac{g}{mol}]$	13.172

Table 2.2: CEA software output for Baseline ED nozzle

The characteristic velocity c^* is used to calculate the throat area A_t of the Baseline TIC-ED nozzle by Eq. 2.52. The mass flow rate $\dot{m}$ of the engine is taken from Tab 2.1. Subsequently, the truncation exit radius $R_{e,trunc}$ is calculated by Eq. 2.53. The truncation expansion ratio ε_{trunc} is 240, as shown in Tab. 2.1.

$$A_t = \frac{c^* \cdot \dot{m}}{p_c} \tag{2.52}$$

$$R_{e,trunc} = \sqrt{\frac{\varepsilon_{trunc} \cdot A_t}{\pi}} \tag{2.53}$$

The specific gas constant of the gas mixture $R_{s,mix}$ is calculated by Eq. 2.54. The quantity R_u is the universal gas constant. The mixture molar mass $\mathcal{M}_{mix}$ is taken from Tab. 2.2.

$$\mathcal{R}_{s,mix} = \frac{\mathcal{R}_u}{\mathcal{M}_{mix}} \tag{2.54}$$

The throat area A_t, the truncation exit radius $R_{e,trunc}$, and the specific gas constant of the mixture $R_{s,mix}$ are summarized in Tab. 2.3. They are input parameters for the supersonic wall contouring.

Throat area	$\mathbf{A_t}$	$[\mathbf{m^2}]$	**0.015**
Truncation exit radius	$\mathbf{R_{e,trunc}}$	$[\mathbf{m}]$	**1.081**
Mixture specific gas constant	$\mathcal{R}_{\mathbf{s,mix}}$	$[\frac{\mathbf{J}}{\mathbf{kg \cdot K}}]$	**631.235**

Table 2.3: Input parameters for the supersonic wall contouring of the Baseline ED nozzle

2.4.3 Reference ED nozzle

In the Subsections 2.4.1 and 2.4.2, input parameters are determined, which are required for the supersonic wall contouring of the Baseline ED nozzle. These parameters are listed in Tab. 2.1, 2.2 and 2.3, and they are highlighted. However, the throat of an ED nozzle is different from that of a conventional nozzle since it is shifted and possibly inclined w. r. t. the symmetry axis, as discussed in Section 2.2. Hence, more specific ED nozzle parameters are required for the design of the Baseline ED nozzle. These parameters are determined in this Subsection. For this, the ED nozzle from EADS-ST [16] with an annular reverse, i. e. counterflow, combustion chamber arrangement is taken as a reference, as shown in Fig. 2.13. This nozzle was primarily developed for *VINCI* engine characteristics. Thus, it is an optimal starting point.

Figure 2.13: 3D color view of EADS-ST *VINCI* ED nozzle [16]

The throat angle Θ_{th}, the truncation length x_{trunc} and the contour point in the throat along the internal wall (x_2/y_2) are adopted from the EADS-ST *VINCI* ED nozzle. These parameters are input parameters for the supersonic wall contouring and listed in Tab. 2.4.

Throat angle	$\mathbf{\Theta_{th}}$	[°]	**− 125**
Truncation length	$\mathbf{x_{trunc}}$	[m]	**2**
1. Wall coordinate	$\mathbf{x_2}$	[m]	**0.013**
2. Wall coordinate	$\mathbf{y_2}$	[m]	**− 0.164**

Table 2.4: ED nozzle specific input parameters for the supersonic wall contouring of the Baseline ED nozzle

In the second design procedure in Fig. 2.8, the parameter r_{non} is an input parameter. This is the dimensionless arc radius of the external wall in the internal expansion region $\frac{R_c}{R_e}$, as shown in Fig. 2.2.
At this point, the second design procedure is slightly modified to the procedure shown in Fig. 2.14, and the absolute arc radius R_c is set to $\mathbf{R_c = 0.05\ m}$ in the input parameters. Accordingly, r_{non} results automatically in the inner loop.

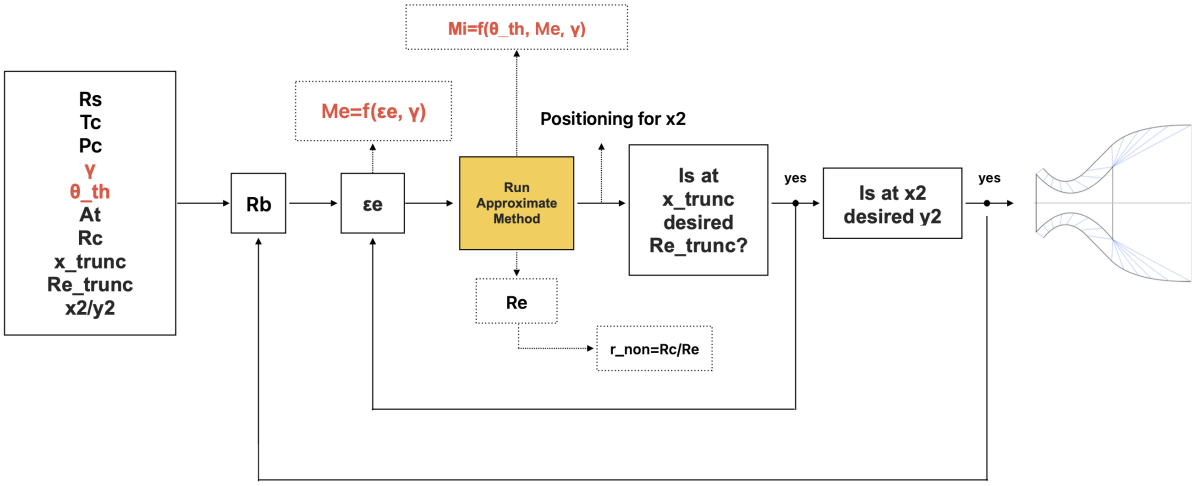

Figure 2.14: Modified second design procedure

By running the modified second design procedure, additional parameters result. These are listed in Tab. 2.5.

Base radius	R_b	$[m]$	0.165
FL expansion ratio	ε_e	$[-]$	330.79
FL mach number	M_e	$[-]$	5.0923
FL exit radius	R_e	$[m]$	1.28
Wall curvature	r_{non}	$[-]$	0.039
internal mach number	M_i	$[-]$	1.0059

Table 2.5: Resulting Baseline ED nozzle parameters

Figure 2.15 shows the supersonic wall profiles of the Baseline TIC-ED nozzle and the straight characteristic lines. In addition, the internal expansion region is shown in more detail. This is very short due to the reverse flow configuration, as discussed in Section 2.2.

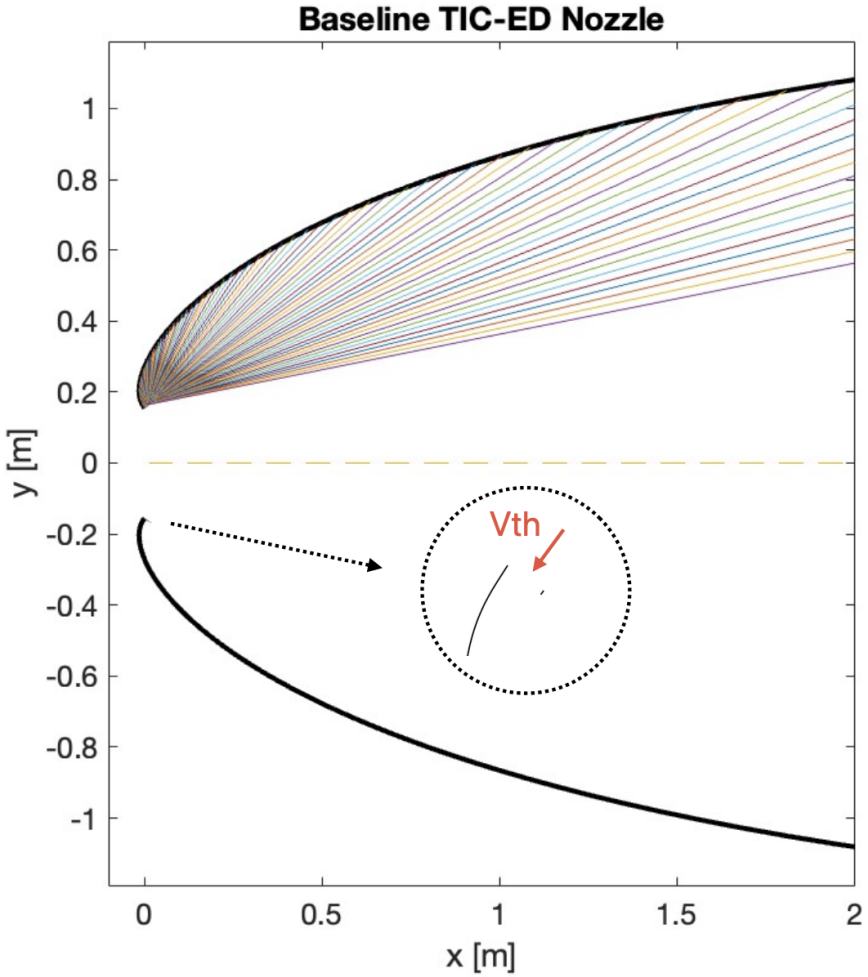

Figure 2.15: Wall profiles of the Baseline TIC-ED nozzle with characteristic lines calculated by the approximate contouring method

However, the approximate contouring method only calculates the supersonic wall sections of the Baseline ED nozzle, as shown in Fig. 2.15. The subsonic wall sections are calculated using the method discussed in Section 2.3. For this, the axial combustion chamber location x_{cc} and the radius of the central body y_{Base} are adopted from the EADS-ST *VINCI* ED nozzle [16], as shown in Tab. 2.6. The internal wall radius R_2 results automatically. The external wall radius R_1 is calculated by applying the ratio of wall radii $\mathbf{\frac{R_1}{R_2} = 3}$.

Axial CC location	$\mathbf{x_{cc}}$	**[m]**	**0.39**
Central body radius	$\mathbf{y_{Base}}$	**[m]**	**– 0.24**
Internal wall radius	R_2	$[m]$	0.05
External wall radius	R_1	$[m]$	0.15

Table 2.6: Input parameters for the subsonic wall contouring of the Baseline ED nozzle

Figure 2.16 shows the Baseline ED nozzle with the sub- and supersonic wall sections. For simplicity reasons, the ED central body is neglected in the design, and a straight wall is realized instead. This is due to three reasons. First, the CFD simulations are simplified because the

expansion and deflection of the flow at the central body are not simulated. Second, the central body only makes around 5 % of the exit area, so no significant performance loss due to the reduction of the expansion ratio is expected. Third, the wall pressure along the central body is low in vacuum operation, so the pressure force is not expected to contribute significantly to the thrust either.

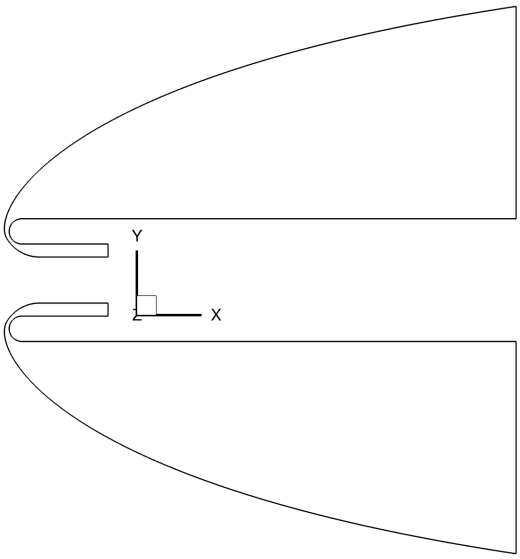

Figure 2.16: Baseline TIC-ED nozzle

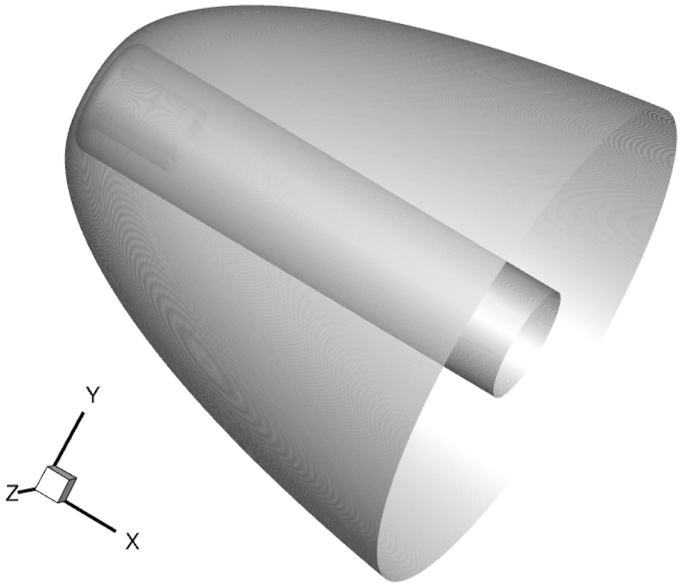

Figure 2.17: 3D view of Baseline ED nozzle

Chapter 3

CFD model for rocket nozzle flows

Figure 3.1 shows a flow chart describing the process of conducting CFD (Computational Fluid Dynamics) simulations. At the beginning, the flow phenomenon is defined, which in this case is the expansion flow inside the nozzle of a rocket engine. The flow phenomenon can be described by a set of governing equations that can be coupled with thermodynamic, transport, and turbulence models. Before the governing equations can be solved in the computational domain, the computational domain and the governing equations need to be discretized. The result is a set of algebraic equations to which numerical methods can be applied to obtain the numerical solution [42]. This chapter aims to give a general overview of these steps.

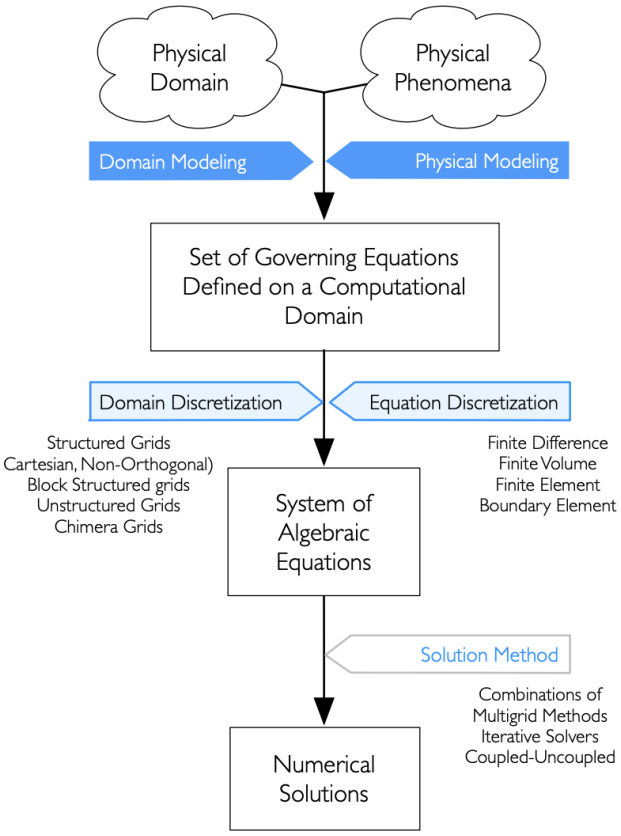

Figure 3.1: Flow chart for CFD simulations [43]

3.1 Physical Phenomena

Different flow regimes are present from the flow inside the nozzle up to the expansion of the exhaust gas in the vacuum outside the nozzle, as shown in Fig. 3.2. Inside the combustion chamber, the gas density is high. The gas density decreases during the expansion inside the nozzle and during the free expansion in vacuum. Inside the nozzle and in the near-field of the exhaust plume, the gas density is still high enough to assume a continuum flow regime. A continuum flow regime means that the molecules collide with each other, exchange their energies, and maintain a thermal equilibrium. Just as the flow travels further downstream and the distance to the nozzle exit plane increases, the gas gets more and more rarefied. A continuum can no longer be assumed from a distance from the nozzle exit plane. The flow first reaches the transition regime until it gradually changes into the free molecular regime.

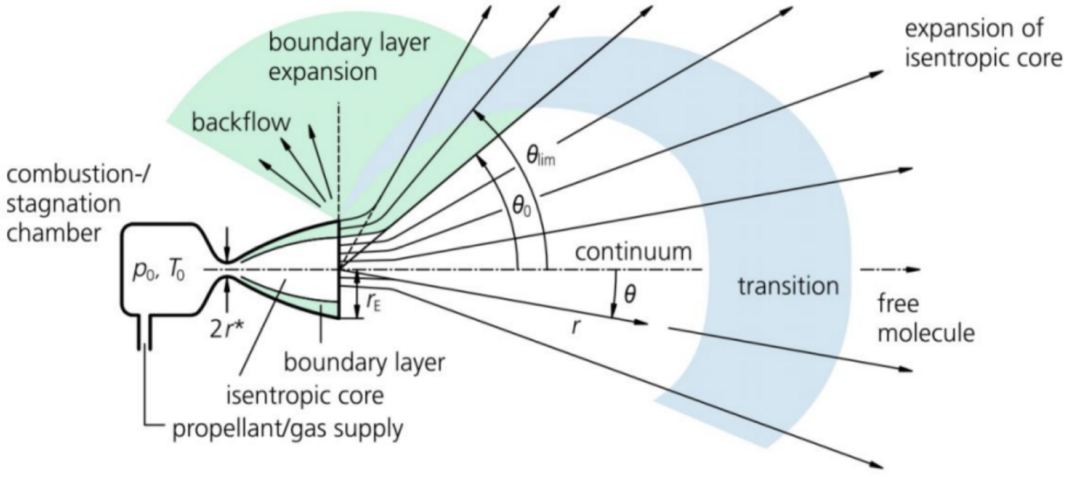

Figure 3.2: Nozzle's plume flow expanding in vacuum [44]

3.2 Navier-Stokes equations

The simulations in this work are only carried out up to the nozzle exit plane so that a full continuum flow can be assumed. Equations that can describe this continuum are the Navier-Stokes (NS) equations. They can be derived from the continuum theory that considers matter as a continuum, and therefore, they are not valid for rarefied flows [45]. The NS equations describe the state of a system by the macroscopic structure of the gas (as in the classic thermodynamics), i. e. the macroscopic state variables of pressure p and temperature T. The NS equations comprise the conservation equations of the physical quantities of mass, momentum, and energy [46], and they form a coupled non-linear system of partial differential equations, also called complete NS equations.

The complete NS equations describe the flow and resolve the smallest flow features, such as turbulent eddies [47]. Besides turbulence and viscosity, the NS equations shown in this Section consider heat exchange, multi-species flow, and chemical reactions. The conservation equations are formulated in the integral form and applied to a fixed finite control volume characterized by the volume V and the control surface S, as shown in Fig. 3.3.

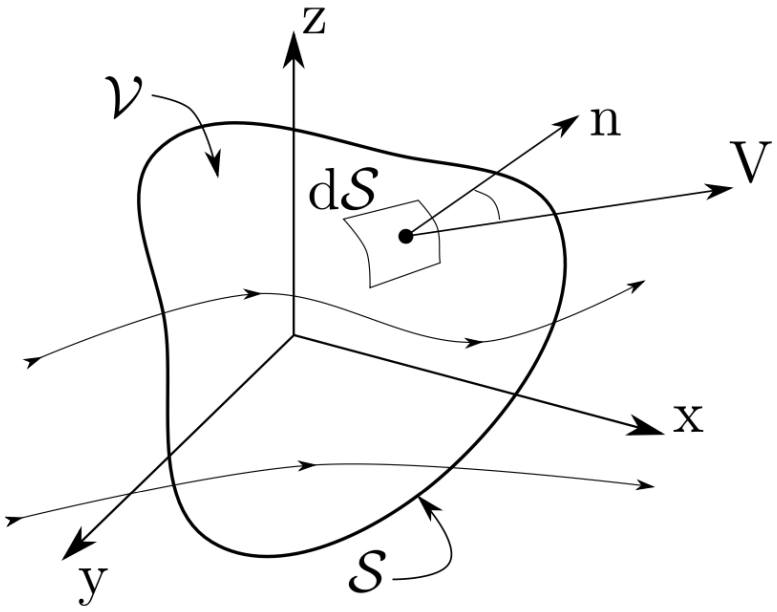

Figure 3.3: Fixed finite control volume [48]

The mass conservation equation

Equation 3.1 states that the net change of mass of the species s in time in the control volume equals the net fluxes of species through the surface S and the species that are created or extinguished by chemical reactions inside the control volume $\mathcal{V}$ [48].

$$\frac{\partial}{\partial t}\int_{\mathcal{V}} \rho_s d\mathcal{V} = -\oint_S \rho_s v_s dS + \int_{\mathcal{V}} \dot{w}_s d\mathcal{V} \tag{3.1}$$

The quantity v_s is the motion velocity of the species and can be written as the sum of the velocity of the mixture v and the species diffusion velocity u_s, as shown in Eq. 3.2. Hence, the mass conservation equation changes to Eq. 3.3.

$$v_s = v + u_s \tag{3.2}$$

$$\frac{\partial}{\partial t}\int_{\mathcal{V}} \rho_s d\mathcal{V} + \oint_S \rho_s v \cdot n dS = -\oint_S \rho_s u_s dS + \int_{\mathcal{V}} \dot{w}_s d\mathcal{V} \tag{3.3}$$

The quantity ρ_s is the density of the individual species. The mixture density ρ can be calculated from the sum of the N_s individual species densities, as shown in Eq. 3.4. In the case of single-species simulations, $N_s = 1$ applies.

$$\rho = \sum_{s=1}^{N_s} \rho_s \tag{3.4}$$

The quantity $\rho_s u_s$ represents the diffusion velocity contribution relevant to each species, which, according to Eq. 3.5, sums to zero for all species:

$$0 = \sum_{s=1}^{N_s} \rho_s u_s \tag{3.5}$$

The quantity $\dot{w}_s$ is the local rate change of the species densities due to chemical reactions in the control volume. If chemical reactions are neglected in the simulations, $\dot{w}_s$ equals zero. The same applies to the sum of $\dot{w}_s$ for all individual species:

$$0 = \sum_{s=1}^{N_s} \dot{w}_s \tag{3.6}$$

The chemical source term $\dot{w}$ can be calculated by Eq. 3.7.

$$\dot{w}_s = \mathcal{M}_s \sum_{j=1}^{N_r} (\nu_{s,j}^P - \nu_{s,j}^R) \left[k_{f,j} \prod_{s=1}^{N_s} \left(\frac{\rho_s}{\mathcal{M}_s} \right)^{\nu_{s,j}^R} - k_{b,j} \prod_{s=1}^{N_s} \left(\frac{\rho_s}{\mathcal{M}_s} \right)^{\nu_{s,j}^P} \right] \alpha_j \tag{3.7}$$

The generic chemical reaction among the species B_s is expressed with the stoichiometric coefficients of the reactants $\nu_{i,j}^R$ and the products $\nu_{i,j}^P$ [49]:

$$\sum_{s=1}^{N_s} \nu_{s,j}^R B_s \rightleftharpoons \sum_{s=1}^{N_s} \nu_{s,j}^P B_s \tag{3.8}$$

and the forward $k_{f,j}$ and backward $b_{b,j}$ reaction rates that are expressed by the Arrhenius law in Eq. 3.9 and 3.10. The quantity A_j is the pre-exponential factor, n_j is the temperature exponent, $E_{a,j}$ is the molar activation energy, R_u is the universal gas constant, and K_j is the equilibrium constant of the j-th reaction.

$$k_{f,j} = A_j T^{n_j} exp \left(-\frac{E_{a,j}}{\mathcal{R}_u T} \right) \tag{3.9}$$

$$k_{b,j} = k_{f,j} / K_j \tag{3.10}$$

The quantity α_j in Eq. 3.7 generally equals one. In the case of reactions involving a third body M, it is defined by Eq. 3.11 with $\hat{\alpha}_{s,j}$ that is the third body efficiency of the s-th species involved in the j-th reaction [49].

$$\alpha_j = \sum_{s=1}^{N_s} \hat{\alpha}_{s,j} \left(\frac{\rho_s}{M_s} \right) \tag{3.11}$$

The momentum conservation equation

The momentum conservation in Eq. 3.12 states that the momentum variation in time of a fluid element equals the total forces acting on the volume $\mathcal{V}$ and on the surface S [48].

$$\frac{\partial}{\partial t} \int_{\mathcal{V}} \rho v d\mathcal{V} + \oint_S (\rho v \cdot n) v dS = \int_{\mathcal{V}} \rho f d\mathcal{V} + \oint_S t dS \tag{3.12}$$

The first term on the right-hand side represents the forces acting on the volume $\mathcal{V}$ (f is the volumetric force per unit mass), such as gravitational and centrifugal forces. These forces can be neglected for the present applications. The second term on the right-hand side is dedicated to the forces acting on the surface (t is the surface force per unit area). The i-th component of the stress vector t in Eq. 3.13 can be described as the product of the stress tensor σ_{ij} and the j-th component of the surface normal vector n_j. The latter is the unit vector orthogonal to the surface and positive since it faces outwards the volume.

$$t_i = \sigma_{ij} n_j \tag{3.13}$$

The stress tensor σ_{ij} can be subdivided into two terms, as shown in Eq. 3.14. First, the spherical tensor based on pressure where $\delta_{ij} = 0$ in case of $i \neq j$ and $\delta_{ij} = 1$ if $i = j$, and second, the viscous stress tensor τ_{ij}. The latter is zero if friction effects are neglected.

$$\sigma_{ij} = -p\delta_{ij} + \tau_{ij} \tag{3.14}$$

The viscous stress tensor can be calculated using the Stokes hypothesis [47] for a Newtonian fluid, as shown in Eq. 3.15. The quantity v_i is the i-th component of the mixture velocity v, x_i the i-th orthogonal axis, and μ the dynamic viscosity of the mixture [48].

$$\tau_{ij} = \mu \left(\frac{\partial v_i}{\partial x_j} + \frac{\partial v_j}{\partial x_i} - \frac{2}{3} \frac{\partial v_k}{\partial x_k} \delta_{ij} \right) \tag{3.15}$$

The energy conservation equation

The energy conservation equation 3.16 states that the total energy variation in time of a fluid element is equal to the total work made by the forces acting on the volume $\mathcal{V}$ and surface S, and the heat transfer rate entering through the surface [48].

$$\frac{\partial}{\partial t} \int_{\mathcal{V}} \rho \left(u + \frac{v^2}{2} \right) d\mathcal{V} + \oint_S \left(u + \frac{v^2}{2} \right) \rho v \cdot n dS = \int_{\mathcal{V}} \rho (f \cdot v) d\mathcal{V} + \oint_S (t \cdot v) dS - \oint_S q \cdot n dS \tag{3.16}$$

The quantity q stands for the vector of the heat flux. It has a positive sign as it is outward-facing the surface. Equations 3.17 and 3.18 demonstrate that the heat flux is composed of a conductive and diffusive component (heat radiation is neglected). The conductive heat transfer depends on the thermal conductivity k of the mixture and the temperature gradient using Fourier's law. The quantity $u_{s,j}$ is the j-th component of the diffusion velocity of the species, and h_s is the absolute enthalpy of the species per unit mass.

$$q = q_c + q_d \tag{3.17}$$

$$q_j = -k \frac{\partial T}{\partial x_j} + \sum_{s=1}^{N_s} \rho_s u_{s,j} h_s \tag{3.18}$$

The expression $\rho \left(u + \frac{v_j v_j}{2} \right)$ is the total energy per unit volume, and u is the specific internal energy.

3.3 Thermodynamic models

The equation of state for the gas mixture is defined in the following, assuming a thermally perfect gas. The equation of state is needed for thermodynamic closure since several macroscopic state variables are linked in one equation. Then, the specific heat capacity at constant pressure c_p, the enthalpy h, the entropy s, and the mathematical models used to describe them are discussed in more detail.

Equation of state

The equation of state is shown in Eq. 3.19. The quantity $\mathcal{R}_s$ is the specific gas constant of the gas mixture. This can be calculated from the universal gas constant $\mathcal{R}_u$ and the molar mass $\mathcal{M}$ of the mixture by Eq. 3.20 or the species mass fractions Y_s and molar masses $\mathcal{M}_s$, as shown in Eq. 3.21.

$$p = \rho \mathcal{R}_s T \tag{3.19}$$

$$\mathcal{R}_s = \frac{\mathcal{R}_u}{\mathcal{M}} \tag{3.20}$$

$$\mathcal{R}_s = \sum_{s=1}^{N_s} Y_s \frac{R_u}{\mathcal{M}_s} \tag{3.21}$$

Alternatively, $\mathcal{R}_s$ can be calculated from the species mass fractions Y_s and specific gas constants $R_{s,s}$, as shown in Eq. 3.22.

$$\mathcal{R}_s = \sum_{s=1}^{N_s} Y_s R_{s,s} \tag{3.22}$$

The species mass fraction Y_s describes the ratio between the species density and the mixture density, as shown in Eq. 3.23. Besides the mass fraction, the mixture composition can also be expressed in terms of mole fraction X_s in Eq. 3.24. The mole fraction is calculated from the number of moles N_s of the species and the number of moles of the whole mixture N.

$$Y_s = \frac{\rho_s}{\rho} \tag{3.23}$$

$$X_s = \frac{N_s}{N} \tag{3.24}$$

The relation between the mass fraction and the mole fraction depends on the ratio between the molecular weight of the species and the molecular weight of the mixture:

$$Y_s = \frac{\rho_s}{\rho} = \frac{N_s}{N}\frac{\mathcal{M}_s}{\mathcal{M}} = \frac{\mathcal{M}_s}{\mathcal{M}} X_s \tag{3.25}$$

Specific heat capacity at constant pressure c_p

Figure 3.4 illustrates an open thermodynamic system ($p = const.$). Adding heat Q to a fluid with the molar amount N increases the temperature from initial T_1 to T_2. The amount by which the temperature increases depends on the **molar-specific heat capacity at constant pressure $\overline{\mathbf{c_p}}$**, as shown in Eq. 3.26. The overline represents the fact that it is a molar quantity. In general, the lower $\overline{c_p}$, the higher the heat absorption of the fluid, which is connected with a more pronounced temperature increase. However, $\overline{c_p}$ is not a constant fluid property but a function of temperature.

$$\Delta T = T_2 - T_1 = \frac{Q}{N \cdot \overline{c_p}(T)} \tag{3.26}$$

In the CFD simulations in this work, the mass-specific heat capacity of constant pressure is used for the simulation setup. Equation 3.27 shows how it is calculated from the molar-specific heat capacities of the individual species.

$$c_p = \sum_{s=1}^{N_s} Y_s \cdot \frac{\overline{c_{p,s}}(T)}{\mathcal{M}_s} \tag{3.27}$$

The species molar-heat capacity at constant pressure as a function of temperature $\overline{c_{p,s}}(T)$ is obtained from a NASA polynomial with the general form shown in Eq. 3.28. The polynomial is characterized by seven polynomial coefficients a_i [50]. In detailed notation, the polynomial can be converted into the form 3.29, which is a fourth-order polynomial. The coefficients a_i are determined through least-squares fit for each species. Hence, they differ from species to species. In addition, the set of the polynomial coefficients of an individual species changes depending on the temperature interval. The intervals are 200 to 1000 K, 1000 to 6000 K and, for some gases

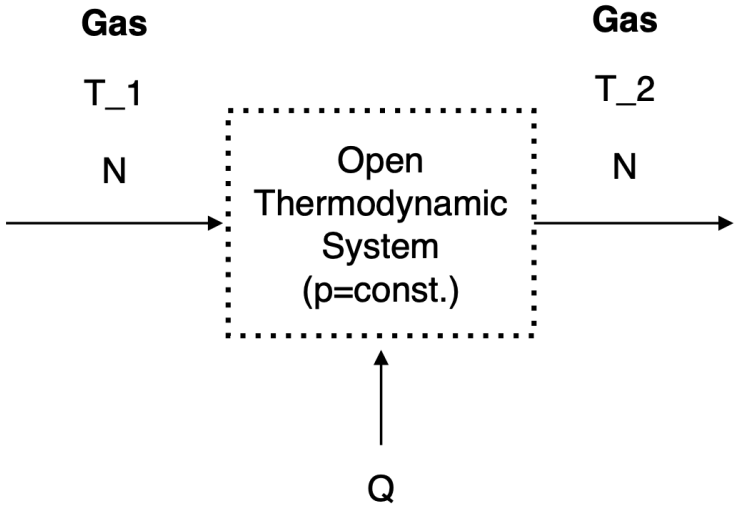

Figure 3.4: Generic open thermodynamic system ($p = const.$)

6000 to 20000 K [51]. The latter temperature interval is not important for the CFD simulations in this work. The reason is that the temperatures in the rocket nozzle from the combustion chamber to the nozzle exit are much lower. However, the sets of coefficients for the chemical species are listed in [51].

$$\overline{c_{p,s}}(T) = \mathcal{R}_u \cdot \sum_{i=1}^{7} a_i \cdot T^{i-3} \tag{3.28}$$

$$\begin{aligned}\overline{c_{p,s}}(T) = R_u \cdot (a_1 \cdot T^{-2} + a_2 \cdot T^{-1} + a_3 + a_4 \cdot T + \\ a_5 \cdot T^2 + a_6 \cdot T^3 + a_7 \cdot T^4)\end{aligned} \tag{3.29}$$

The ratio of the specific heat capacity at constant pressure c_p and constant volume c_v is defined as the specific heat ratio:

$$\gamma = \frac{c_p}{c_v} = \frac{c_p}{c_p - \mathcal{R}_s} \tag{3.30}$$

Specific enthalpy h

The equation for the **molar-specific enthalpy** $\overline{\mathbf{h}}$ can be derived from the general definition of the enthalpy H that, according to Eq. 3.31, is defined as the sum of the internal energy U and the product of pressure and volume $P \cdot V$. Under consideration of an isobaric process, the difference of enthalpy ΔH can be expressed by Eq. 3.32.

$$H = U + P \cdot V \tag{3.31}$$

$$\Delta H = \Delta U + \Delta(P \cdot V) = \Delta U + P \cdot \Delta V \tag{3.32}$$

According to the first law of thermodynamics, the difference in the internal energy can be described as the cause of heat Q and work W done. This is shown in Eq. 3.33. For an isobaric process and the assumption that the only work done is the pressure-volume work $-P \cdot \Delta V$, Eq. 3.34 is obtained.

$$\Delta U = Q + W \tag{3.33}$$

$$\Delta U = Q - P \cdot \Delta V \tag{3.34}$$

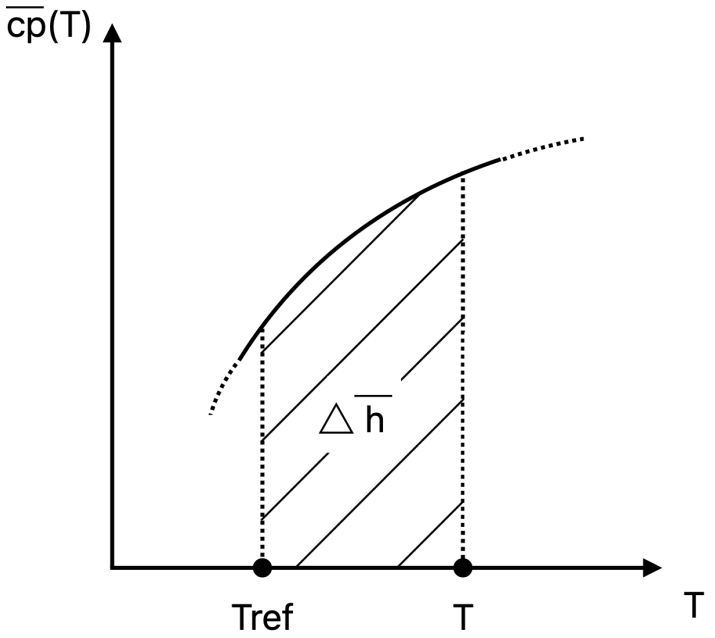

Figure 3.5: Generic curve of molar-specific heat capacity at constant pressure $\overline{c_p}$ as a function of temperature T and correlation to the difference of molar-specific enthalpy $\Delta\overline{h}$

By substituting Eq. 3.34 into Eq. 3.32 it becomes clear that the difference in enthalpy ΔH equals the heat Q:

$$\Delta H = Q \tag{3.35}$$

Substituting Eq. 3.26 into 3.35 yields Eq. 3.36. From this equation, the difference in molar-specific enthalpy $\Delta\overline{h}$ can be derived, as shown in Eq. 3.37.

$$\Delta H = N \cdot \overline{c_p}(T) \cdot \Delta T \tag{3.36}$$

$$\frac{\Delta H}{N} = \Delta\overline{h} = \overline{c_p}(T) \cdot \Delta T \tag{3.37}$$

Two things are to be mentioned. On the one hand, $\Delta\overline{h}$ is the integral of $\overline{c_p}$ w. r. t. temperature (see Eq. 3.38), i. e. the area under the $\overline{c_p}$ graph between the two interval bounds T_{Ref} and T, as illustrated in Fig. 3.5. The integration constant is represented by a_8. The reference temperature T_{Ref} refers to the standard conditions ($293.15\ K$ and $1atm$), and the reference state is assumed to be thermodynamically stable (equilibrium).
On the other hand, $\Delta\overline{h}$ is the sensible component of enthalpy and the difference of the absolute molar-specific enthalpies $\overline{h}$ at the respective integration i. e. temperature bounds.

$$\Delta\overline{h} = \int_{T_{Ref}}^{T} \overline{c_p}(T)dT + R_u \cdot a8 = \overline{h}(T) - \overline{h}(T_{Ref}) \tag{3.38}$$

Equation 3.39 shows the absolute molar-specific enthalpy $\overline{h}$ as a function of the enthalpy of formation $\Delta\overline{h_f^0}(T_{Ref})$ and the sensible enthalpy $\Delta\overline{h}$. In the case of $T = T_{Ref}$, the sensible enthalpy component $\Delta\overline{h}$ becomes zero, and the absolute molar-specific enthalpy $\overline{h}$ equals the enthalpy of formation $\Delta\overline{h_f^0}(T_{Ref})$. The enthalpy of formation is the chemical bond energy, i. e. the energy that is needed to form (subscript f) a substance from its pure constituent elements at standard (reference) conditions (superscript 0) [52]. Table 3.1 shows the enthalpies of formation

	$\mathcal{M}$ $[\frac{\mathbf{g}}{\mathbf{mol}}]$	$\mathbf{\Delta\overline{h^0_{f,s}}}$ $[\frac{\mathbf{kj}}{\mathbf{mol}}]$
H	1.008	217.999
O	15.999	249.175
H_2	2.016	0
OH	17.007	37.278
H_2O	18.015	− 241.826
O_2	31.999	0

Table 3.1: Standard enthalpies of formation $\Delta\overline{h^0_f}$ and molar masses $\mathcal{M}$ of the at the freezing point present species, compare with table 2.2 and [51]

of the chemical species present in the throat of the LOX/LH_2 Baseline ED nozzle in Section 2.4. Noticeably, $\Delta\overline{h^0_f}$ of H_2 and O_2 is zero since they are already pure substances. A negative sign for $\Delta\overline{h^0_f}$, like in the case for H_2O, indicates that the formation of a compound is exothermic. This means that the energy released during the formation is greater than the energy required to break the bond.

$$\overline{h}(T) = \Delta\overline{h^0_f}(T_{Ref}) + \underbrace{[\overline{h}(T) - \overline{h}(T_{Ref})]}_{\Delta\overline{h}} \tag{3.39}$$

The absolute molar-specific enthalpy $\overline{h_s}(T)$ of the individual species can be expressed by the polynomial shown Eq. 3.40. The polynomial is derived from the integration of the polynomial for $\overline{c_{p,s}}$ in Eq. 3.29. The set of the seven coefficients a_1 to a_7 are extended by another integration constant a_8 that can be obtained by least-squares fit [51].

$$\begin{aligned}\overline{h_s}(T) = R_u \cdot T(-a_1 \cdot T^{-2} + \frac{a_2 \cdot ln(T)}{T} + a_3 + \\ \frac{a_4 \cdot T}{2} + \frac{a_5 \cdot T^2}{3} + \frac{a_6 \cdot T^3}{4} + \frac{a_7 \cdot T^4}{5} + \frac{a_8}{T})\end{aligned} \tag{3.40}$$

The mass-specific enthalpy of the mixture is calculated as follows:

$$h = \sum_{s=1}^{N_s} Y_s \cdot \frac{\overline{h_s}(T)}{\mathcal{M}_s} \tag{3.41}$$

Specific entropy s

A general expression for the entropy can be derived from the Gibbs energy G in Eq. 3.42, which links the general expression of enthalpy H and entropy S. The difference of the Gibbs energy ΔG is shown in Eq. 3.43.

$$G = H - T \cdot S \tag{3.42}$$

$$\Delta G = \Delta H - T \cdot \Delta S \tag{3.43}$$

Since the reference state is assumed to be thermodynamically stable (equilibrium), the difference of the Gibbs energy ΔG becomes zero. Consequently, rearranging Eq. 3.43 to ΔS results in:

$$\Delta S = \frac{\Delta H}{T} \tag{3.44}$$

and under consideration of Eq. 3.36 for ΔH in:

$$\Delta S = \frac{N \cdot \overline{c_p}(T)\ \Delta T}{T} \tag{3.45}$$

Equation 3.46 expresses the difference in the molar-specific entropy. Accordingly, $\Delta\overline{s}$ results from the integration of $\frac{\overline{c_p}(T)}{T}$ w. r. t. temperature, as shown in Eq. 3.47.

$$\frac{\Delta S}{N} = \Delta\overline{s} = \frac{\overline{c_p}(T)\ \Delta T}{T} \tag{3.46}$$

$$\Delta\overline{s} = \int_{T_{Ref}}^{T} \frac{\overline{c_p}(T)}{T} dT + R_u \cdot a9 = \overline{s}(T) - \overline{s}(T_{Ref}) \tag{3.47}$$

For the molar-specific entropy of the individual species $\overline{s_s}(T)$, this leads to the polynomial in Eq. 3.48. The integration constant a_9 is obtained by least-squares fit.

$$\begin{aligned}\overline{s_s}(T) = R_u \cdot (-\frac{a_1 \cdot T^{-2}}{2} - a_2 \cdot T^{-1} + a_3 \cdot ln(T) + \\ a_4 \cdot T + \frac{a_5 \cdot T^2}{2} + \frac{a_6 \cdot T^3}{3} + \frac{a_7 \cdot T^4}{4} + a_9)\end{aligned} \tag{3.48}$$

The mass-specific entropy of the mixture is calculated by Eq. 3.49:

$$s = \sum_{s=1}^{N_s} Y_s \cdot \frac{\overline{s_s}(T)}{\mathcal{M}_s} \tag{3.49}$$

For the chemical species and mass fractions in the throat of the Baseline LOX/LH_2 ED nozzle in Subsection 2.4.2, Fig. 3.6 to 3.8 show the trends of the mixture mass-specific heat capacity at constant pressure c_p, enthalpy h and entropy s as a function of temperature. The latter two feature a linear and logarithmic trend, respectively. The mixture properties in the actual temperature range of interest are shown in Fig. 3.9 to 3.11. This is the gas setup used for the CFD simulations of the Baseline ED nozzle in Chapter 5 and the parametric analyses in Chapter 6.

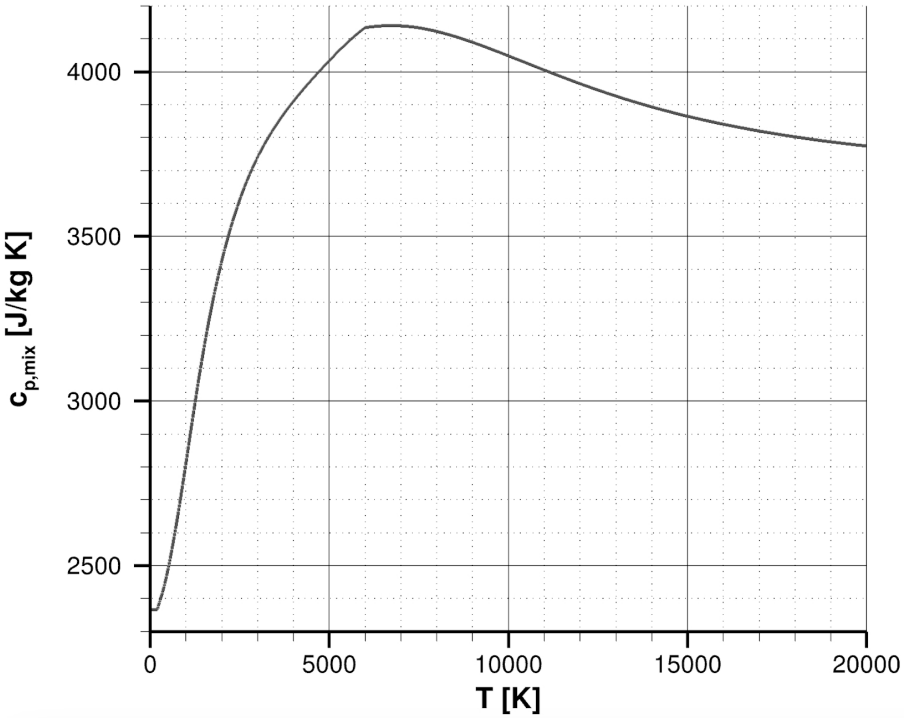

Figure 3.6: Mixture mass-specific heat capacity at constant pressure $c_{p,mix}$ for the gas composition in the throat of the Baseline ED nozzle - full range

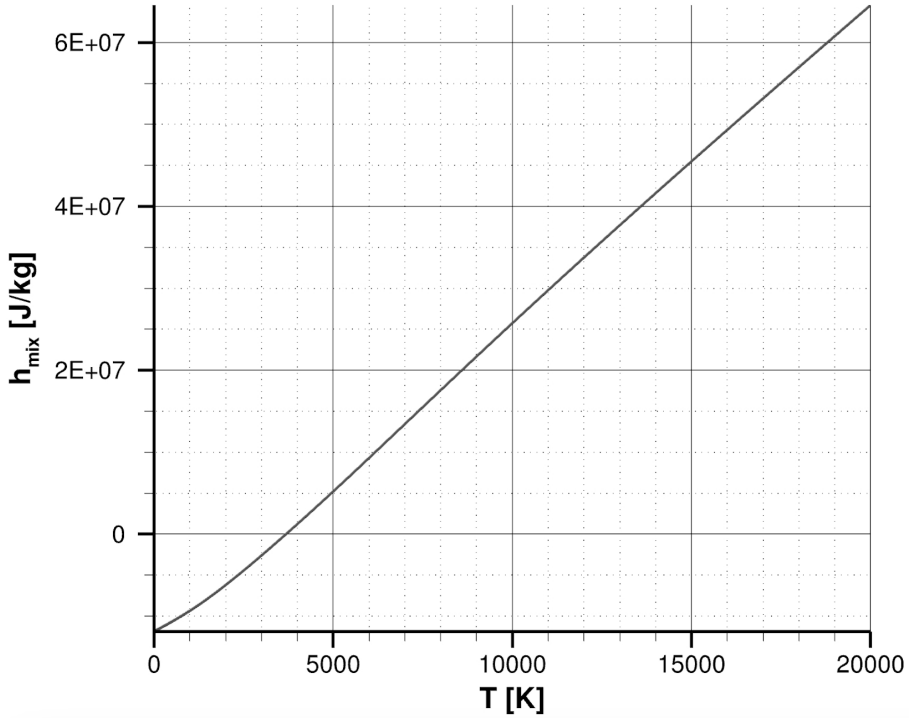

Figure 3.7: Mixture mass-specific enthalpy h_{mix} for the gas composition in the throat of the Baseline ED nozzle - full range

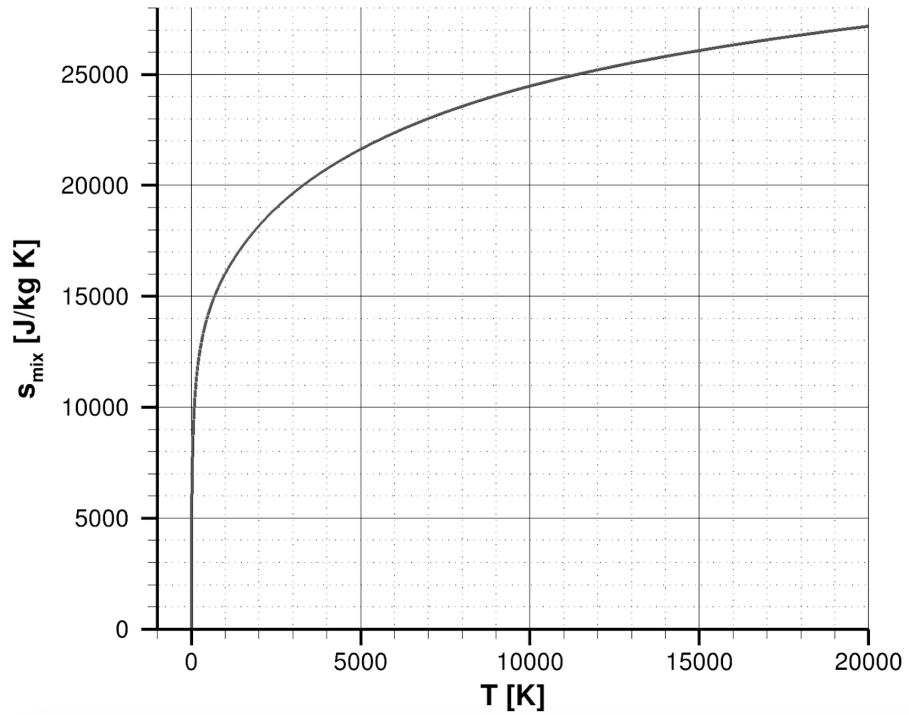

Figure 3.8: Mixture mass-specific entropy s_{mix} for the gas composition in the throat of the Baseline ED nozzle - full range

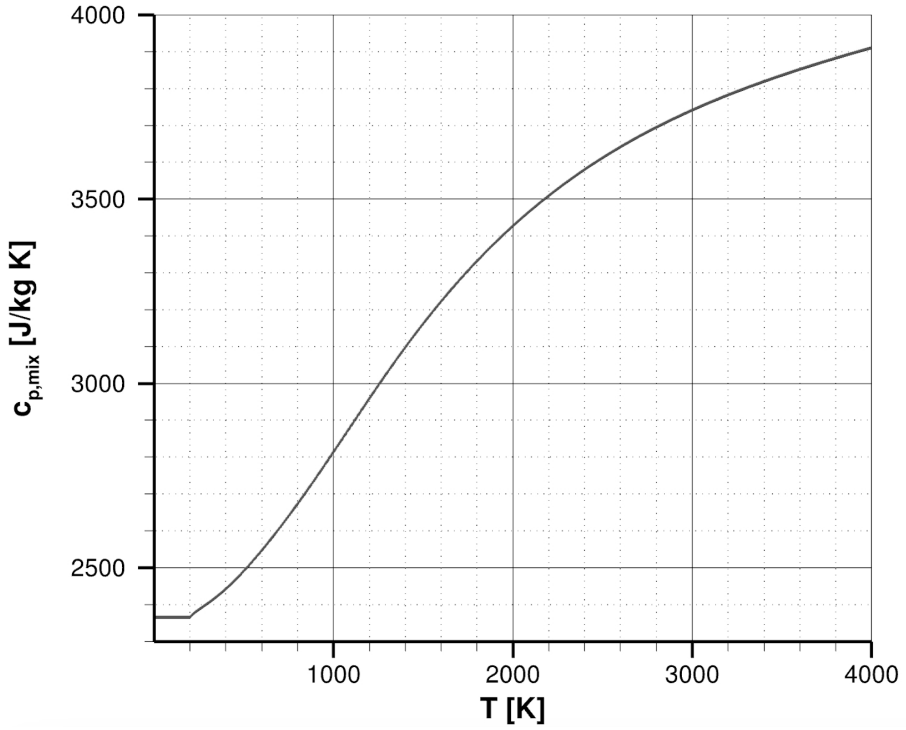

Figure 3.9: Mixture mass-specific heat capacity at constant pressure $c_{p,mix}$ for the gas composition in the throat of the Baseline ED nozzle - range of interest

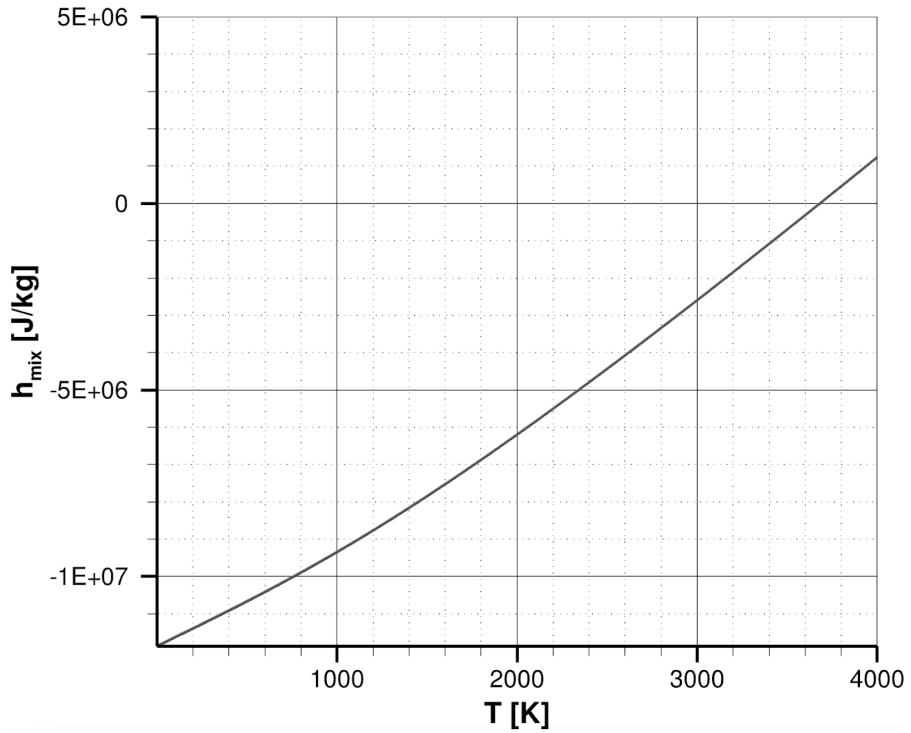

Figure 3.10: Mixture mass-specific enthalpy h_{mix} for the gas composition in the throat of the Baseline ED nozzle - range of interest

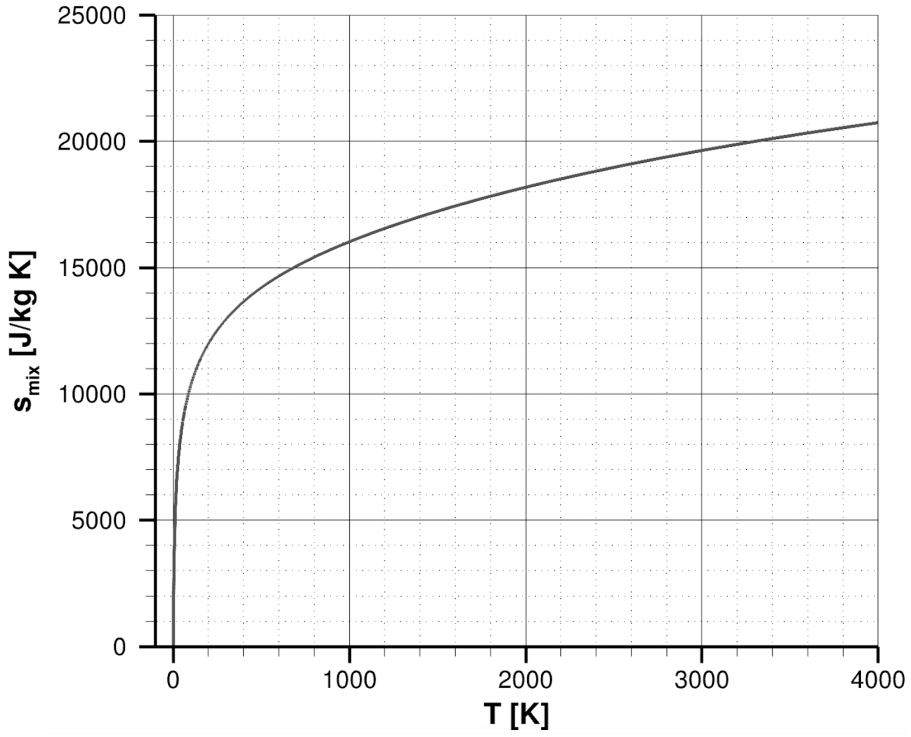

Figure 3.11: Mixture mass-specific entropy s_{mix} for the gas composition in the throat of the Baseline ED nozzle - range of interest

3.4 Transport models

In this Section, the dynamic viscosity, thermal conductivity, and molecular diffusion due to species concentration gradients are discussed.

Dynamic viscosity μ and Thermal conductivity k

The species dynamic viscosity μ_s and thermal conductivity k_s are modeled by the exponential function in Eq. 3.50. The coefficients b_i for each species are obtained from least-squares fit for different temperature intervals [53], as in the case of the thermodynamic modeling in Section 3.3.

$$\left.\begin{matrix}\mu_s(T)\\ k_s(T)\end{matrix}\right\} \rightarrow e^{b_1 \cdot ln(T) + \frac{b_2}{T} + \frac{b_3}{T^2} + b_4} \tag{3.50}$$

The mixture values are calculated from the dynamic viscosity and thermal conductivity values of each species through the *Wilke* semi-empirical relations in Eq. 3.51 and 3.52. These are obtained on the basis of the kinetic theory.

$$\mu = \sum_{s=1}^{N_s} \frac{X_s \cdot \mu_s}{X_s + \sum\limits_{\substack{j=1 \\ j \neq s}}^{N_s} X_j \cdot \phi_{sj}} \tag{3.51}$$

$$k = \sum_{s=1}^{N_s} \frac{X_s \cdot k_s}{X_s + \sum\limits_{\substack{j=1 \\ j \neq s}}^{N_s} X_j \cdot \psi_{sj}} \tag{3.52}$$

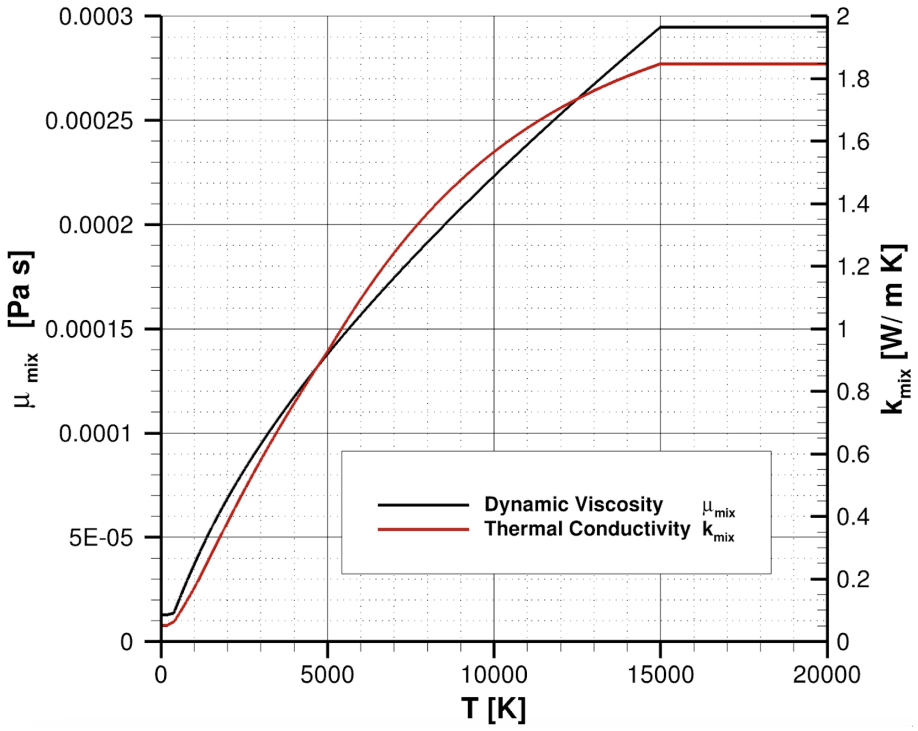

Figure 3.12: Mixture dynamic viscosity μ_{mix} and thermal conductivity k_{mix} for the gas composition in the throat of the Baseline ED nozzle - full range

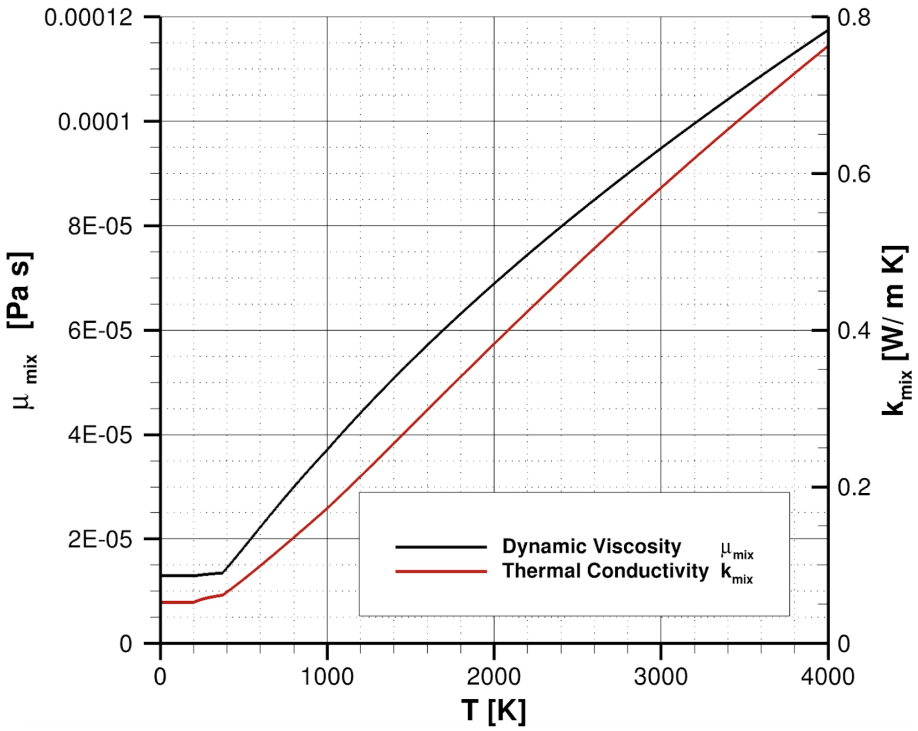

Figure 3.13: Mixture dynamic viscosity μ_{mix} and thermal conductivity k_{mix} for the gas composition in the throat of the Baseline ED nozzle - range of interest

The quantities ϕ_{sj} and ψ_{sj} are the viscosity and thermal conductivity interaction coefficients calculated by Eq. 3.53 and 3.54.

$$\phi_{sj} = \frac{1}{4} \cdot \left[1 + \left(\frac{\mu_s}{\mu_j} \right)^{\frac{1}{2}} \cdot \left(\frac{\mathcal{M}_j}{\mathcal{M}_s} \right)^{\frac{1}{4}} \right]^2 \cdot \left(\frac{2 \cdot \mathcal{M}_j}{\mathcal{M}_s + \mathcal{M}_j} \right)^{\frac{1}{2}} \tag{3.53}$$

$$\psi_{sj} = \phi_{sj} \cdot \left[1 + \frac{2.41 \cdot (\mathcal{M}_s - \mathcal{M}_j) \cdot (\mathcal{M}_s - 0.142 \cdot \mathcal{M}_j)}{(\mathcal{M}_s + \mathcal{M}_j)^2} \right] \tag{3.54}$$

For the chemical species and mass fractions in the throat of the Baseline LOX/LH_2 ED nozzle in Subsection 2.4.2, Fig. 3.12 and 3.13 show the trends of the mixture dynamic viscosity μ and thermal conductivity k as a function of temperature. This is the gas setup used for the CFD simulations of the Baseline ED nozzle in Chapter 5 and the parametric analyses in Chapter 6.

Molecular Diffusion

Molecular diffusion is a physical phenomenon that arises mostly because of the presence of gradients of mass or molecule concentrations in the mixture. Dependencies influencing diffusion are pressure and temperature gradients and the effect of body forces. However, for simple analysis, they are often neglected. For a binary mixture of species i and j, the mass flux of species i can be written by Fick's Law in Eq. 3.55 [54] [48].

$$\rho_i u_i = -\rho \mathcal{D}_{ij} \nabla y_i \tag{3.55}$$

The quantity $\mathcal{D}_{ij}$ is the binary diffusion coefficient and can be evaluated by Eq. 3.56 [55]:

$$\rho \mathcal{D}_{ij} = 7.1613x10^{-25} \frac{\sqrt[\mathcal{M}]{T \left(\frac{1}{\mathcal{M}_i} + \frac{1}{\mathcal{M}_j} \right)}}{\Omega_{ij}} \tag{3.56}$$

where Ω_{ij} are the collision cross-section values function of temperature. Additionally, the binary diffusion coefficient is mutual, and the self-diffusion coefficient is not zero, hence:

$$\mathcal{D}_{ij} = \mathcal{D}_{ji} \ , \ \mathcal{D}_{ii} \neq 0$$

In the case of more than two species, the multi-component diffusion coefficient $\mathcal{D}_{im}$ in Eq. 3.57 is used, which describes the diffusion of species i through the mixture. However, for the assumption of a constant Schmidt number Sc, the diffusion coefficient can also be calculated by Eq. 3.58 where a Schmidt number of $Sc = 1$ is a reasonable value for most gases.

$$\mathcal{D}_{im} = \frac{1 - X_i}{\sum_{i \neq j} X_j / \mathcal{D}_{ij}} \tag{3.57}$$

$$\mathcal{D}_{im} = \mathcal{D} = \frac{\mu}{\rho Sc} \ , \ Sc = constant \tag{3.58}$$

3.5 RANS equations

The complete NS equations can only be solved analytically in special cases, such as the one-dimensional flow around a flat plate. In the case of more complex flow applications, they must be solved using numerical methods. Turbulent flows, which can be assumed in rocket nozzles, cause small disturbances due to nonlinearities, which can influence the numerical solution [46]. This results in the requirement to resolve even the smallest turbulence scales. When using direct

numerical simulations (DNS), this can only be realized by very small volume elements, i. e. very fine grids, resulting in very long computing times. Therefore, RANS simulations based on the Reynolds-averaged Navier-Stokes equations are often used.
The RANS equations are derived by dividing the flow variables into a low-frequency mean value (-) and a high-frequency fluctuation variable (') in accordance with the statistical turbulence modeling [42]. This is known as Reynolds-averaging and is shown in the case of the velocity u in Eq. 3.59. The high-frequency fluctuation terms contain the turbulent fluctuations.

$$u = \overline{u} + u' \tag{3.59}$$

Finally, the RANS equations are obtained by inserting the Reynolds-averaging into the Navier-Stokes equations. Within the RANS equations, the turbulent fluctuations of the high-frequency fluctuation terms lead to terms such as $\rho\overline{u_i' u_j'}$ [56], also called Reynolds stresses. As shown in Eq. 3.60, the Reynolds stresses result from the correlation of the mean velocity fluctuations and must be solved to close the RANS equation system.

$$\overline{u'_i u'_j} = \begin{pmatrix} \overline{u'^2_1} & \overline{u'_1 u'_2} & \overline{u'_1 u'_3} \\ \overline{u'_2 u'_1} & \overline{u'^2_2} & \overline{u'_2 u'_3} \\ \overline{u'_3 u'_1} & \overline{u'_3 u'_2} & \overline{u'^2_3} \end{pmatrix} \tag{3.60}$$

At this point, accuracy is lost compared to the DNS, as the Reynolds stresses are not calculated directly but modeled using turbulence models. In contrast to these high-frequency fluctuations, the medium- and low-frequency fluctuations are still described by the complete equations. One advantage is that, in contrast to the DNS, the grid can be resolved much more coarsely, which means significantly shorter computing times.

3.6 Turbulence modelling

Various turbulence models can be used in the context of RANS simulations [46]. A distinction can be made between eddy viscosity and Reynolds stress models. The latter require more modeling work. Hence, they are not discussed further in this work. The eddy viscosity models are based on the eddy viscosity hypothesis of Boussinesq [47]. This leads to the approximation of the Reynolds stresses, as shown for a simple shear flow in Eq. 3.61.

$$\mu\frac{du}{dy} - \overline{u'_i u'_j} = (\mu + \mu_t)\frac{du}{dy} \tag{3.61}$$

Equation 3.61 shows that the laminar, i. e. molecular viscosity μ, is extended by a turbulent viscosity (also eddy viscosity) μ_t. Instead of approximating the Reynolds stresses directly, the eddy viscosity is modeled. There are various options, ranging from zero-equation models based on algebraic equations to two-equation models using two differential equations, such as the $k-\omega$ and $k-\epsilon$ models. The Spalart-Allmaras turbulence model used for the numerical simulation in this work belongs to the family of the one-equation models [57]. Only one differential equation is used to approximate the eddy viscosity, as shown in Eq. 3.62.

$$\begin{aligned} \frac{\partial\hat{\nu}}{\partial t} + u_j\frac{\partial\hat{\nu}}{\partial x_j} = c_{b1}(1-f_{t2})\hat{S}\hat{\nu} - \left[c_{w1}f_w - \frac{c_{b1}}{\kappa^2}f_{t2}\right]\left(\frac{\hat{\nu}}{d}\right)^2 + \\ \frac{1}{\sigma}\left[\frac{\partial}{\partial x_j}\left((\nu+\hat{\nu})\frac{\partial\hat{\nu}}{\partial x_j}\right) + c_{b2}\frac{\partial\hat{\nu}}{\partial x_i}\frac{\partial\hat{\nu}}{\partial x_i}\right] \end{aligned} \tag{3.62}$$

The turbulent eddy viscosity is computed from Eq. 3.63

$$\mu_t = \rho\hat{\nu} f_{v1} \tag{3.63}$$

where:

$$f_{v1} = \frac{\mathcal{X}^3}{\mathcal{X}^3 + c_{v1}^3} \tag{3.64}$$

$$\mathcal{X} = \frac{\hat{\nu}}{\nu} \tag{3.65}$$

$$\nu = \mu/\rho \tag{3.66}$$

$$\hat{S} = \Omega + \frac{\hat{\nu}}{\kappa^2 d^2} f_{v2} \tag{3.67}$$

$$\Omega = \sqrt{2W_{ij}W_{ij}} \tag{3.68}$$

$$W_{ij} = \frac{1}{2}\left(\frac{\partial u_i}{\partial x_j} - \frac{\partial u_j}{\partial x_i}\right) \tag{3.69}$$

$$f_{v2} = 1 - \frac{\mathcal{X}}{1 + \mathcal{X} f_{v1}} \tag{3.70}$$

$$f_w = g\left[\frac{1 + c_{w3}^6}{g^6 + c_{w3}^6}\right]^{1/6} \tag{3.71}$$

$$g = r + c_{w2}(r^6 - r) \tag{3.72}$$

$$r = min\left[\frac{\hat{\nu}}{\hat{S}\kappa^2 d^2}, 10\right] \tag{3.73}$$

$$f_{t2} = c_{t3} exp(-c_{t4}\mathcal{X}^2) \tag{3.74}$$

and the constants are:

$$c_{b1} = 0.1355 \tag{3.75}$$

$$c_{b2} = 0.622 \tag{3.76}$$

$$\sigma = 2/3 \tag{3.77}$$

$$\kappa = 0.41 \tag{3.78}$$

$$c_{w1} = \frac{c_{b1}}{\kappa^2} + \frac{1 + c_{b2}}{\sigma} \tag{3.79}$$

$$c_{w2} = 0.3 \tag{3.80}$$

$$c_{w3} = 2 \tag{3.81}$$

$$c_{v1} = 7.1 \tag{3.82}$$

$$c_{t3} = 1.2 \tag{3.83}$$

$$c_{t4} = 0.5 \tag{3.84}$$

Although the accuracy of the numerical solution increases with the complexity of the turbulence model, the computational effort also increases [46]. The Spalart-Allmaras turbulence model offers a good compromise between computing time and modeling errors, which are inevitable in every model.

3.7 Discretization and finite volume method

The numerical mesh discretizes the computational domain, i. e. it subdivides the computational domain by a finite number of finite control volumes. There are a variety of approaches to discretize the governing equations. For modern CFD solvers, finite volume discretization is used. The Finite Volume discretization represents a good compromise between accuracy and flexibility compared to the finite difference and finite element methods, as it can be applied to structured and unstructured meshes. The Finite Volume method used in this work is the Godunov method. The numerical scheme is second-order accurate in space and third-order accurate in time. Local time stepping is used to speed up convergence to steady state. The Godunov method is a cell-centered method, i. e. the calculation nodes are located in the center of the control volumes or surfaces in the case of two-dimensional simulations, as shown in Fig. 3.14. The flow variables, such as pressure, temperature, and density, are calculated at these nodes. The values at the interfaces of the cells are determined by interpolation with the neighbor cell. The (black) filled nodes in Fig. 3.14 represent the borders of the computational domain for which the boundary conditions are defined. The Godunov method is adopted by an in-house solver [48], which determines the numerical solution iteratively.

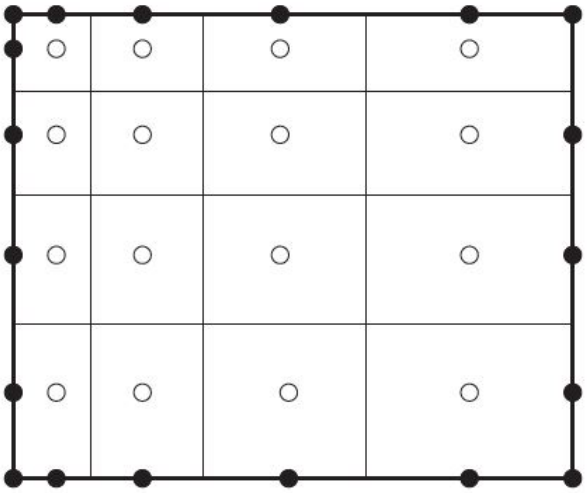

Figure 3.14: Cell-centred procedure using the example of a two-dimensional grid

Chapter 4

CFD model verification and results validation

In Chapter 3, it is mentioned that an in-house solver is used for the CFD simulations. In addition, the CFD models adopted by the solver are discussed in detail. In this Chapter, for two test cases, the CFD models are verified, and the results are validated. Verification and validation are key processes to quantify the correctness of the computational simulations to assess the reliability of numerical solvers as analysis tools for engineering systems [48] [58]. Verification is checking whether the CFD models are implemented correctly regarding coding and solution. In the case of steady-state simulations, this is done by grid convergence studies (GCS). Validation is proven when the CFD model can also correctly describe the physical phenomena, such as the rocket nozzle expansion flow. This can be done by comparing the numerical results with experimental results.
The *RL10A-3-3A* [59] and the *RS-25* [60] (also known as the Space Shuttle Main Engine - *SSME*) are chosen as reference engines and introduced in Section 4.1. In Section 4.2, the simulation setup is discussed. Finally, in Section 4.3 and 4.4, the verification and validation results are shown.

4.1 Description of test cases

The first engine considered a test case is the *RL10A-3-3A* engine. The origins of the *RL10* rocket engine family go back to Pratt & Whitney in the 1960s. The engines gained recognition for their remarkable performance, reliability, and adaptability. The engines use LOX/LH_2 as a propellant combination, such as the *VINCI* engine based on which the Baseline ED nozzle in Section 2.4 is designed. In addition, the thrust of the *RL10A-3-3A* and *VINCI* engines is in the same order of magnitude. The *RL10A-3-3A* design is based on an expander cycle. The engine schematic is shown in Fig. 4.1. In the expander cycle, the fuel, i. e. hydrogen is used to cool the thrust chamber and the nozzle. As a result, hydrogen absorbs thermal energy and is then guided into the turbine to drive the turbopumps [61]. After exiting the turbine, the fuel is guided into the combustion chamber and burned with the oxidizer. The propellants are precisely mixed by the injector, resulting in a steady and effective combustion. Advanced materials, such as lightweight composites and high-temperature alloys, are included in the engine design to withstand extreme operating conditions. The *RL10* engine exhibits high specific impulses, enabling missions requiring significant Delta-V maneuvers. These aspects make the *RL10* engine a very efficient propulsion system for critical space missions [59].

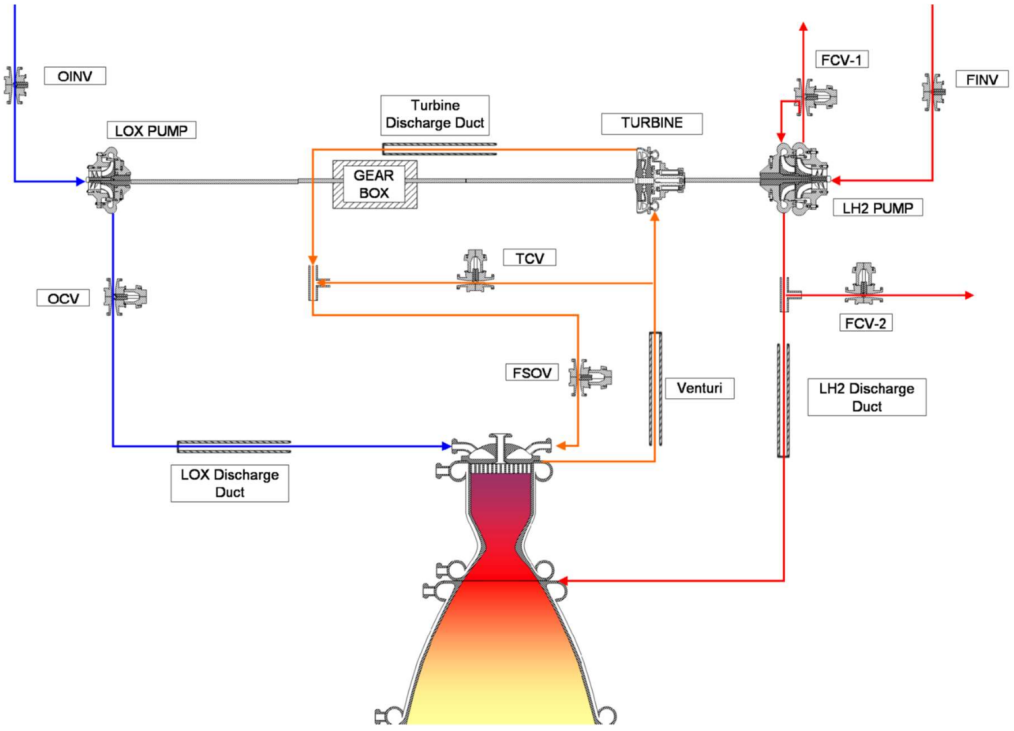

Figure 4.1: *RL10A-3-3A* engine diagram [61]

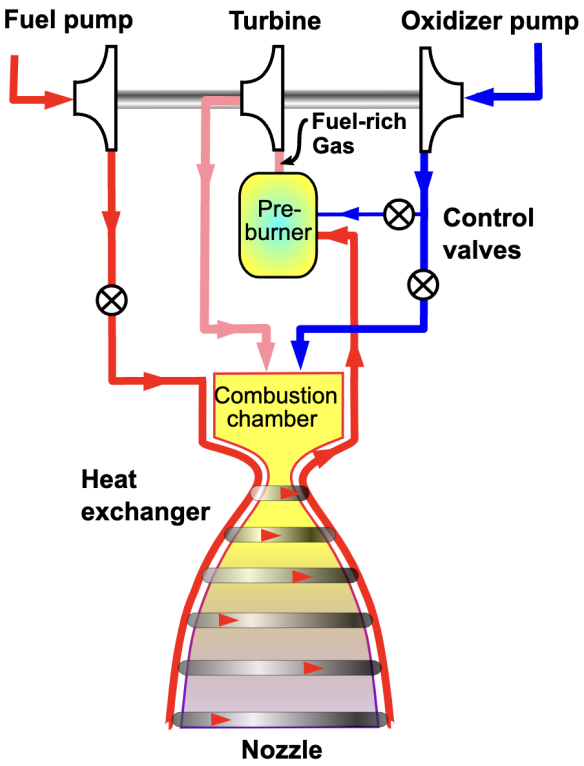

Figure 4.2: *SSME* diagram [62]

The second test case engine is the *SSME*. This engine also operates with LOX/LH_2 propellant combination but delivers higher thrust than the *VINCI* engine. The *SSME* is the first fully reusable, high-performance, liquid rocket engine rated for human spaceflight. The *SSME* uses a two-staged combustion cycle, as shown in Fig. 4.2. First, most of the hydrogen and part of the oxygen are guided into the pre-burner, producing a fuel-rich gas. Afterward, the gas is guided into the turbine to drive the high-pressure turbopumps. Then, the gas is guided into the main combustion chamber, where the fuel burns completely, producing a high-pressure and temperature exhaust gas. Finally, the exhaust gas expands within the rocket nozzle to produce thrust.

4.2 Nozzle design and simulation setup

Tables 4.1 and 4.2 summarize some of the combustion chamber data and nozzle characteristics of the *RL10A-3-3A* engine and the *SSME*. With this data, the *RL10A-3-3A* and *SSME* nozzles are reconstructed by the MOC (for variable specific heat ratio γ) as a TIC and also a Thrust Optimized Contour (TOC) nozzle. These nozzles are shown in the upper half of Fig 4.3 and Fig. 4.4. It can be seen that the *RL10A-3-3A* contour can be well approximated by the TIC profile. The *SSME* can be better approximated by the TOC profile. The CFD simulations are performed for these profiles in the verification study. Then, the specific impulse I_{sp} is evaluated from the simulations and compared to the literature values in Tab. 4.1 and 4.2.

$\mathbf{R_{th}}$ [m]	$\mathbf{R_u/R_{th}}$ $\mathbf{R_d/R_{th}}$	L [m] ε [-]	$\mathbf{P_c}$ [bar]	$\mathbf{T_c}$ [K]	O/F	$\mathbf{I_{sp}}$ [s]
0.063	1.6 0.2	1.16 61	33.23	3283.5	5.26	440.3

Table 4.1: Data of LOX/LH_2 *RL10A-3-3A* engine [59]

$\mathbf{R_{th}}$ [m]	$\mathbf{R_u/R_{th}}$ $\mathbf{R_d/R_{th}}$	L [m] ε [-]	$\mathbf{P_c}$ [bar]	$\mathbf{T_c}$ [K]	O/F	$\mathbf{I_{sp}}$ [s]
0.136	1.6 0.2	3.072 77.5	202.41	3639.0	6.0	453.3

Table 4.2: Data of LOX/LH_2 *SSME* [60][63]

A thermally perfect gas is assumed for the simulations of the *RL10A-3-3A* TIC and the *SSME* TOC nozzles. In addition, both non-reactive (NR) and reactive (R) cases are considered. For the former, the gas composition corresponds to that in the combustion chamber and does not change during the expansion, i. e. it is frozen. The reactive case considers chemical kinetics. The chosen scheme is a reactive scheme for H_2 and O_2 reactions published by Yetter [64] and used in [65]. The reaction scheme considers 19 reactions involving the eight species: $H_2, H, H_2O, HO_2, H_2O_2, O, O_2$, and OH. For both the non-reactive and reactive cases, the initial chamber compositions are calculated with the CEA code.
For these non-reactive and reactive setups, first, viscous-adiabatic (VA) and Eulerian (E) simulations are conducted on three different grid levels (refinement factor $r = 2$ along the axial and radial directions). The grids are single-block structured and two-dimensional. The medium grid of the viscous simulations (7200 cells) is shown in the lower half of Fig. 4.3 and 4.4 for the

RL10A-3-3A and *SSME* nozzles. The grids have a stretch towards the walls to guarantee even for the coarse grid everywhere $y^+ \leq 1$ to resolve the thin boundary layer. In this way, related quantities like wall shear stresses and heat fluxes are supposed to be numerically correct. The Eulerian grid has no stretch towards the wall but more cells (medium grid 14400 cells).
The nozzle inlet boundary conditions are chamber equilibrium conditions (total temperature and pressure) computed by CEA for the pressure and mixture ratio given in Tab. 4.1 and 4.2. For the viscous simulation, the one-equation turbulence model Spalart-Allmaras is used.

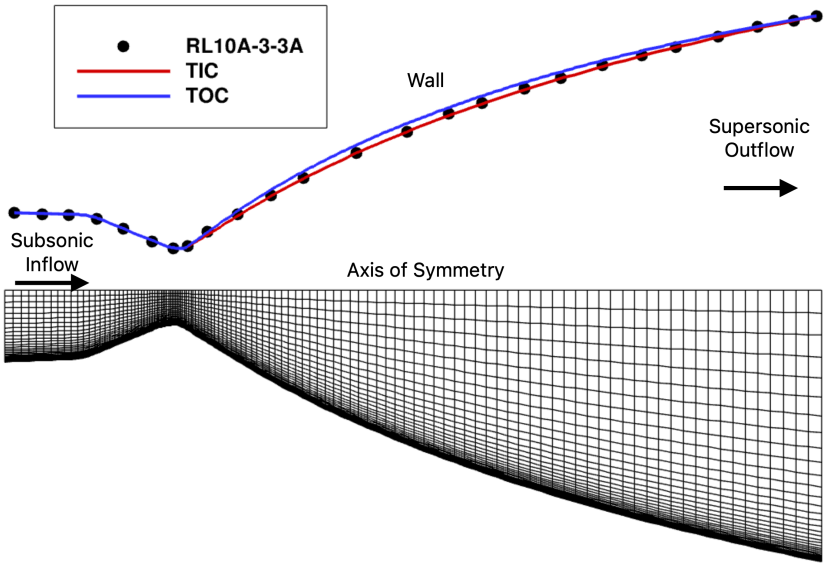

Figure 4.3: TIC and TOC profiles for *RL10A-3-3A* and TIC medium viscous grid

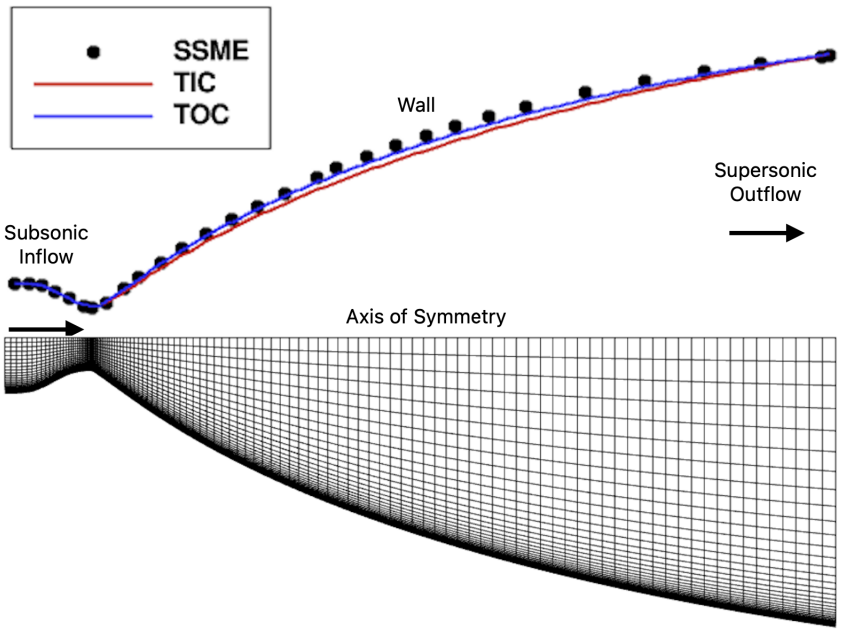

Figure 4.4: TIC and TOC profiles for *SSME* and TOC medium viscous grid

4.3 Verification

Tables 4.3 and 4.4 show the specific impulse I_{sp} that is determined for the different simulation cases and grid levels for the *RL10A-3-3A* and *SSME*. The specific impulse is calculated by Eq. 4.1. The thrust F and mass flow rate $\dot{m}$ are obtained by integration over the nozzle exit plane.

$$I_{sp} = \frac{F}{\dot{m} \cdot g_0} = \frac{\int (\rho \cdot {U_x}^2 + p)\, dA_e}{\int (\rho \cdot U_x)\, dA_e \cdot g_0} \tag{4.1}$$

Once the simulations are performed, the results of the GCS are evaluated. The results are shown in Tab. 4.3 and 4.4. First, the grid convergence order p is computed as follows:

$$p = ln\left(\frac{f_3 - f_2}{f_2 - f_1}\right) / ln(r) \tag{4.2}$$

where f_1 is the fine-grid solution, f_2 is the medium-grid solution, and f_3 is the coarse-grid solution. The quantity r is the constant refinement ratio, hence $r = 2$. The convergence orders deviate slightly from $p = 2$, which can be attributed, among other things, to grid imperfections and turbulence modeling (for the viscous simulations).
Then, the grid convergence indexes GCI_{12} and GCI_{23} are calculated according to Roach [66]:

$$GCI_{12} = F_s \cdot \left|\frac{\varepsilon_{12}}{r^p - 1}\right| \tag{4.3}$$

$$GCI_{23} = F_s \cdot \left|\frac{\varepsilon_{23}}{r^p - 1}\right| \tag{4.4}$$

where F_s is a safety factor that equals 1.25 in case three grids are used for the GCS. The quantities ε_{12} and ε_{23} are the errors that are calculated from the simulation results:

$$\varepsilon_{12} = \frac{f_1 - f_2}{f_1} \tag{4.5}$$

$$\varepsilon_{23} = \frac{f_2 - f_3}{f_2} \tag{4.6}$$

Then, by applying Eq. 4.7, it is proven that the asymptotic range of convergence is reached in the simulations. Finally, the performances which would result for infinitely fine grids are calculated using Richardson extrapolation. For this, Eq. 4.8 is used.

$$\frac{GCI_{23}}{r^p \cdot GCI_{12}} \approx 1 \tag{4.7}$$

$$f_{exact} = f_1 + \frac{f_1 - f_2}{r^p - 1} \tag{4.8}$$

Considering the extrapolated I_{sp} values in Tab. 4.3 and 4.4, two things need to be highlighted. First, the reactive cases perform better than the non-reactive cases. This is due to recombination reactions, which release (heat) energy to the fluid expanding in the nozzle. This energy is then converted into kinetic energy, i. e. I_{sp}. Second, for the respective reactive and non-reactive cases, the Eulerian I_{sp} is higher than that of the viscous-adiabatic simulations. This is because viscous effects are neglected in the Eulerian simulations.
For the medium grid also, reactive-viscous-isothermal simulations (R-VI) are performed, assigning constant wall temperatures of $T_w = 700,\ 800,\ 900$, and $1000\ K$ for the *RL10A-3-3A* and $T_w = 700\ K$ for the *SSME*. The results are shown in Tab. 4.5. Even though the values are

Case	Grid	I_{sp} [s]	p GCI_{12} [%] GCI_{23} [%] Check	Extra-polated I_{sp} [s]
R-E	3 2 1	457.28 457.68 457.8	1.695 0.015 0.048 1.0002658	457.85
R-VA	3 2 1	452.54 454 454.44	1.753 0.050 0.170 1.0009543	454.62
NR-E	3 2 1	435.76 436.11 436.22	1.701 0.014 0.045 1.0002511	436.27
NR-VA	3 2 1	431.57 432.91 433.3	1.762 0.047 0.161 1.0009083	433.46

Table 4.3: TIC simulation results for coarse (3), medium (2), and fine (1) grids

Case	Grid	I_{sp} [s]	p GCI_{12} [%] GCI_{23} [%] Check	Extra-polated I_{sp} [s]
R-E	3 2 1	462.43 462.85 462.95	2.017 0.009 0.037 1.0002208	462.98
R-VA	3 2 1	457.61 459.35 459.82	1.902 0.046 0.173 1.0010139	459.99
NR-E	3 2 1	438.87 439.25 439.34	2.038 0.008 0.035 1.0002102	439.37
NR-VA	3 2 1	434.49 436.10 436.53	1.908 0.045 0.167 1.0009821	436.69

Table 4.4: TOC simulation results for coarse (3), medium (2), and fine (1) grids

RL10A-3-3A	$\mathbf{I_{sp}}$ **[s]**
$T_w = 700\ K$	447.29
$T_w = 800\ K$	447.52
$T_w = 900\ K$	447.77
$T_w = 1000\ K$	448.04
SSME	$\mathbf{I_{sp}}$ **[s]**
$T_w = 700\ K$	455.79

Table 4.5: Reactive-viscous-isothermal (R-VI) simulation results for the medium grid of the *RL10A-3-3A* TIC and *SSME* TOC nozzle

not extrapolated under the assumption of infinite fine grid resolution, they are lower than the viscous-adiabatic values due to additional heat exchange. However, for the *RL10A-3-3A* simulation results, it can be seen that the heat exchange decreases with increasing wall temperature T_w, leading to increased performance.

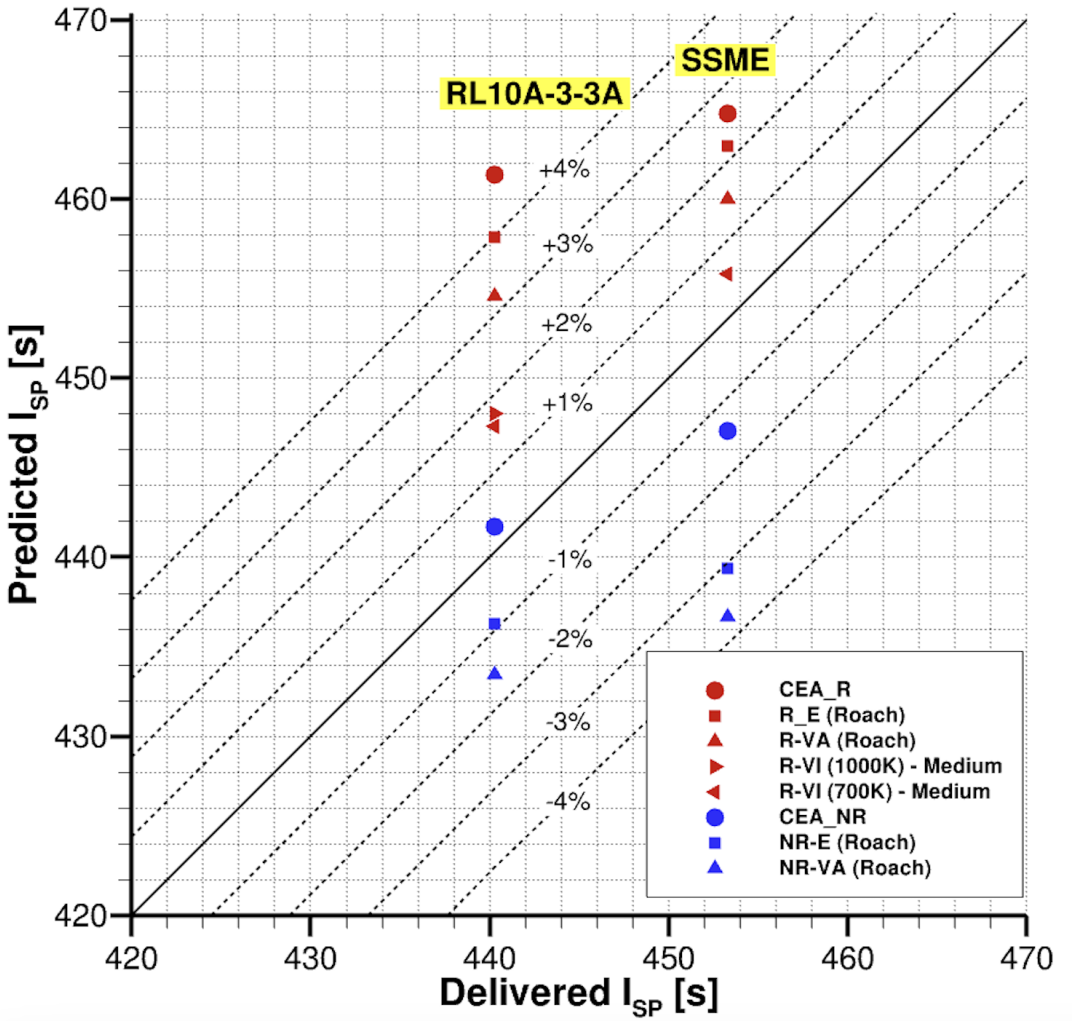

Figure 4.5: Comparison of various predicted I_{sp} values with the delivered literature value

4.4 Validation

Figure 4.5 shows graphically the percentage deviations of various predicted performance values from the delivered literature I_{sp} in Tab. 4.1 and 4.2. The predicted values are, on the one hand, the extrapolated values in Tab. 4.3 and 4.4 and those for $T_w = 700$ and 1000 K in Tab. 4.5. On the other hand, there are the ideal performance values of the reactive and non-reactive cases, which are $I_{sp} = 461.38$ s and $I_{sp} = 441.72$ s, respectively. These ideal values are calculated with the CEA code. The plot shows that the ideal performance values are always higher for the reactive and non-reactive cases than for the simulations. This is plausible as the ideal performance analysis does not consider performance losses attributed to two-dimensional effects, divergence, viscosity, heat exchange, and non-equilibrium reactions. For the reactive-viscous-isothermal case of $T_w = 700$ K of the *RL10A-3-3A* and *SSME*, the predicted values show good agreement with the delivered literature values. In case of the *RL10A-3-3A*, the simulation slightly overpredicts the I_{sp} by 1.587 %. For the *SSME*, the simulation results are even closer to the delivered I_{sp} since the simulation overpredicts the I_{sp} by just 0.549 %.

Chapter 5

Results for Baseline ED and conventional nozzle

In Chapter 4, the in-house solver is verified and validated using the *RL10A-3-3A* engine and the *SSME* as examples. Then, the in-house solver is applied for CFD simulations of the Baseline ED nozzle (in Fig. 2.16) and a comparable conventional TIC nozzle. Both nozzles are designed for *VINCI* characteristics. The simulations are done under Eulerian, viscous-adiabatic, and viscous-isothermal ($T_w = 700\ K$) conditions on three different grid levels (refinement factor $r = 2$ along both axes). This is a GCS, and the results are discussed in this Chapter. The objective is to demonstrate verification of the numerical models for the Baseline cases, which is an optimal basis for the parametric analyses in Chapter 6.

5.1 Nozzle design and simulation setup

The design of the Baseline ED nozzle is already discussed in Section 2.4. The Baseline TIC nozzle is designed for the same constant design specific heat ratio γ, truncation exit radius, and throat area as the Baseline ED nozzle (see Tab. 2.2). However, the TIC is designed with the MOC for a truncation length of $x_{trunc} = 3.\overline{3}\ m$. For the wall curvature radii up- and downstream the throat, $R_u = R_{th}$ and $R_d = \frac{1}{2}R_{th}$ are used.
In the simulations, the gas is modeled as a thermally perfect gas, and chemical reactions are neglected. The nozzle inlet conditions are calculated with the CEA code, as described in Section 2.4. These include, on the one hand, the gas composition that corresponds to that of the throat and, on the other hand, the total pressure and temperature, as discussed in Section 2.4. As in the test case study in Chapter 4, the Spalart-Allmaras turbulence model is used for the viscous simulations.
Figure 5.1 shows the Baseline ED and TIC nozzle contours. In addition, the medium grids of the viscous ED and TIC nozzle simulations are shown. Table 5.1 summarizes the number of cells in axial and radial directions for the different simulation cases for all medium meshes. As in the test case study in Chapter 4, the viscous grids feature a stretch towards the wall to resolve the boundary layer well.

5.2 Verification and grid selection

In Tab. 5.2 and 5.3, the I_{sp} values of the ED and TIC nozzles for the different simulation cases and grid levels are shown. Besides that, the convergence orders p and grid convergence indexes GCI_{12} and GCI_{23} are calculated according to Roach [66]. Then, it is proven that the asymptotic range of convergence is reached, and the extrapolated I_{sp} is calculated assuming zero grid spacing.
Figure 5.2 shows the absolute grid errors on I_{sp} as a function of the normalized grid resolution for the different ED and TIC nozzle cases graphically. These are calculated by comparing the respective grid solutions with the extrapolated values. For a second-order method, the error is ideally quartered at grid refinements $r = 2$ along the axial and radial directions. However, simulations slightly deviate from the convergence order. For instance, the TIC nozzle slopes are steeper than the ED nozzle since the simulations demonstrated higher convergence orders. Nevertheless, Fig. 5.3 shows that the grid errors for the medium ED and fine TIC nozzle grids are sufficiently low. Hence, the simulated performance values are already close to the extrapolated values. These grids offer a good compromise between accuracy and low computing resources. Therefore, they are used for the parametric analyses in Chapter 6.

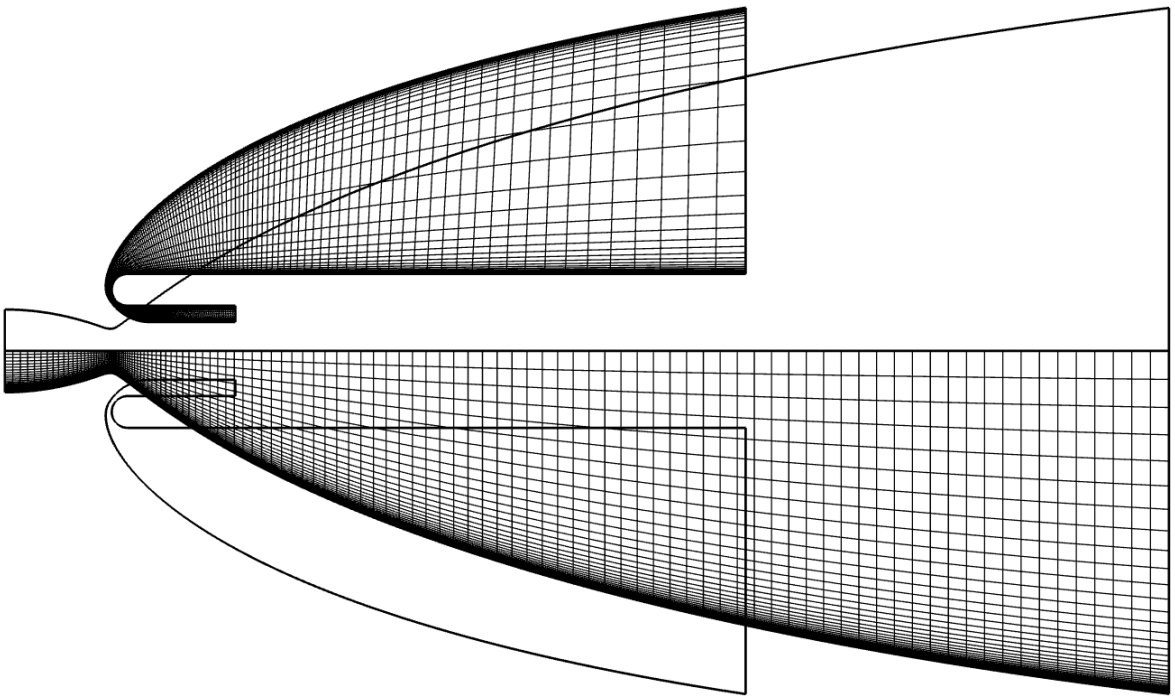

Figure 5.1: Baseline ED and TIC nozzles with medium viscous-isothermal meshes used for verification study

Nozzle	Case	Number of Cells
ED	E	800 X 120
ED	VA & VI	400 X 60
TIC	E	240 X 60
TIC	VA & VI	120 X 60

Table 5.1: Number of Cells for the medium meshes of the Eulerian (E), viscous-adiabatic (VA), and viscous-isothermal (VI) ED and TIC simulations

ED Case	Grid	I_{sp} [s]	p GCI_{12} [%] GCI_{23} [%] Check	Extra-polated I_{sp} [s]
NR-E	3 2 1	456.92 457.08 457.13	1.822 0.005 0.017 1.0001001	457.15
NR-VA	3 2 1	451.27 452.17 452.44	1.745 0.032 0.106 1.0005962	452.56
NR-VI	3 2 1	430.1 434.35 435.51	1.878 0.124 0.458 1.0026655	435.94

Table 5.2: ED simulation results for coarse (3), medium (2), and fine (1) grids

TIC Case	Grid	I_{sp} [s]	p GCI_{12} [%] GCI_{23} [%] Check	Extra-polated I_{sp} [s]
NR-E	3 2 1	459.11 459.35 459.40	2.113 0.004 0.019 1.0001190	459.42
NR-VA	3 2 1	453.65 454.96 455.28	2.004 0.030 0.119 1.0007163	455.39
NR-VI	3 2 1	446.66 447.86 448.14	2.105 0.024 0.101 1.0006232	448.22

Table 5.3: TIC simulation results for coarse (3), medium (2), and fine (1) grids

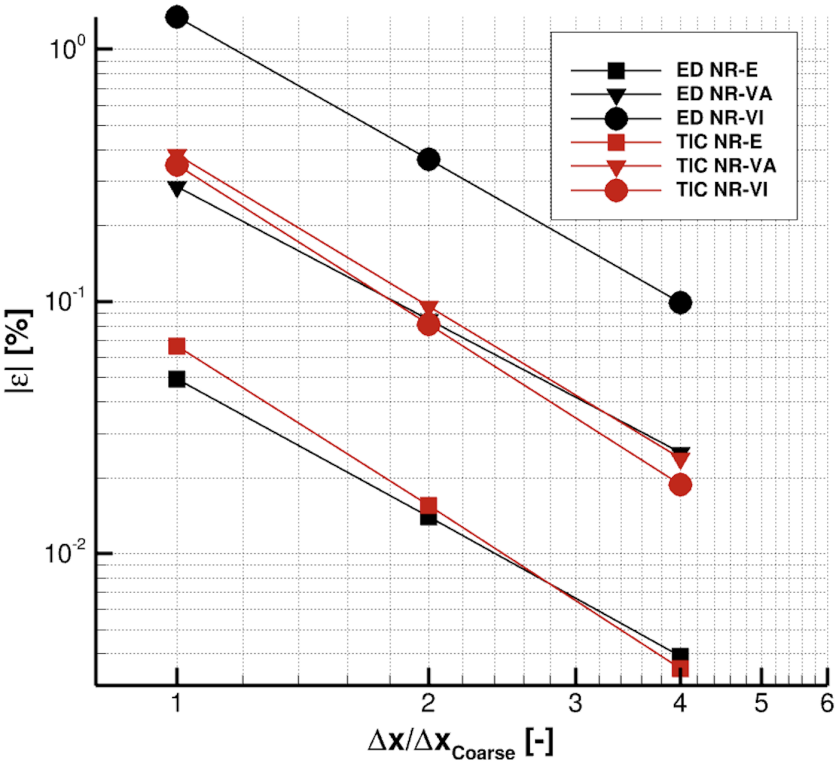

Figure 5.2: Absolute numerical grid errors on specific impulse I_{sp} as a function of normalized grid spacing

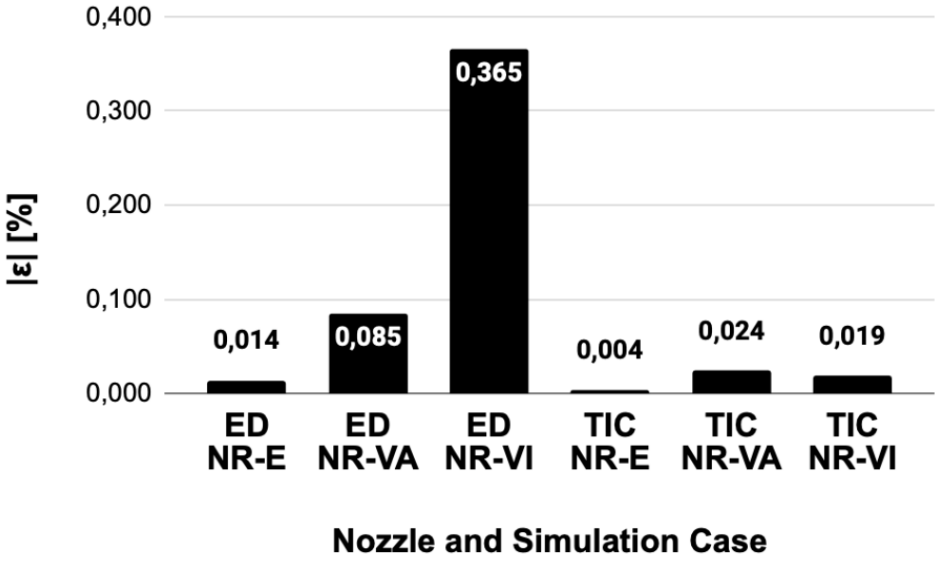

Figure 5.3: Absolute numerical grid errors on specific impulse I_{sp} for medium ED and fine TIC nozzle grids

Chapter 6

Parametric analyses

Many different design parameters exist for an ED nozzle, as discussed in Chapter 2. Figure 6.1 shows some of them using a generic counterflow ED nozzle as an example. First, there are the outer nozzle dimensions, i. e. the truncation length x_{trunc} and radius $R_{e,trunc}$. Second, for the approximate contouring method introduced in Section 2.1, there is the constant design value for the specific heat ratio γ. Third, there are the design parameters describing the throat, such as the radial throat shift y_2 and the throat wall curvature radii R_1 and R_2. Finally, there is the overall size of the nozzle, i. e. the geometrical scaling factor S_F.
In this Chapter, the CFD analyses in Chapter 5 are extended, and the influence of the above parameters on the performance, i. e. the I_{sp} is investigated. In these parametric analyses, a distinction is made between performance losses due to divergence, viscosity, and heat exchange. Eulerian, viscous-adiabatic, and viscous-isothermal CFD simulations are conducted to evaluate them. The same simulation setup as in Chapter 5 is used.

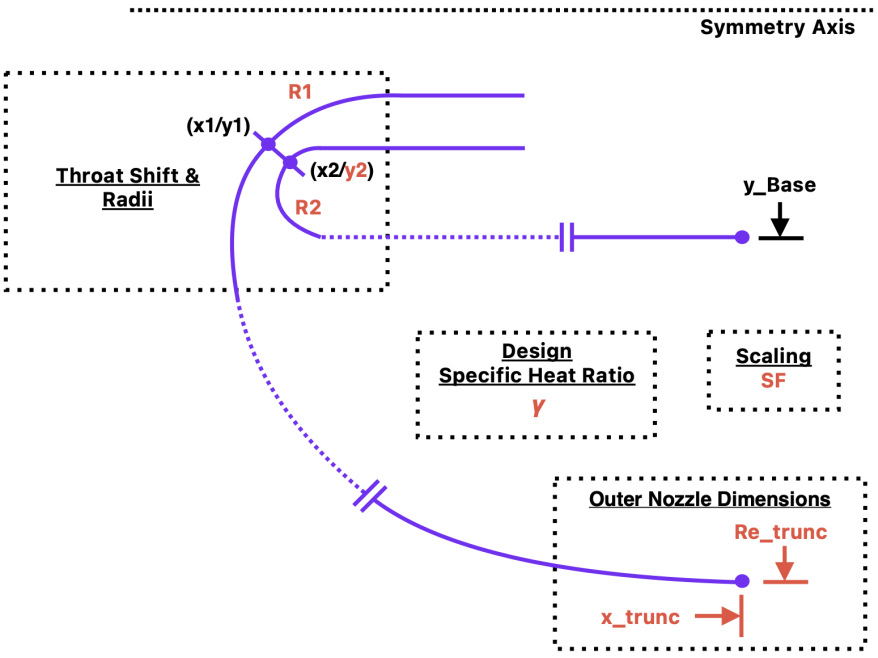

Figure 6.1: Generic ED nozzle and red marked parameters that are subject of the parametric analyses

The Baseline ED nozzle is the starting point of the parametric analyses. The design is discussed in more detail in Section 2.4. The design input and output parameters for the supersonic and subsonic wall contouring are summarized in Tab. 6.1 to 6.4.

$\mathcal{R}_s$ [J/kgK]	T_c [K]	p_c [bar]	γ	Θ_{th} [°]	A_t [m^2]	R_c [m]	x_{trunc} [m]	$R_{e,trunc}$ [m]	x_2 [m]	y_2 [m]
631.235	3555.66	61.2	1.138	-124.977	0.015	0.05	2	1.081	0.013	-0.164

Table 6.1: Design input parameters for the supersonic wall contouring of Baseline ED nozzle

R_e [m]	ε_e	M_e	M_i	R_b [m]	r_{non}
1.28	330.79	5.09	1.006	0.165	0.039

Table 6.2: Design output parameters for the supersonic wall contouring of Baseline ED nozzle

Axial CC location x_{cc} [m]	0.39
Central body radius y_{Base} [m]	−0.24
Ratio of wall radii R_1/R_2	3

Table 6.3: Design input parameters for the subsonic wall contouring of Baseline ED nozzle

Wall radius R_1 [m]	0.05
Wall radius R_2 [m]	0.15

Table 6.4: Design output parameters for the subsonic wall contouring of Baseline ED nozzle

6.1 Outer nozzle dimensions

6.1.1 Truncation length

The design of the ED nozzles with varying truncation length x_{trunc} based on the Baseline ED nozzle is done with the first design procedure. The first design procedure is discussed in more detail in Subsection 2.2.1. The input parameters are taken from the Baseline ED nozzle in Tab. 6.1 and 6.2. Only the truncation length x_{trunc} is varied for all designs. The shortest design features a truncation length of $x_{trunc} = 1\ m$. The longest design is the FL ED nozzle. This nozzle features a FL exit radius equal to the truncation radius of the truncated nozzles. Besides the Baseline ED nozzle, the shortest and longest designs are shown in Fig. 6.2.
Figure 6.3 shows that the throat angle Θ_{th} increases with increasing ED nozzle length. This means a short ED nozzle can only be designed for low throat angles Θ_{th}. This can be explained by Eq. 2.5, which describes the throat angle Θ_{th} as the difference of the Prandtl-Meyer functions $\nu(Mi, \gamma)$ and $\nu(M_{e,FL}, \gamma)$. The internal Mach number M_i and the specific heat ratio γ remain constant for all designs and thus also $\nu(M_i, \gamma)$. However, the FL exit radius $R_{e,FL}$ and the FL exit Mach number $M_{e,FL}$ decrease with increasing ED nozzle length, as shown in Fig. 6.3. As a result, the Prandlt-Meyer function $\nu(M_{e,FL}, \gamma)$ decreases, and the throat angle Θ_{th} increases. For the throat wall curvature radii R_1 and R_2, the axial combustion chamber location x_{cc} and

the straight base radius y_{Base}, the same values as for the Baseline ED nozzle are used. These are shown in Tab. 6.3 and 6.4.

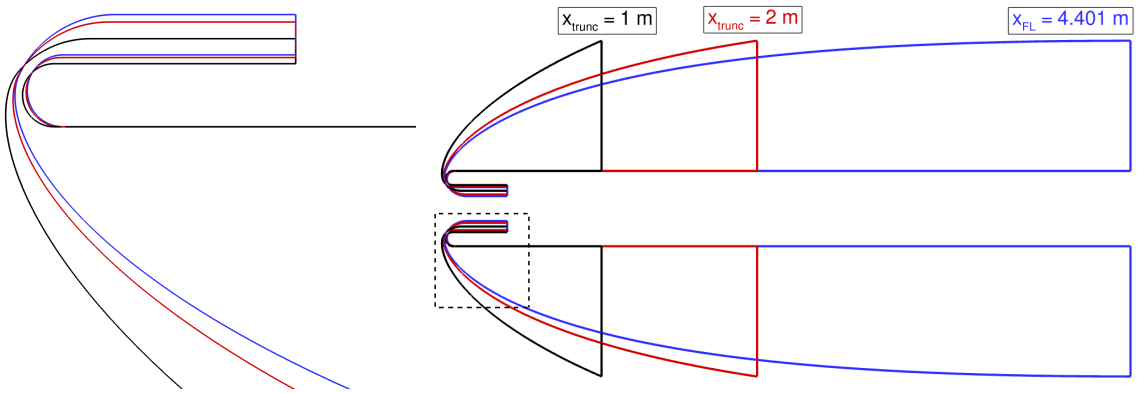

(a) Detail view **(b)** Normal view

Figure 6.2: Variation of truncation length x_{trunc} for constant truncation radius $R_{e,trunc}$

Figure 6.4 shows the Eulerian I_{sp} of several ED and TIC nozzles from 1 m length up to the FL. In addition, the theoretical ED nozzle length-saving over an equally performing TIC nozzle is shown as a function of length. It can be seen that for short lengths, the ED nozzles perform much better than the TIC nozzles. This is due to lower divergence losses. A measure of this is the higher divergence efficiency η_{Div} in Fig. 6.5 that is calculated by normalizing the Eulerian I_{sp} at a given length to the Eulerian I_{sp} of the FL. The lower divergence losses of the ED nozzles are coming from less divergent profiles, as shown in Fig. 6.6. This advantage is particularly evident for short lengths, leading to theoretical length reductions of approximately 36 %. However, as the length increases, this advantage decreases and even vanishes completely at $L = 4.23\ m$. The ED-FL nozzle performs even worse than the TIC-FL nozzle by 0.129 %. This is because the ED nozzles are designed with a central body that does not contribute to the exit area, leading to a 5 % lower effective expansion ratio. However, the ED nozzle reaches its FL at a much (31.905 %) shorter length.

The influence of viscosity on the I_{sp} is evaluated by viscous-adiabatic simulations. Figure 6.7 shows that the ED nozzle still performs better at short lengths, leading to approximately 34 % theoretical length savings. However, the ED nozzle loses its compactness advantage more quickly than in the Eulerian case, i. e. at a shorter length of $L = 3.151\ m$. This is due to higher viscous losses represented by lower viscosity efficiencies η_{Vis}, as shown in Fig. 6.8. These are defined as the quotient of the viscous-adiabatic and Eulerian I_{sp}. Viscosity efficiencies greater than one for the TIC nozzle at very small lengths are due to the fact that the nozzle profile is very divergent, and due to the boundary layer displacement, the (smaller) effective expansion ratio in the viscous-adiabatic simulations performs better than the geometric expansion ratio in the Eulerian simulations. The higher viscous losses of the ED nozzle are caused by a higher total wall surface. For all lengths, this is almost constantly $50 - 60$ % higher than that of the TIC. The external ED nozzle wall surface constantly makes up around $76 - 78$ % of the total ED wall area, regardless of the length.

The viscous-isothermal simulations demonstrate that performance losses of ED nozzles related to heat exchange (at $T_w = 700\ K$) are even more pronounced than the viscous losses, as shown Fig. 6.9. Consequently, for all lengths, the heat exchange efficiencies η_{Heat} of the ED nozzles are significantly lower than those of the TIC nozzles (see Fig. 6.10). They are obtained by referring the viscous-isothermal to the viscous-adiabatic I_{sp}. The integral wall heat flux Q is a measure of the heat exchange. According to Eq. 6.1, it is calculated by integrating the wall heat flux density q_w over the surface area A_w.

$$Q = \int q_w \, dA_w \tag{6.1}$$

For the ED nozzles, Q is particularly higher than for the TIC nozzles, for example, by a factor of 3.546 for the smallest length. However, the factor decreases with length and reaches 2.068 for the ED FL. Regardless of the length, for the ED nozzle, constant $63 - 66$ % of the integral heat flux comes from the external wall.
Figure 6.11 shows for the 2 m ED and TIC nozzles the peak heat fluxes q_w and the radial wall distance r from the symmetry axis as a function of the dimensionless axial coordinate S. Equation 6.2 can be used to discuss the general behavior of these curves. It can be derived from the general definition of heat in Eq. 3.26 and describes the peak heat flux one-dimensionally. According to Eq. 6.2, the peak heat flux increases continuously from the chamber to the throat since $\frac{\dot{m}}{A}$ constantly increases. The reason is that the mass flow rate $\dot{m}$ stays constant, and the cross-sectional area A decreases. In the throat region, A is minimal, and the peak heat flux is maximal. The peak heat flux decreases downstream of the throat since the cross-sectional area increases. However, the CFD simulations also consider two-dimensional effects, so after the chamber, the peak heat flux decreases first and then increases, as shown in Fig. 6.11. This is due to the formation of the boundary layer.

$$q_w = \frac{\dot{m}}{A} \cdot c_p \cdot \Delta T \tag{6.2}$$

Along the nozzle walls, the no-slip condition is applied in the simulations. This means that the fluid is decelerated to zero velocity on the wall. In this case, the heat transfer between the fluid and the wall can be described by heat conduction and convection, as shown in Eq. 6.3 and 6.4. In the ED and TIC nozzle throat, the flow is expanded to the same Mach number $M = 1$. Hence, the ED and the TIC theoretically feature the same fluid temperature T_f and peak heat flux q_w in the throat region since the isothermal wall temperature T_w is the same for both nozzles. However, the simulations show that the peak heat flux along the internal and external ED nozzle walls is approximately $8 - 14$ % higher than for the TIC. This is due to the annular throat of the ED nozzle, i. e. the smaller throat gap, increasing the viscous effects and the heat exchange. The fact that the ED peak heat flux is not much higher may also be due to the relatively high wall curvature radii r_{curv} in the throat region along the external and internal walls. According to Bartz's correlation in Eq. 6.5, this has a decreasing effect on the heat transfer coefficient h.

$$q_w = q_{w,cond.} = q_{w,conv.} \tag{6.3}$$

$$q_w = k \cdot \frac{T_f - T_w}{dy} = h \cdot (T_f - T_w) \tag{6.4}$$

$$h = 0.026 \cdot \left(\frac{p_c}{c^*}\right)^{0.8} \left(\frac{\mu_c^{0.2} \cdot C_{p,c}}{Pr^{0.6} \cdot D_t^{0.2}}\right) \cdot \left(\frac{D_t}{r_{curv}}\right)^{0.1} \cdot \sigma \tag{6.5}$$

Hence, the peak heat flux is not solely responsible for the high heat exchange. Indeed, the surface area A is because, as mentioned before, it is higher in the case of the ED nozzle and can already justify higher heat exchange. Additionally, for an ED nozzle, critical areas of high peak heat flux are located at high radial wall distances r, i. e. wall surface areas, so that they contribute even more substantially to the wall heat exchange. This is not the case for the TIC nozzle, which explains the big difference in wall heat losses between the ED and TIC nozzles.
For the 2 m ED nozzle, it is investigated to which extent the individual wall areas contribute to the total heat exchange. As shown in Fig. 6.12, three areas along the external and two areas along the internal wall are defined. Figure 6.13 and Fig. 6.14 show the ratio of two quantities as a function of the dimensionless axial coordinate S along the external and internal nozzle walls. The first quantity is the sum of the integral wall heat flux emitted by the wall up to S. The second quantity is the integral wall heat flux of the whole wall. Hence, the entire external and internal walls ($S = 1$) account for approximately 65 % and 35 % of the total wall heat flow.
Along the external wall, the first wall area is up to the end of the cylindrical part after the nozzle inlet. A linear increase in the heat exchange characterizes this area. The heat exchange increases even more linearly in the second wall area, which includes the wall curvature in the throat region. The third wall area starts with an expansion around the straight central body. In this area, the heat exchange increases logarithmically. The heat exchange along the internal wall nearly comes exclusively from the first wall area that ends with the beginning expansion around the straight central body. The second wall interval (the straight base) almost does not contribute to the wall heat exchange.
Figures 6.13 and 6.14 show that approximately 34 % of the total integral wall heat flow is caused along the external wall up to the end of the second wall area and along the internal wall up to the end of the first wall area. Hence, both walls account for approximately 68 % percent of the total wall heat exchange in these areas.
However, the high heat exchange can also be advantageous when using an expander engine cycle by recovering heat energy from regenerative cooling. This additional energy can then be used to drive the turbopumps more and to increase the chamber pressure significantly. The I_{sp} can be optimized by reducing the throat area while the mass flow rate remains unchanged.
Figure 6.10 shows that the Baseline ED nozzle ($x_{trunc} = 2\ m$) features 2.557 times more heat exchange than the TIC nozzle. As a result, the ED nozzle performs even slightly worse than the TIC, as shown in Fig. 6.9. However, this is only true for an isothermal wall temperature of $T_w = 700\ K$. Additionally, for the Baseline ED nozzle, simulations are carried out with isothermal wall temperatures of $T_w = 1000, 1500, 2000$ and $2500\ K$. Changing the isothermal wall temperature will change the integral wall heat flux Q and thus the I_{sp}. Figure 6.15 shows the ratio of the integral wall heat flux and performance of the ED nozzle for various wall temperatures and the integral wall heat flux and performance of a TIC nozzle with an isothermal wall temperature of $T_w = 700\ K$. The plot shows that the heat exchange of the ED nozzle decreases almost linearly with increasing wall temperature. Equivalently, the performance increases. For an isothermal wall temperature of $T_w = 2300\ K$, the ED nozzle features the same integral wall heat flux, i. e. heat exchange as the TIC nozzle with $T_w = 700\ K$. In this case, the ED nozzle delivers approximately 2.1 % more I_{sp} than the TIC nozzle. This equals an I_{sp} gain of approximately 9.15 s.

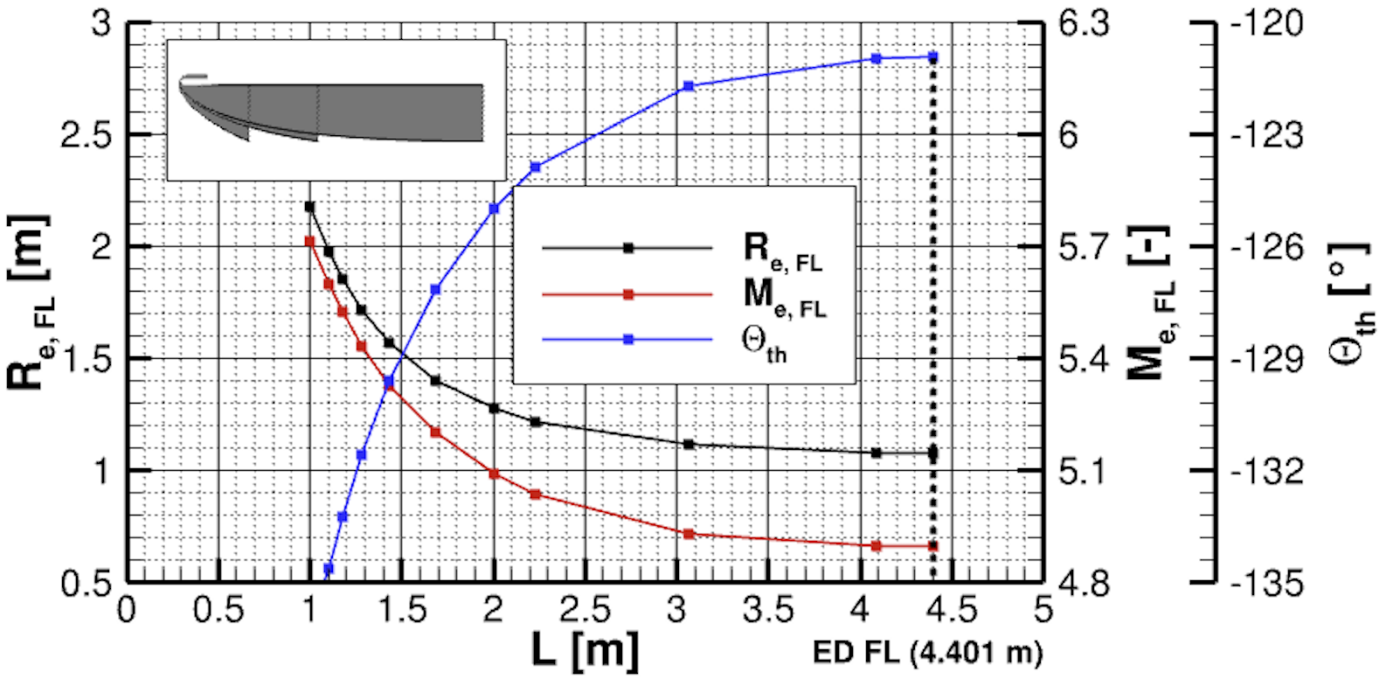

Figure 6.3: FL exit radius $R_{e,FL}$, Mach number $M_{e,FL}$ and throat angle Θ_{th} as a function of length L

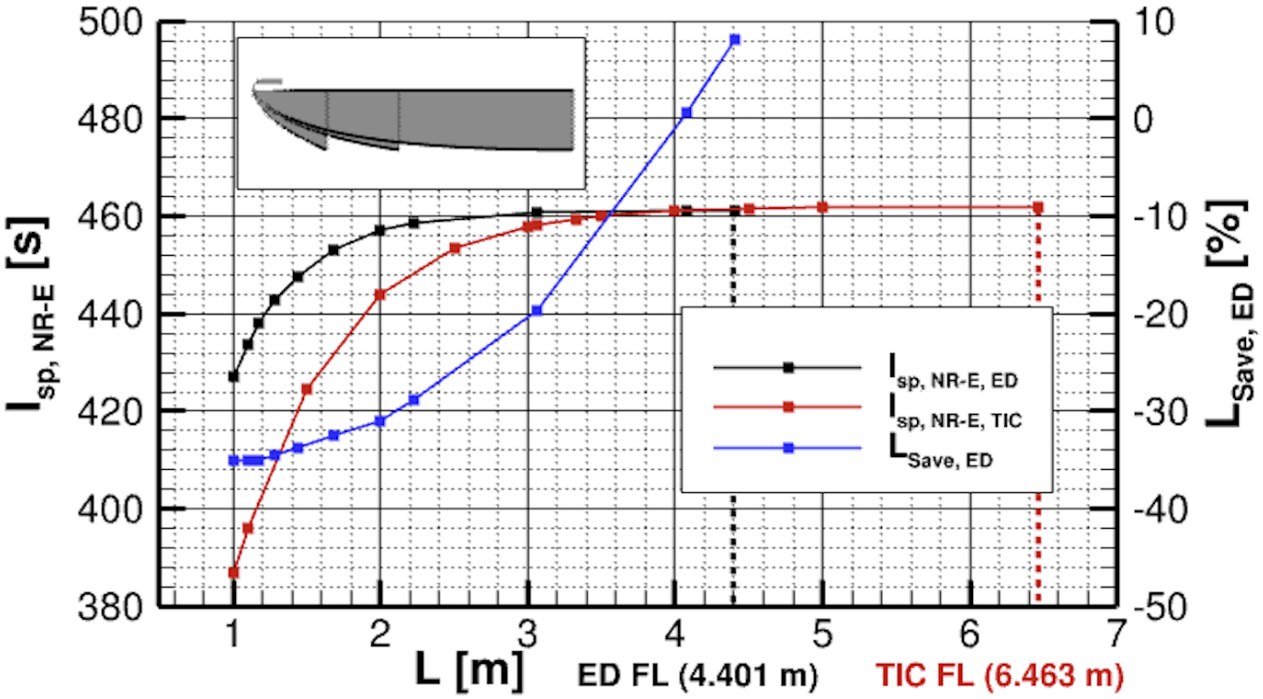

Figure 6.4: Eulerian I_{sp} of ED and TIC and potential ED length savings $L_{Save,ED}$ as a function of length L

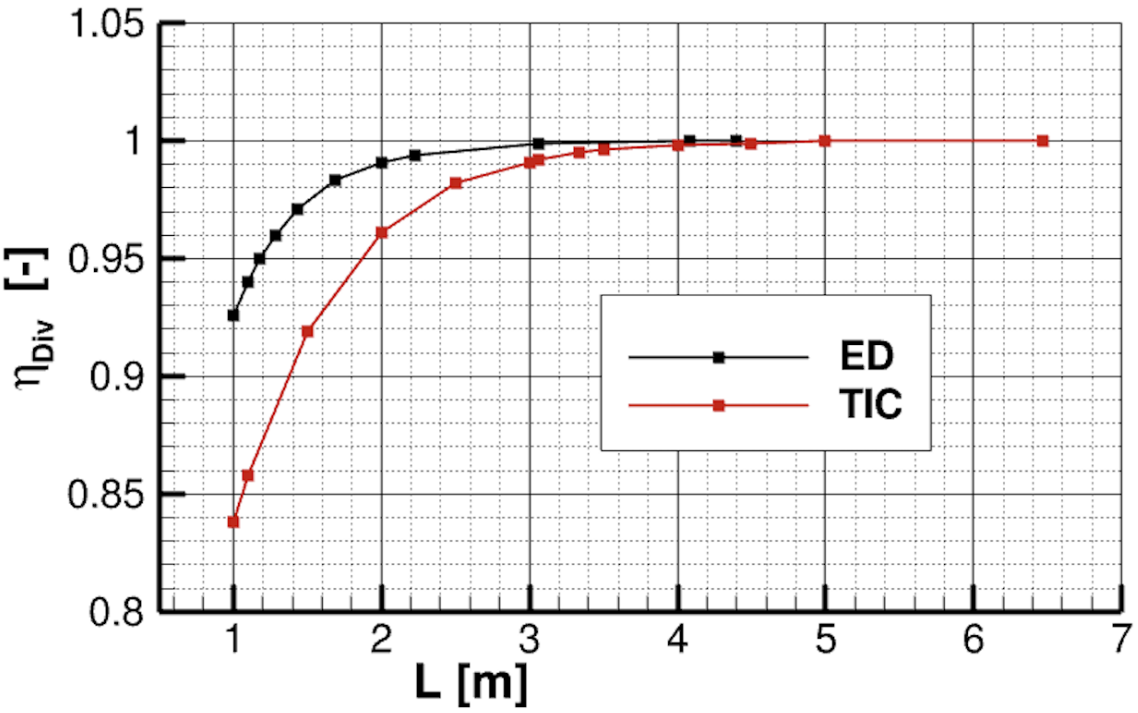

Figure 6.5: Divergence efficiency η_{Div} of ED and TIC as a function of length L

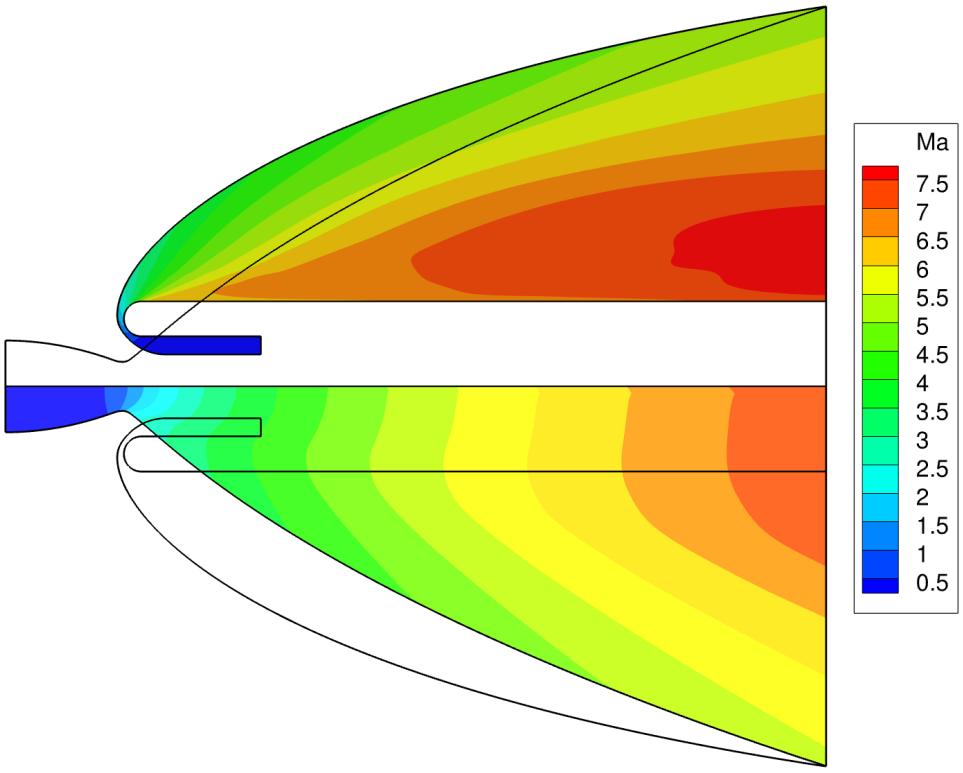

Figure 6.6: ED and TIC profiles for $L = 2\ m$ and Mach fields derived from Eulerian CFD simulations

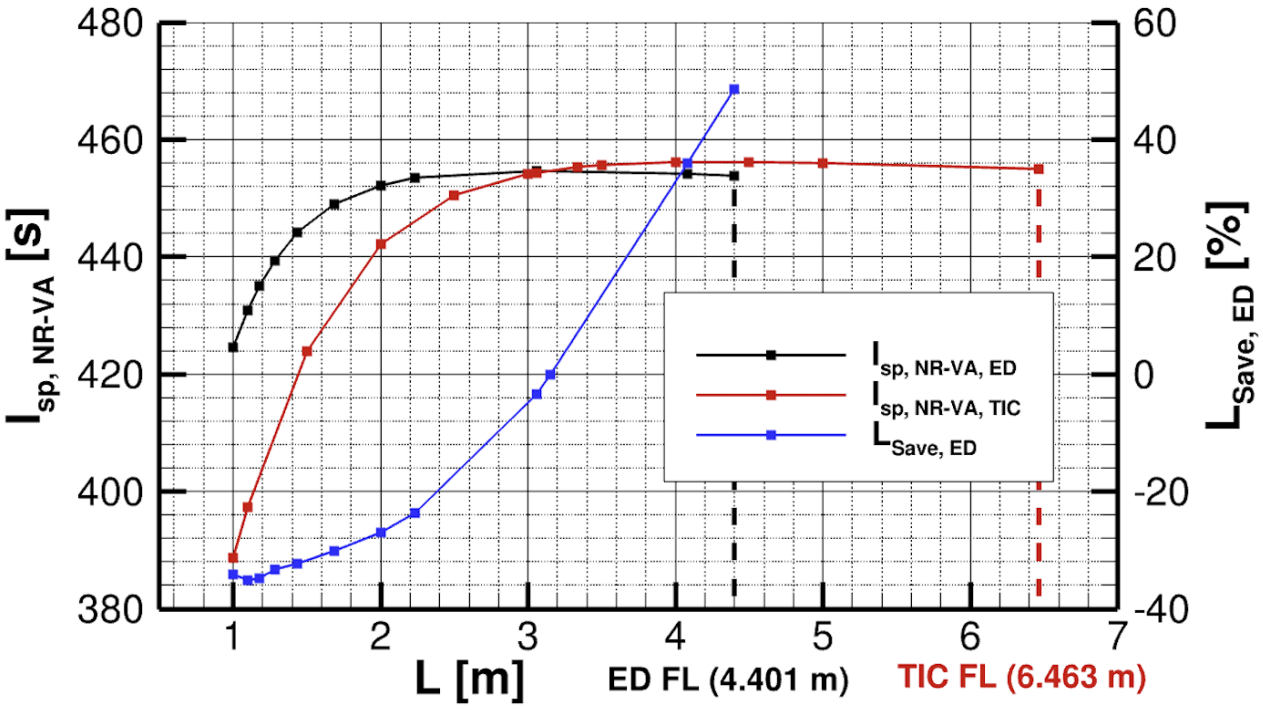

Figure 6.7: Viscous-adiabatic I_{sp} of ED and TIC and potential ED length savings $L_{Save,ED}$ as a function of length L

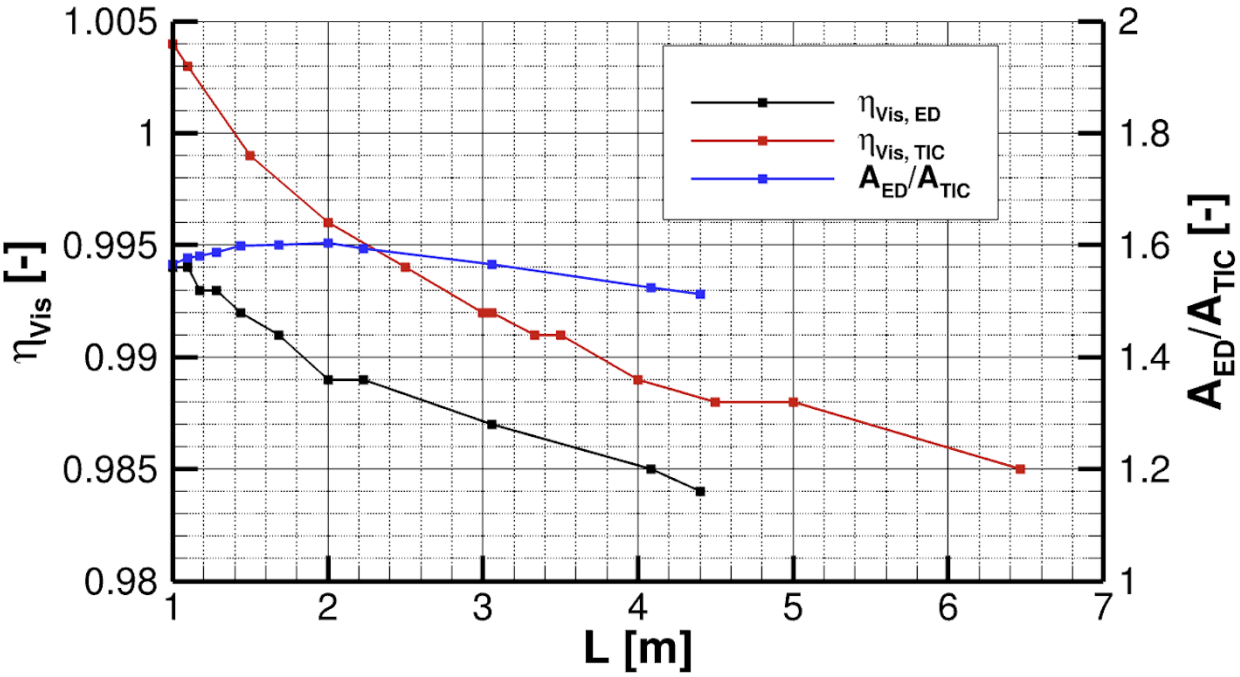

Figure 6.8: Viscosity efficiency η_{Vis} and ratio of the surface area of ED and TIC A_{ED}/A_{TIC} as a function of length L

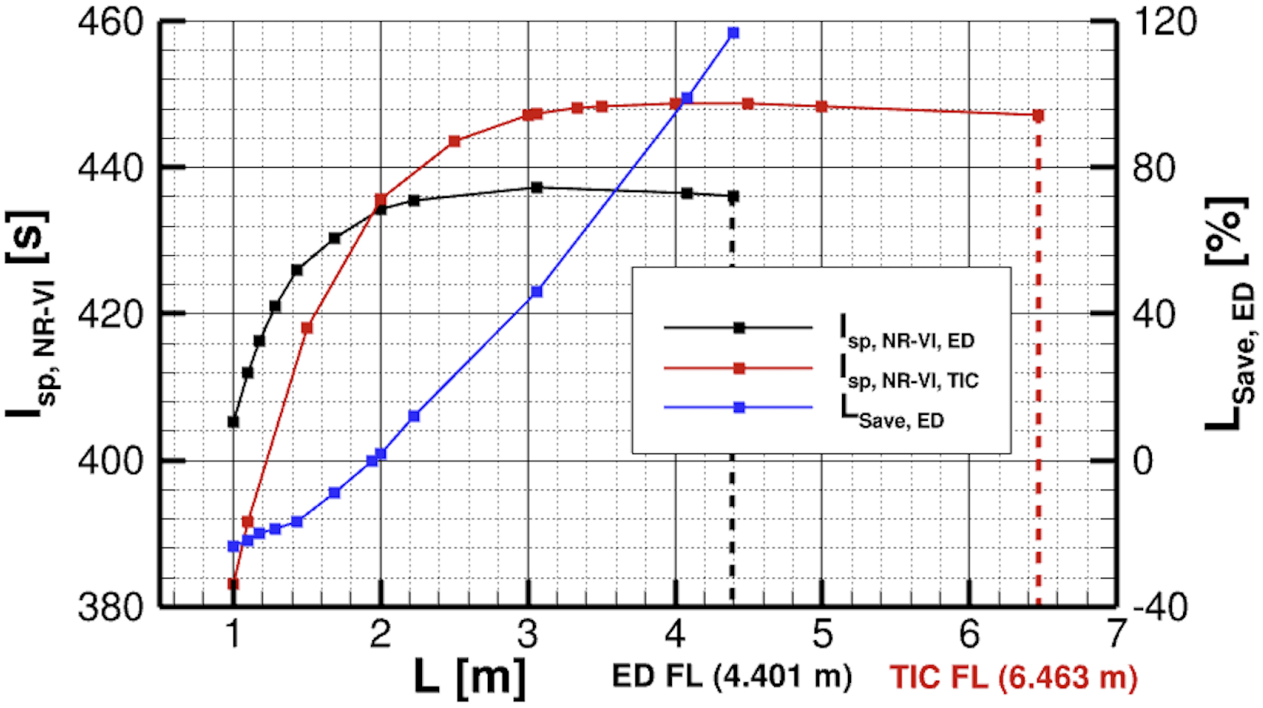

Figure 6.9: Viscous-isothermal I_{sp} of ED and TIC and potential ED length savings $L_{Save,ED}$ as a function of length L ($T_w = 700\ K$)

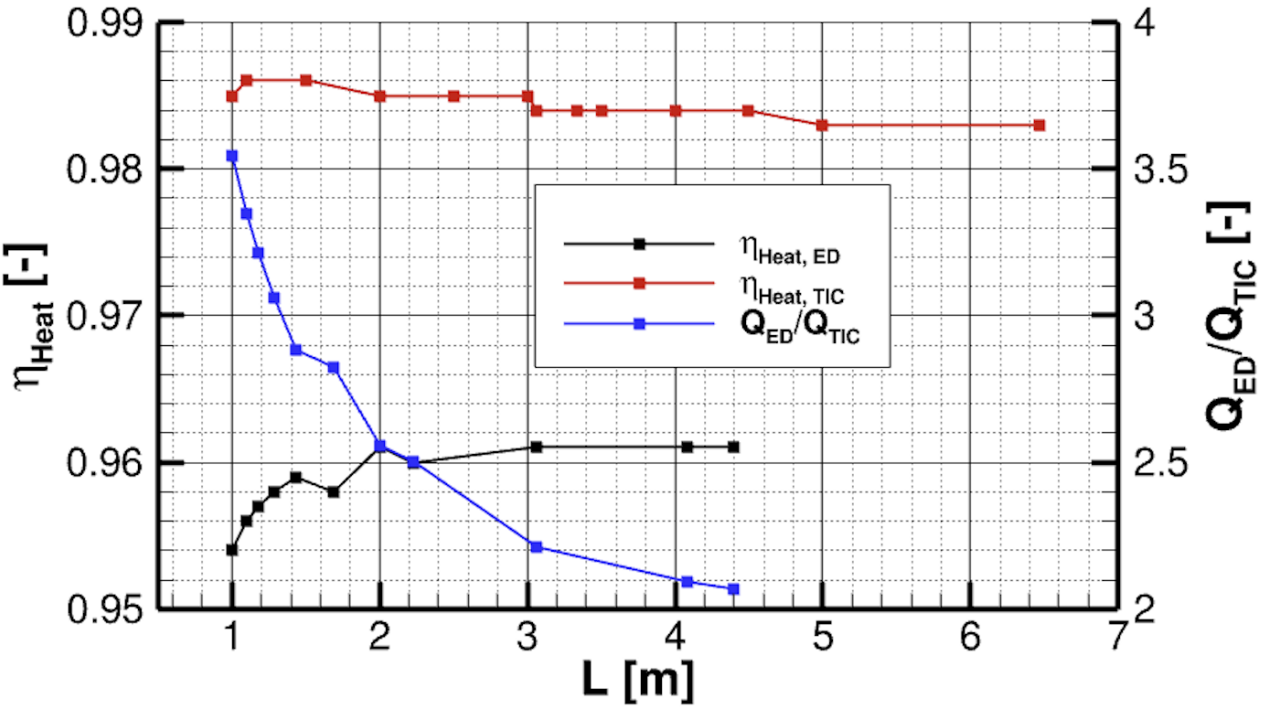

Figure 6.10: Heat exchange efficiency η_{Heat} and ratio of integral wall heat flux of ED and TIC Q_{ED}/Q_{TIC} as a function of length L ($T_w = 700\ K$)

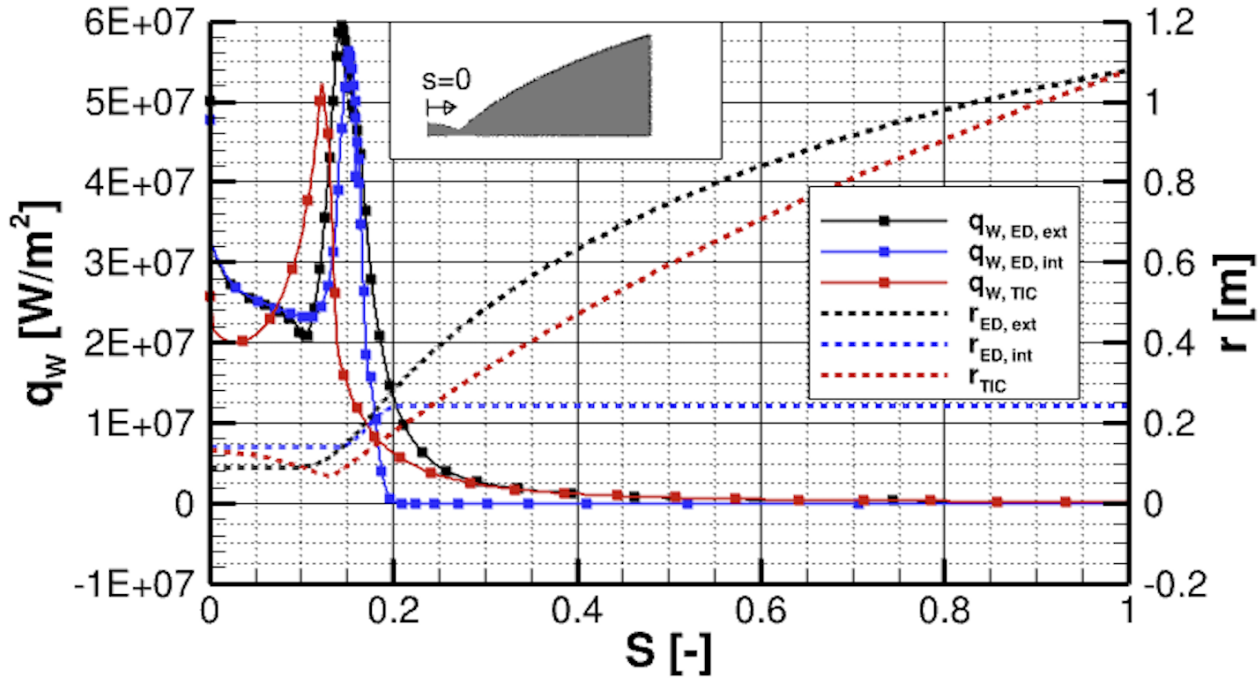

Figure 6.11: Heat flux density q_w and radial wall distance r of ED and TIC as a function of dimensionless axial coordinate S ($T_w = 700\ K$)

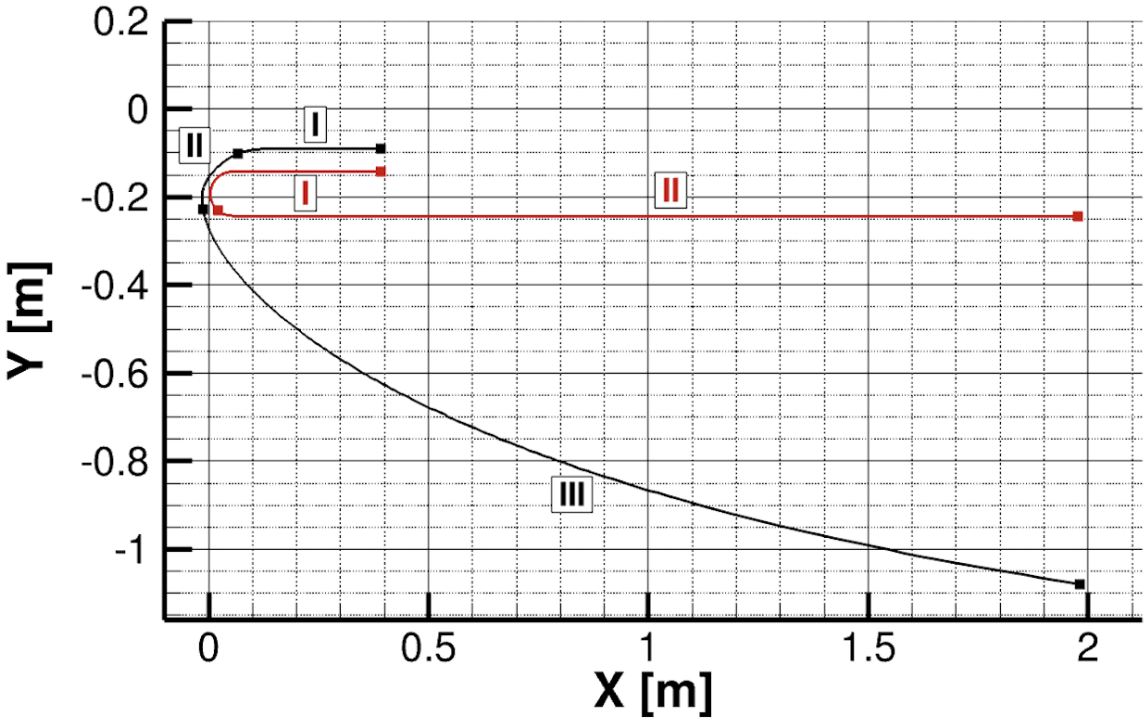

Figure 6.12: Baseline ED nozzle and defined wall areas along the external and internal walls

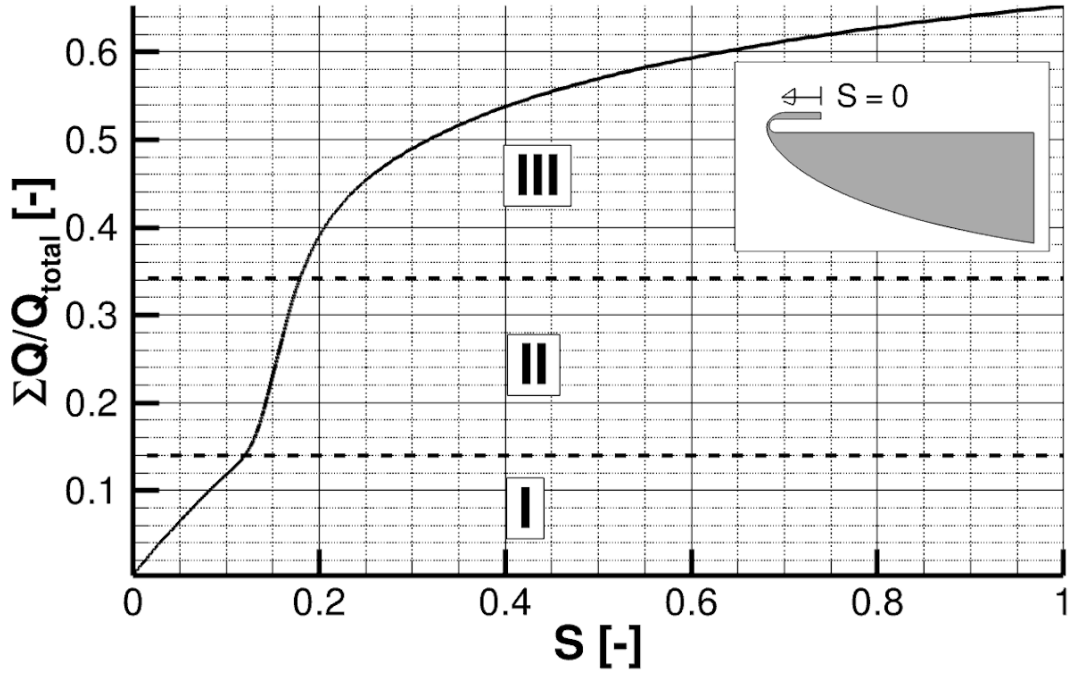

Figure 6.13: Ratio of local external heat exchange and total ED nozzle (external and internal walls) $\sum Q/Q_{total}$ as a function of dimensionless axial coordinate S ($T_w = 700\ K$)

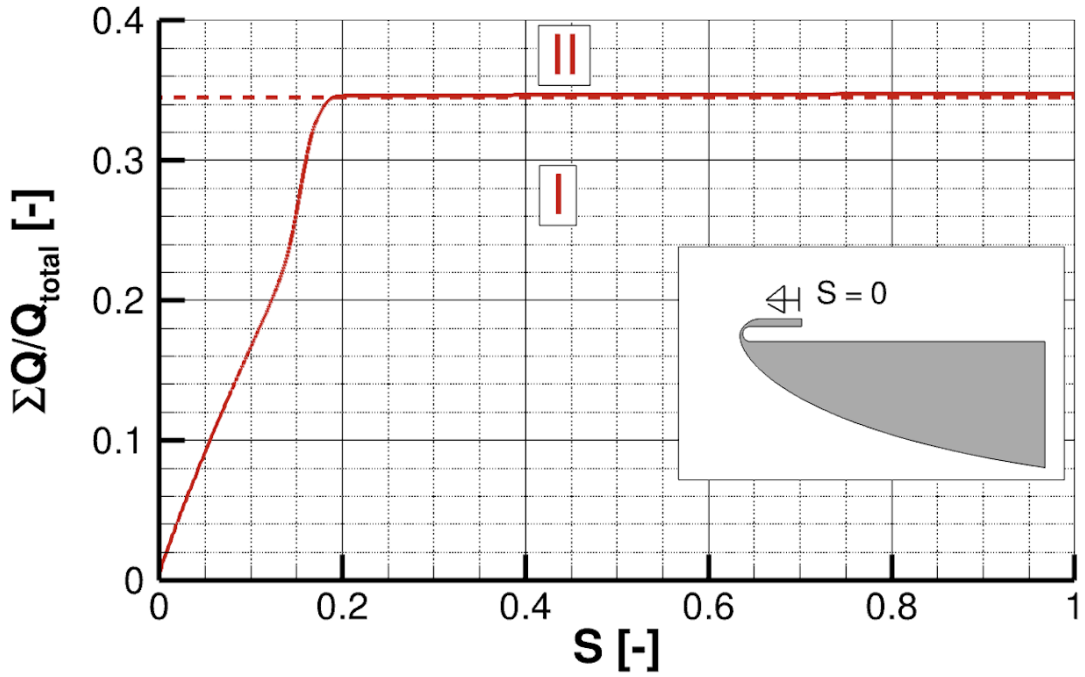

Figure 6.14: Ratio of local internal heat exchange and total ED nozzle (external and internal walls) $\sum Q/Q_{total}$ as a function of dimensionless axial coordinate S ($T_w = 700\ K$)

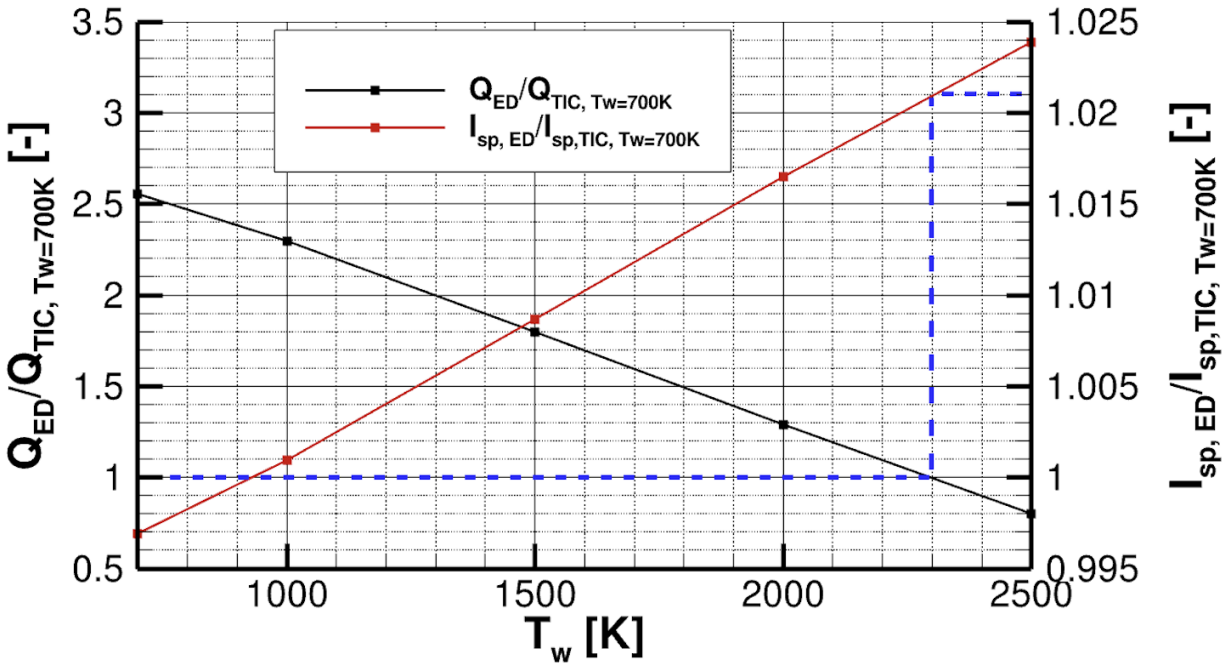

Figure 6.15: Ratio of integral wall heat flux of ED and TIC ($T_w = 700\ K$) as well as I_{sp} of ED and TIC ($T_w = 700\ K$) as a function of isothermal wall temperature T_w

6.1.2 Truncation radius

The design of the ED nozzles with varying truncation radius $R_{e,trunc}$ based on the Baseline ED nozzle is done with the first design procedure. The first design procedure is discussed in more detail in Subsection 2.2.1. The input parameters are adopted from the Baseline ED nozzle in Tab. 6.1 and 6.2. Only the truncation exit radius is changed. The truncation exit radii are varied between 70 % and 120 % of the Baseline truncation radius. Figure 6.16 shows the smallest and largest nozzle configurations.

Figure 6.17 shows that the throat angle Θ_{th} decreases with increasing truncation exit radius R_e. This can be explained by Eq. 2.5. Since the internal Mach number M_i and the specific heat ratio γ stay constant for all designs, also the Prandlt-Meyer function $\nu(M_i, \gamma)$ does. However, the FL exit radius $R_{e,FL}$ and the FL exit Mach number $M_{e,FL}$ increase with increasing truncation exit radius, as shown in Fig. 6.17. Consequently, the Prandtl-Meyer function $\nu(M_{e,FL}, \gamma)$ also increases, and as a result, the throat angle Θ_{th} decreases. For the wall radii R_1 and R_2, the axial combustion chamber location x_{cc} and the straight base radius y_{Base}, the same values as for the Baseline ED nozzle are used. These are shown in Tab. 6.3 and 6.4.

Figure 6.18 shows the Eulerian I_{sp} as a function of the radius for several ED and TIC nozzles truncated at 2 m and the ideal FLs. The curves are generated by curve-fitting the CFD results with 3rd-degree polynomial and 2nd-degree exponential functions. The $L = 2\ m$ curves show a peak that can be explained in the following way. At small radii, an increase in exit radius, i. e. expansion ratio, causes an I_{sp} increase similar to the ideal contours since the divergence losses are small. These are shown for the ED and TIC nozzles in Fig. 6.19. However, with increasing radius, the divergence losses also increase and counteract the theoretical performance yield from the expansion ratio. This results in a maximum point beyond which the divergence losses are so evident that the I_{sp} decreases again for even higher radii. For the Baseline ED nozzle ($R_e/R_{e,Baseline} = 1$), it can be seen that the exit radius reaches almost maximum I_{sp}. However, the performance could be increased even more by reducing marginally the exit radius.

The I_{sp} curve of the ED nozzles is generally above that of the TIC due to lower divergence losses for all radii, as shown in Fig. 6.19. The divergence losses differ less for small radii, leading to a less significant difference in performance. For very small radii, for instance, the ED is performing even worse than the TIC due to the design assumption of the central body. The same applies also to the FLs for all radii. For higher radii, the divergence losses differ more, and so does the performance, making the ED nozzle even more advantageous. Additionally, the performance loss resulting from neglecting the central body is negligible for large radii.
Figure 6.20 shows that the ED nozzles suffer more from viscosity than the TIC as the exit radius is varied. Even though the ED nozzles perform better, the I_{sp} curve is shifted more toward the TIC than in the case of the Eulerian simulations. Correspondingly, the viscosity efficiencies of the ED nozzles are generally lower. This is because the ED surface is roughly $53 - 70$ % larger. Due to the design, the inner wall surface remains roughly constant as the exit radius increases. The external wall surface increases linearly, accounting for roughly 73 to 80 % of the total wall area. The increase of the viscosity efficiency, i. e. the decrease of viscous losses with increasing radius can be explained by the fact that the boundary layer becomes less significant to the core flow.
Under consideration of viscosity and heat exchange ($T_w = 700\ K$), the ED nozzle almost completely loses its performance advantages and only performs better than the TIC for large radii, as shown in Fig. 6.22. Accordingly, for all radii, the ED heat exchange efficiency is significantly lower than that of the TIC (see Fig. 6.23) and decreases more rapidly for increasing radius. This is because the ratio of integral wall heat flux of the ED and TIC also increases over the radius from an initial factor of 2.288 to 2.833. Regardless of the length, for the ED nozzle, constant $63 - 65$ % of the integral heat flux comes from the external wall.
The reason for the higher heat exchange is, on the one hand, the larger surface area of the ED nozzle and, on the other hand, the distribution of peak heat flux and surface area, as already explained in more detail in Subsection 6.1.1.

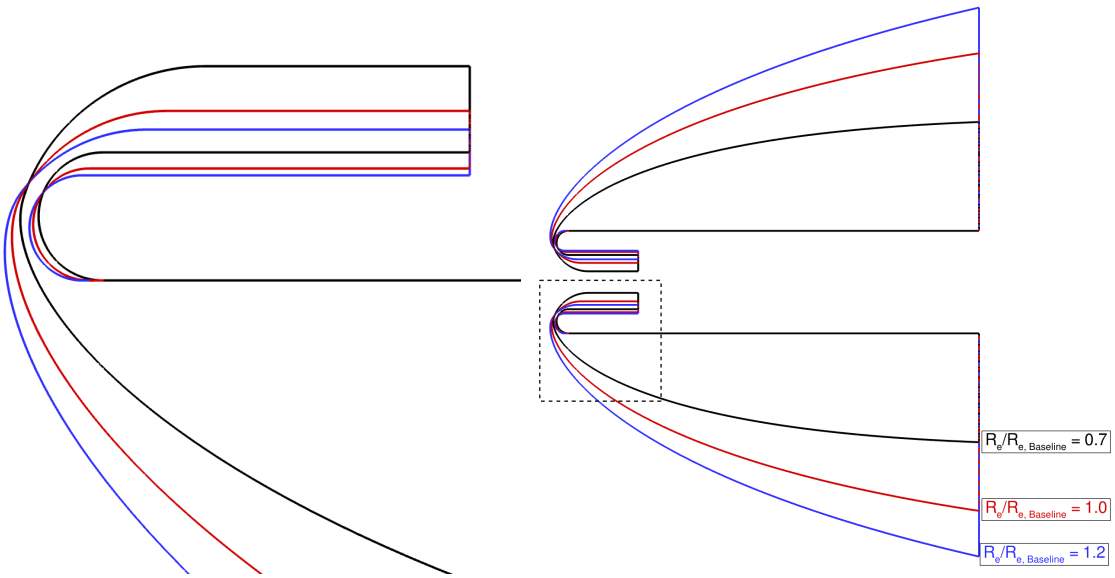

(a) Detail view **(b)** Normal view

Figure 6.16: Variation of truncation radius $R_{e,trunc}$ for constant truncation length x_{trunc}

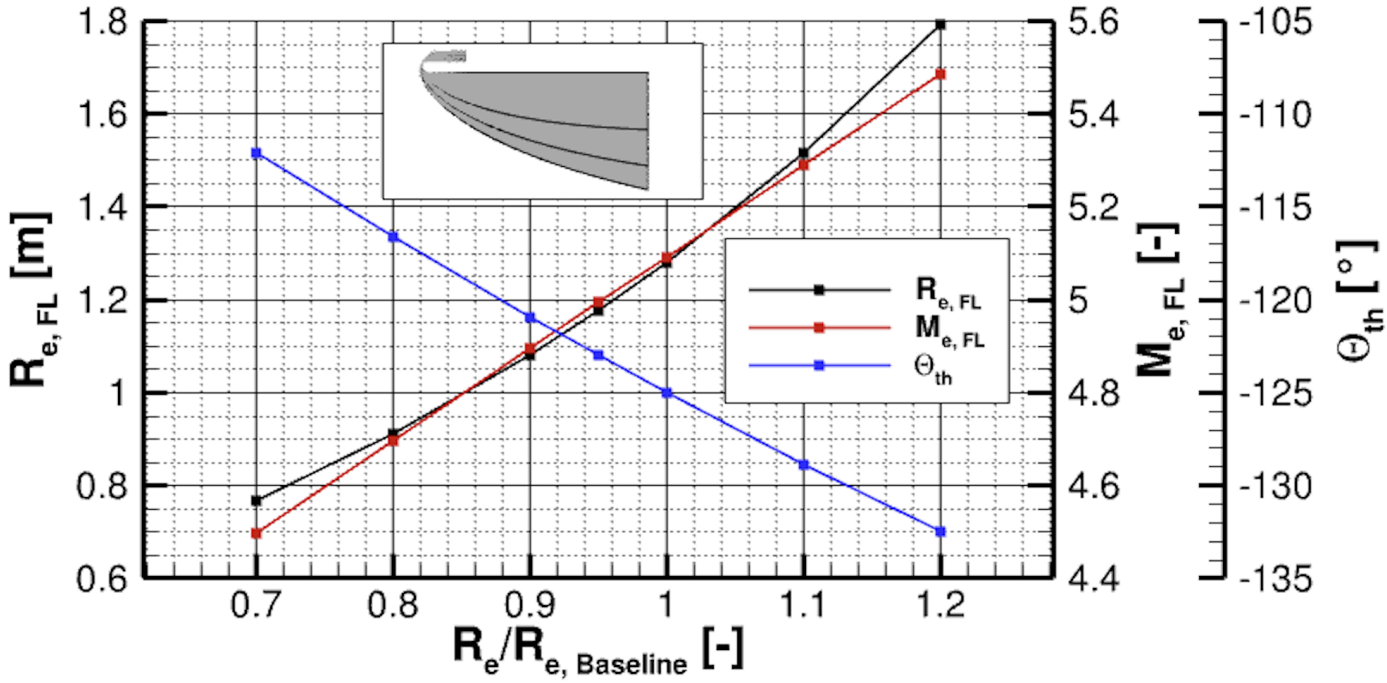

Figure 6.17: FL exit radius $R_{e,FL}$, Mach number $M_{e,FL}$ and throat angle Θ_{th} as a function of radius

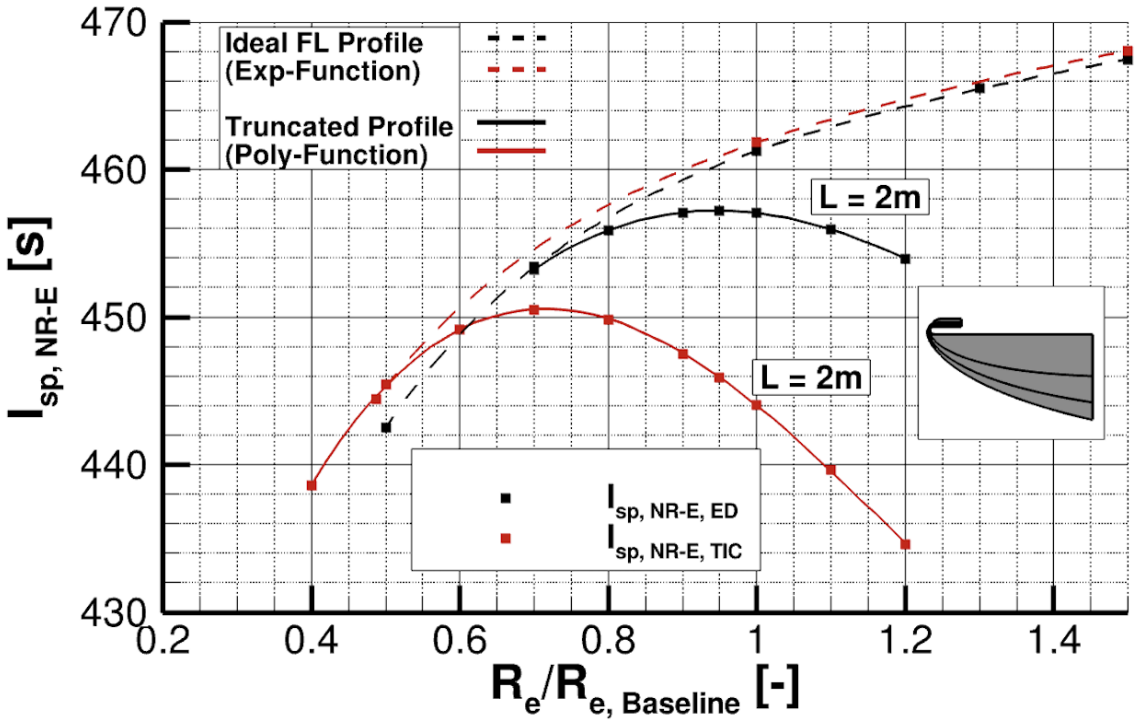

Figure 6.18: Eulerian I_{sp} of 2 m ED and TIC and FLs as function of radius

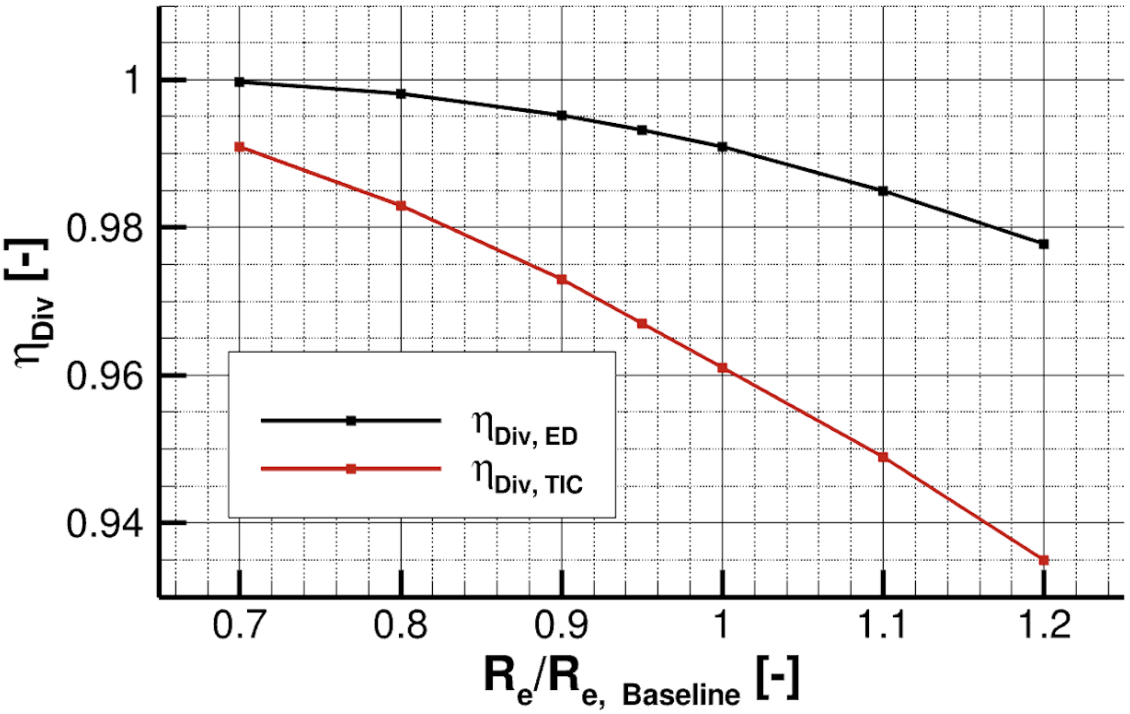

Figure 6.19: Divergence efficiency η_{Div} of 2 m ED and TIC as function of radius

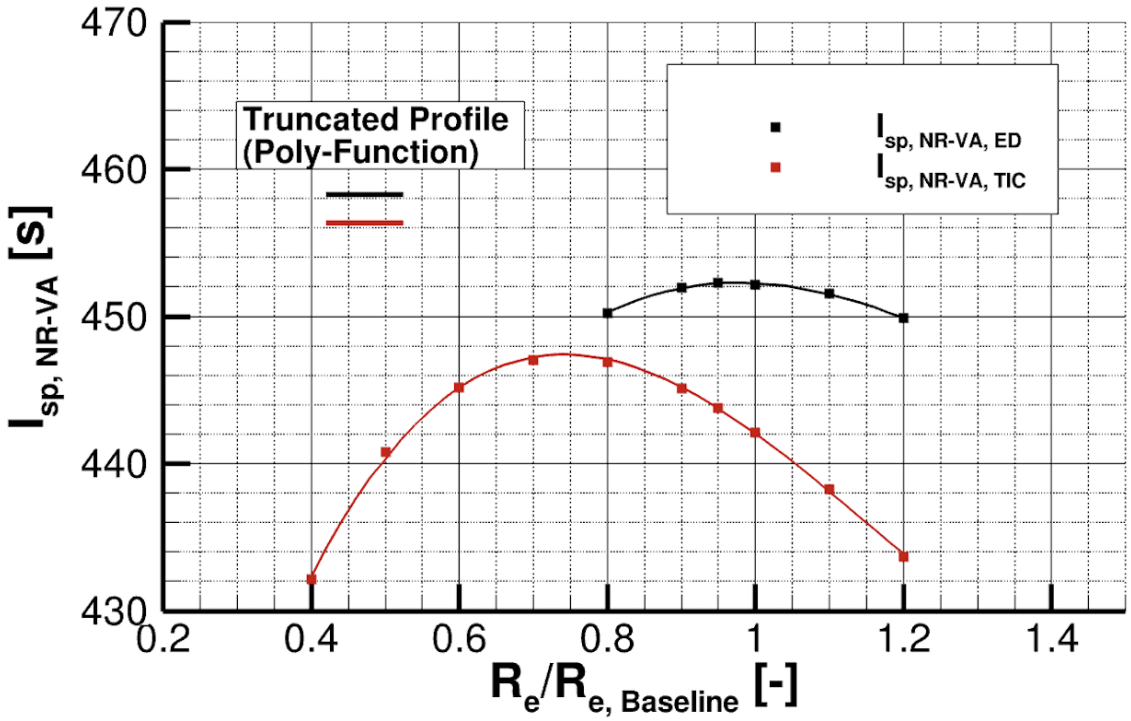

Figure 6.20: Viscous-adiabatic I_{sp} of 2 m ED and TIC as a function of radius

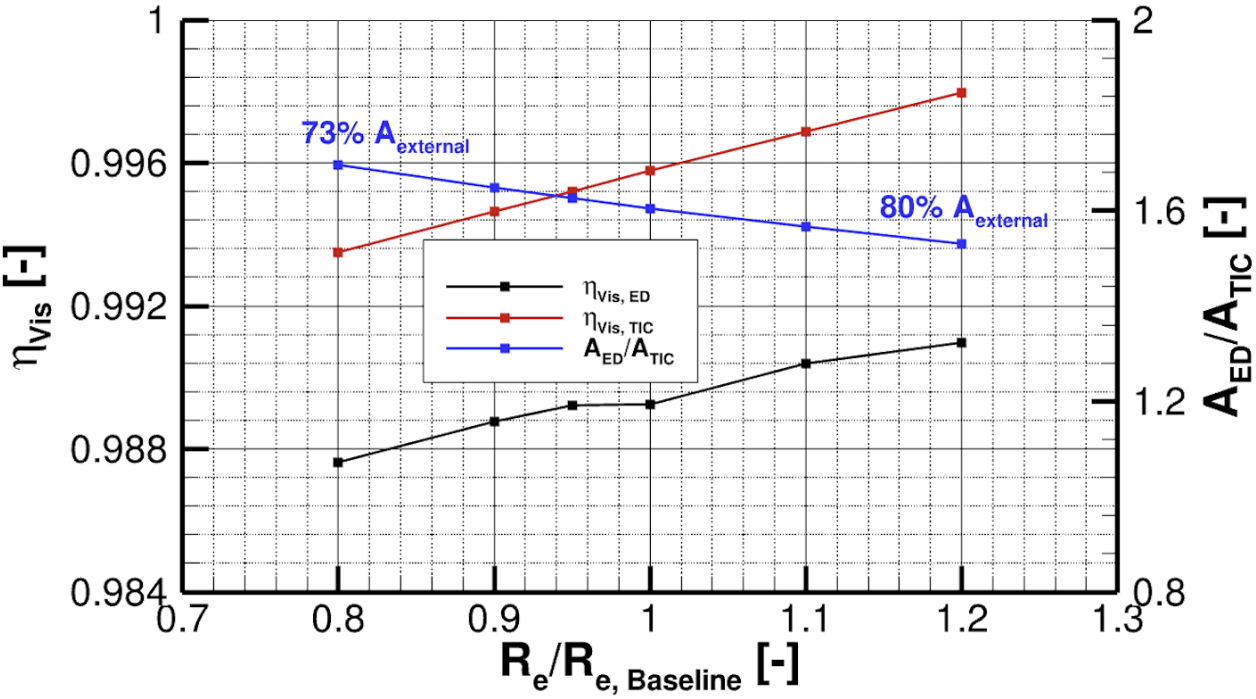

Figure 6.21: Viscosity efficiency η_{Vis} and ratio of surface area A_{ED}/A_{TIC} of 2 m ED and TIC as function of radius

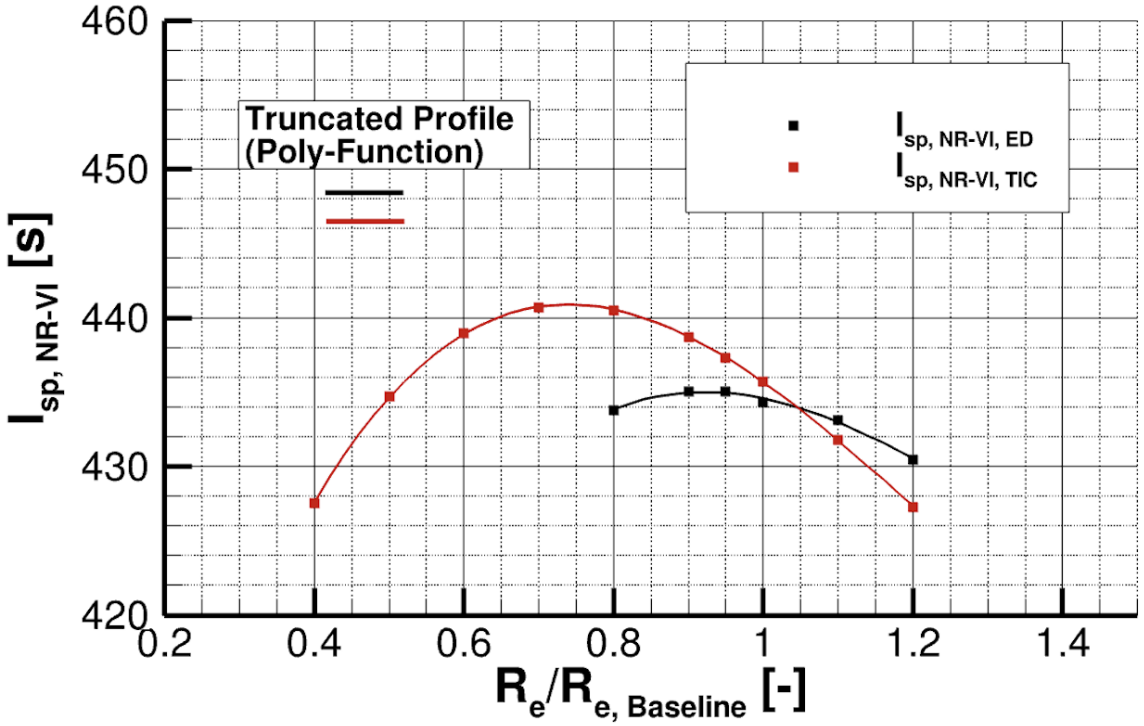

Figure 6.22: Viscous-isothermal I_{sp} of 2 m ED and TIC as function of radius ($T_w = 700\ K$)

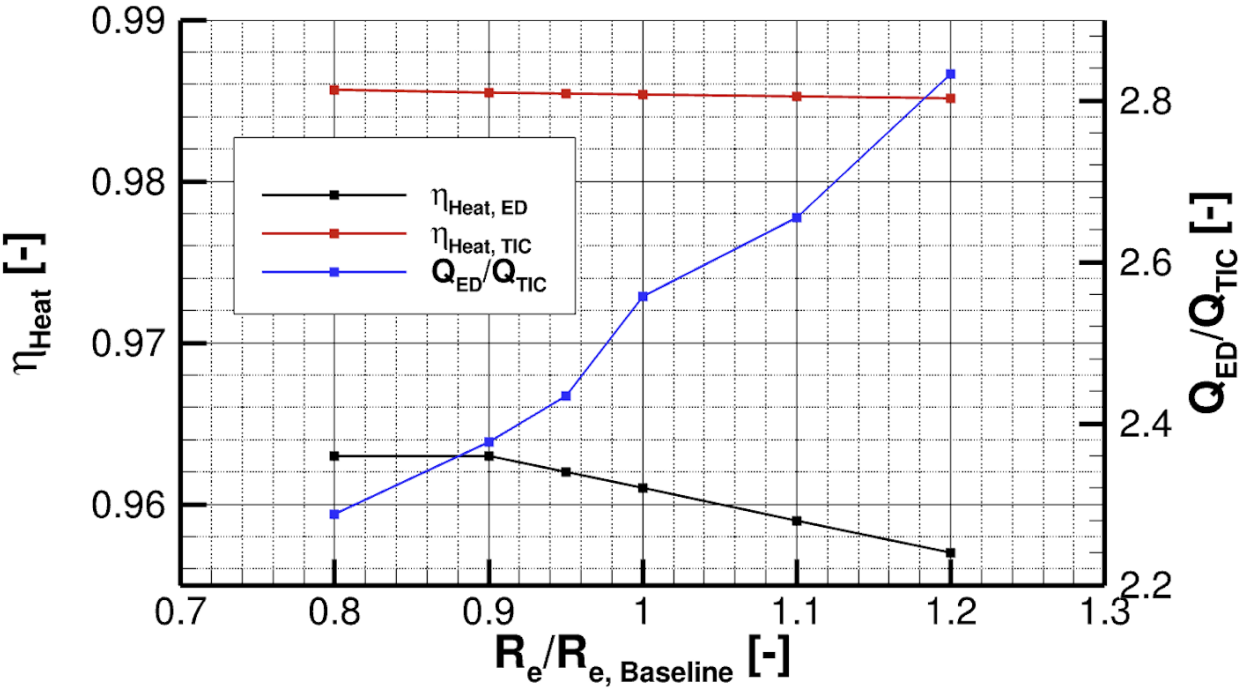

Figure 6.23: Heat exchange efficiency η_{Heat} and ratio of integral wall heat flux Q_{ED}/Q_{TIC} as a function of radius ($T_w = 700\ K$)

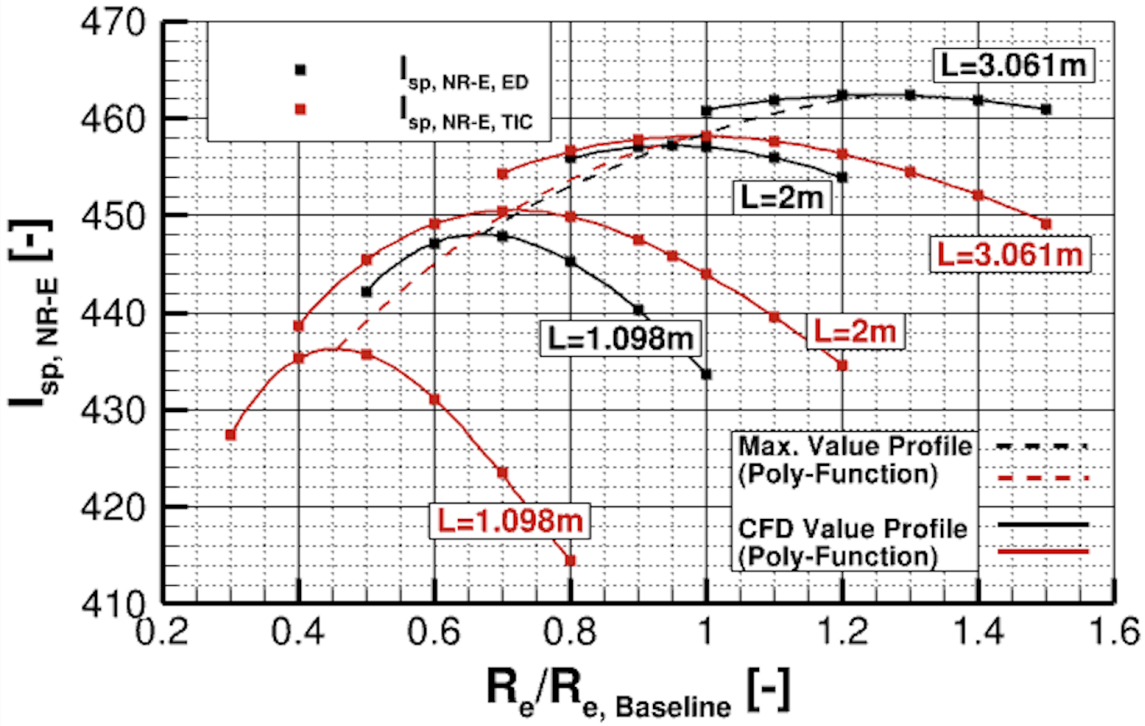

Figure 6.24: Characteristic diagram of Eulerian I_{sp} of ED and TIC

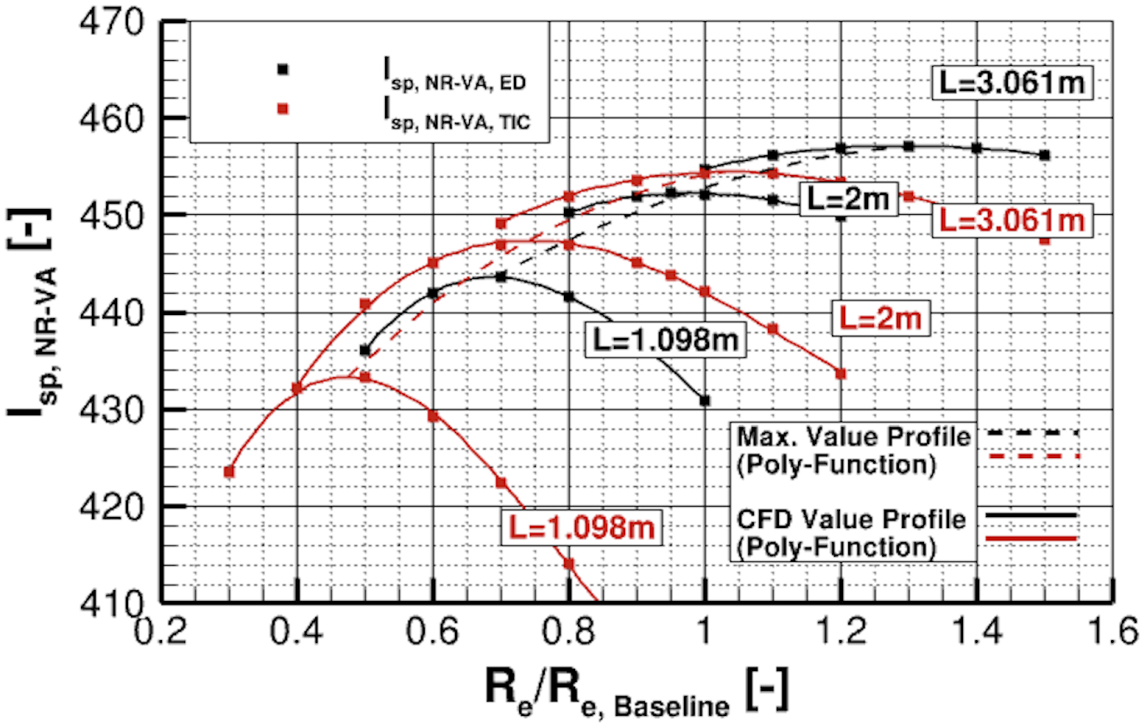

Figure 6.25: Characteristic diagram of viscous-adiabatic I_{sp} of ED and TIC

6.1.3 Characteristic Diagrams

Figures 6.24 and 6.25 show the Eulerian and viscous-adiabatic I_{sp} as a function of the truncation radius also for a smaller and larger truncation length than the 2 m Baseline. Moreover, the maximal performance values that result for a certain truncation length are shown. The curves are generated by curve fitting the CFD results with 3rd-degree and 2nd-degree polynomial functions. The graphs show that a variation of the truncation radius has a more substantial effect on the I_{sp} at shorter lengths than it does for larger lengths. This means that the expansion ratio and, thus, the radial dimensions of the nozzle can be reduced for the ED and TIC nozzles without significantly reducing the performance.

6.2 Influence of design specific heat ratio

The design of the ED nozzles with varying design value for the specific heat ratio γ based on the Baseline ED nozzle is done with the first design procedure. The first design procedure is discussed in more detail in Subsection 2.2.1. The input parameters are taken from the Baseline ED nozzle in Tab. 6.1 and 6.2. Only the design value for γ is changed. Figure 6.26 shows the Baseline ED nozzle obtained with a constant $\gamma = 1.138$, corresponding to the nozzle throat according to the CEA code, as discussed in Subsection 2.4.2. In addition, four other ED nozzle contours are shown, obtained with constant values for $\gamma = 1.2015, 1.2306, 1.3232$, and 1.4. The specific heat ratio $\gamma = 1.3232$ corresponds to the nozzle exit (CEA code), and $\gamma = 1.2306$ is the arithmetic mean value between the throat and exit γ values. The specific heat ratio $\gamma = 1.2015$ is the value that provides the same I_{sp} with the one-dimensional constant γ performance analysis as the variable γ performance analysis in the CEA code. Finally, $\gamma = 1.4$ is a test value to explore values higher than the nozzle exit value. This value is outside the physical range inside the nozzle.

Figure 6.26 shows that the external ED nozzle wall is bulgier and less divergent for low γ values. The reason is that the throat angle Θ_{th} is also very low, as shown in Fig. 6.27. However, the throat angle Θ_{th} increases with increasing γ, and the external ED nozzle wall becomes more divergent. This can be explained in the following way.
Generally, the Prandtl-Meyer function ν increases with increasing Mach number M and decreases with increasing γ, as shown in Fig. 2.4. However, the higher M, the more pronounced the decrease in ν with increasing γ. The Mach number at the end of the internal expansion region M_i is the same in all designs. In addition, the design Mach number M_i is very low and close to $M_i = 1$. As a result, $\nu(M_i, \gamma)$ is already close to zero and decreases only marginally with an increase in γ, as shown in Fig. 6.28.
In addition, an increase in the design γ has an increasing effect on the FL exit radius $R_{e,FL}$ and the FL exit Mach number $M_{e,FL}$, as shown in Fig. 6.27. In theory, this also has an increasing effect on the Prandtl-Meyer function $\nu(M_{e,FL}, \gamma)$. However, as shown in Fig. 6.28, $\nu(M_{e,FL}, \gamma)$ decreases with increasing γ due not the dominating effect of γ.
Figure 6.28 shows that the decrease in $\nu(M_{e,FL}, \gamma)$ is more pronounced than the decrease in $2{\cdot}\nu(M_i, \gamma)$ with increasing γ. According to Eq. 2.5, the throat angle Θ_{th} increases with increasing γ. For the wall radii R_1 and R_2, the axial combustion chamber location x_{cc} and the straight base radius y_{Base}, the same values as for the Baseline ED nozzle are used. These are shown in Tab. 6.3 and 6.4.
Figure 6.29 shows the Eulerian I_{sp} and the efficiency η_L as a function of the design value of the specific heat ratio γ. The efficiency η_L is the ratio of the Eulerian I_{sp} of the respective ED nozzle and the Baseline ED nozzle with a design $\gamma = 1.138$. Accordingly, the efficiency η_L equals one for the Baseline $\gamma = 1.138$. However, as the design γ increases, the Eulerian I_{sp} and the efficiency η_L decrease. This is because the external wall of the ED nozzles becomes increasingly divergent as γ increases. As a result, the performance divergence losses increase.

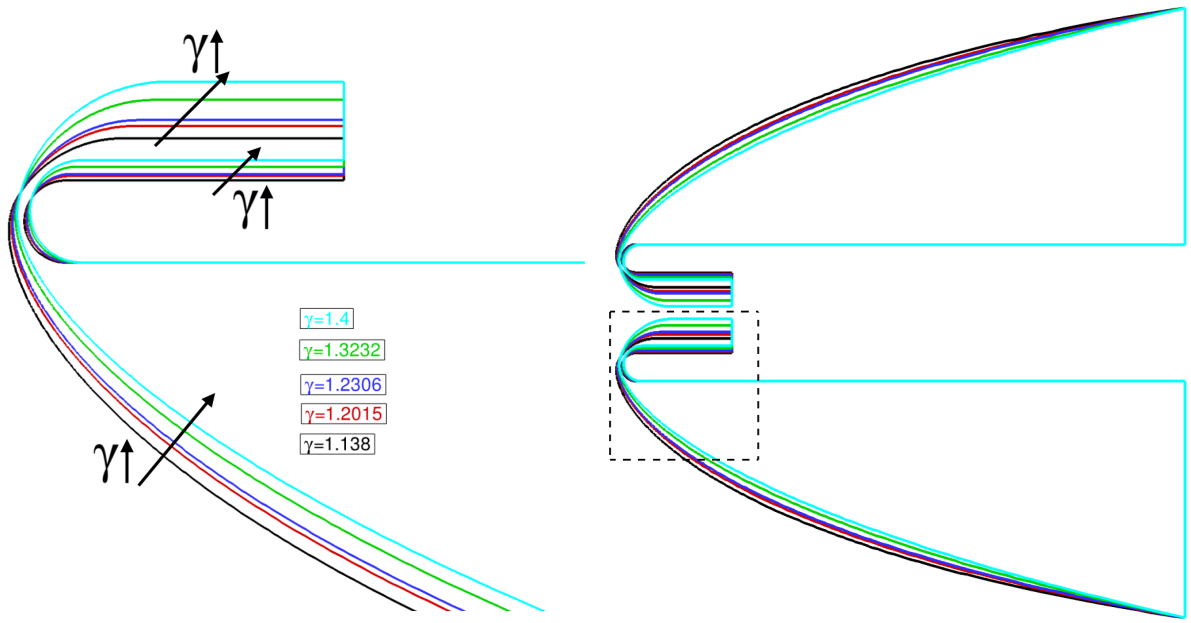

(a) Detail view **(b)** Normal view

Figure 6.26: Variation of constant specific heat ratio γ in design

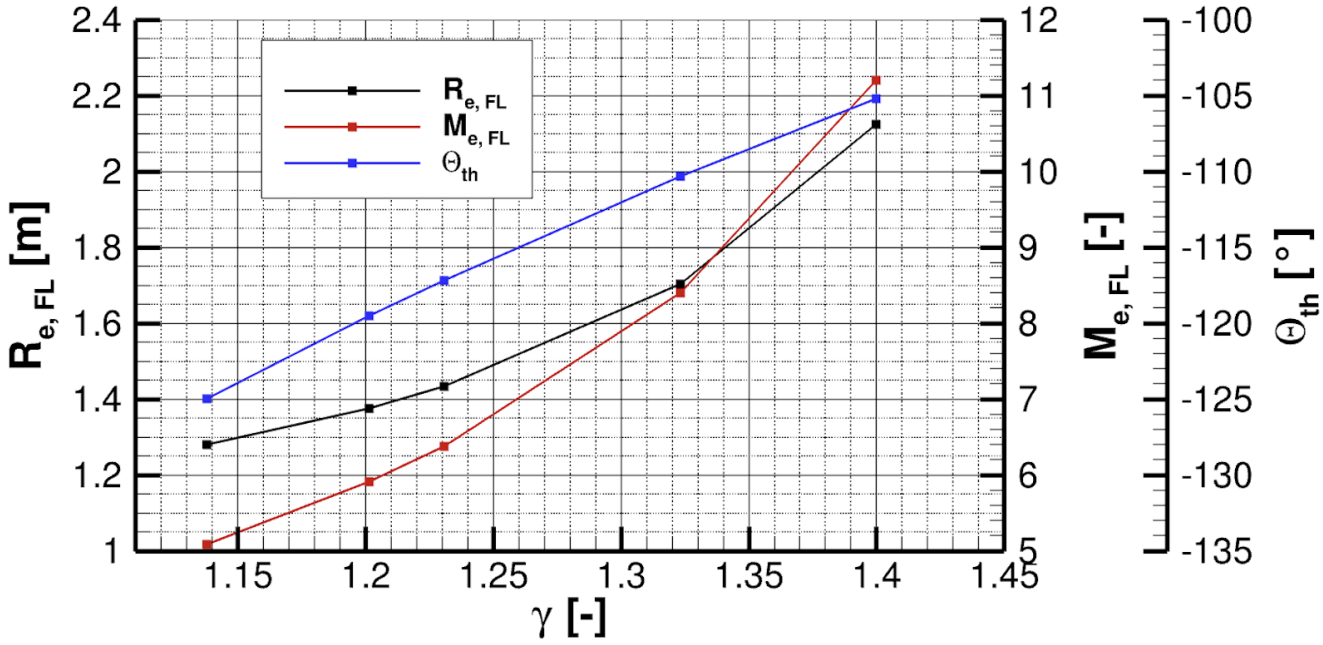

Figure 6.27: FL exit radius $R_{e,FL}$, Mach number $M_{e,FL}$ and throat angle Θ_{th} as a function of design γ

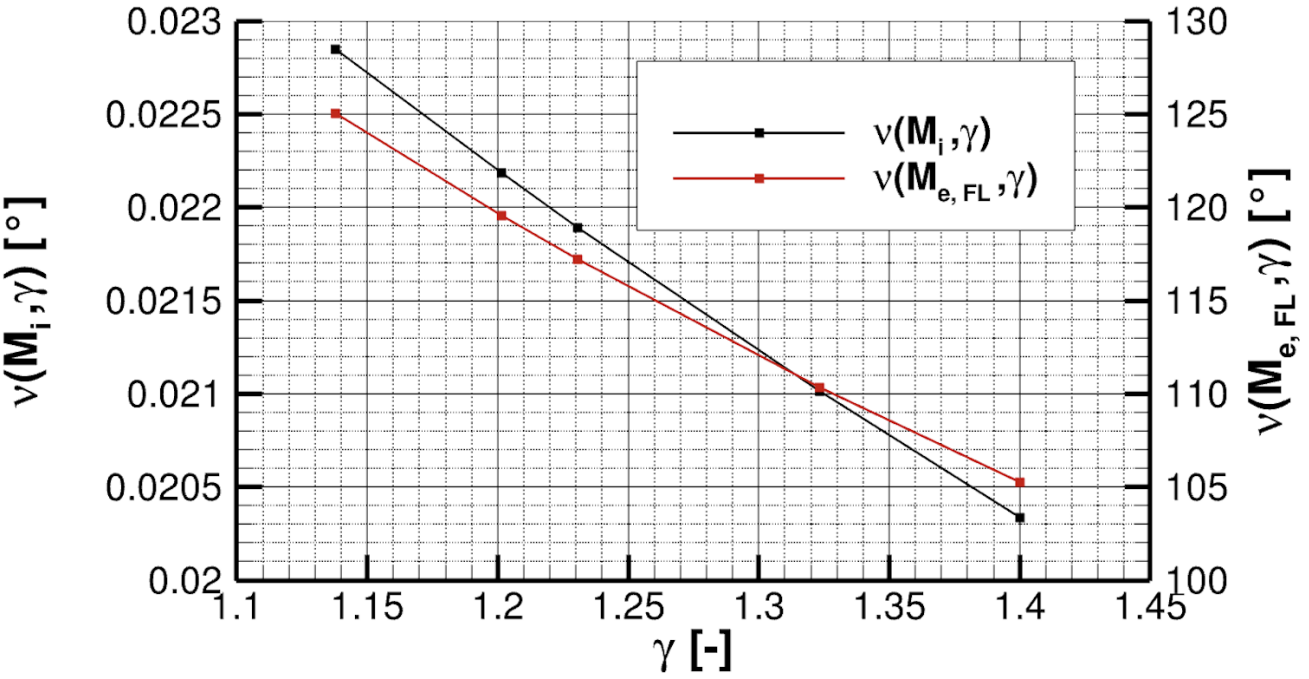

Figure 6.28: Prandtl-Meyer functions ν for the various ED nozzle designs with various design γ

Figure 6.30 shows the viscous-adiabatic I_{sp} as a function of the design γ. The curve is generated by curve-fitting the CFD results with a 3rd-degree polynomial function. The simulations show a peak for the specific impulse that can be explained in the following way. At small design values of γ, an increase in γ causes an increase in I_{sp}. This is because the profiles derived with small design values of γ feature low divergence losses, and the viscous losses decrease with increasing γ. Accordingly, the viscosity efficiency η_{Vis} increases, as shown in Fig. 6.31. The reason is that the wall surface decreases with increasing design γ. Correspondingly, the ratio of the ED and the Baseline ED nozzle wall surface $A_{ED}/A_{ED,Baseline}$ decreases with increasing γ, as shown in Fig. 6.31. The decrease in the wall surface comes mostly from the external wall. The external wall surface decreases nearly linearly with increasing γ, accounting for approximately $77-76$ % of the total wall area. In contrast, the internal wall surface remains roughly constant for all designs. However, as the design value for γ increases, the divergence losses increase and counteract the performance yield from lower viscous losses. This results in a maximum point beyond which the divergence losses are so evident that the I_{sp} decreases for even higher design γ. The simulations show that the Baseline ED nozzle with a design value of $\gamma = 1.138$ is already close to the maximum. The maximum can be obtained with $\gamma = 1.201$, and the simulations demonstrate an I_{sp} of approximately 452.296 s.
Figure 6.32 shows the viscous-isothermal I_{sp} ($T_w = 700\ K$) as a function of the design γ. The curve is generated by curve-fitting the CFD results with a 3rd-degree polynomial function. The curve demonstrates a peak and qualitatively the same behavior as in the viscous-adiabatic case in Fig. 6.30. The difference to the viscous-adiabatic curve is that the viscous-isothermal performance values are lower due to additional heat exchange. In addition, the maximum I_{sp} is shifted towards a higher design γ values and is 435.977 s at $\gamma = 1.3084$. The reason is that the ED nozzle suffers substantial heat exchange for small γ. Accordingly, the heat exchange efficiency η_{Heat} is low, and the integral wall hat flux is high for small γ, as shown in Fig. 6.33. The behavior of the I_{sp} curve can be explained as follows.
For small design γ an increase in γ results in an increase of I_{sp}. This is because the heat exchange efficiency η_{Heat} increases, and the integral wall heat flux Q decreases, as shown in Fig. 6.33. Figure 6.34 and 6.35 show the peak heat flux along the external and internal ED nozzle wall for the profiles generated with $\gamma = 1.138$ (smallest and Baseline value) and $\gamma = 1.4$ (highest value). The plots show that the peak heat flux in both cases is in the same order of magnitude and even slightly higher in the case of $\gamma = 1.4$. Hence, the peak heat flux cannot explain the decrease in the heat exchange with increasing γ. Indeed, the surface area can, because it decreases with increasing γ and can justify the decrease in heat exchange. Additionally, with increasing γ, the nozzle walls get shifted more toward the symmetry axis, so the peak heat flux is exposed to less wall surface and contributes less to heat exchange.
However, as the design γ increases, the divergence losses increase and counteract the increase in performance due to lower heat exchange. This results in a maximum I_{sp} from which a further increase in γ results in even lower I_{sp} due to the domination of divergence losses.

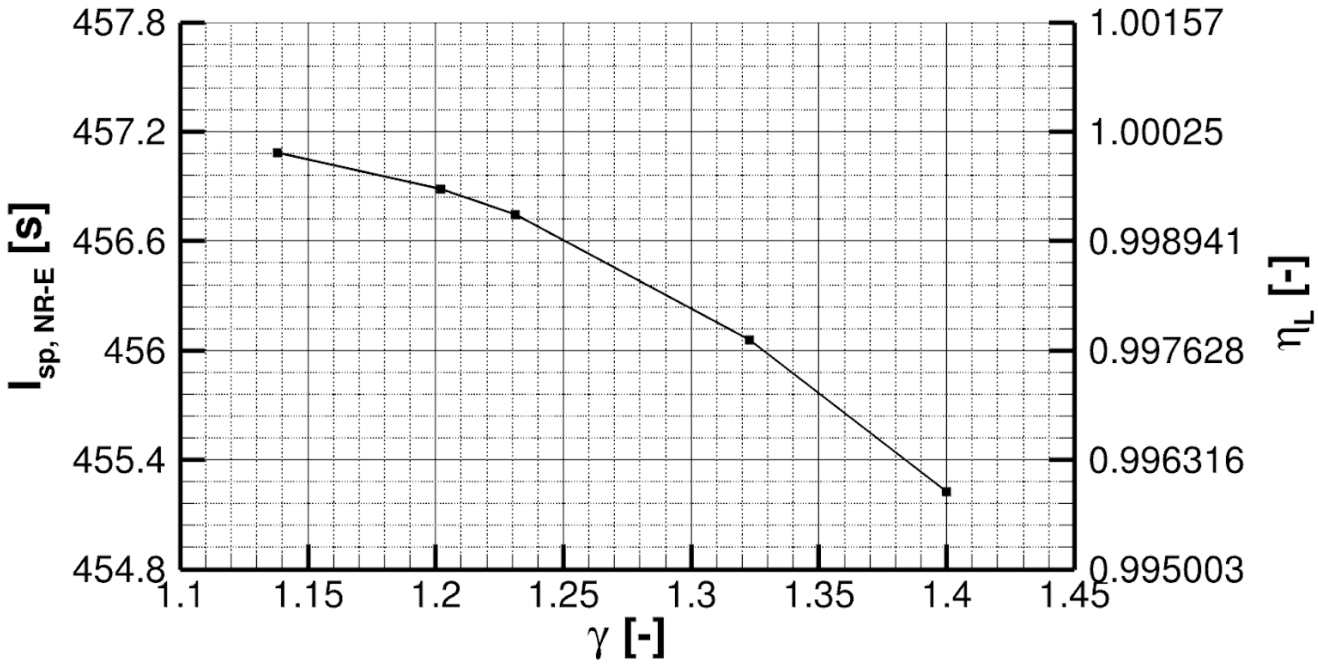

Figure 6.29: Eulerian I_{sp} of ED and efficiency η_L as a function of design γ

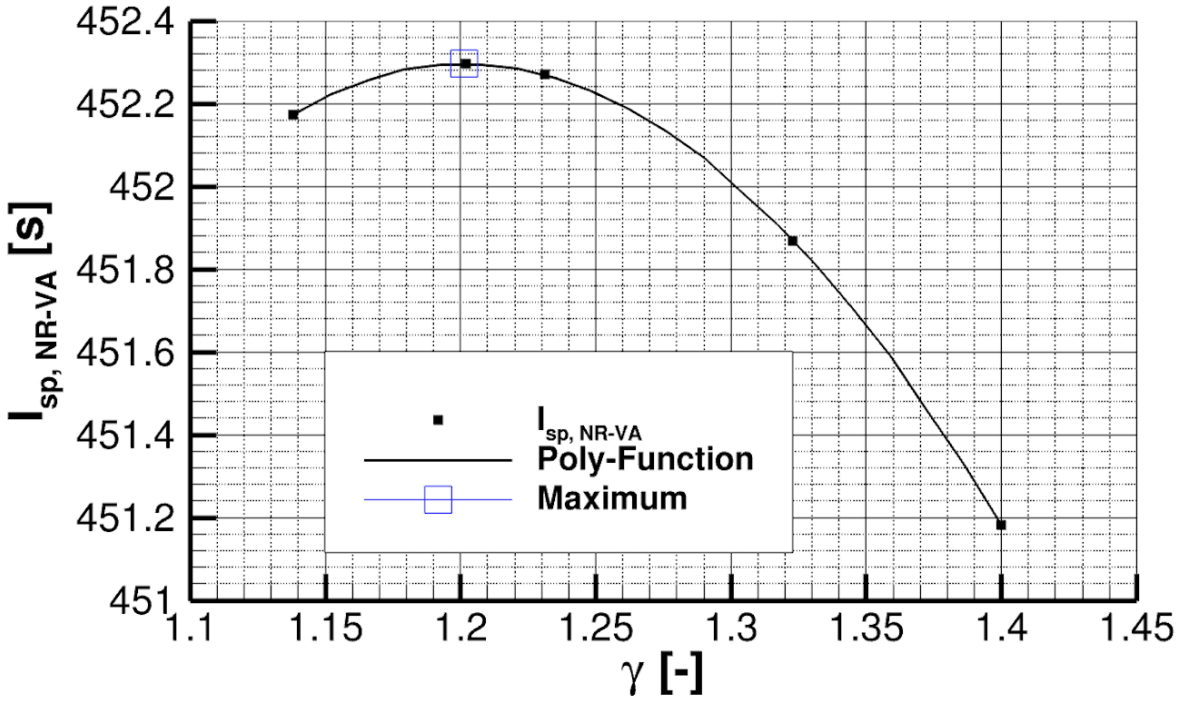

Figure 6.30: Viscous-adiabatic I_{sp} of 2 m ED as a function of design γ

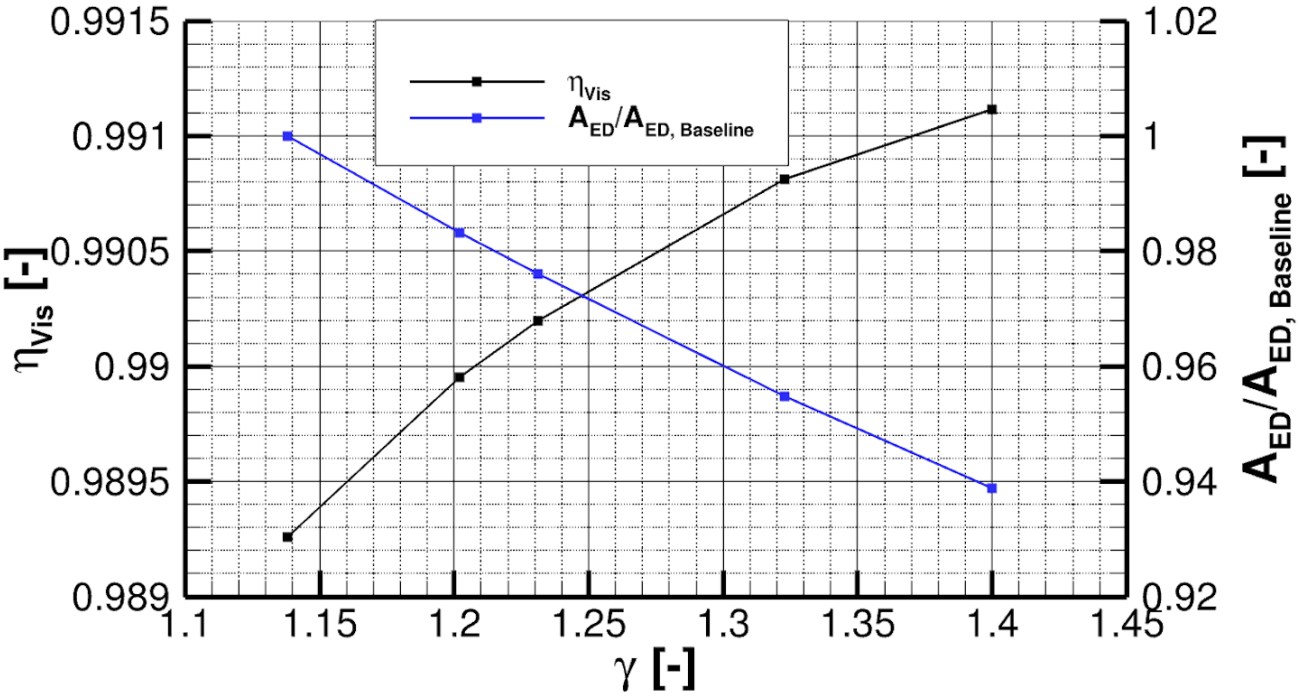

Figure 6.31: Viscosity efficiency η_{Vis} and ratio of surface area of ED and Baseline ED as a function of design γ

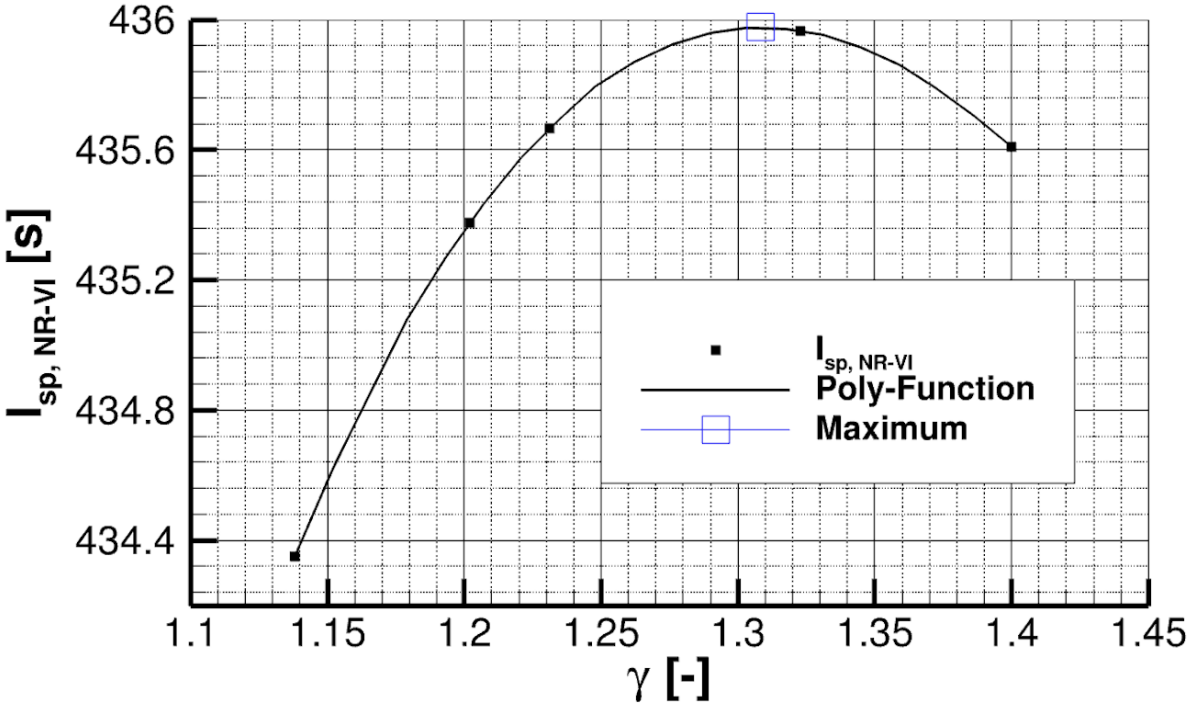

Figure 6.32: Viscous-isothermal I_{sp} of 2 m ED as a function of design γ ($T_w = 700\ K$)

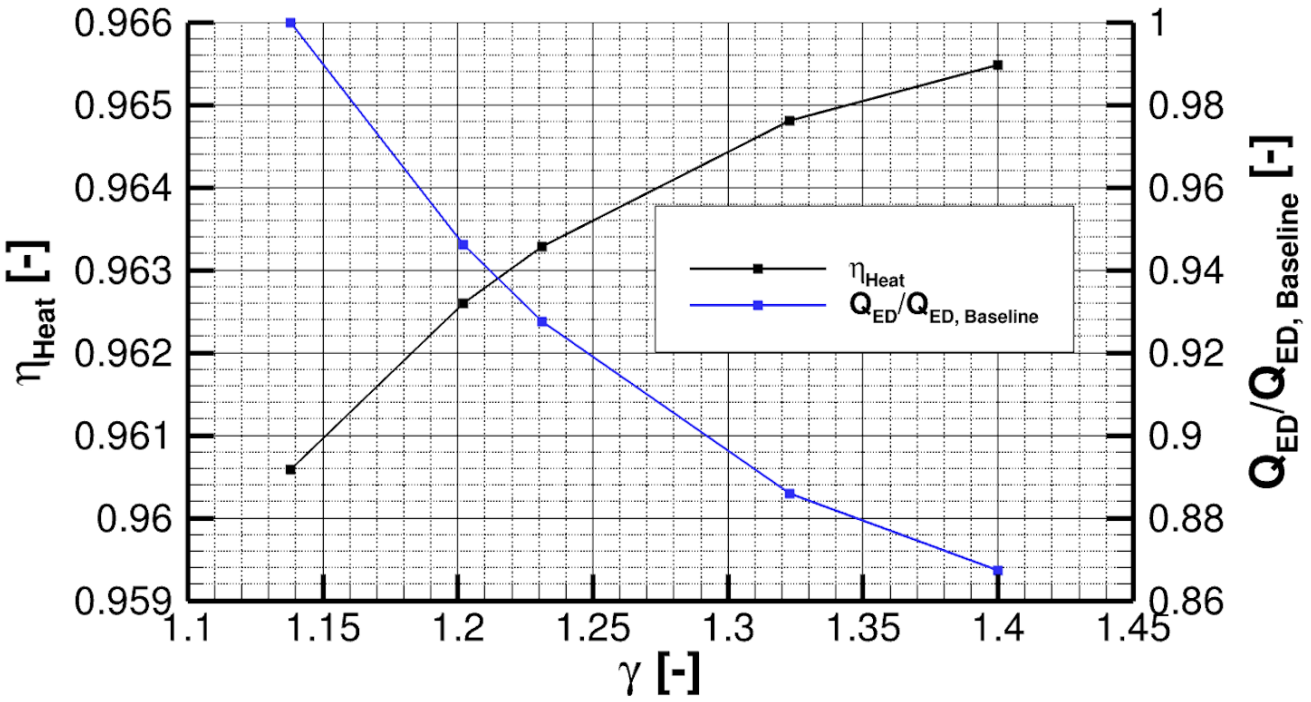

Figure 6.33: Heat exchange efficiency η_{Heat} and ratio of integral wall heat flux of ED and Baseline ED as a function of design γ ($T_w = 700\ K$)

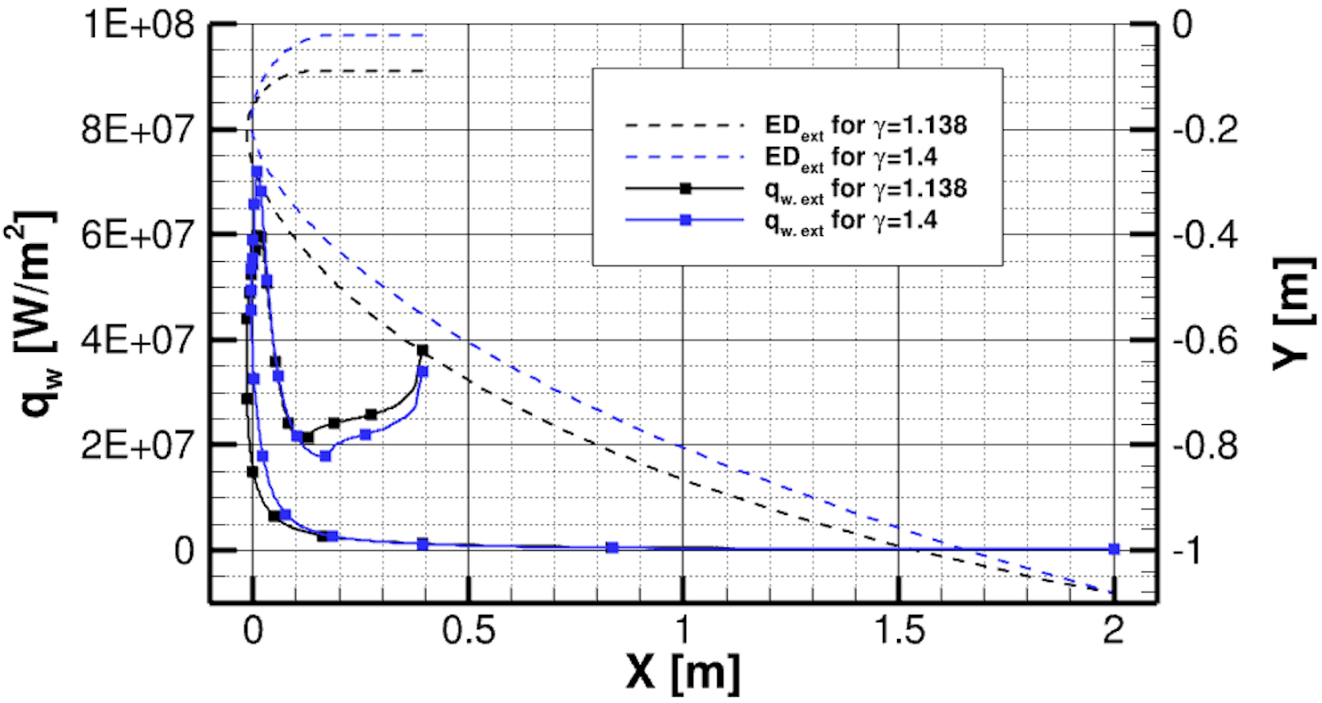

Figure 6.34: Heat flux density q_w and radial coordinate Y of external ED wall as a function of axial coordinate X and design γ ($T_w = 700\ K$)

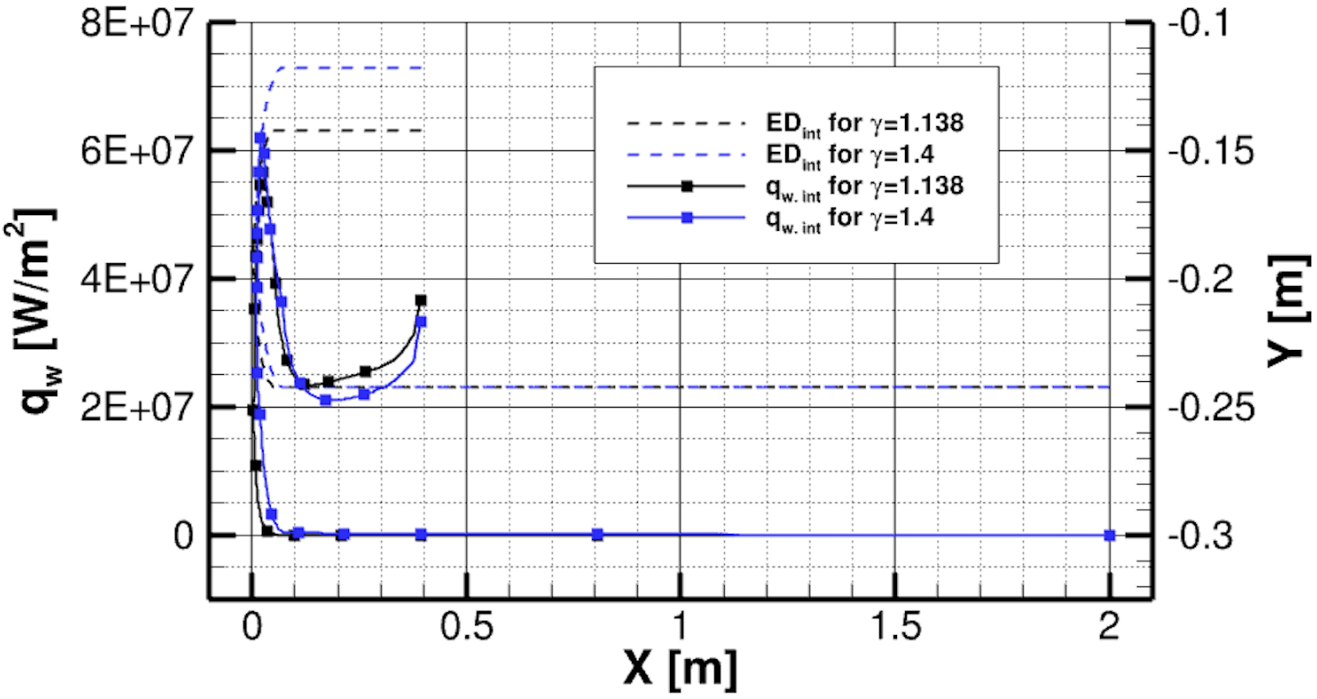

Figure 6.35: Heat flux density q_w and radial coordinate Y of internal ED wall as a function of axial coordinate X and design γ ($T_w = 700\ K$)

6.3 Influence of radial throat shift

The design of the ED nozzles with varying design value for the radial throat shift Y_2 based on the Baseline ED nozzle is done with the third design procedure. The third design procedure is discussed in more detail in Subsection 2.2.2. The input parameters are taken from the Baseline ED nozzle in Tab. 6.1 and 6.2. Only the radial throat shift Y_2 is changed. Figure 6.36 shows the Baseline ED nozzle and further ED nozzles with radial throat shifts of $Y_2 = 75, 125$, and 150 % of the value of the Baseline ED nozzle.

All ED nozzles feature the same assigned throat angle Θ_{th}. According to Eq. 2.5, this is only possible when the two terms $2 \cdot \nu(M_i, \gamma)$ and $\nu(M_{e,FL}, \gamma)$ from the difference of which the throat angle Θ_{th} is calculated, change to the same extend as the radial throat shift Y_2 is changed. This is explained in the following.

Increasing the radial throat shift Y_2 causes the outer nozzle contour to be shifted further away from the symmetry axis and to be less divergent, as shown in Fig. 6.36. In addition, the FL exit radius $R_{e,FL}$ and the FL exit Mach number $M_{e,FL}$ decrease, as shown in Fig. 6.37.

The Mach number at the end of the internal expansion M_i, is the same in all designs. In addition, the design Mach number M_i is very low and close to $M_i = 1$. For very small Mach numbers, the Prandtl-Meyer function $\nu(M_i, \gamma)$ reacts with almost zero changes on a variation of γ, as shown in Fig. 2.4. The Prandtl-Meyer function $\nu(M_{e,FL}, \gamma)$ decreases more with a decrease in $M_{e,FL}$. Since $2 \cdot \nu(M_i, \gamma)$ and $\nu(M_{e,FL}, \gamma)$ need to change equally to keep the throat inclination Θ_{th} constant, γ needs to be decreased (see Fig. 6.37) having an increasing effect on $\nu(M_{e,FL}, \gamma)$. Figure 6.38 shows the Prandtl-Meyer functions $\nu(M_i, \gamma)$ and $\nu(M_{e,FL}, \gamma)$ as a function of the radial throat shift.
Figure 6.39 shows the Eulerian I_{sp} and the efficiency η_L as a function of the radial throat shift. The efficiency η_L is the quotient of the Eulerian I_{sp} of the respective ED nozzles with the Baseline ED nozzle. The throat shift is dimensionless, and the ratio of the radial throat shifts of the ED nozzles and the Baseline ED nozzle. The simulations show that the I_{sp} increases roughly linearly by increasing Y_2. Actually, the effective exit area, i. e. expansion ratio decreases as the radial throat shift Y_2 increases having a decreasing effect on the I_{sp}. However, for the smallest and largest radial throat shift configurations with $Y_2/Y_{2,Baseline} = 0.75$ and 1.5, the straight central body reduces the effective expansion ratio by just 3.5 or 9 % respectively. This does not have a strong influence on the performance. Indeed, the nozzle profiles get less divergent as Y_2 increases. Hence, also the divergence losses on performance decrease, and the I_{sp} increases.
Figure 6.40 shows the viscous-adiabatic I_{sp} as a function of the radial throat shift. The curve is generated by curve-fitting the CFD results with a 3rd-degree polynomial function. The curve demonstrates a peak that can be explained in the following way. In contrast to the decrease in divergence losses, the viscous losses increase with an increase in the radial throat shift Y_2. Hence, the viscosity efficiency decreases, as shown in Fig. 6.41. The increase in viscous losses counteracts the performance yield from reducing the divergence losses. This leads to a point of optimal performance from which a further increase in Y_2 leads to a reduction of the performance due to the domination of the viscous losses. The increase in viscous losses with increasing Y_2 is due to increased surface area, as shown in Fig. 6.41. For the smallest value of the radial throat shift $Y_2/Y_{2,Baseline} = 0.75$, the external wall accounts for approximately 80 % of the total wall surface. Increasing Y_2 increases the internal wall area relative to the external wall. As a result, for the largest value of $Y_2/Y_{2,Baseline} = 1.25$, the external wall accounts for approximately 72 % of the total wall area.
The change in I_{sp} gets more pronounced if heat exchange is added to the simulations, as shown in Fig. 6.42. In contrast to the Eulerian simulations, the I_{sp} decreases roughly linearly by increasing the radial throat shift Y_2. The reason is that the integral wall heat flux also increases linearly over Y_2, leading to high heat exchange losses. Accordingly, the heat exchange efficiency decreases linearly with increasing Y_2. For the smallest and highest radial throat shifts $Y_2/Y_{2,Baseline} = 0.75$ and 1.5, the external wall accounts for 66 % and 63 % of the total integral wall heat flux. For these two configurations, Fig. 6.44 and 6.45 show the peak heat flux q_w as a function of the axial coordinate along the external and internal walls. The curves show that the peak heat flux is slightly higher in the case of the larger radial throat shift $Y_2/Y_{2,Baseline} = 1.5$. This is because increasing the radial throat shift also decreases the throat gap since the design throat area A_t and angle Θ_{th} are the same for all designs. However, the difference in peak heat flux between both nozzles is small and cannot explain the strong difference in heat exchange. Indeed, the surface area can be responsible because it increases for increasing Y_2 and can justify higher heat exchange. In addition, for ED nozzles with high radial throat shifts, the regions of high peak heat flux are exposed to even higher wall surface, so the peak heat flux contributes even more to high heat exchange.

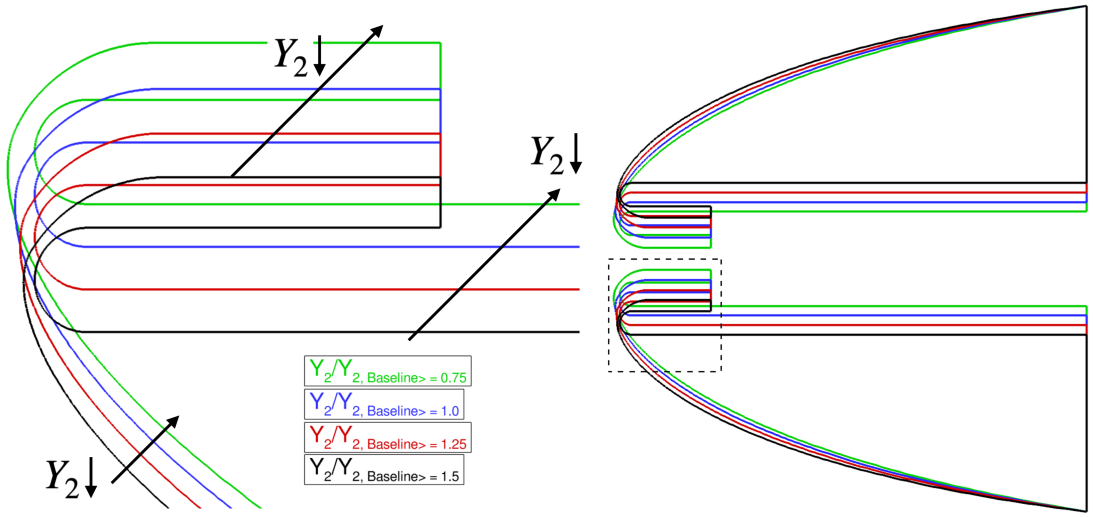

(a) Detail view **(b)** Normal view

Figure 6.36: Variation of throat shift Y_2

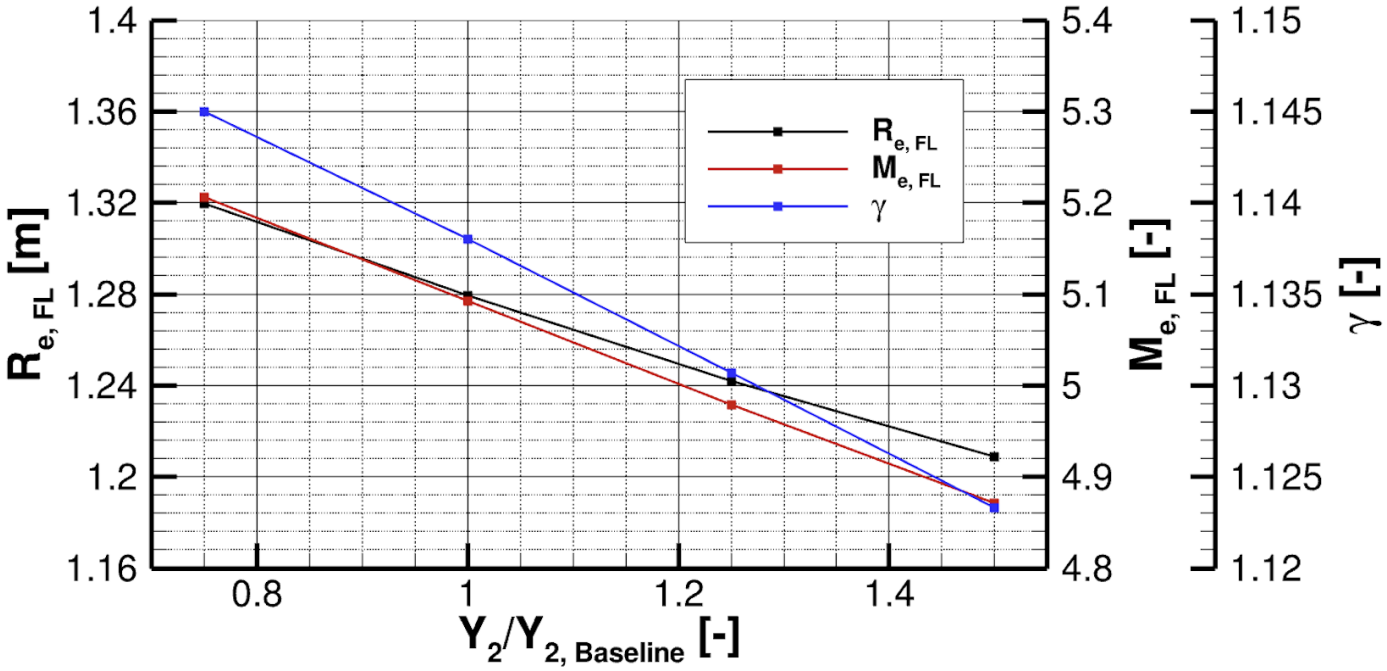

Figure 6.37: FL exit radius $R_{e,FL}$, Mach number $M_{e,FL}$ and throat angle Θ_{th} as a function of the radial throat shift

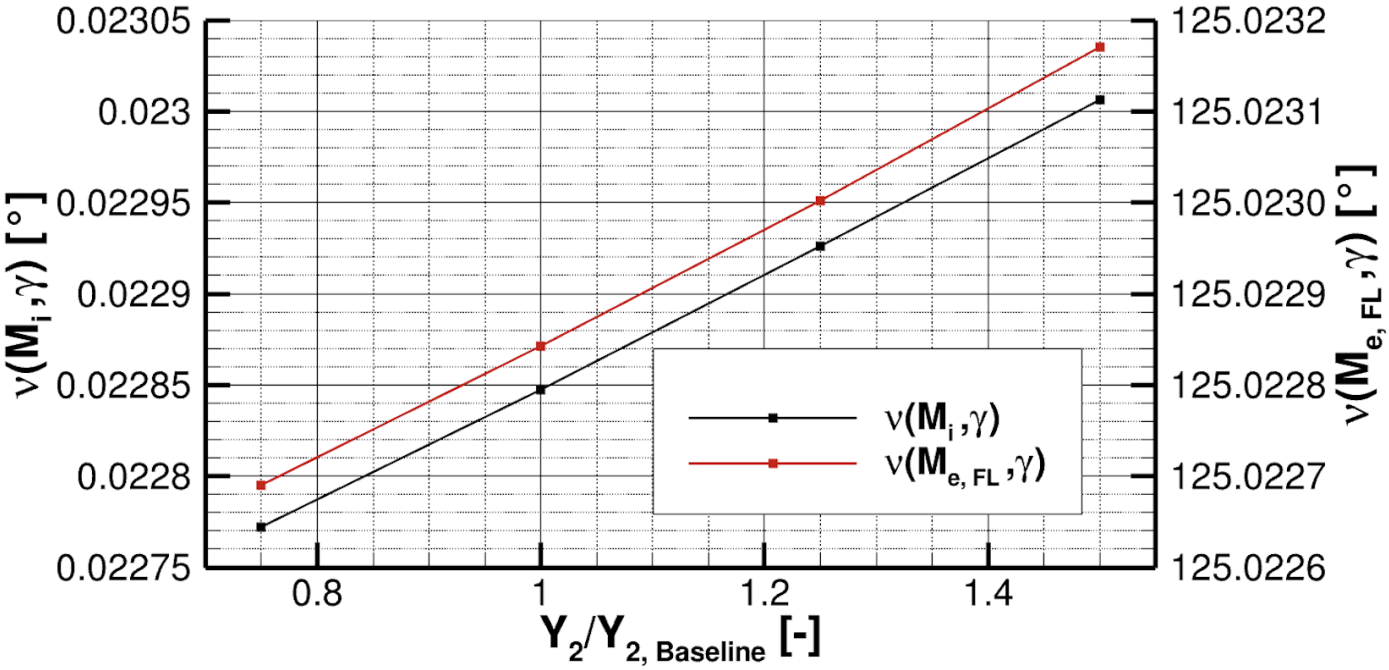

Figure 6.38: Prandtl-Meyer functions ν for the various ED nozzle designs with various radial throat shifts

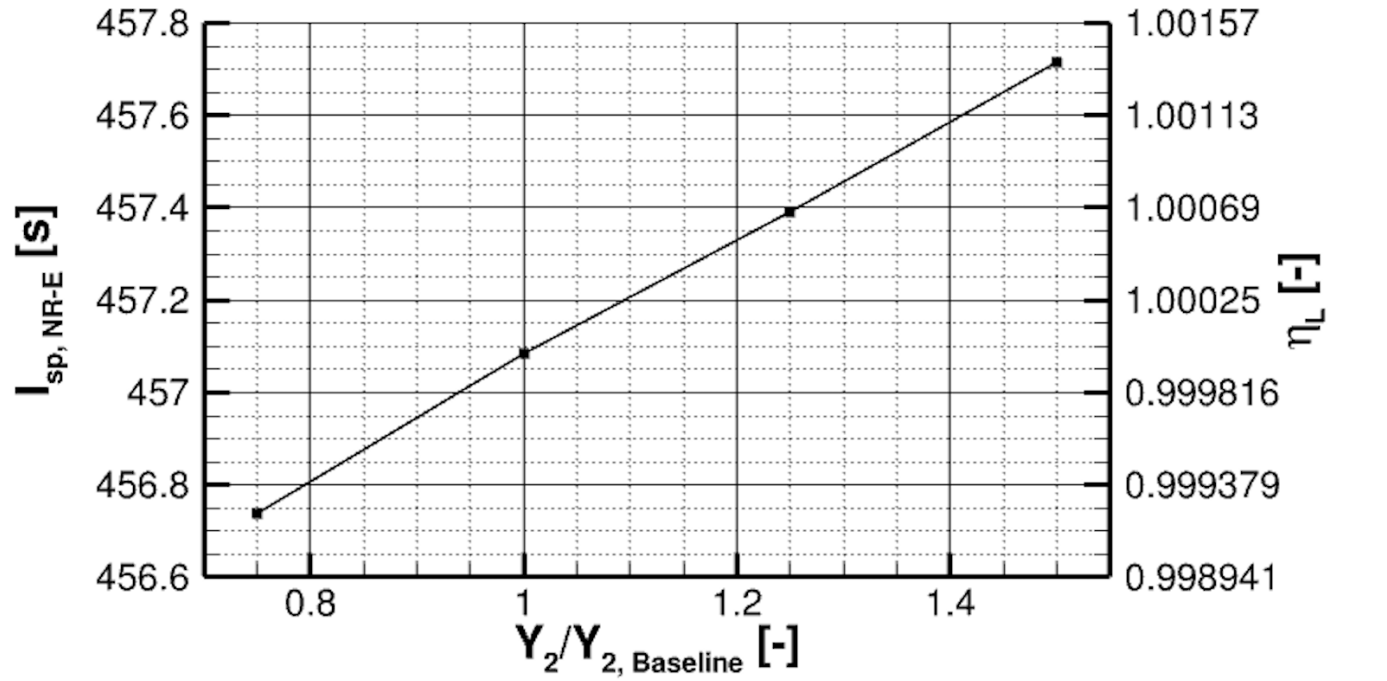

Figure 6.39: Eulerian I_{sp} of ED and efficiency η_L as a function of the radial throat shift

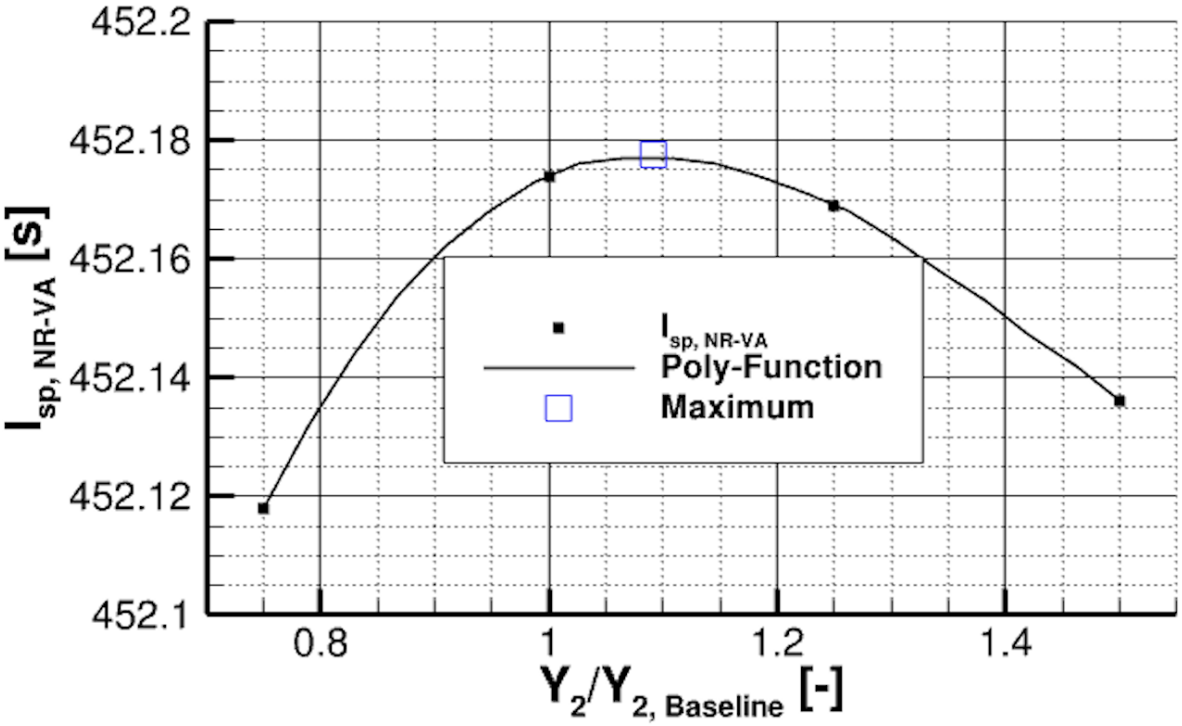

Figure 6.40: Viscous-adiabatic I_{sp} of 2 m ED as a function of the radial throat shift

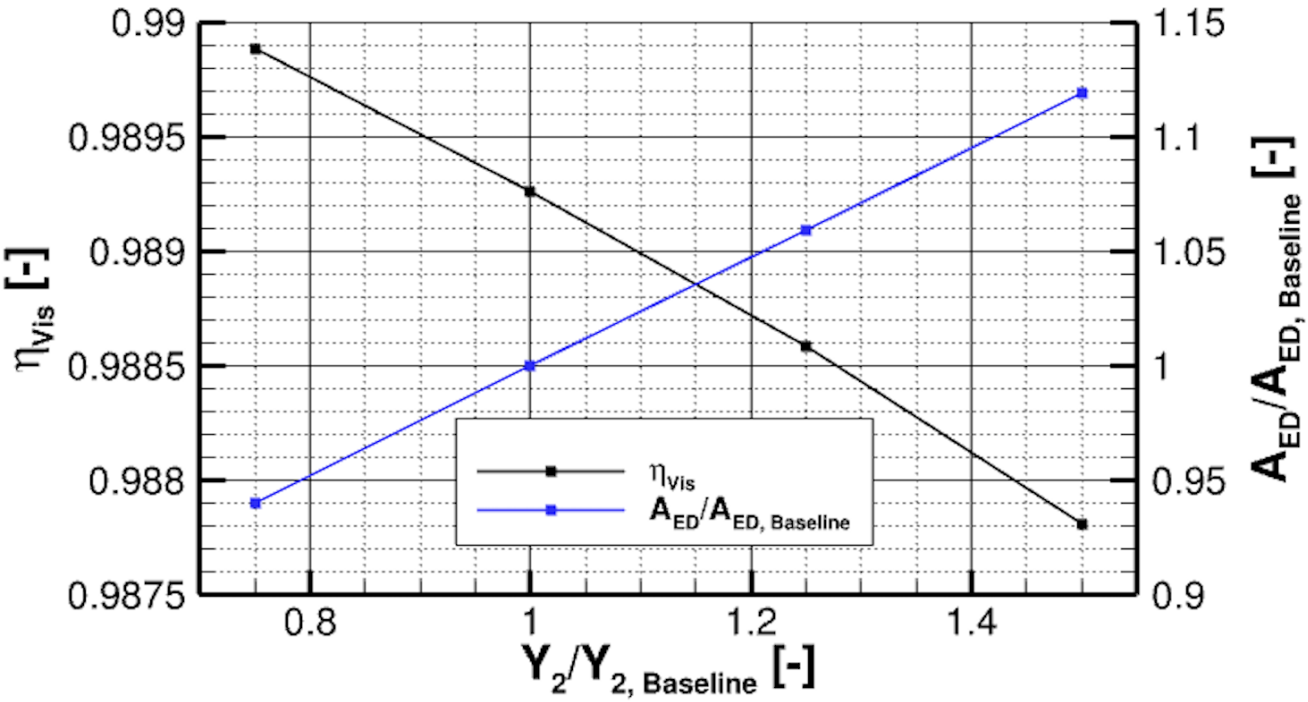

Figure 6.41: Viscosity efficiency η_{Vis} and ratio of surface area of ED and Baseline ED as a function of the radial throat shift

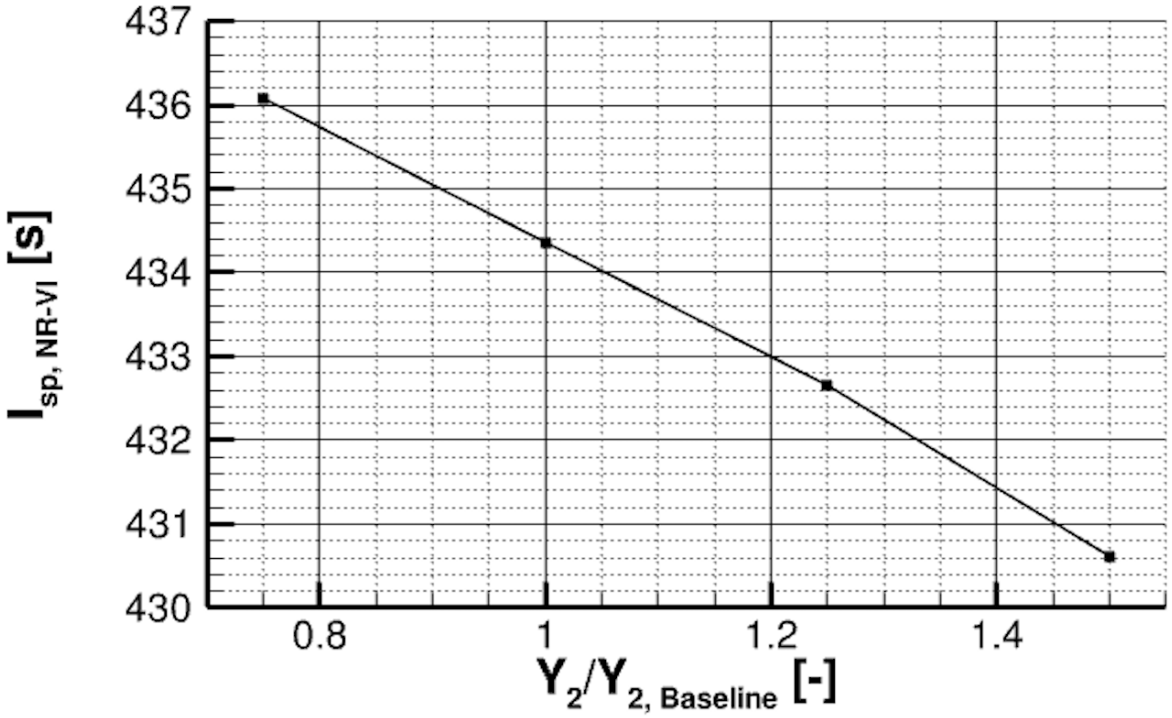

Figure 6.42: Viscous-isothermal I_{sp} of 2 m ED as a function of the radial throat shift ($T_w = 700\ K$)

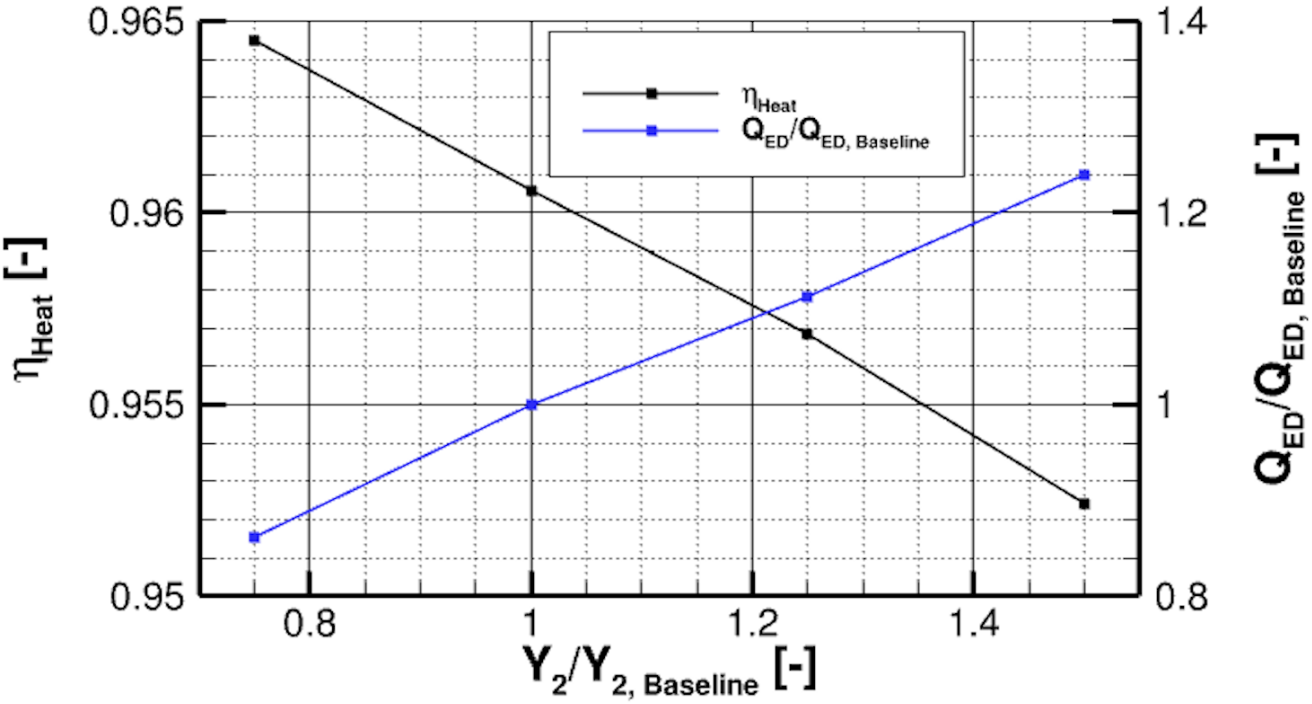

Figure 6.43: Heat exchange efficiency η_{Heat} and ratio of integral wall heat flux of ED and Baseline ED as a function of the radial throat shift ($T_w = 700\ K$)

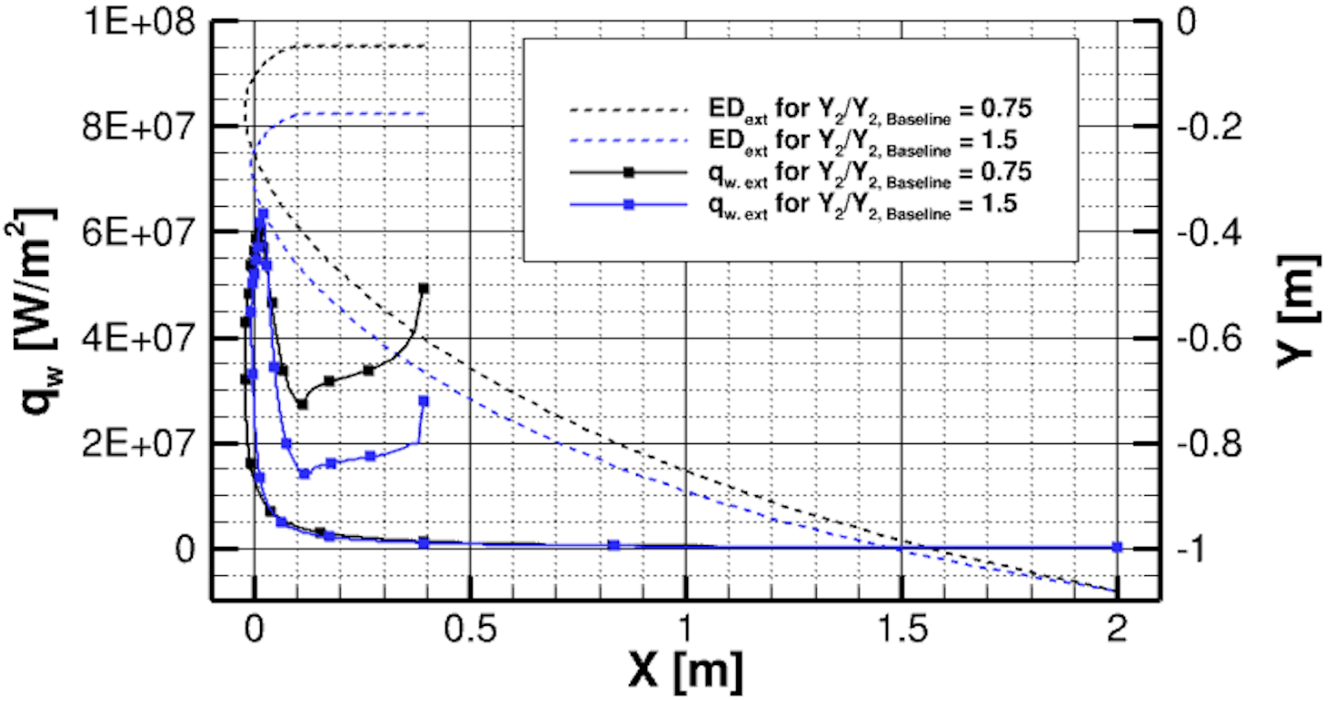

Figure 6.44: Heat flux density q_w and radial coordinate Y of external ED wall as a function of axial coordinate X and the radial throat shift ($T_w = 700\ K$)

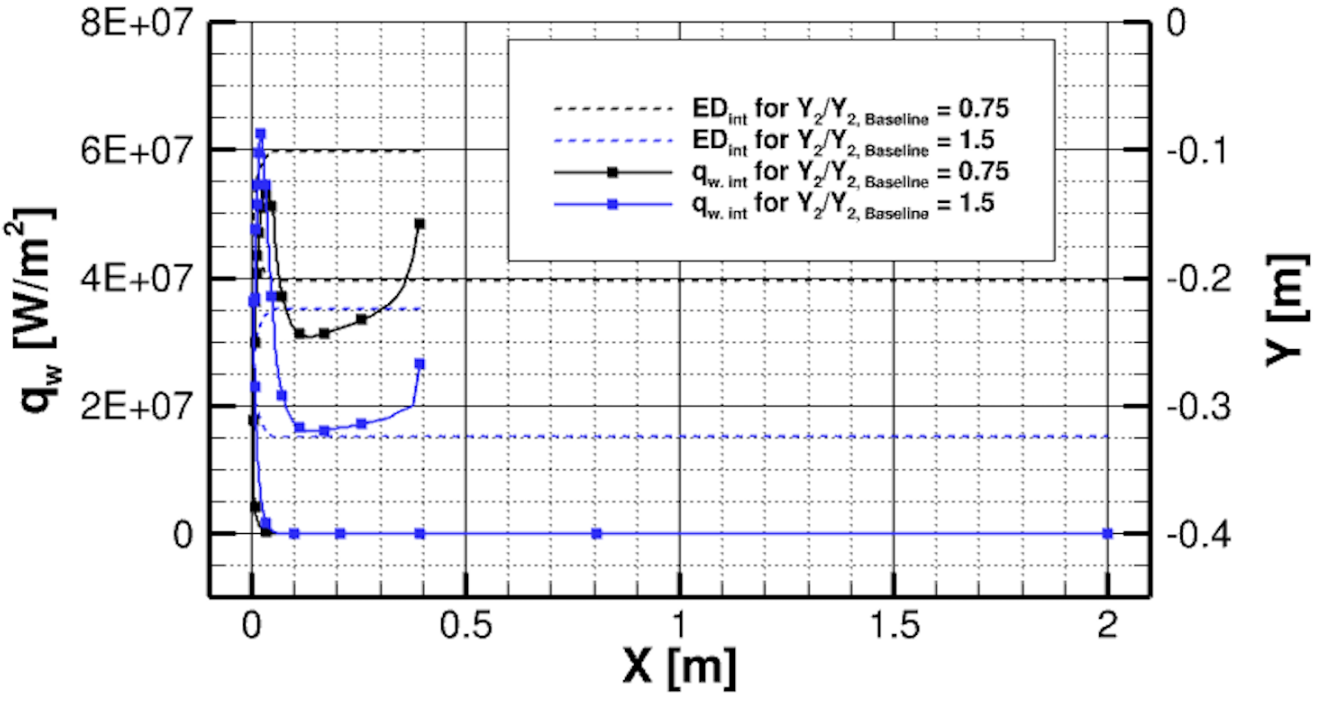

Figure 6.45: Heat flux density q_w and radial coordinate Y of internal ED wall as a function of axial coordinate X and the radial throat shift ($T_w = 700\ K$)

6.4 Influence of the throat wall curvature radii

In Fig. 6.12 to 6.14, it is shown for the Baseline ED nozzle that most of the wall heat exchange, i. e. approximately 68 %, comes from the cylindrical wall areas after the combustion chamber and in the throat region. These regions are the wall areas I and II along the external wall and I along the internal wall, as shown in Fig. 6.12. By changing R_1 and R_2, the nozzle's divergence is unaffected, and the effect on the viscous losses is assumed to be negligible. For this reason, only the influence of the throat wall curvature radii R_1 and R_2 on the heat exchange performance losses is examined in this Section for the Baseline ED nozzle. For this, viscous-adiabatic and viscous-isothermal ($T_w = 700\ K$) simulations are performed. The different wall profiles are shown in Fig. 6.46.
The external throat wall curvature radius R_1 is varied to 75 %, 150 % and 200 % of the Baseline value. The radius R_1 cannot be increased arbitrarily due to the existence of the symmetry axis. The internal throat wall curvature radius R_2 is varied to 75 % and 125 % of the Baseline value. In this case, the maximum value is also limited, as too large values for R_2 would not enable an increase in the cross-sectional area and thus expansion downstream of the throat.

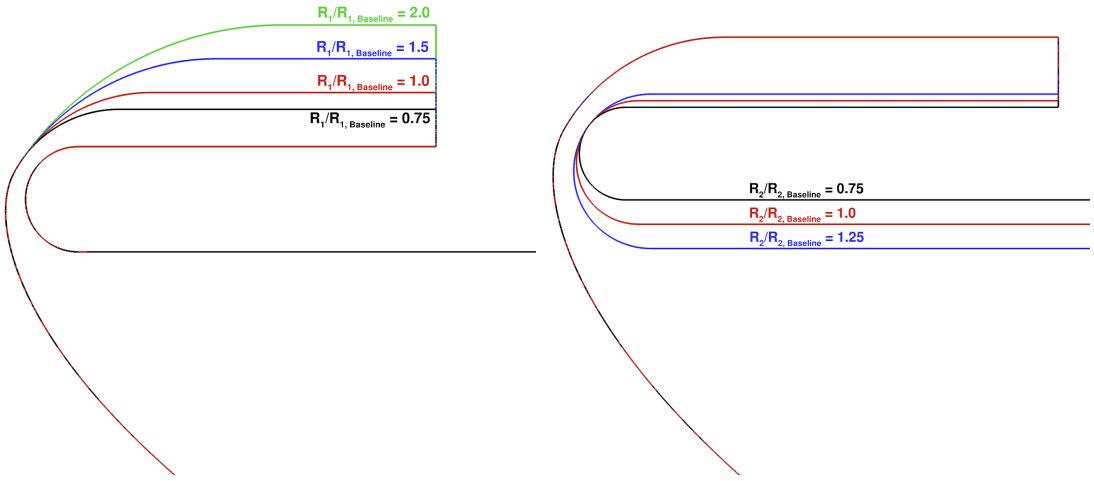

(a) Wall curvature radii for R_1 **(b)** Wall curvature radii for R_2

Figure 6.46: Variation of the external and internal throat wall curvature radii R_1 and R_2

Figure 6.47 shows that the I_{sp} from the viscous-isothermal simulations (at $T_w = 700\ K$) increases with increasing external throat wall curvature radius R_1. This is because the heat exchange losses decrease, corresponding to an increase in the heat exchange efficiency η_{Heat}, as shown in Fig. 6.48. The decrease in the heat exchange losses is due to a decrease in the integral wall heat flux. This is explained in the following.
Figures 6.49 and 6.50 show the heat flux density q_w along the external and internal walls as a function of the axial wall coordinates for the smallest and highest external throat wall curvature radii R_1. By increasing R_1, the heat flux density q_w along the external and internal walls in the cylindrical section after the combustion chamber decreases significantly. In addition, the internal wall surface exposed to the peak heat flux remains constant in contrast to the external wall surface that reduces by increasing R_1. As a result, the integral wall heat flux decreases along the internal and external walls, leading to a less pronounced total heat exchange of the nozzle.

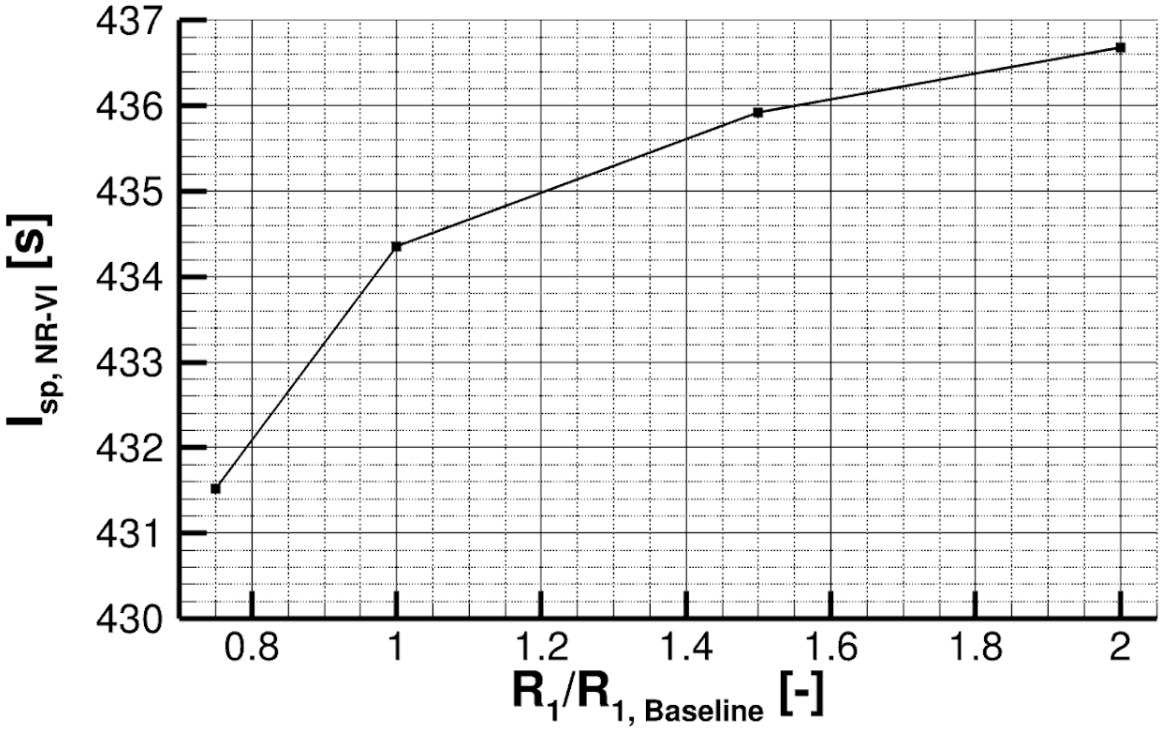

Figure 6.47: Viscous-isothermal I_{sp} of 2 m ED as a function of the external throat wall curvature radius ($T_w = 700\ K$)

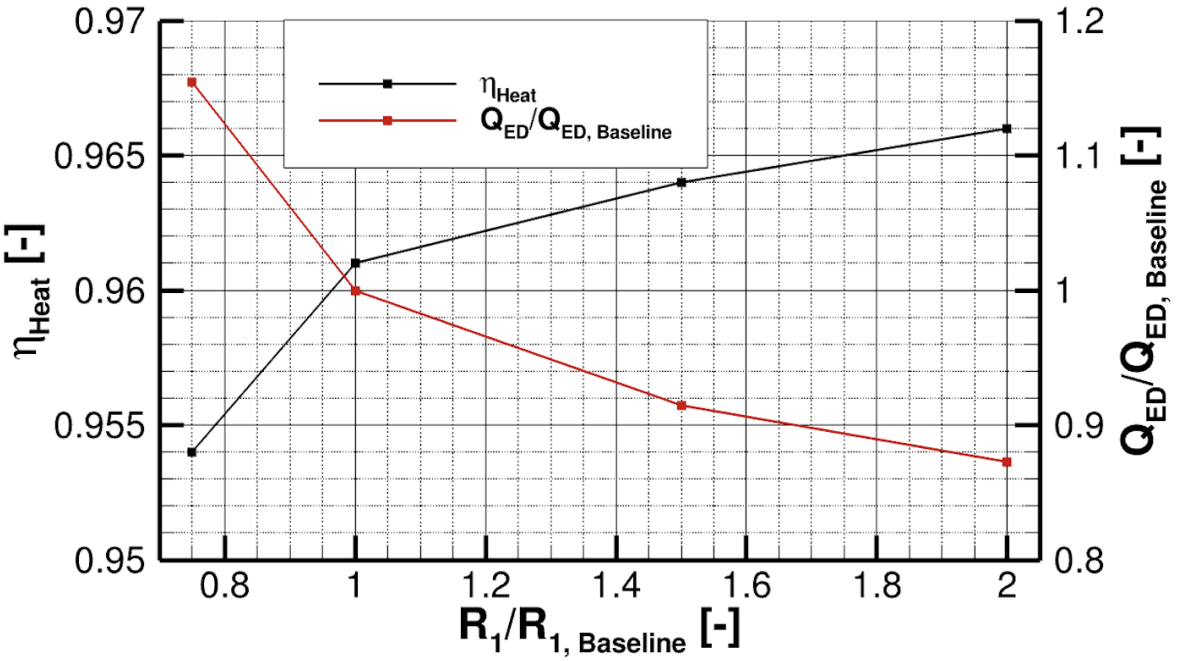

Figure 6.48: Heat exchange efficiency η_{Heat} and ratio of integral wall heat flux of ED and Baseline ED as a function of the external throat wall curvature radius ($T_w = 700\ K$)

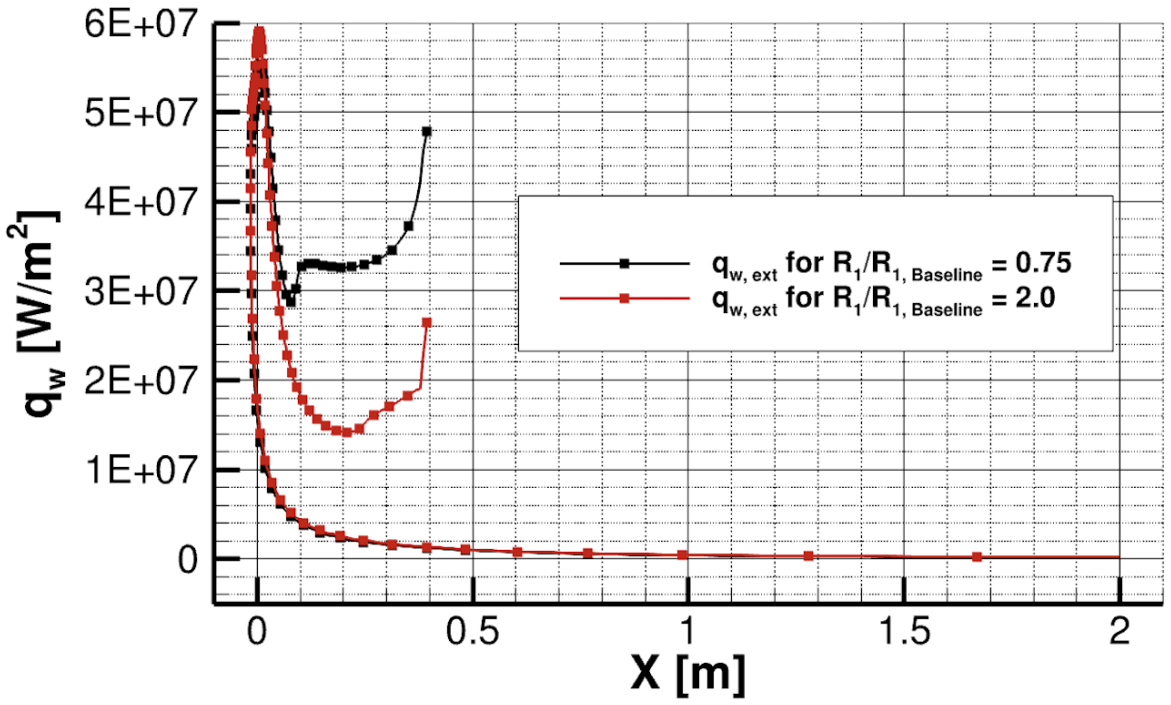

Figure 6.49: Heat flux density q_w of external ED wall as a function of axial coordinate X and the external throat wall curvature radius ($T_w = 700\ K$)

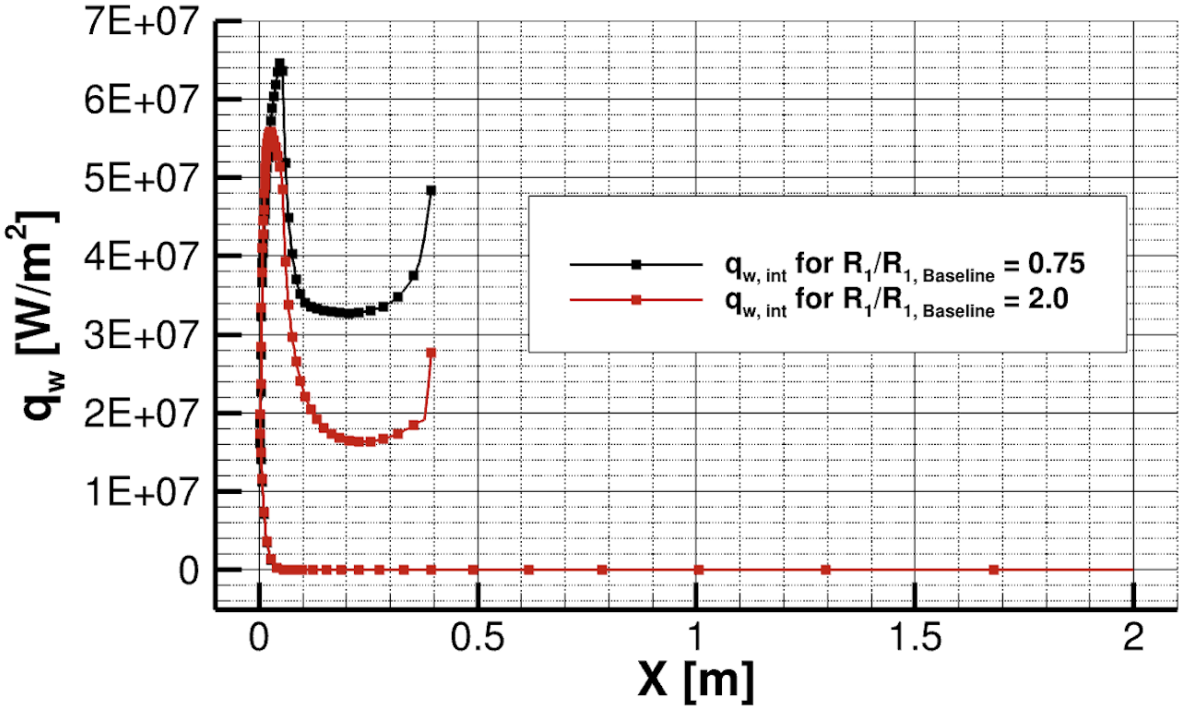

Figure 6.50: Heat flux density q_w of internal ED wall as a function of axial coordinate X and the external throat wall curvature radius ($T_w = 700\ K$)

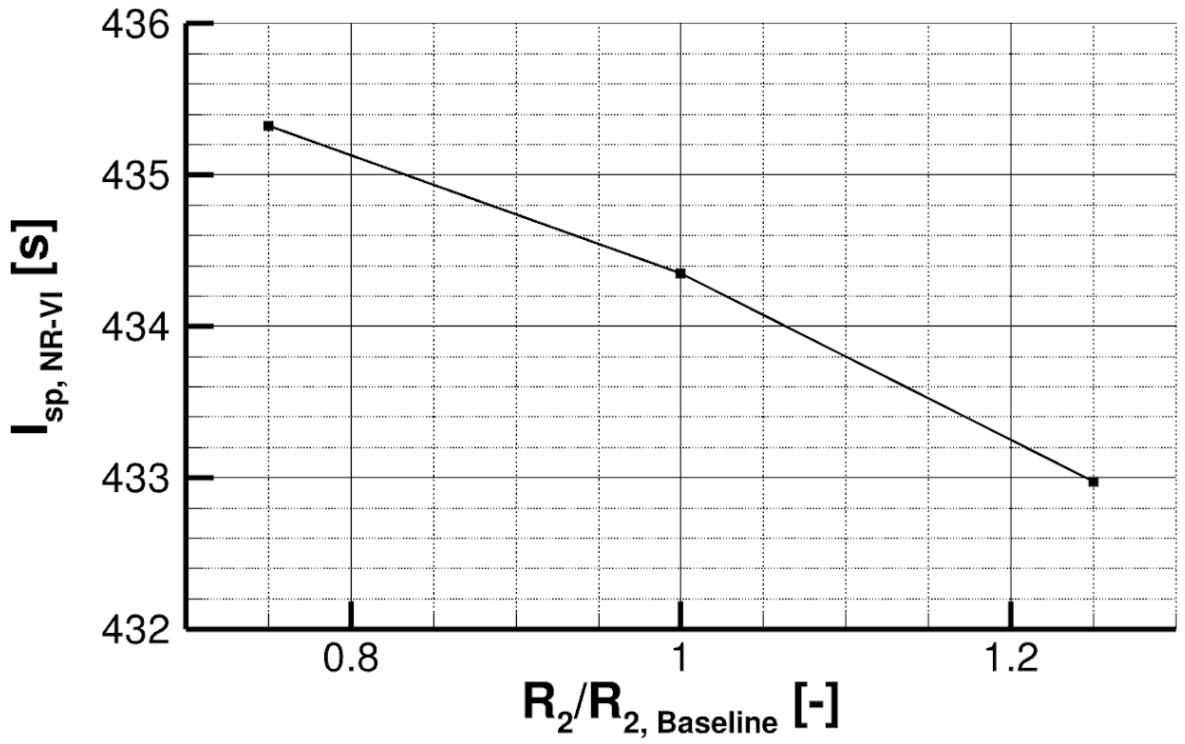

Figure 6.51: Viscous-isothermal I_{sp} of 2 m ED as a function of the internal throat wall curvature radius ($T_w = 700\ K$)

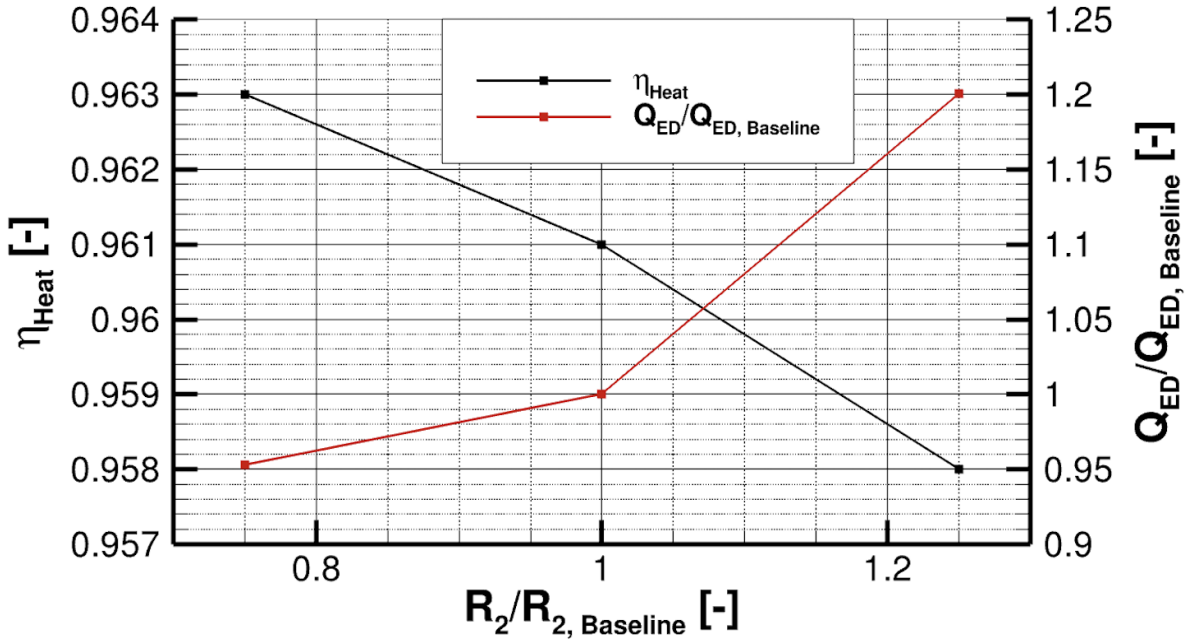

Figure 6.52: Heat exchange efficiency η_{Heat} and ratio of integral wall heat flux of ED and Baseline ED as a function of the internal throat wall curvature radius ($T_w = 700\ K$)

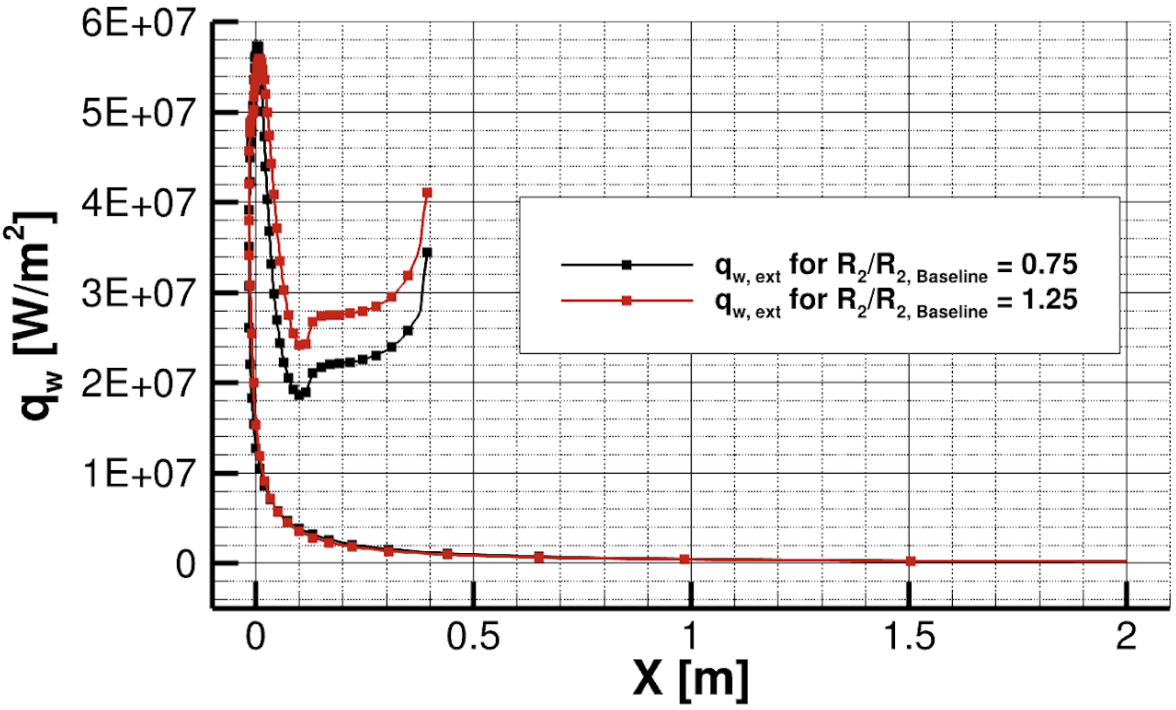

Figure 6.53: Heat flux density q_w of external ED wall as a function of axial coordinate X and the internal throat wall curvature radius ($T_w = 700\ K$)

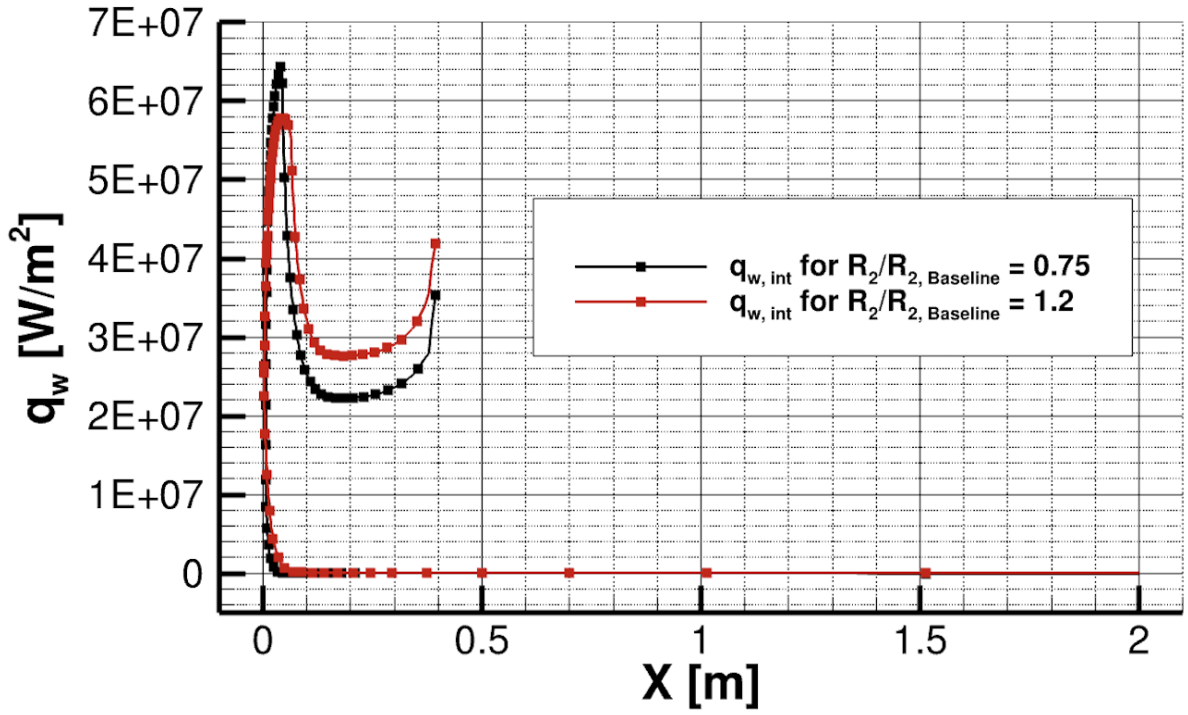

Figure 6.54: Heat flux density q_w of internal ED wall as a function of axial coordinate X and the internal throat wall curvature radius ($T_w = 700\ K$)

Figure 6.51 shows that the I_{sp} from the viscous-isothermal simulations (at $T_w = 700\ K$) decreases with increasing internal throat wall curvature radius R_2. This is due to increased heat exchange losses corresponding to a decreased heat exchange efficiency η_{Heat}, as shown in Fig. 6.52. The reason is that the integral wall heat flux increases as R_2 increases. This is explained in the following.
Figure 6.53 and 6.54 show the heat flux density q_w along the external and internal walls as a function of the axial wall coordinates for the smallest and highest value of R_2. Increasing R_2 increases the heat flux density along the external and internal walls in the cylindrical section after the combustion chamber. The external wall surface exposed to the peak heat flux remains constant, and the internal wall area downstream of the throat increases. As a result, these wall areas contribute more to heat exchange, leading to an increased integral wall heat flux.

6.5 Influence of geometrical scaling

The influence of the geometrical scaling factor S_F on the nozzle performance losses is discussed in this Section. The starting point of this investigation is the Baseline ED nozzle in Fig. 2.16 and the TIC nozzle featuring the same truncation length and radius. Both nozzles feature the geometrical scaling factor $S_F = 1.0$. Based on these nozzles, other ED and TIC nozzles are designed by varying the geometrical scaling factor S_F equally in the axial and radial directions to $S_F = 0.25, 0.5, 1.5$, and 2.0. Figure 6.55 shows the ED nozzles for all geometrical scaling factors.

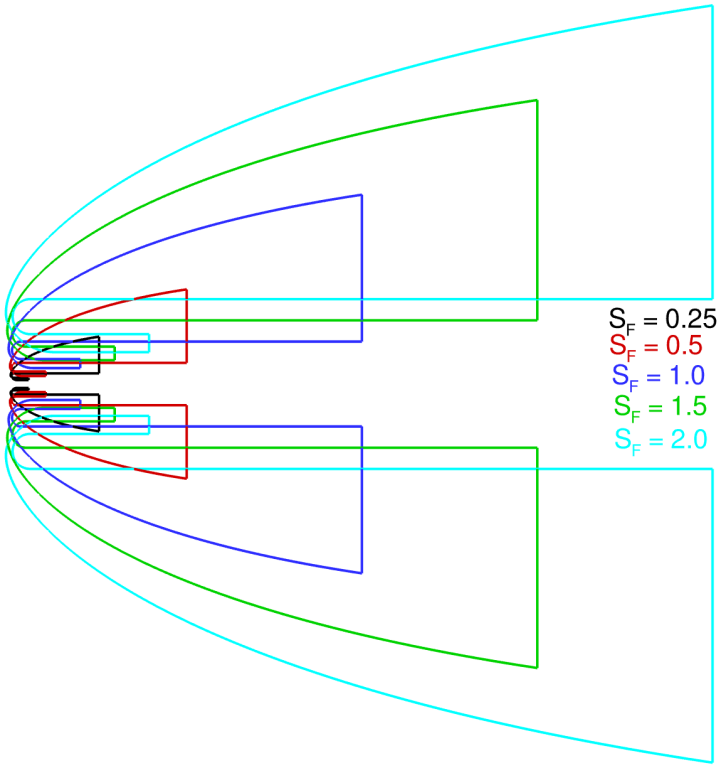

Figure 6.55: Variation of the Geometrical scaling factor S_F

Geometrical up- and downscaling does not change the expansion ratio and divergence characteristics of the ED and TIC nozzles. As a result, for all geometrical scaling factors S_F, the Eulerian I_{sp} is the same as for $S_F = 1.0$ since viscous effects and heat exchange are not considered. For all ED and TIC nozzles, the Eulerian I_{sp} is 457.084 s and 444.029 s. These are the I_{sp} values corresponding to those in Fig. 6.4 with a truncation length of $L = 2\ m$.
Then, viscous-adiabatic and viscous-isothermal simulations are performed for the ED and TIC nozzles with various geometrical scaling factors S_F, and the I_{sp} is evaluated. The viscosity and heat exchange efficiencies η_{Vis} and η_{Heat} are calculated from the Eulerian, viscous-adiabatic, and viscous-isothermal performances. These are shown graphically in Fig. 6.56 as a function of the geometrical scaling factor S_F. The viscosity efficiencies η_{Vis} decrease for the ED and TIC nozzles as S_F decreases. This is because of increasing boundary layer effects corresponding to higher friction losses. In the case of the ED nozzle, the viscosity efficiencies are lower than that of the TIC nozzle and decrease even more rapidly as S_F decreases due to the larger wall surface. For the scaling factor $S_F = 1$, the ratio of surface areas A_{ED}/A_{TIC} is approximately 1.6, as shown in Fig. 6.8 for $L = 2\ m$. However, by changing the geometrical scaling factor S_F equally for the ED and TIC nozzles, the ratio of surface areas will not change since the wall surface areas of both nozzles change by the same factor. For instance, halving the geometrical scaling factor quarters the wall surface area of the nozzle.

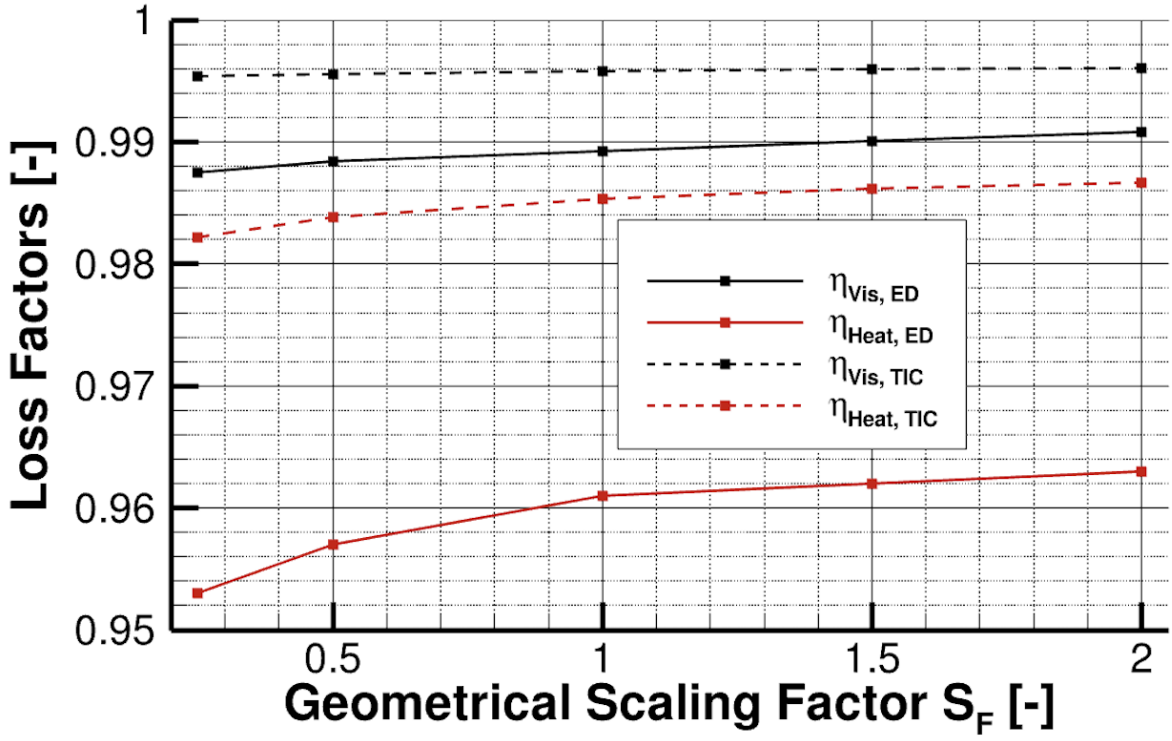

Figure 6.56: Viscous and heat exchange efficiencies η_{Vis} and η_{Heat} as a function of the geometrical scaling factor S_F

Besides the viscosity efficiencies η_{Vis}, the heat exchange efficiencies η_{Heat} of the ED nozzles are lower than those of the TIC for all geometrical scaling factors S_F, as shown in Fig. 6.56. This is due to higher integral wall heat flux, as shown in Fig. 6.57. The reasons for the higher ED nozzle heat exchange are larger wall surface areas and high wall surface areas exposed to high peak heat flux. For the ED and TIC nozzles with $S_F = 1.0$, this is explained in more detail in Subsection 6.1.1. In addition, the ED nozzles feature a more pronounced decrease in η_{Heat} with decreasing scaling factor S_F than the TIC nozzles. The reason is that the ED nozzles suffer more from heat exchange, and as a result, the ED nozzle integral wall heat flux increases roughly linearly relative to that of the TIC as S_F is decreased.

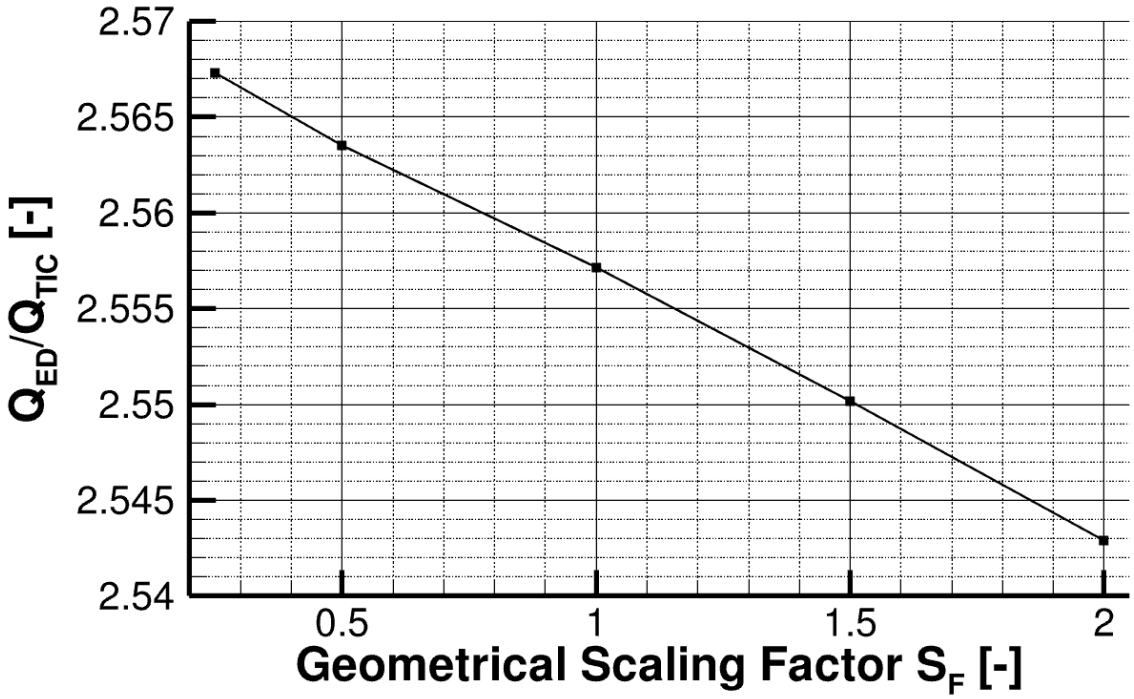

Figure 6.57: Ratio of integral wall heat flux of ED and TIC Q_{ED}/Q_{TIC} as a function of the geometrical scaling factor S_F

Chapter 7

Conclusion

Conventional nozzles demonstrate low performance-to-weight ratios when achieving high area ratios, negatively impacting the accessible orbit payload capacity. This is because the high area ratio needed for high vacuum performance inevitably results in long and heavy nozzles. Advanced nozzle concepts (ANC) like plug/ aerospike, dual bell, and expansion-deflection (ED) nozzles have been explored to address this issue since the 1950s and 60s. ED nozzles continuously adapt to the local ambient pressure, demonstrating, in theory, ideal performance. However, they suffer from overexpansion losses and aspiration drag, making them inferior to plug nozzles and even dual bell nozzles for moderate nozzle pressure ratios. In high altitude operation, ED nozzles show advantages over conventional nozzles due to lower divergence losses and, thus, possibly shorter design lengths promising higher performance-to-weight ratios as the plug nozzle. However, in contrast to plug nozzles, they feature less radial throat distances from the symmetry axis, reducing the wall surface exposed to the peak heat flux and thus the needed heat pick up from the cooling system. All these combined make the ED nozzle a promising concept for upper-stage applications.

The ideal supersonic wall contours of the ED nozzle which provide isentropic, i. e. shock-free expansion, are calculated by a method approximating the MOC. Friction effects are not taken into account, and the expansion process is considered adiabatic. The method is based on the Prandtl-Meyer expansion. Hence, the characteristic lines are assumed to be straight, the specific heat ratio constant, and theoretically, the method is only valid for planar flows. The design of an ED nozzle is more complex than the design of a conventional nozzle because the throat is shifted in the radial direction and possibly inclined w. r. t. the symmetry axis. As a result, many different design parameter combinations are possible. For this reason, the approximate contouring method is integrated into several design procedures that find an ED nozzle iteratively based on given input parameters. The design of the subsonic nozzle walls is kept as simple as possible and realized only by straight lines and arcs. By using the design tool, a Baseline ED nozzle is designed based on *VINCI* engine characteristics.

An in-house solver is used for the CFD simulations in this work. The CFD models are verified, and the results are validated for two conventional test case engines. On the one hand, the *RL10A-3-3A* engine is considered, which delivers less thrust than the reference *VINCI* engine. On the other hand, the *SSME* is used, providing higher thrust than *VINCI*. A thermally perfect gas is assumed for the simulations. In addition, both non-reactive and reactive cases are considered. For the non-reactive and reactive setups, first, viscous-adiabatic and Eulerian simulations are conducted on three different grid levels, and the I_{sp} is evaluated for the different grid levels. Verification is proven from the results. For the medium grids of the *RL10A-3-3A* and the *SSME* engines, also reactive-isothermal simulations ($T_w = 700\ K$) are performed. Validity is

demonstrated since the delivered I_{sp} is overpredicted by just 1.587 % for the *RL10A-3-3A* and 0.549 % for the *SSME*.
Then, for the Baseline ED nozzle and a comparable Baseline TIC nozzle, preliminary non-reactive Eulerian, viscous-adiabatic, and viscous isothermal ($T_w = 700\ K$) simulations are conducted assuming a thermally perfect gas. The simulations are conducted for three grid levels, and the I_{sp} values are evaluated. The grid errors are calculated by comparing the performance values with the extrapolated I_{sp} for an infinitely fine grid. In this way, suitable meshes with low grid errors and possibly low computing times are selected for the Baseline ED and TIC nozzles that can be used in the parametric analyses. The parametric analyses discuss the influence of several design parameters on the performance.
First, the influence of the outer nozzle dimensions, i. e. the truncation length and radius is investigated. The simulations demonstrate ED nozzle performance advantages over the TIC nozzles due to lower divergence losses. This advantage is particularly evident for short truncation lengths (assuming always a constant truncation radius) and high truncation radii (assuming always a constant truncation length). However, if the ED and TIC nozzles are designed for the same performance, lower divergence losses can also lead to more compactness. Moreover, the ED nozzles suffer more from viscous losses due to a larger wall surface area coming mainly from the external wall. Even though this means that the ED nozzle loses some of its performance or compactness advantages, the viscous losses are not the primary loss source. Indeed, heat exchange losses are more critical, assuming that no heat is recovered, for instance, by not using an expander engine cycle. The heat exchange of the ED nozzles is higher than that of the TIC nozzles due to a larger wall surface area and the large wall surface being exposed to high peak heat flux.
The design value of the specific heat ratio and the radial throat shift have a similar effect on the performance losses. Reducing the design value for the specific heat ratio and increasing the radial throat shift increases the radial shift of the external and internal walls from the symmetry axis. This makes the external wall bulgier, reducing the divergence losses. However, also the wall surface increases. Even if this slightly increases the viscous losses, the influence on the performance can be neglected. In contrast, the influence on heat exchange cannot be neglected since the wall surface exposed to the peak heat flux increases, contributing to higher heat exchange.
The internal and external throat wall radii do not influence the divergence losses and have a negligible effect on an ED nozzle's viscous losses. This is not the case for the heat exchange. An increase of the internal and a decrease of the external wall throat radius considerably increases the wall surface area exposed to high peak heat flux and, thus, the heat exchange.
Finally, the influence of the geometrical scaling is analyzed for the TIC and ED nozzles. The Baseline ED and TIC nozzles are the starting point for this investigation. The simulations show that the ED nozzle suffers more from geometrical downscaling than the TIC nozzle. This is due to higher boundary layer effects and higher heat exchange.

Bibliography

[1] NASA Webpage. (2023). *Space Shuttle System.* `http://www.nasa.gov/returntoflight/system/system_STS.html`. Accessed: 15-8-2023.

[2] Gulczynski, Mateusz & Vennitti, Andrea & Scarlatella, Giuseppe & Dominguez Calabuig, Guillermo J. & Blondel-Canepari, Lily & Weber, Felix & Sarritzu, Alberto & Bach, Christian & Deeken, Jan & Schmiel, Tino & Bianchi, Daniele & Pasini, Angelo. (2021). *RLV applications: challenges and benefits of novel technologies for sustainable main stages.*

[3] Gloder, Alessia & Apel, Uwe & Bianchi, Daniele & Bonetti, Davide & Deeken, Jan & Hendrick, Patrick & Hijlkema, Jouke & Lavagna, Michelle & Pasini, Angelo & Sippel, Martin & Stoll, Enrico & Waxenegger-Wilfing, Günther & Tajmar, Martin & Bach, Christian & Prevereaud, Ysolde. (2020). *Ascension: An innovative network to train the pace access leaders of tomorrow.*

[4] Sutton, G. P. & Biblarz, O.. (2017). *Rocket Propulsion Elements.* Ninth Edition. John Wiley and Sons, Inc.. ISBN 978-1-118-75388-0.

[5] Stark, Ralf. (2005). *Flow Separation in Rocket Nozzles, a Simple Criteria.* DOI: 10.2514/6.2005-3940.

[6] Summerfield, M. & Forster, C. & Swan, W.. (1954). *Flow Separation in Overexpanded Supersonic Exhaust Nozzles.* Jet propulsion, Volume 24. Number 9. Pages 319-321.

[7] Hagemann, Gerald & Immich, Hans & Nguyen, T. & Dumnov, Gennady. (1998). *Advanced Rocket Nozzles.* Journal of Propulsion and Power. Volume 14. Pages 620-633.

[8] Castro, J. H. & Bustamante, R. B.. (1993). *Development and qualification of a translating nozzle extension system for the RL10A-4 rocket engine.* AIAA/SAE/ASME/ASEE, Joint Propulsion Conference and Exhibit. `https://doi.org/10.2514/6.1993-2135`.

[9] Pichon, T. & Barreteau, R.. (2017). *Composite Nozzle Extension Assembly for the RL10 Engine Family.* 53rd AIAA/SAE/ASEE Joint Propulsion Conference. DOI: 10.2514/6.2017-5066.

[10] Rao, G. V. R.. (1960). *The ED Nozzle.* Astronautics, Pages 28-51.

[11] Taylor, N. V.. (2002). *An integrated approach to expansion deflection nozzle analysis (Ph.D. Thesis).* University of Bristol.

[12] Rao, G. V. R.. (1960). *Analysis of a new concept rocket nozzle.* Journal of Liquid Rockets and Propellants. 2:669-682.

[13] Nasuti, Francesco & Fiore, Matteo & Messina, Vincenzo & Valeriani, Alessio & Bianchi, Daniele. (2021). *Design and Evaluation of Aerospike Nozzles for an Upper Stage Applica-*

tion. Conference: 7th edition of the Space Propulsion Conference SP2020+1 (Online virtual conference). Book: Proceeding of the Space Propulsion Conference 2010+1.

[14] Wasko, R. A. (1968). *Performance of annular Plug and Expansion - Deflection nozzles including external flow effects at transonic Mach numbers*. Lewis Research Center. Technical Note NASA TN D-4462.

[15] Taylor, Neil & Steelant, Johan & Bond, Robert. (2011). *Experimental comparison of Dual Bell and Expansion Deflection Nozzles*. 47th AIAA/ASME/SAE/ASEE Joint Propulsion Conference and Exhibit 2011. DOI: 10.2514/6.2011-5688.

[16] Goetz, Andreas & Hagemann, Gerald & Kretschmer, Joachim & Schwane, Richard. (2005). *Advanced Upper Stage Propulsion Concept - The Expansion - Deflection Upper Stage*. DOI: 10.2514/6.2005-3752.

[17] Meyers, R. A.. (2001). *Encyclopedia of Physical Science and Technology*. Elsevier Science Ltd.

[18] Löbbecke, W.. (1964). *Entwicklung und Erprobung einer ED Düse*. MBB-TR-588.

[19] Koelle, D. E.. (1965). *Design Criteria of Advanced High-Energy Upper Stages*. MBB-RF-121-PUB.

[20] Goroch, W. D. et. al.. (2001). *Development of an Advanced Combustion Chamber Construction*. Scientific and Technical Anniversary Collection. ISBN 5-89981-226-5.

[21] Mayer, W.. (2001). *Cryogenic rocket engine research within the National Technology Program TEKAN at the German Aerospace Center*. Aerospace Science and Technology. Volume 5. Page 273-282. DOI: .1016/S1270-9638(01)01106-3

[22] Astronautix Webpage. (2019). *RD0126E rocket engine*. `http://www.astronautix.com/r/rd-0126.html`. Accessed: 25-10-2023.

[23] Sauer, R. (1944). *General characteristics of the flow through nozzles at near critical speeds*. Technical Report TM1147, NACA.

[24] Schorr, C. (1970). *Constant chamber pressure throttling of an expansion-deflection nozzle*. Journal of Spacecraft. 7(7):843-847, Jul 1970.

[25] Mueller, T. J.. (1968). *Determination of the Turbulent Base Pressure in Supersonic Axisymmetric Flow*. Journal of Spacecraft and Rockets. Volume 5. Number 1.

[26] Taylor, N. V. & Hempsell, C. M.. (2002). *Vacuum Thrust Optimised Expansion Deflection Nozzles*. IAC-02-S.2.02.

[27] Angelino, Gianfranco. (1964). *Approximate Method for Plug Nozzle Design*. AIAA Journal. Volume 2. Number 10.

[28] Mathworks Webpage. (2023). *fzero - Root of nonlinear function*. `https://www.mathworks.com/help/matlab/ref/fzero.html`. Accessed: 22-11-2023.

[29] Mathworks Webpage. (2023). *fsolve - Solve system of nonlinear equations*. `https://it.mathworks.com/help/optim/ug/fsolve.html`. Accessed: 23-11-2023.

[30] Ariane Group Webpage. (2023). *HM-7B Engine*. `https://www.ariane.group/wp-content/uploads/2020/06/HM7B_2017_11_PS_EN_Web.pdf`. Accessed: 01-12-2023.

[31] Alliot, Patrick & Delange, J. F. & Korver, V. & Sannino, J. M. & Lekeux, A. & Vieille, B.. (2019). *VINCI, the european reference for ariane 6 upper stage cryogenic propulsive system.* Pages 481-494. DOI: 10.1051/eucass/201911481.

[32] Sabin, P. & Michallet, A. & Meyers, N. & Durteste, S. & Delange, J. F.. (2019). *VULCAIN 2.1, the European reference for Ariane 6 Lower stage cryogenic propulsive system.* 8th European Conference for Aeronautics and Space Sciences (EUCASS). DOI: 10.13009/EUCASS2019-639.

[33] Merino, J. & Patzelt, A. & Steinacher, A. & Windisch, M. & Heinrich, G. & Forster, R. & Bauer C.. (2017). *ARIANE 6 – Tanks and Structures for the new European Launcher.* Deutscher Luft- und Raumfahrtkongress. DocumentID: 450255.

[34] McBride, B. J. & Gordon, S.. (1994). *Computer Program for Calculation of Complex Chemical Equilibrium Compositions and Applications I. Analysis.* NASA Lewis Research Center.

[35] McBride, B. J. & Gordon, S.. (1996). *Computer Program for Calculation of Complex Chemical Equilibrium Compositions and Applications. II. Users Manual and Program Description.* NASA Lewis Research Center.

[36] Ariane Group Webpage. (2023). *Ariane Group - Vinci engine.* `https://www.ariane.group/wp-content/uploads/2020/06/VINCI_2020_04_DS_EN_Eng_Web.pdf`. Accessed: 30-11-2023.

[37] Leto, Angelo & Votta, Raffaele & Bonfiglioli, Aldo. (2016). *Preliminary Design Method of a Turbopump Feed System for Liquid Rocket Engine Expander Cycle.* Energy Procedia (Elsevier). Volume 101. Pages 614-621. DOI:10.1016/j.egypro.2016.11.078.

[38] Alliot, Patrick & Fiorentino, Costanza & Edeline, Emmanuel. (2013). *Progress of the VINCI engine system development.* 4th European Conference for Aeronautics and Space Sciences (EUCASS). DOI: 10.2514/6.2011-5552.

[39] ESA Webpage. (2023). *All engines for Ariane 6 complete qualification tests.* `https://www.esa.int/Enabling_Support/Space_Transportation/Ariane/All_engines_for_Ariane_6_complete_qualification_tests`. Accessed: 30-11-2023.

[40] (Old) EADS Webpage. (Memento: 29-09-2015). *HM-7 and HM-7B Rocket Engine - Thrust Chamber.* `https://web.archive.org/web/20150929022705/http://cs.astrium.eads.net/sp/launcher-propulsion/rocket-engines/hm7b-rocket-engine.html`. Accessed: 01-12-2023.

[41] NASA Webpage. (2023). *Chemical Equilibrium Applications (CEA).* `https://software.nasa.gov/software/LEW-17687-1`. Accessed: 04-12-2023.

[42] Schwarze, R.. (2013). *CFD-Modellierung - Grundlagen und Anwendungen bei Strömungsprozessen.* Springer. ISBN 978-3-642-24378-3.

[43] Moukalled, F. & Mangani, L. & Darwish M. (1954). *The Finite Volume Method in Computational Fluid Mechanics - An Advanced Introduction with OpenFOAM and MATLAB.* Fluid Mechanics and its Applications 113. Series Editor A. Thess.

[44] Herráiz, P. J. et. al.. (2019) *Development of a MATLAB plume impingement tool for fast system analysis.* 8th European Conference for Aeronautics and Aerospace Sciences (EUCASS).

[45] G.A.B. Consulting Pty Ltd. (2006). *The DS2V Program User's Guide.* Version 3.8.

[46] Lecheler, S.. (2014). *Numerische Strömungsberechnung*. Springer. ISBN 978-3-658-05201-0.

[47] Friedrichs, J. & Bode, C.. (2014). *Numerische Simulation (CFD)*. Lecture Scripts. TU Brunswick. Institute for Aircraft propulsion and fluid machines.

[48] Betti, B.. (2012). *Flow Field and Heat Transfer Analysis of Oxygen / Methane Liquid Rocket Engine Thrust Chambers*. PhD Thesis. Sapienza University of Rome.

[49] Concio, P.. (2022). *Heat Transfer Modelling and Analysis of Oxygen/Methane Uncooled and Film-Cooled Liquid Rocket Engines*. PhD Thesis. Sapienza University of Rome.

[50] Wang, Rong & Balciunaite, Ugne & Chen, Juncai & Yuan, Cheng & Owens, Alec & Tennyson, Jonathan. (2013). *NASA Polynomial representation of molecular specific heats*. Journal of Quantitative Spectroscopy and Radiative Transfer (Elsevier). Volume 306.

[51] McBride, B. J. & Zehe, M. J.. (2002). *NASA Glenn Coefficients for Calculating Thermodynamic Properties of Individual Species*. Glenn Research Center.

[52] McAllister, Sarah & Chen, Jyh-Yuan & Fernandez-Pello, A. Carlos. (2011). *Fundamentals of Combustion Processes*. Springer. Mechanical Engineering Series.

[53] Svehla, R. A.. (1995). *Transport Coefficients for the NASA Lewis Chemical Equilibrium Program*. NASA Lewis Research Center.

[54] Anderson, J. D.. (1993). *Hypersonic and High-Temperature Gas Dynamics*. AIAA Education series. second edition ed.

[55] Sutton, K. & Gnoffo, P. A.. (1998). *Multi-Component Diffusion with Application to Computational Aerodynamics*. 7th AIAA/ASME Joint Thermophysics and Heat Transfer Conference, AIAA 98-2575.

[56] Ferziger, J. H. & Perić, M.. (2002). *Computational Methods for Fluid Dynamics*. Springer. ISBN 978-3-642-56026-2.

[57] Spalart, P. R. & Allmaras, S. R.. (1994). *A One-Equation Turbulence Model for Aerodynamic Flow*. La Recherche Aerospatiale: Bulletin Bimestriel de l'Office National d'Etudes et de Recherches Aerospatiales 1, Page 5–21.

[58] Roy, C. J. & McWherter-Payne, M. A. & Oberkampf W. L. (2003). *Verification and Validation for Laminar Hypersonic Flowfields, Part 1: Verification*. AIAA Journal, Vol. 41, No. 10.

[59] Binder, M. & Tomsik, T. & Veres, J. P.. (1997). *RL10A-3-3A Rocket Engine Modeling Project*. NASA Lewis Research Center.

[60] Thompson, J. R.. (1980). *Space Shuttle Main Engine*. The Space Congress Proceedings. 5.

[61] Leto, A. J. (2020). *Investigation of a Radial Turbines Compatibility for Small Rocket Engine*. E3S Web of Conferences 197, 11009. 75th National ATI Congress.

[62] Bozic, O. (2017). *Lecture Script Space Propulsion*. Institute for Space Systems. Technical University Braunschweig, Germany.

[63] Wang, Ten-See. & Ghent, Yen-Sen. (1993). *Unified Navier-Stokes Flowfield and Performance Analysis of Liquid Rocket Engines*. Journal of Propulsion and Power. Volume 9. No. 5.

[64] Yetter, R. A. & Dryer, F. L. & Rabitz, H.. (1991). *A comprehensive reaction mechanism for carbon monoxid/hydrogen/oxygen kinetic*. Combustion Science and Technology, 79:97-128.

[65] Betti, B. & Bianchi, D. & Nasuti, F. & Martelli, E.. (2016). *Chemical reaction effects on heat loads of CH4/O2 and H2/O2 rockets*. AIAA Journal. Volume 54. Number 5.

[66] Roach, P. J.. (1997). *Quantification of Uncertainty in Computational Fluid Dynamics*. Annual review of Fluid Mechanics.

Appendix A

Contouring codes

A.1 Supersonic walls

```
format long;
close all;
clear all;
clc;

%%%%%%%%%%%%%%%%%%%%
% Program Start    %
% Ideal Contouring %
% Const. Gamma     %
%%%%%%%%%%%%%%%%%%%%

myfun = @(AR_desired,A_t,pc,Tc,R,r_non,Rb,r_trunc_desired,...
    x_trunc,calculation_option) calc(AR_desired,A_t,pc,Tc,R,...
    r_non,Rb,r_trunc_desired,x_trunc,calculation_option);

% '1' - 1. Design procedure
% '2' - 2. Design procedure
% '3' - 3. Design procedure
calculation_option='1';

% Throat area
A_t=0.015289469;

% Chamber pressure
pc=6120000;
% Chamber temperature
Tc=3555.66;
% Specific gas constant
R=631.23497604;

% Base radius Rb
Rb=0.165;
```

```
% Dimensionless arc radius of the external wall
% in the internal expansion region
r_non=0.039077663733155;

% Truncation exit radius
r_trunc_desired=-1.0807540850;

% Truncation exit length
x_trunc=2;

fun = @(AR_desired) myfun(AR_desired,A_t,pc,Tc,R,...
    r_non,Rb,r_trunc_desired,x_trunc,calculation_option);

% Iteration interval for full-length expansion ratio
int=[330 331]

AR_desired_obtained = fzero(fun,int)

function r_diff = calc(AR_desired,A_t,pc,Tc,R,r_non,...
    Rb,r_trunc_desired,x_trunc,calculation_option)

% Function area ratio
AR = @(M,g) (1./M)*((1.+0.5*(g-1.)*M^2)/(0.5*(g+1.)))...
    ^(0.5*(g+1.)/(g-1.));

% Function vacuum thrust coefficient
CFvac = @(M,g) sqrt(g*((2)/(g+1))^((g+1)/(g-1)))*...
    sqrt((g*M^2)/(1.+0.5*(g-1.)*M^2))+ AR(M,g)/...
    (1.+0.5*(g-1.)*M^2)^(g/(g-1.));

% Function Prandtl-Meyer function
om = @(M,g) sqrt((g+1.)/(g-1.))*atan(sqrt((g-1.)/...
    (g+1.)*(M^2-1.))) - atan(sqrt(M^2-1.));

%%%%%%%%%%%%%%%%%%%%%%%%%%%%%%%%
% Set up for Design Procedures %
%%%%%%%%%%%%%%%%%%%%%%%%%%%%%%%%

switch calculation_option
    case '1'
        % Exit Mach number internal expansion
        Mi=1.005903052692835;
        % Specific heat ratio
        g=1.138;
        func = @(x) AR(x,g)-AR_desired;
        Me_int = [4.0 12.00];
        Me = fzero(func,Me_int);
    case '2'
        % Specific heat ratio
```

```
        g=1.138;
        % Throat angle
        throat_angle = -125;
        func = @(x) AR(x,g)-AR_desired;
        Me_int = [9.0 11];
        Me = fzero(func,Me_int);
        func = @(x) 2*om(x,g)-om(Me,g)-throat_angle*...
            pi/180;
        Mi_int = [1.0 3];
        Mi = fzero(func,Mi_int)
    case '3'
        % Exit Mach number internal expansion
        Mi=1.005903052692835;
        % Throat angle
        throat_angle = -125;
        fun=@(x) [AR(x(1),x(2))-AR_desired; 2*...
            om(Mi,x(2))-om(x(1),x(2))-throat_angle*pi/180];
        x = fsolve(fun,[4.98 1.13])
        Me=x(1)
        g=x(2)
    otherwise
        warning('choose a correct calculation option')
end

%%%%%%%%%%%%%%%%%
%%%%%%%%%%%%%%%%%%%%%%%%%%%%%%%%%%%%%%%%
%%%%% Start of Simple Calculations %%%%%
%%%%%%%%%%%%%%%%%%%%%%%%%%%%%%%%%%%%%%%%

% Calculation of the full-length exit radius
Re=sqrt((AR(Me,g)*A_t/pi)+Rb^2);

% Calculation of the dimensionless base radius
etab=Rb/Re;

% Calculation of the full-length exit area
A_e=pi*(Re^2-(etab*Re)^2);

% Arc radius of the external wall
% in the internal expansion region
Rc=Re*r_non;

% Full-length area ratio
AR2=AR(Me,g);

%%%%%%%%%%%%%%%%%%%%%%%%%%%%%%%%%%%%%%%%
%%%%% Start of Angelino Method %%%%%
%%%%%%%%%%%%%%%%%%%%%%%%%%%%%%%%%%%%%%%%
```

```
% Angle of that velocity vector is turned between Mi and Me
tt = om(Mi,g)-om(Me,g);
tt_deg=(om(Mi,g)-om(Me,g))*180/pi;

% Coordinates of last internal Characteristic on Pintle
% (y value)
et=-sqrt(etab^2 - Mi*sin(-(tt+asin(1./Mi)))*AR(Mi,g)/...
    AR(Me,g)*(1-etab^2));

% Coordinates of last internal Characteristic on Pintle
% (x value)
xt=-(-etab-et)/tan((tt+asin(1./Mi)));

% Middle point of the Circle creating the throat (Rc/Re)
% coordinates normalized to Re
xi_c  = xt + (Rc/Re)*sin(tt);
eta_c = et - (Rc/Re)*cos(tt);

%%%%%%%%%%%%%%%%%%%%%%%%%%%%%%
%%%%% Internal Expansion %%%%%
%%%%%%%%%%%%%%%%%%%%%%%%%%%%%%

% 101 internal Characteristics
for i = 1:101

    M(i)  = 1. + (Mi-1.)*(i-1.)/100.;

    % Theta of the respective internal characteristic
    th(i) = 2.*om(Mi,g)-om(Me,g)-om(M(i),g);

    % Coordinates of the inf contour of internal expansion
    % area (x values)
    xi_inf(i)  = xi_c  - (Rc/Re)*sin(th(i));

    % Coordinates of the inf contour of internal expansion
    % area (y values)
    eta_inf(i) = eta_c + (Rc/Re)*cos(th(i));

    % Coordinates of the sup contour of the internal
    % expansion area (y values)
    eta_sup(i)=-sqrt((eta_inf(i))^2-(AR(M(i),g)/AR(Me,g))* ...
        M(i)*sin(pi-(th(i)+asin(1./M(i))))*(1-etab^2));

    % Coordinates of the sup contour of the internal
    % expansion area (x values)
    xi_sup(i)=xi_inf(i)-((eta_sup(i)-eta_inf(i))/ ...
        tan((pi-(th(i)+asin(1./M(i))))));

    % Calculate other flow properties along the characteristics
```

```
    T(i)   = Tc/(1.+0.5*(g-1.)*M(i)^2);
    p(i)   = pc/(1.+0.5*(g-1.)*M(i)^2)^(g/(g-1.));
    rho(i) = p(i)/(R*T(i));
    a(i)   = sqrt(g*R*T(i));
    V(i)   = M(i)*a(i);
end

%%%%%%%%%%%%%%%%%%%%%%%%%%%%%%
%%%%% External Expansion %%%%%
%%%%%%%%%%%%%%%%%%%%%%%%%%%%%%

% 101 external Characteristics
for i = 102:202

    M(i)  = Mi + (Me-Mi)*(i-102.)/100.;

    % Theta of the respective internal characteristic
    th(i) = om(M(i),g)-om(Me,g);

    % Coordinates of the inf contour of external
    % expansion area (y values)
    eta_inf(i)=-sqrt(etab^2+sin(-(th(i)-asin(1./M(i))))* ...
        M(i)*(AR(M(i),g)/AR(Me,g))*(1-etab^2));

    % Coordinates of the inf contour of external expansion
    % area (x values)
    xi_inf(i)=(eta_inf(i)+etab)/tan((th(i)-asin(1./M(i))));

    % Calculate other flow properties along the characteristics
    T(i)   = Tc/(1.+0.5*(g-1.)*M(i)^2);
    p(i)   = pc/(1.+0.5*(g-1.)*M(i)^2)^(g/(g-1.));
    rho(i) = p(i)/(R*T(i));
    a(i)   = sqrt(g*R*T(i));
    V(i)   = M(i)*a(i);

end

%%%%%%%%%%%%%%%%%%%%%%%%%%%%%%%%%%%%%%%%
% Full Length Coordinate Handling %
%%%%%%%%%%%%%%%%%%%%%%%%%%%%%%%%%%%%%%%%

% absolute inf contour points before positioning
x_inf_abs_before=xi_inf*Re;
y_inf_abs_before=eta_inf*Re;

% absolute sup contour points before positioning
x_sup_abs_before=xi_sup*Re;
y_sup_abs_before=eta_sup*Re;
```

```
%%%%%%%%%%%%%%%%%%%%%%% Positioning Input %%%%%%%%%%
x_0_location=-(0.012518010855843-x_sup_abs_before(1));
%%%%%%%%%%%%%%%%%%%%%%%%%%%%%%%%%%%%%%%%%%%%%%%%%%%%

% Repositioning of the inf and abs contour
for i = 1:length(x_inf_abs_before)
    x_inf_abs(i)=x_inf_abs_before(i)-x_0_location;
    y_inf_abs(i)=y_inf_abs_before(i);
end

for i = 1:length(x_sup_abs_before)
    x_sup_abs(i)=x_sup_abs_before(i)-x_0_location;
    y_sup_abs(i)=y_sup_abs_before(i);
end


%%%%%%%%%%%%%%%%%%%%%%%%%%%%%%%%%%%%%%
%%%%% Plot in absolute Coordinates %%%%%
%%%%%%%%%%%%%%%%%%%%%%%%%%%%%%%%%%%%%%

figure(1)

plot(x_inf_abs,y_inf_abs)

hold on

plot(x_sup_abs,y_sup_abs)

% Symmetry axis
plot([x_sup_abs(1) x_inf_abs(end)],[0 0],'--')

axis equal

% Formatting of the Plot
title(['ED Nozzle (Full Length)'])
xlabel('x [m]')
ylabel('y [m]')


%%%%%%%%%%%%%%%%%%%%%%%%%%%%%%%%%%%%%%%%%%%%%%%%%%%%%%%%%%%%%%%%%%%%%%%
%%%%% Plot in absolute Coordinates with Truncation %%%%%
%%%%%%%%%%%%%%%%%%%%%%%%%%%%%%%%%%%%%%%%%%%%%%%%%%%%%%%%%%%%%%%%%%%%%%%

figure(2)

plot(x_inf_abs,y_inf_abs)

hold on
```

```
plot(x_sup_abs,y_sup_abs)

% Symmetry axis
plot([x_sup_abs(1) x_inf_abs(end)],[0 0],'--')

plot(x_inf_abs,-y_inf_abs)

hold on

plot(x_sup_abs,-y_sup_abs)

axis equal

% Formatting of the Plot
title(['ED Nozzle (Truncated)'])
xlabel('x [m]')
ylabel('y [m]')

% Calculation of y value at truncation point
r_trunc = interp1(x_inf_abs,y_inf_abs,x_trunc,'linear');

% Formatting of the Plot
title(['ED Nozzle (Truncated) at x_{trunc}= ' ...
    num2str(x_trunc) ' m'])
xlabel('x [m]')
ylabel('y [m]')
xlim([0 x_trunc])
ylim([r_trunc*1.1 -r_trunc*1.1])


r_diff=r_trunc-r_trunc_desired;

%%%%%%%%%%%%%%%%%%%%%%%%%%%%%%%%%%%%%%%%%%%%%%%%%%%%%%%%%%%%%%%%%%%%%%%
%%%%%%%%%%%%%%%% Control of Parameters %%%%%%%%%%%%%%%%%%
%%%%%%%%%%%%%%%%%%%%%%%%%%%%%%%%%%%%%%%%%%%%%%%%%%%%%%%%%%%%%%%%%%%%%%%

% the y value of the beginning of the sup contour
y_sup_abs_start=y_sup_abs(1)
angle_throat=(2*om(Mi,g)-om(Me,g))*180/pi

end
```

A.2 Subsonic walls

```
format long;
close all;
clear all;
clc;

% Import dataset of inf and sup contours
% from supersonic wall contouring
data_inf = importdata('data_inf.txt')
data_sup = importdata('data_sup.txt')

% Allocation of the x and y coordinates
x_inf=data_inf.data(:,1);
y_inf=data_inf.data(:,2);
x_sup=data_sup.data(:,1);
y_sup=data_sup.data(:,2);

% plot imported inf and sup contours
figure(1)
plot(x_inf,y_inf,'ok')
hold on
plot(x_sup,y_sup)
axis equal

% plot imported inf contour and throat point
% of sup contour
figure(2)
plot(x_inf,y_inf)
hold on
axis equal
plot(x_inf(1),y_inf(1),'ok')
hold on
plot(x_sup(1),y_sup(1),'ok')
hold on

%%%%%%%%%%%%%%%%%%%%%%%%%%%%%
% Start Subsonic Contouring %
%%%%%%%%%%%%%%%%%%%%%%%%%%%%%

% Angle first and second wall contour point
% along the inf contour dowstream the throat
last_ang_inf=atan((y_inf(1)-y_inf(2))/(x_inf(1)-x_inf(2)));

% orthogonal line to last_ang_inf
new_angle_orth_inf=-(pi/2-last_ang_inf);

% slope of orthogonal line to last_ang_inf
m_orth_inf=tan(new_angle_orth_inf);
```

```
% y-axis crossing of orthogonal line to last_ang_inf
n_orth_inf=y_inf(1)-m_orth_inf*x_inf(1);

% several coordinates along orthogonal line of
% last_ang_inf
x_line_orth_inf=linspace(x_inf(1),0.4);
y_line_orth_inf=m_orth_inf*x_line_orth_inf+n_orth_inf;
plot(x_line_orth_inf,y_line_orth_inf,'r')

%%%%%%%%%%%%%%%
% Second Step %
%%%%%%%%%%%%%%%

% Calculation of the throat angle
angle_throat=atan((y_sup(1)-y_inf(1))/(x_sup(1)-x_inf(1)));

% slope of throat line
m=tan(angle_throat);

% y-axis crossing of throat line
n=y_sup(1)-m*x_sup(1);

% several coordinate points along throat line
x_line=linspace(x_inf(1),0.4);
y_line=m*x_line+n;
plot(x_line,y_line,'--k')

%%%%%%%%%%%%%%%%%%%%%%%%%
% Some Input Parameters %
%%%%%%%%%%%%%%%%%%%%%%%%%

% radial shift of straight base
y_base=-0.24;
% axial location of cumbustion chamber
x_cc=0.39;

%%%%%%%%%%%%%%
% Third Step %
%%%%%%%%%%%%%%

% Calculation of middle point of internal wall arc
y_PR2=(y_sup(1)-sin(angle_throat)*y_base)/(1-sin(angle_throat));
x_PR2=x_sup(1)+((y_PR2-y_sup(1))/tan(angle_throat))

plot(x_PR2,y_PR2,'ok')

%%%%%%%%%%%%%%%%%%%%%%%%%
% Some Input Parameters %
%%%%%%%%%%%%%%%%%%%%%%%%%
```

```
% Calculation of the inner thoat circle R1
R2=y_PR2-y_base
% Calculation of the outer circle R2 (From Paper we take R1=3*R2)
R1=R2*3;

%%%%%%%%%%%%%%%
% Fourth Step %
%%%%%%%%%%%%%%%

% Plot of the middle point for outer circle R2
y_PR1=y_inf(1)+sin(new_angle_orth_inf)*R1;
x_PR1=x_inf(1)+cos(new_angle_orth_inf)*R1;

plot(x_PR1,y_PR1,'ok')

%%%%%%%%%%%%%%%%%%%
% Wall Segment VI %
%%%%%%%%%%%%%%%%%%%

angle_out_circle=linspace(new_angle_orth_inf*1.0001, ...
    -90*pi/180,1000);
y_out_circle=y_PR1-sin(angle_out_circle)*R1;
x_out_circle=x_PR1-cos(angle_out_circle)*R1;
plot(x_out_circle,y_out_circle)

%%%%%%%%%%%%%%%%%%%%
% Wall Segment VII %
%%%%%%%%%%%%%%%%%%%%

x_out_straight=linspace(x_out_circle(end)*1.0001, ...
    x_cc,1000);
y_out_straight=linspace(y_out_circle(end),y_out_circle(end), ...
    1000);
plot(x_out_straight,y_out_straight)

%%%%%%%%%%%%%%%%%%
% Wall Segment II %
%%%%%%%%%%%%%%%%%%

angle_inner_circle_1=linspace(angle_throat*1.0001, ...
    -90*pi/180,1000);
y_inner_circle_1=y_PR2-sin(angle_inner_circle_1)*R2;
x_inner_circle_1=x_PR2-cos(angle_inner_circle_1)*R2;
plot(x_inner_circle_1,y_inner_circle_1)

%%%%%%%%%%%%%%%%%
% Wall Segment I %
%%%%%%%%%%%%%%%%%
```

```
x_inner_straight=linspace(x_inner_circle_1(end)*1.0001, ...
    x_cc,1000);
y_inner_straight=linspace(y_inner_circle_1(end), ...
    y_inner_circle_1(end),1000);
plot(x_inner_straight,y_inner_straight)

%%%%%%%%%%%%%%%%%%%%
% Wall Segment III %
%%%%%%%%%%%%%%%%%%%%

angle_inner_circle_2=linspace(angle_throat, ...
    90*pi/180,1000);
y_inner_circle_2=y_PR2-sin(angle_inner_circle_2)*R2;
x_inner_circle_2=x_PR2-cos(angle_inner_circle_2)*R2;
plot(x_inner_circle_2,y_inner_circle_2)

%%%%%%%%%%%%%%%%%%%%%%%%%%%%%%%%%%
% Wall Segment IV (Straight Base) %
%%%%%%%%%%%%%%%%%%%%%%%%%%%%%%%%%%

x_inner_straight_2=linspace(x_inf(end),x_inner_circle_2(1)* ...
    1.0001,1000);
y_inner_straight_2=linspace(y_inner_circle_2(1), ...
    y_inner_circle_2(1),1000);
plot(x_inner_straight_2,y_inner_straight_2)
```